TAILORING STIFFNESS OF DEPLOYABLE ORIGAMI STRUCTURES

BY

EVGUENI T. FILIPOV

DISSERTATION

Submitted in partial fulfillment of the requirements
for the degree of Doctor of Philosophy in Civil Engineering
in the Graduate College of the
University of Illinois at Urbana-Champaign, 2016

Urbana, Illinois

Doctoral Committee:

Professor Glaucio H. Paulino, Georgia Institute of Technology, Chair
Professor Paolo Gardoni
Professor Arif Masud
Doctor Mark Schenk, University of Bristol
Assistant Professor Tomohiro Tachi, University of Tokyo

Abstract

Origami has gained popularity in science and engineering because a compactly stowed system can be folded into a transformable 3D structure with increased functionality. Origami can also be reconfigured and programmed to change shape, function, and mechanical properties. In this thesis, we explore origami from structural and stiffness perspectives, and in particular we study how geometry affects origami behavior and characteristics. Understanding origami from a structural standpoint can allow for conceptualizing and designing feasible applications in all scales and disciplines of engineering.

We improve, verify, and test a bar and hinge model that can analyze the elastic stiffness, and estimate deformed shapes of origami. The model simulates three distinct behaviors: stretching and shearing of thin sheet panels; bending of the flat panels; and bending along prescribed fold lines. We explore the influence of panel geometry on origami stiffness, and provide a study on fold line stiffness characteristics. The model formulation incorporates material characteristics and provides scalable, and isotopic behavior. It is useful for practical problems such as optimization and parametrization of geometric origami variations.

We explore the stiffness of tubular origami structures based on the Miura-ori folding pattern. A unique orientation for zipper coupling of rigidly foldable origami tubes substantially increases stiffness in higher order modes and permits only one flexible motion through which the structure can deploy. Deployment is permitted by localized bending along folds lines, however other deformations are over-constrained and engage the origami sheets in tension and compression. Furthermore, we couple compatible origami tubes into a variety of cellular assemblages that can enhance mechanical characteristics and geometric versatility. Practical applications such as deployable slabs, roofs, and arches are also explored.

Finally, we introduce origami tubes with polygonal cross-sections that can reconfigure into numerous geometries. The tubular structures satisfy the mathematical definitions for flat and rigid foldability, meaning that they can fully unfold from a flattened state with deformations occurring only at the fold lines. From a global viewpoint, the tubes do not need to be straight, and can be constructed to follow a non-linear curved line when deployed. From a local viewpoint, their cross-sections and kinematics can be reprogrammed by changing the direction of folding at some folds.

Acknowledgments

I would like to sincerely thank my research advisor, Professor Glaucio H. Paulino, for his guidance, encouragement and support. His teachings have been profound, and through him I have learned to appreciate research, dedication, and lifelong education. He has inspired me and has brought out the best in me both academically and professionally. I am also indebted to Professor Tomohiro Tachi who welcomed me into his research group at the University of Tokyo in 2014. I have greatly enjoyed his mentorship and assistance since then. His input has helped guide my work and he has presented me with numerous ideas that will encourage my research for years to come. I would like to thank Professor Paolo Gardoni who has also been an invaluable mentor to me. In addition to serving on my committee, I am grateful for his guidance with teaching and navigating academia. I very gratefully thank Professor Arif Masud and Dr. Mark Schenk for their valuable contributions as members of my dissertation committee.

Beyond the formal mentoring through the university my research and academic experiences have been greatly expanded through my colleagues and friends. I have had the privilege to collaborate with many great students, including Ke (Chris) Liu, Junho Chun, Larissa Novelino, Nauroze Abdullah, and Ryan Bahr. They have all brought tremendous ideas that motivated my research. I am also thankful to my colleagues for their valuable insight on research and for many lively discussions. I would like to thank Daniel Spring, Oliver Giraldo-Londono, Leonardo Duarte, Ke (Chris) Liu, Heng Chi, Arun Gain, Xiaojia (Shelly) Zhang, Tomas Zegard, Junho Chun, Tuo Zhao, Emily Daniels, Yang Jiang, Will Colletti, Ludimar Lima de Aguiar, Cameron Talischi, Lauren Beghini, Sofie Leon, Peng Wei, Helio Emmendoerfer Junior, Rejane Canha, and many others for their valuable comments and inspiration. Additionally, I would like to thank Laura Eckstein for her valuable insight to my research as well as her unconditional support, patience, and confidence. She has made me cherish and enjoy the days of my PhD. I am also thankful to my parents and sister who have taught me the value of education and hard work, but have also reminded me to enjoy life.

I am greatly thankful for the financial support from the Natural Science Foundation (NSF) Graduate Research Fellowship (GRFP) and Graduate Research Opportunities Worldwide

(GROW) program. Without their funding I would not have had the flexibility to explore and pursue interesting research topics. Their financial support throughout my Doctorate degree has been a blessing. Furthermore, I gratefully recognize the financial support of the NSF grants CMMI 1538830 and CMMI 1234243. Additionally, I would like to thank the Mavis Future Faculty Fellows Program for their funding and the outstanding preparation provided as part of their engagement.

TABLE OF CONTENTS

CHAPTER 1

INTRODUCTION

Origami is a traditional Japanese art of folding paper into a three dimensional model or figurine. The art form itself has transformed tremendously and has been used as design inspiration for fashion (Waibel, 2016), jewelry (De Ruysser, 2016), architecture (Arquitectos, 2008), and more. In recent years, origami has inspired innovation in a number of fields beyond art, such as education, medicine, science, and engineering (Miura et al., 2015). In its traditional art form, origami requires that a model is folded from a single piece of paper without any cutting or tearing of the paper. However, in the world of technology and engineering, origami has become an umbrella term defining systems that are created from relatively thin material and can be moved or folded into different three dimensional states. In fact, origami has proved to be a technology with numerous practical applications and the potential for future implementations seem to be endless.

1.1 Origami in engineering

Origami brings numerous benefits and improvements to engineering philosophy and design. Historically, origami has gained popularity because a compactly stowed or flat system can be folded into a transformable 3D structure with increased functionality. Folding a flat patterned sheet can reduce manufacturing costs, and can allow for rapid deployment that is otherwise not possible with conventional systems. More recently, innovation with origami has pivoted on its capability to create programmable and re-programmable systems that can change shape, function, and mechanical properties. These new capabilities can lead to applications in various scales from nanometer to meter (Cho et al., 2011); and in various disciplines from bio-medicine to architecture (Peraza-Hernandez et al., 2014).

Some examples of possible applications at different scales are shown in Figure 1.1. At large scales, civil engineering and architectural systems can be deployed to provide disaster relief shelters (Thrall and Quaglia, 2014), or could be used to create façades that adapt to the elements (Del Grosso and Basso, 2010). For space structures, solar arrays could be launched

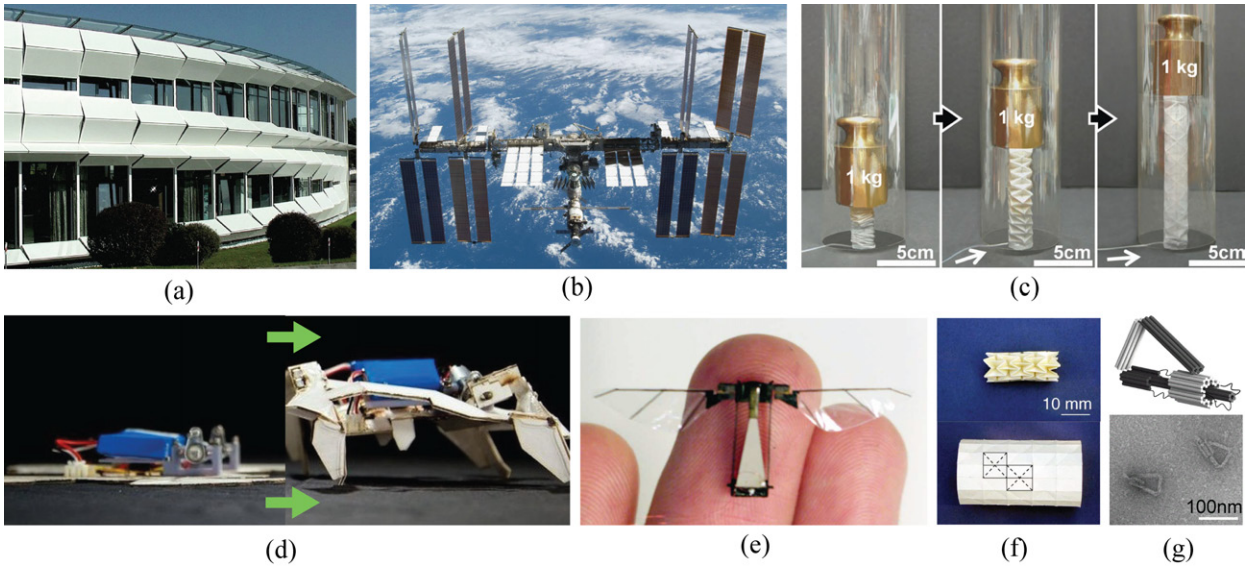

Figure 1.1: Potential engineering structures employing origami based design. (a) Reconfigurable façade on the *Kiefer Technic Showroom*. The panels can be moved to control light and shading within the building (Ernst Giselbrecht + Partner, 2007). (b) International Space Station. Solar arrays can be compactly folded during launch and can deploy for a maximum surface area. The system can also reconfigure to maximize solar insolation (NASA, 2009). (c) Actuator folded using origami concepts can be deployed using internal pressure. Origami can allow for a compact initial configuration, an increased stroke, and a variety of actuator shapes (from Martinez et al. (2012)). (d-e) Robotic systems that use origami to assemble themselves. Origami concepts can also be used to allow for motion within the robotic device (from Felton et al. (2014) and Wood (2008)). (f) Design for a deployable origami stent graft. Biomedical devices created with origami can be placed with minimally invasive techniques and can be deployed within the body (from Kuribayashi et al. (2006)). (g) Nanoscale mechanisms created by folding of DNA. The systems can have controlled reversible motion in multiple directions (from Marras et al. (2015)).

in a compact payload, yet with origami principles they can deploy to maximize surface area and functionality (Campbell et al., 2006; Zirbel et al., 2013). Aircraft with adaptable components could be designed to improve efficiency and flight capabilities (Barbarino et al., 2011). In intermediate (medium) scales, origami could be used for reconfigurable robotics (Felton et al., 2014), actuators (Martinez et al., 2012), toys, and educational tools (Lang, 2011). At much smaller scales, origami could revolutionize biomedical devices (Randall et al., 2012), and could be used for self-assembling robots that would be difficult to construct with conventional methods (Ma et al., 2012). Furthermore, origami inspired metamaterials and devices can be reconfigured, and their mechanical properties can be tuned and tailored (Fuchi et al., 2012; Schenk and Guest, 2013; Silverberg et al., 2014; Filipov et al., 2015a).

Depending on the application, a variety of materials, construction practices, and deploy-

ment techniques may be used (see Appendix A for related literature review). For example, microscopic sheets can be bent by inducing stress concentrations, or large hinged panels can be moved with the use of hydraulic actuators. In this work, we focus on the structural stiffness and geometric aspects of origami, but we do so in an application, scale, and material independent manner. We explore the characteristics of origami forms and assemblages, and aim to tailor the structural stiffness through geometric reconfiguration. The work is applicable at multiple scales (Figure 1.2), and can help in making envisioned origami applications to become a practical reality.

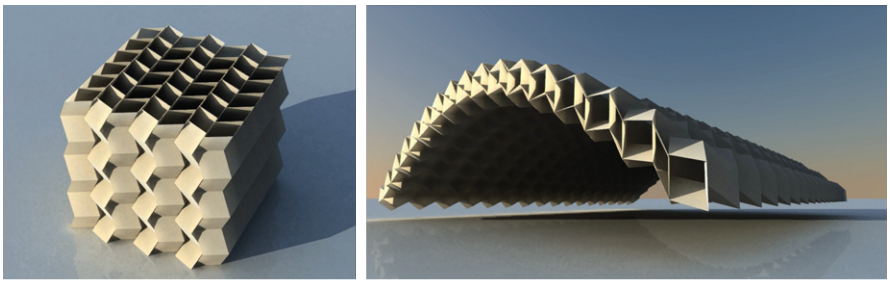

(a) (b)

Figure 1.2: Scale of potential applications of the tubular origami assemblages developed in this thesis (Filipov et al., 2015a). (a) Anisotropic metamaterial with variable stiffness. (b) Deployable roof structure with high out-of-plane stiffness for transformable building design.

1.2 Geometric versatility of origami

Origami can typically be described as a patterned thin sheet consisting of *panels* (facets) and prescribed *folds* (creases). The folds are assigned a polarity of mountain or valley to indicate their direction of folding. The geometry of the pattern is crucial in understanding the appearance, folding kinematics, and structural properties of the origami system. In recent years, the theory and mathematics that govern the folding of origami patterns have received tremendous interest. Similarly, the design of patterns with new intrinsic properties has become an important topic of study. In this section, we briefly discuss different geometric characterizations of origami and show the importance of achieving versatile designs for origami.

1.2.1 Classification of origami systems

Classifying different origami systems is important for understanding their general properties and capabilities. Origami described as ***flat foldable*** are systems that can theoretically fold in a two dimensional plane without panels stretching or intersecting (Justin, 1986; Kawasaki, 1989; Bern and Hayes, 1996; sarah-marie Belcastro and Hull, 2002b,a). This property allows a large system to fold down completely. Origami systems that are ***developable*** can be created by folding of a continuous flat sheet. These systems can allow for easy manufacturing of a three dimensional system that starts from flat sheets. As an example, we show the popular Miura-ori pattern in Figures 1.3 and 1.4.

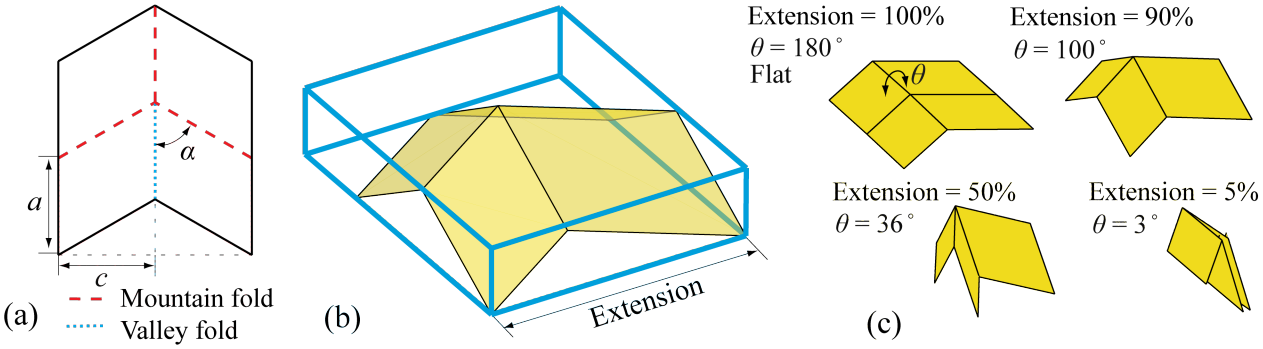

Figure 1.3: A unit cell of the Miura-ori folding pattern. The structure is flat foldable, rigid foldable, developable, and has 1 DOF of folding. (a) Dimensions with mountain and valley fold assignment of the pattern. (b) Pattern folded into a three dimensional unit cell. We use an extension measure calculated as a percentage of the fully deployed system to define the configuration of the structure. The extension, shown as a percentage is typically a more intuitive way to represent the pattern configuration than using specific fold angles. (c) Four folded configurations of the Miura-ori cell. The system can fold from one flat state to another completely flat state (developable and flat foldable).

Rigid foldable origami are those that can deploy with deformations concentrated only at the prescribed fold lines of the pattern (Huffman, 1976; Tachi, 2009a, 2010b; Hull, 2012). Rigid foldability ensures that the panels of the structure do not bend and stretch during the deployment. This property is important for creating large scale structures because distinct hinge elements can be used to facilitate the motion of folds, and realistic materials can be used to create thickened panels of the structure. The number of ***degrees of freedom (DOF) of folding*** is used to describe the possible ways that a system can fold at any given time. When in a folded configuration, a rigid origami vertex with four folds is said to have 1

DOF of folding and can fold through only one motion. Finally, ***reconfigurable*** origami are systems that can change their prescribed folding motion. Multi-DOF systems (# DOF > 1) are always reconfigurable, however many 1 DOF systems can also be reconfigurable. For example, the Miura-ori cell can be folded with different fold assignments than those shown in Figure 1.3 (a).

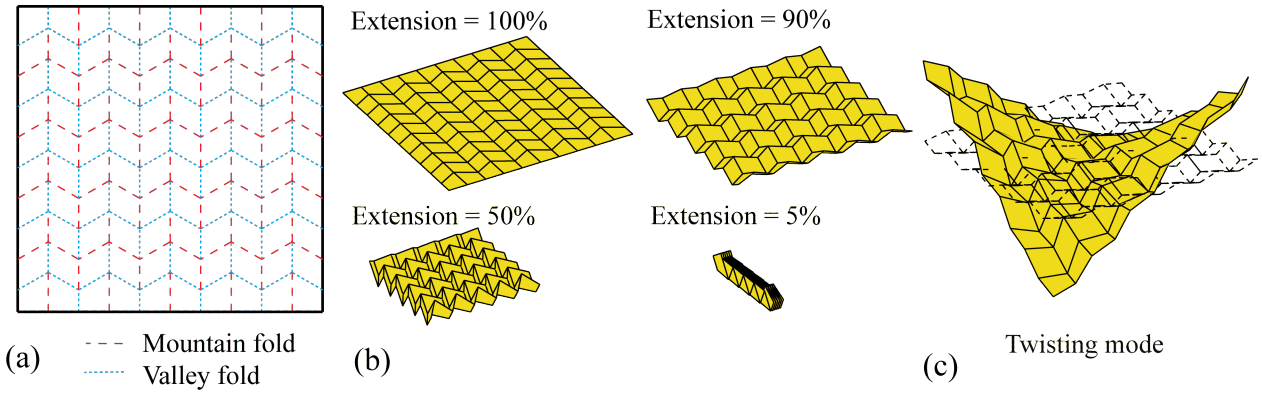

Figure 1.4: A Miura-ori pattern with ten panels in each direction. (a) Mountain and valley fold assignment of the pattern. (b) Kinematic folding of the pattern into four different configurations. (c) Twisting mode of Miura-ori pattern shows that the structure can deform in more ways than defined purely by kinematic rigid folding. Elastic deformations are discussed in Section 1.3.

1.2.2 Geometric variations in origami

The Miura-ori pattern was first explored as a naturally occurring pattern in the buckling of thin sheets (Miura, 2009), and has gained popularity as it is flat foldable, rigid foldable and developable. The Miura-ori pattern has been studied in substantial detail from its physical properties (Mahadevan and Rica, 2005; Schenk and Guest, 2011; Wei et al., 2013), its design and arrangement (Schenk and Guest, 2013), and its nonlinear behavior (Silverberg et al., 2014). Further research has often aimed to expand geometric variations of the pattern, while also retaining its desirable properties (Tachi, 2009a, 2010a; Gattas et al., 2013; Xie et al., 2015b; Dudte et al., 2016).

Being able to vary and control the origami geometry is important for several reasons. First is the ability to create aesthetically pleasing and geometrically functional shapes. Additionally, varied origami geometries could be useful for fitting into pre-constrained spaces and fulfilling new functions. The geometric design can affect manufacturing and fabrication

considerations of the system. The geometry of the origami also affects the structural and stiffness properties of the system. Finally, systems with multi-physical aspects could have intrinsic properties that can be tailored by geometric reconfiguration.

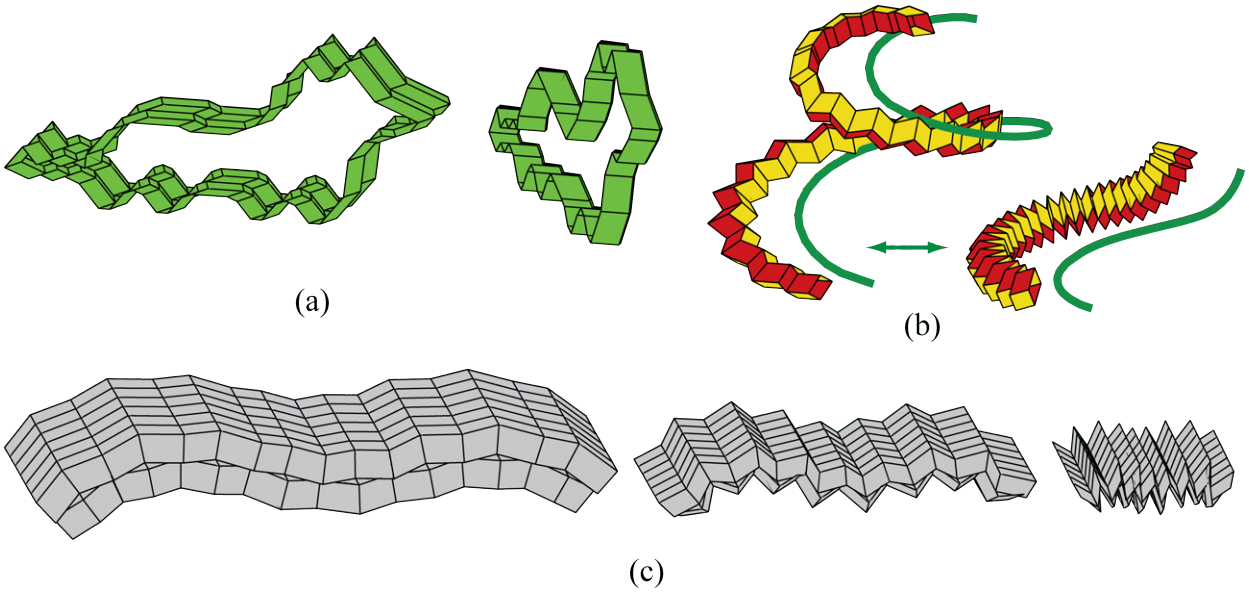

Figure 1.5: Tubular origami systems introduced in this thesis. All of these variations are rigid and flat foldable. (a) A tubular system that has the cross-section of a dog (Section 6.2). (b) A tube that follows a three dimensional spiral (Section 6.3.3). (c) An undulated canopy created from coupled tubes (Section 5.6.2).

This thesis introduces designs for tubes and coupled tube variations that are inspired by the Miura-ori pattern. We present tubes with different polygonal cross-sections that can be programmed by changing the fold directions at some folds (Figure 1.5 (a) - Chapter 6). Origami tubes can take a wide variety of curved shapes and can follow arbitrary spirals in space (Figure 1.5 (b) - Chapters 5 and 6). When tubes are coupled together they can make structures that are deployable, yet stiff and can be used for various practical applications (Figure 1.5 (c) - Chapters 4 and 5). The tubular assemblages can be made in a wide variety of geometries and can have unique and tunable mechanistic properties. We focus our work on flat foldable and rigid foldable tubes, however, origami tubes are not developable and they require gluing or some other connectivity for creating the complete structure. Despite the higher complexity of manufacturing, origami tubes greatly extend the functionality of engineered thin sheet structures. Tubular origami can be inflatable similar to actuators and bellows. Furthermore origami tubes and coupled origami tubes have a self-constraining

geometry that makes them suitable as stiffened structures, energy absorption devices, and systems with enhanced mechanical characteristics.

1.3 Structural characterization of origami

The theory behind rigid origami has been studied in detail in recent years, and mathematical definitions have been used to show rigid foldable vertices and patterns (Huffman, 1976; Tachi, 2009a, 2010b; Hull, 2012). Despite the mathematical definitions for rigid folding, origami in the real world can bend and twist in a multitude of ways. Figure 1.4 (c), for example, shows a twisting mode of the Miura-ori shape. The system deforms in a fashion different from simply folding the prescribed fold lines. This means that, in reality, the Miura-ori pattern has more than one degree of freedom for elastic deformation. In fact, this is true for origami structures, and it is possible to deform them in a variety of ways different from the intended kinematic motion. In this thesis, we study these deformations that include panel stretching and shearing, panel bending, as well as fold bending. Understanding, quantifying and analyzing these motions is important for the practical design of origami systems. The geometry of the origami has a significant effect on stiffness and deformation modes. Furthermore, by better understanding the structural stiffness of origami, we could aim to tailor and improve their properties, functionality, and practicality.

1.3.1 Local behavior of origami

The local physical characteristics of thin folded structures are not thoroughly understood yet. The bending, stretching and folding of thin sheets can be complex and involve nonlinear behavior. The thin sheet panels are prone to buckling from having large length-to-thickness ratios, yet they are also partially braced and stiffened by the adjacent panels in the origami pattern (Witten, 2007). Furthermore, a major issue that often occurs with origami systems is that they are typically constructed with the assumption of "zero thickness," meaning that the panels have no finite thickness. In reality, however, the finite thickness leads to stress concentrations at the fold vertices and thus thickness needs to be accounted for in practical designs (Chen et al., 2015).

Localized effects at the fold lines can also be important to the global structural behavior (Vliegenthart and Gompper, 2006). The folds undergo large deformations, which are typically nonlinear for most types of creased materials (e.g. Nagasawa et al. (2003); Lechenault et al. (2014)). Origami folds that are also bent numerous cycles may experience fatigue, cracking, or localized failures that would affect behavior (Durney and Pendley, 2004). An alternative to these issues may be to use rotating hinges in lieu of the fold lines, however these may experience stick slip friction or other nonlinearities.

We explore some of the local origami effects in Chapter 2. We primarily do this to simplify, distill and linearize the most important origami behaviors. We explore the scale dependence of these behaviors and aim to quantify the stiffness of origami in terms of length scales and material properties. Ultimately, we develop constitutive and phenomenological relations to quantify the stiffness of origami for global system analysis.

1.3.2 Global analysis of origami

Beyond analyzing the local effects, characterizing the global stiffness and deformations of the origami is important for evaluating the feasibility and practicality of full structures. The global analysis of origami systems could be performed in several ways: 1) Analytical solutions for elasticity problems related to origami, where typically a unit cell or a portion of the pattern is explored empirically, e.g. Hunt and Ario (2005), Hanna et al. (2014), Qiu et al. (2016), Brunck et al. (2016). These analytical approaches are typically suited for one specific origami pattern and cannot be readily used for origami systems; they also often assume that deformation only occurs as folding along the prescribed fold lines. 2) A bar and hinge method where panel in-plane deformations are restrained using bar elements while bending of panels and folds is modeled using rotational hinges, e.g. Schenk and Guest (2011), Wei et al. (2013). 3) Numerical methods, and particularly, finite element (FE) methods where the system is discretized in a detailed fashion, e.g. Schenk et al. (2014a), Lv et al. (2014), Gattas and You (2015b), Peraza Hernandez et al. (2016). The FE approach often provides higher accuracy, however, it tends to be computationally expensive, and depending on the discretization technique may not be suitable for studying patterns with varying geometries. In this work, we focus on the bar and hinge modeling approach because it is simple and computationally

efficient, yet it provides sufficient accuracy and information about the origami behavior.

When we study the various origami tubes and coupled tube assemblages, we use eigenvalue as well as static analyses to explore and quantify behavior. The eigenvalue analyses give a global overview of the stiff and flexible deformation modes of the origami structure. These are characteristic properties of the actual origami system and thus are independent from the force-displacement cases and practical applications. Eigenvalue *bandgaps* could also be used for the analysis to separate desirable deformation modes, such as kinematic folding; and non-desirable modes, such as bending and twisting. The static analyses, on the other hand, are useful when tailoring the structures to more practical applications. For example, we evaluate different structures as cantilevers, or beams subjected to three point bending. These global analyses can be used to better understand the wide variety of geometric origami variations introduced in this thesis.

1.4 Thesis scope and organization

The overarching objective of this thesis is to explore the structural properties of origami systems, and particularly, to understand how geometric variation can be used to tailor stiffness. We use well known origami patterns such as the Miura-ori, and explore new tubular origami systems. The structural properties are investigated on a local as well as a global scale, aiming to create a paradigm for characterizing stiffness of origami. The thesis explores reconfiguring systems and other origami that have novel properties and characteristics. The first part of the thesis discusses the modeling techniques used to simulate origami and also establishes scaling properties for different structural behaviors. We show basic applications of these analytical tools and discuss their abilities to rapidly evaluate geometric variations of origami. In the remainder of the thesis, we develop new types of origami and explore how their geometry affects the structural properties. We introduce a coupled tube system that is easy to deploy, yet difficult to bend and twist. We explore variations and assemblages of these coupled systems and introduce a new set of polygonal tubes. We focus on creating generalized methods that can define origami tubes and that can simultaneously be used to predict behavior and reconfigurable properties of the systems. A more detailed discussion of the thesis organization follows.

Chapter 2 explores the stiffness of thin origami type sheets with the objective of informing the stiffness parameters used in the bar and hinge model. We first explore the in-plane stretching and shearing of a thin sheet which is some orders of magnitude stiffer than the bending behaviors. We introduce and show a new (so called *N5B8*) bar and hinge model that can provide a scalable and isotropic estimate for in-plane effects. We next perform a detailed study on the bending behaviors of the thin restrained origami panels. We explore the behaviors for small and large displacement and show that the panel geometry significantly affects the bending stiffness. At the end of this chapter, we perform a literature review on experimental testing of fold line bending. We explore the experimental characteristics and develop scalable parameters that can be used to inform bar and hinge models.

In **Chapter 3**, we improve, verify, and test a bar and hinge model that can be used for analyzing elastic stiffness, and estimating deformed shapes of origami. The model simulates three distinct behaviors: stretching and shearing of thin sheet panels; bending of the initially flat panels; and bending along prescribed fold lines. Within our study we introduce the *N5B8* model that employs five nodes and eight bars to model the system. The model is simple and efficient, yet it can provide a realistic representation of the structural characteristics of origami assemblages. It can be adapted for different problems and can be used to model a variety of three dimensional origami structures. The simplicity and efficiency of this model makes it suitable for practical problems such as optimization and parametrization of geometric origami variations.

The so-called "zipper" coupled origami tubes are introduced in **Chapter 4**. The chapter first shows the basic structural characteristics of a single origami tube, and then explores the effect of coupling tubes in different ways. We show that the zipper tubes can deploy with deformation localized at the flexible folds lines, however, for other motions, the system is over-constrained and the thin sheets become engaged in tension and compression.

In **Chapter 5**, we develop a more generalized definition for the coupled tube systems, such that they can be created with different cross-sections and can take on curved profiles. We present a methodology to create slab and roof type structures that have a flat top and have a maximum stiffness when fully deployed. We explore how geometry affects stiffness of the structures, and we find that tubes that have more of a zig-zag geometry can have reasonably high out-of-plane stiffness at all points during deployment.

Chapter 6 presents origami tubes with polygonal cross-sections that can reconfigure into numerous geometries. We develop a generalized approach to construct these tubes where a cross-section is projected in space. We discuss the variety of tubular structures that can be conceived and we show limitations that govern the geometric design. The cross-section and kinematics of the tubular structures can be reprogrammed by changing the direction of folding at some folds. Reconfiguring the cross-sections can be used to change the geometry, volume, and stiffness characteristics of the origami tubes. We show that tubes can be constructed such that they have a high out-of-plane stiffness similar to corrugated pipes.

In **Chapter 7**, we provide an overview of the main findings and conclusions from this thesis. We also provide short and long term research ideas that can build upon this work or are important research topics in the general field of origami engineering.

The focus of the thesis is to characterize the stiffness of origami, with a particular emphasis on new tubular systems. The scope of the thesis is intentionally limited in some aspects. While we explore and point to specific applications that can be achieved with origami and with the newly developed systems, we do not explore, design, or produce any specific application. Our work has not explored many other phenomena that affect origami structures, for example, the effect of finite thickness or nonlinear behavior are not studied here. We believe that this work provides a baseline that can be used by future researchers and designers to create physical implementations. Similarly, we have performed most of this work to be scale and material independent as the concepts produced here are valid for a variety of sizes and physical creations.

CHAPTER 2

SCALABLE PROPERTIES OF ORIGAMI SYSTEMS

In this chapter, we study the deformations of typical origami components, and we explore how origami stiffness is affected by geometry. We focus on three fundamental physical behaviors of origami: 1) stretching and shearing of thin sheet panels, 2) bending of the initially flat panels, and 3) bending along prescribed fold lines. This study is performed primarily to inform the stiffness parameter definitions of a so called N5B8 bar and hinge model discussed in detail in Chapter 3 (the name N5B8 is because the model has five nodes and eight bars). The bar and hinge model is simple and efficient, yet it can provide realistic representation of stiffness characteristics and deformed shapes. In this chapter, we perform detailed finite element analyses to better understand the physical origami behaviors and to create phenomenological relations that define stiffness of the bar and hinge model. The stiffness of the fold lines is also informed by existing experimental research on origami type materials. We show that the model can be made scalable, isotropic and its stiffness can be defined using length scales and material properties.

Origami typically consists of flat thin sheet *panels* (or facets) that are interconnected by *fold lines* (or hinges). The specific fold pattern and geometry have a large influence on both the folding behavior and the mechanical characteristics of the folded structure. In this chapter, we explore the stiffness of the panels and fold lines locally, so that we can inform the bar and hinge model for global analyses of origami. Although the bar and hinge model could be adapted for different origami structures and various elastic behaviors, we make some preliminary assumptions so we can have a more focused approach. We assume rigid foldable origami that can fold through a kinematic motion where panels remain flat and deformation occurs only at the fold lines. We also also assume that the thin sheets are continuous and no cuts are present.

The kinematics and elastic deformations of origami can be readily observed from physical models and have been studied by many researchers (e.g. Demaine et al. (2011); Schenk and Guest (2011); Wei et al. (2013); Evans et al. (2015); Brunck et al. (2016)). If we ignore buckling (or crumpling) of the thin sheets, the elastic behavior of origami can typically be

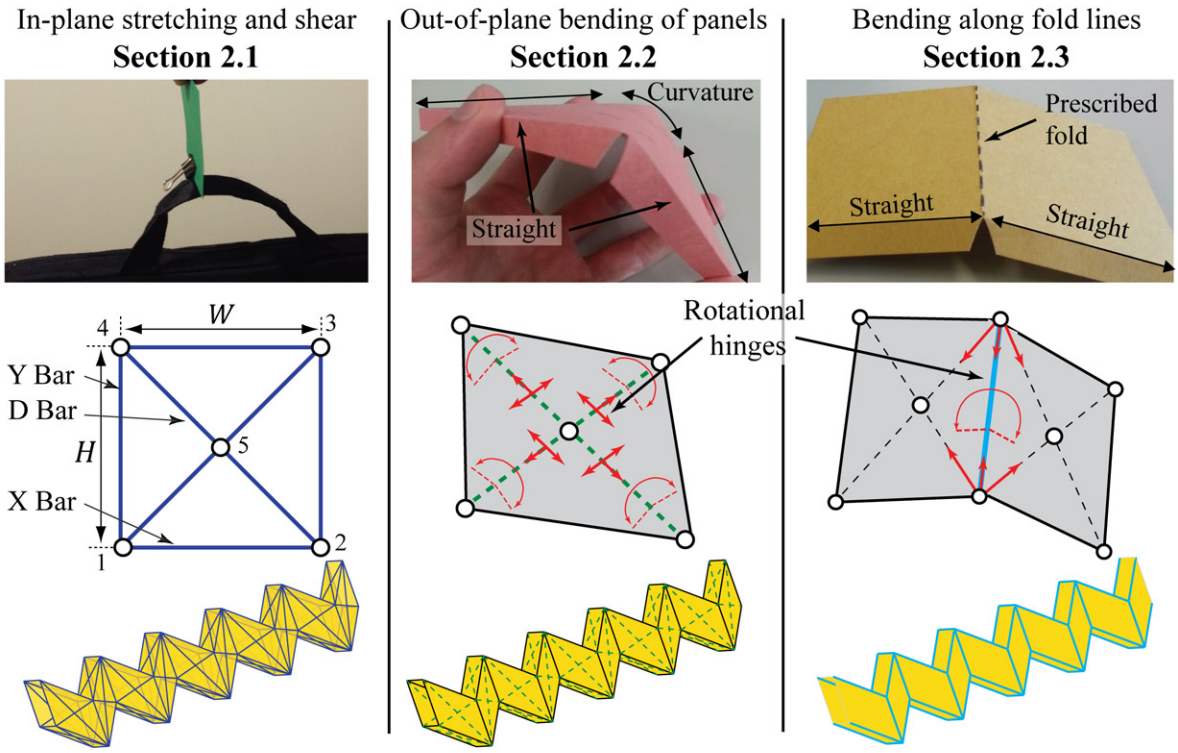

Figure 2.1: The fundamental elastic behaviors of origami are discussed in this chapter. A physical paper model (top row), the bar and hinge placement for one panel in the N5B8 model (middle row), and bar and hinge placement on an origami tube (bottom row). A thin sheet is significantly stiffer in shear and stretching and can support the weight of a bag. Bending of panels results in localized curvature about the shorter diagonal, while the fold lines are assumed to be more flexible and bend along a prescribed line. The behavior of each origami panel and fold (simulated using bars and hinges) can be placed into a global system model.

grouped into three distinct fundamental behaviors that are presented in Figure 2.1. This chapter is dedicated to these three behaviors and thus it is organized as follows: In Section 2.1 we study the *in-plane stretching and shear of flat thin panels*; Section 2.2 discusses the *out-of-plane bending of the initially flat panels*; and in Section 2.3 we explore the *bending along prescribed fold lines*. Section 2.4 presents concluding remarks from this chapter.

The in-plane behavior of origami has been largely ignored by previous research because the in-plane stiffness is orders of magnitude higher than the bending stiffness. However, we believe that it is important to accurately quantify the in-plane stiffness, and capture the corresponding behaviors. As we show in the following chapters, in-plane behaviors of the origami could be quite important for many origami structures. The origami tubes discussed in this thesis and cellular origami assemblages are often over-constrained, and they experience

tension, compression and shear when loaded. We explore the in-plane deformations, quantify the stiffness for square and skewed origami panels, and we provide a formulation for the bar and hinge model that can efficiently capture in-plane response.

Out-of-plane bending of origami panels is important as it contributes to deformations beyond the rigid origami kinematics (folding only at fold lines). The bending of panels has been modeled in different ways, but most simplified origami models use a rotational hinge to connect two triangular facets that define the panel. This is likely a valid simplification for origami. The adjacent panels of origami have some orthogonality to the flat panel and thus bending of the panel is restrained at the fold lines. The panel bending would thus occur along the shorter diagonal (lower energy than the long diagonal). This phenomenon has been verified for origami and for typical thin sheets and crumpled sheets. Due to these added restrictions, the bending energy and thus stiffness of these restricted sheets is higher, than unrestricted sheets (Lobkovsky et al., 1995; Vliegenthart and Gompper, 2006; Witten, 2007). In our study, we verify this increased stiffness, and we explore the effect of the panel geometry for both small and large bending.

In the final section of this chapter, we discuss the bending along prescribed fold lines. The true behavior of fold lines is likely highly nonlinear and dependent on the materials and methods used to fabricate the origami structure. We make the assumptions that the fold has an infinitesimally small width and that thickness of the panels is negligible. We model the prescribed fold with a single rotational hinge, that has linear elastic behavior. These assumptions are representative of current practice, but there is certainly a need and interest to improve understanding and stiffness simulation of fold lines. We use existing experimental results to inform the stiffness of the folds and we study the interplay between panel and fold bending.

2.1 In-plane stretching and shear of flat thin panels

In this section, we explore the behavior and stiffness of flat thin panels when they are subjected to in-plane loads (see left column of Figure 2.1). The stiffness of stretching and shearing a thin sheet is typically several orders of magnitude greater than its bending stiffness as discussed in subsequent sections. Therefore, bending stiffness of adjacent panels is

considered insignificant with respect to the in-plane behavior of the panel. Here we study a single origami panel with different geometries subjected to in-plane loads. When assembled into a full origami system, multiple panels would interact and combine their in-plane responses as determined by the global geometry of the system. The bar frame is used essentially as a single element to model the in-plane behavior of the panel, thus at the connection of two panels, there will be two bars at the same location and connecting to the same two nodes. In this work, we assume that the material properties are locally isotropic and that the sheet behaves in the same way in all different directions. We also base our formulation on an unbent panel; when a panel is bent out-of-plane, some of the stretching and shearing behaviors may change, however we feel that the bar and hinge model would provide a reasonable estimate of the stiffness and deformation.

2.1.1 Definition of bar stiffness for the N5B8 model

For the N5B8 model, we use an indeterminate frame consisting of five nodes and eight bars. The bars are labeled as horizontal (X), vertical (Y), and diagonal (D) bars based on their location in the frame (see left column of Figure 2.1). The formulation for the bar elements is discussed in more detail in Section 3.2.2, and it requires a stiffness parameter K_S for each bar element. The bar stiffness parameters (i.e. components of the $\mathbf{K}_S$ matrix) are defined for each bar as

$$K_S = EA_B/L_B, \tag{2.1}$$

where L_B is the bar length and A_B is the bar area. When the indeterminate N5B8 frame is rectangular, the bar areas can be defined such that the frame will exactly exhibit Poisson effects for tensile loading in both directions (i.e. isotropic behavior). The bar areas are defined as:

$$A_X = t\frac{H^2 - \nu W^2}{2H(1-\nu^2)}, \tag{2.2}$$

$$A_Y = t\frac{W^2 - \nu H^2}{2W(1-\nu^2)}, \tag{2.3}$$

$$A_D = t\frac{\nu(H^2+W^2)^{3/2}}{2HW(1-\nu^2)}, \tag{2.4}$$

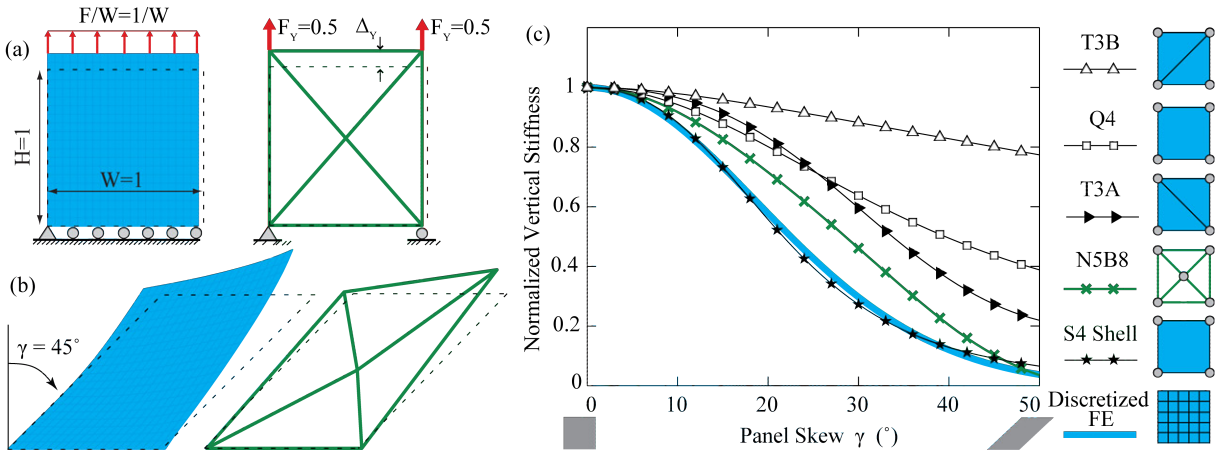

Figure 2.2: Tensile test performed by applying a uniform distributed load to the top edge of a panel ($F = 1$) and restraining the bottom edge with a pin and rollers. (a) Deformed shapes of a square panel simulated with a discretized FE model (left) and the N5B8 model (right). Deformation is scaled by 1000 and undeformed outline is shown with dotted line. (b) Deformed shapes of skewed panels scaled by 100. (c) Normalized vertical stiffness of the panel with respect to the skew γ. The analysis is presented for the discretized FE case, the N5B8 model, and different FE cases using one or two elements only (S4 shell, Q4, T3A, and T3B).

for the horizontal (X), vertical (Y), and diagonal (D) bars, respectively. The isotropic behavior for a tensile load on a square panel is shown in Figure 2.2 (a). For tensile loads, a rectangular N5B8 frame will have a stiffness equivalent to a solid block of material (i.e. $EA/L = EWt/H$). These definitions are based on square panels, however, in subsequent sections we show that these assumptions provide reasonable estimates when the panels are skewed.

When subjected to shear (Figure 2.3) the frame stiffness is dependent on the chosen Poisson's ratio. From Equation 2.4, when a low ν is used, the diagonal bars have a low area, and the frame demonstrates a low shear stiffness. The converse is also true, and increasing ν increases the shear stiffness. This behavior is opposite to real isotropic materials where shear stiffness decreases as ν increases. A serendipitous case occurs when ν is set to 1/3, the behavior of the frame model in shear is identical to that of a homogeneous, isotropic block of material. As shown on the right of Figure 2.3 (d) the top of the frame displaces laterally in the direction of loading and each diagonal bar carries a force of $F/2$ in the X direction. The frame displacement matches the lateral displacement of a solid block with dimensions $W \times H \times t$ loaded in simple shear, analytically defined as $\Delta_x = F_X H/GWt$, where F_X is the total shear force and G is the shear modulus, defined as $G = E/2(1+\nu)$ for a homogeneous,

isotropic, linear elastic material. With $\nu = 1/3$, the frame is scale independent for shear loadings, similar to any generic FE approach. In Figures 2.3 (c) and (f), notice that the trends of discretized FE and N5B8 are similar.

When considering skewed and irregular panels, the height (H) of the panel is calculated as the average distance between nodes 1 to 4 and 2 to 3, while the width (W) is the average distance between nodes 1 to 2 and 4 to 3 (see Figure 2.1). As will be shown in the subsequent section, these basic definitions provide a realistic behavior for the panel for various in-plane loads. In the future, it may be possible to find more advanced definitions for the individual bar stiffness that may improve the performance of the indeterminate N5B8 frame.

2.1.2 The shear and stretching of skewed panels

In Figure 2.2 we study a flat thin panel subjected to a tensile test, where a uniform load of $F = 1$ is applied upward at the top of the panel, while the bottom is restrained in the vertical direction. The system is fully restrained out-of-plane. In our work, we use arbitrary units for force and length, although we could use any consistent units (e.g. newtons and millimeters). The panel has a height and width of 1 and a thickness of 0.01. A Young's modulus $E = 10^6$ is chosen arbitrarily, and has units of force per length squared. A Poisson's ratio of $\nu = 1/3$ is used such that the N5B8 model exhibits a simple shear behavior.

As a reference, we use a discretized FE model to study the behavior of a flat thin panel. In this and subsequent sections of the chapter we use the Abaqus FE software (Dassault Systemes Simulia Corp, 2010) with the S4 general purpose shell elements with finite membrane strains that are appropriate for small and large deformation analyses (these elements typically outperform other shell elements - for more information on the FE analyses, see Section 4.2.3). We have evaluated mesh convergence for the stretching and shear examples, and we choose a discretization of 20 x 20 elements which provides a displacement solution for a skewed panel that is within 0.013% of a mesh with double the number of DOFs. The displaced shapes of the discretized FE and the N5B8 models are shown for square and skewed cases in Figure 2.2 (a) and (b) respectively. The N5B8 model is able to capture the isotropy of the panel and the general deformed shape relatively well. The philosophy of the bar and hinge model is similar to the FE inspired models used by Resch and Christiansen (1971),

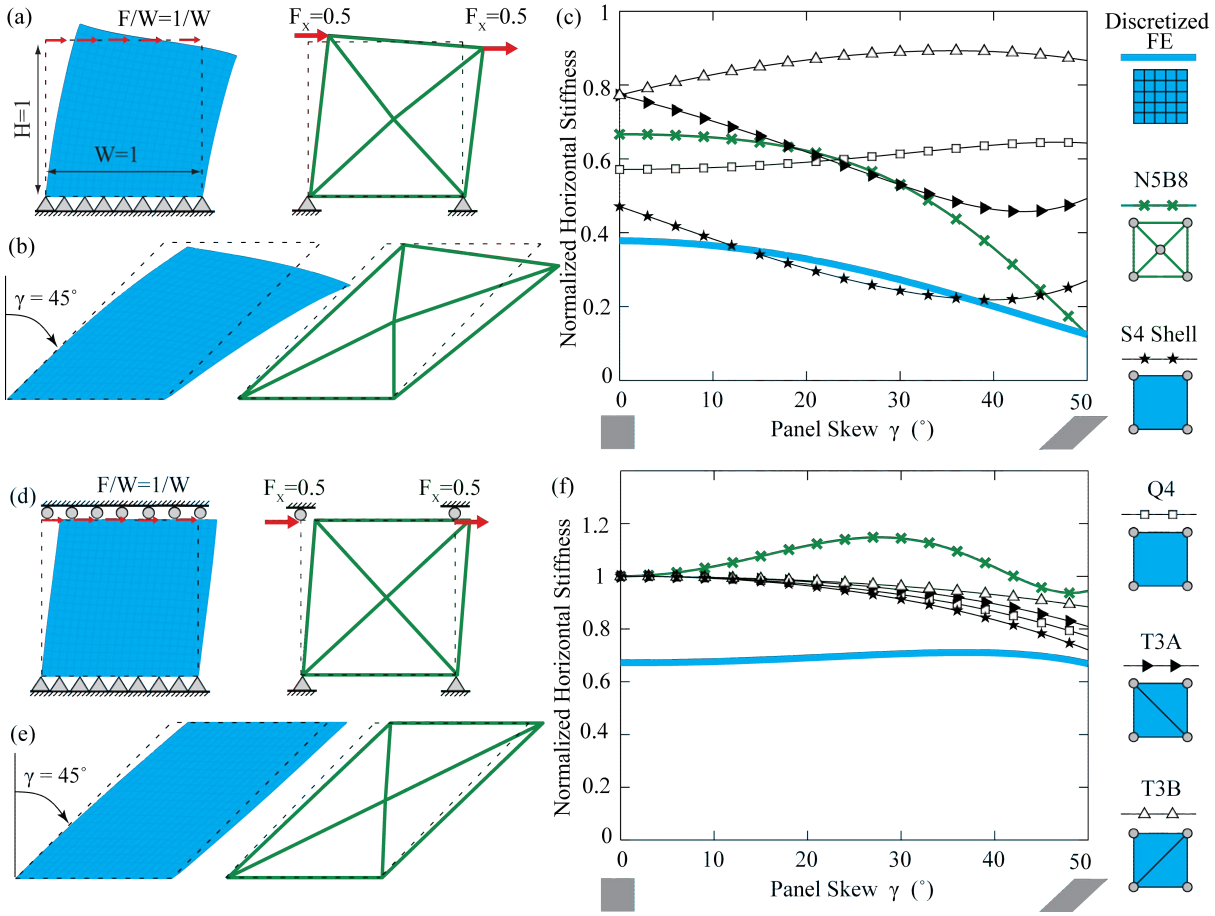

Figure 2.3: Shear test performed by applying a uniform distributed load to the top edge of a panel ($F = 1$). In (a-c) only the bottom edge is restrained with pins, while in (d-f) the top edge is also restrained with rollers. (a) Deformed shapes of a square panel simulated with a discretized FE model (left) and the N5B8 model (right). Deformation is scaled by 300 and undeformed outline is shown with dotted line. (b) Deformed shapes of skewed panels scaled by 100. (c) and (f) Normalized horizontal stiffness of the sheet with respect to the skew γ. (d) and (e) Deformed shapes scaled by 300. The analysis is presented for the discretized FE case, the N5B8 model, and different FE cases using one or two elements only (S4 shell, Q4, T3A, and T3B).

however, it is clear that the N5B8 is able to capture isotropy and stiffness better than models that employ T3 elements.

In Figure 2.2 (c), we show the normalized vertical stiffness with respect to skew, where the behavior of the discretized FE model is considered an accurate representation of the real behavior. The vertical stiffness for each case is calculated as $K = F/(\overline{\Delta_Y})$, where $\overline{\Delta_Y}$ is the average vertical displacement at the top surface of the panel. The stiffness is then normalized by the axial stiffness of the square piece of thin elastic sheet shown in Figure 2.2 (a) (i.e. by EWt/H). The stiffness vs. skew is approximated by the N5B8 model as well as by conventional elements. The different models used with number of DOFs active in-plane are: discretized FE - 1323 DOFs; N5B8 - 10 DOFs; a single shell (S4) - 12 DOFs; a quad (Q4) - 8 DOFs; and two triangular elements (T3A and T3B) - 8 DOFs. The N5B8 model approximates axial stretching stiffness well for various amounts of skew.

Similar analysis are performed for two cases of shear applied to the thin panel. In one case, the element is restrained only on the bottom (Figure 2.3 a-c), and in the other it is restrained on both the top and bottom, and is subjected to (theoretically) simple shear (Figure 2.3 d-f). The shear stiffness is calculated as $K = F/(\overline{\Delta_X})$, where $\overline{\Delta_X}$ is the average horizontal displacement at the top surface of the panel. The stiffness is then normalized by the shear stiffness of a square piece of thin elastic sheet subjected to simple shear (i.e. by GtW/H). The N5B8 and other single element models typically overestimate the shear stiffness by about 30-80%. Of particular interest is the simple shear case with no skew ($\gamma = 0°$) where most models match the stiffness of a simple shear panel, while in reality the discretized case is more flexible. The higher flexibility occurs because the material in an actual panel experiences both tension and shear, and not theoretical simple shear.

Although the N5B8 model overestimates the shear stiffness for both cases, it follows similar trends to the discretized FE analysis. When not restrained on top, the shear stiffness reduces with skew, and when restrained on top the shear stiffness slightly increases and then decreases with higher skew. The deformed shape for shear loading of the N5B8 model is similar to the discretized FE case, however the displacements are underestimated. It should be noted that shear in a complete origami structure would likely be more complex than the two cases presented here, as it may be accompanied with moments and localized axial forces. In summary, the N5B8 model is capable of capturing tensile isotropic deformations of flat thin

panels with and without skew. The model approximates axial stiffness well, and although it overestimates shear stiffness, the stiffness follows expected trends with respect to skew.

2.2 Out-of-plane bending of flat panels

The out-of-plane bending of origami panels presents an interesting phenomenon because adjacent panels can be oriented orthogonally and can restrict bending (see middle column of Figure 2.1). This restriction prevents the panel from bending with a single curvature over the length of the long axis, and instead a more complicated bending occurs where the panel deforms along its diagonals (Demaine et al., 2011). This phenomenon tends to be more pronounced for large deformation bending and has been studied in previous research (Lobkovsky et al., 1995; DiDonna, 2002; Witten, 2007). The restricted bending is related to the conical dislocation problem where a flat circular sheet is forced to bend into a hole with a smaller diameter (e.g. Cerda et al. (1999); Cambou and Menon (2011)). The large deformation bending leads to crumpling of the material and localized stretching and shearing of the thin sheet (e.g. Pereira et al. (2010)). For modeling of origami, we investigate the stiffness of both small and large deformation bending of the thin panels. The bar and hinge models use an angular constraint to approximate the deformation and stiffness of panel bending. By studying the detailed bending of thin panels, we formulate analytical expressions for the bar and hinge model that scale stiffness based on material and geometric effects.

2.2.1 Panel bending stiffness: from small to large displacements

We explore the stiffness scaling of a thin panel that is restrained, meaning that there are adjacent panels positioned out-of-plane along the edges (at fold lines), and thus these orthogonal panels limit out-of-plane deformation of the flat sheet. In Figure 2.4 (a-b) we show a FE discretization of a restrained rhombus panel with a long diagonal $D_L = 1.4$, a short diagonal $D_S = 1.0$, and four restraining panels with a vertical width of 0.4 (for more information on the FE analyses, see Section 4.2.3). Boundary conditions are imposed on three corners and a displacement control is placed on the fourth. We constrain the minimum six

degrees of freedom to make the system statically determinate. With the problem set-up, it is possible to achieve panel bending along either of the two diagonals of the restrained panel. For different geometries of this problem, we have verified that for large displacements, bending always occurs about the shorter diagonal and thus we limit the dimensions to $D_S < D_L$. For subsequent analyses, we apply a displacement control trajectory that follows a rotation of the bending angle θ_B about the short diagonal. The vertical reaction on the left corner (R_A) is used to calculate the bending moment about the sheet as $M_B = R_A * D_L/2$.

The problem converges successfully, and our chosen discretization of 30x30 shell elements for the flat sheet provides solutions that are close to a FE model with double the number of DOFs (0.12% difference for small deformations $\theta_B = 0.1°$ and 0.21% for large deformations $\theta_B = 70°$). The moment bending relation of the entire panel can be represented as $M_B = \theta_B K_B$, which can subsequently be used to formulate the stiffness for the angular constraints. The FE analysis from small to large displacements for three sheets with different geometries is shown in Figure 2.4. In this section, we discuss different scaling properties, and basic definitions for the N5B8 model, while in the next section we explore the geometric effects.

We use several parametric analyses to explore the bending behavior of thin restrained panels for small and for large displacements. The in-plane stiffness of the thin adjacent panels is high enough to prevent bending and buckling at the edge connecting two panels (i.e. at the fold line on the perimeter of a panel). We confirm that the stiffness of restrained bending is higher than that of unrestrained sheets that are free to bend along the edges. Some of the stiffness scaling characteristics are the same for both small and large deformations. In particular, in Figure 2.5 we show that bending moment scales approximately with $k(D_S/t)^{1/3}$ where k is the bending modulus of the sheet, defined as $k = Et^3/12(1-\nu^2)$. These results are same as those by Lobkovsky et al. (1995), where the bending energy scales with roughly $t^{8/3}$ when thickness is varied. In other words, t^3 from the bending modulus times $t^{-1/3}$ from the additional scaling relations. The scaling with respect to the short diagonal length (i.e.$(D_S/t)^{1/3}$) is discussed again in Figure 2.7. The relation with this length scale becomes an important consideration when comparing the panel to fold stiffness as later discussed in Section 2.3.

The small displacement results for restrained origami panels had not been explored in detail previously. When a relatively small bending angle ($\theta_B < 6° \approx 0.1$rad) is imposed,

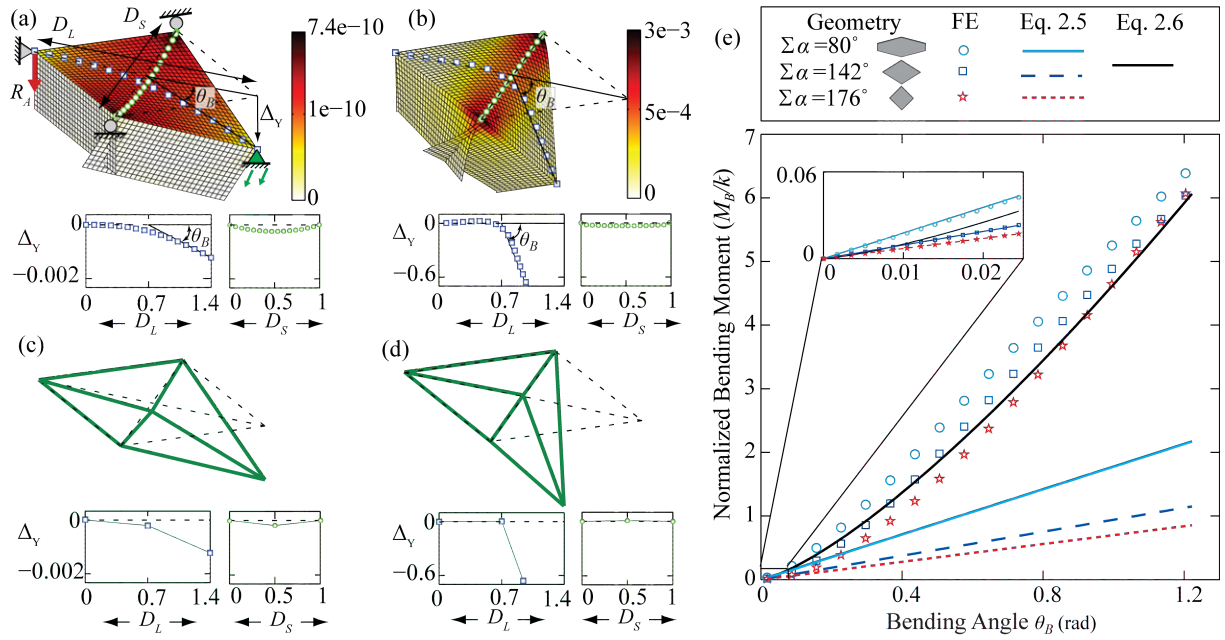

Figure 2.4: Bending behavior of thin panels with restrained edges. (a) and (b) FE discretized thin sheet with restrained edges bent about the shorter diagonal. The total energy in each element is shown with color. (c) and (d) show the panel bending simulated with the bar and hinge model. In (a) and (c) the sheet is bent with $\theta_B = 0.1°$, and displacements are scaled by 300. In (b) and (d) the sheets are bent with $\theta_B = 70°$. In (a) through (d) displacements along the diagonals are shown below the deformed structure. (e) The bending moment normalized by k vs. bending angle for different geometries of thin restrained sheets. The numerical FE solutions (points) are plotted together with the bar and hinge solutions (lines) defined using Equations 2.5 and 2.6.

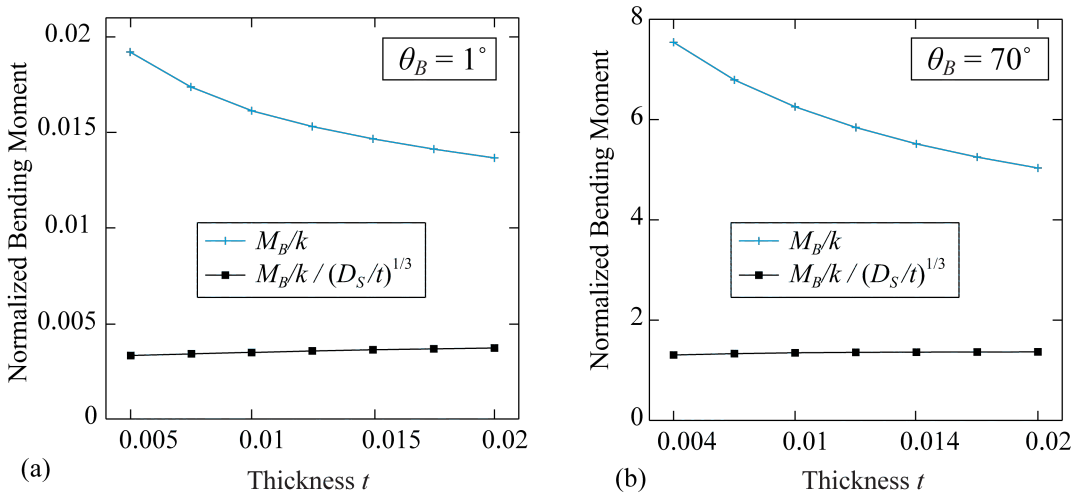

Figure 2.5: Bending moment of thin sheet panels with respect to thickness for (a) small displacements ($\theta_B = 1°$) and (b) large displacements ($\theta_B = 70°$). Bending moment normalized by the bending modulus of the sheet k is not linear and reduces with increasing thickness. The bending moment normalized by k and by $(D_S/t)^{1/3}$ results in a flat line - thus we verify that bending moment and stiffness scale with $(D_S/t)^{1/3}$ (Lobkovsky et al., 1995). See Figure 2.7 (d) and (h) for the same scaling relation presented with respect to the length of the short diagonal D_S.

the panel experiences double curvature with bending along both diagonals (Figure 2.4 (a)). The double curvature matches expected theoretical behavior. The bending moment relation remains linear for small displacements, the moment scales with θ_B, and the energy scales with θ_B^2. There is no tension in the sheet, and bending energy is distributed throughout the panel with higher concentration at the corners on the short diagonal (Figure 2.4 (a)). The bending stiffness for small deformation bending is highly dependent on the geometry of the panels which is explored in detail in Section 2.2.2. The stiffness scales with a parameter $\Sigma\alpha$ that is introduced to describe the corner geometry of the short diagonal. The parameter $\Sigma\alpha$ represents the deviation of the short diagonal corners from being flat edges where the restraining panels on the side are collinear (see Figure 2.7). A square panel will have all corners of 90° and $\Sigma\alpha = 180° = \pi$. Based on the scaling observations and the geometric investigation (in the next section), we formulate an equation to define the bending moment for small displacements of the panels as

$$M_{BS} = \theta_B(0.55 - 0.42\frac{\Sigma\alpha}{\pi})k\left(\frac{D_S}{t}\right)^{1/3} = \theta_B(0.55 - 0.42\frac{\Sigma\alpha}{\pi})\frac{Et^3}{12(1-\nu^2)}\left(\frac{D_S}{t}\right)^{1/3}. \quad (2.5)$$

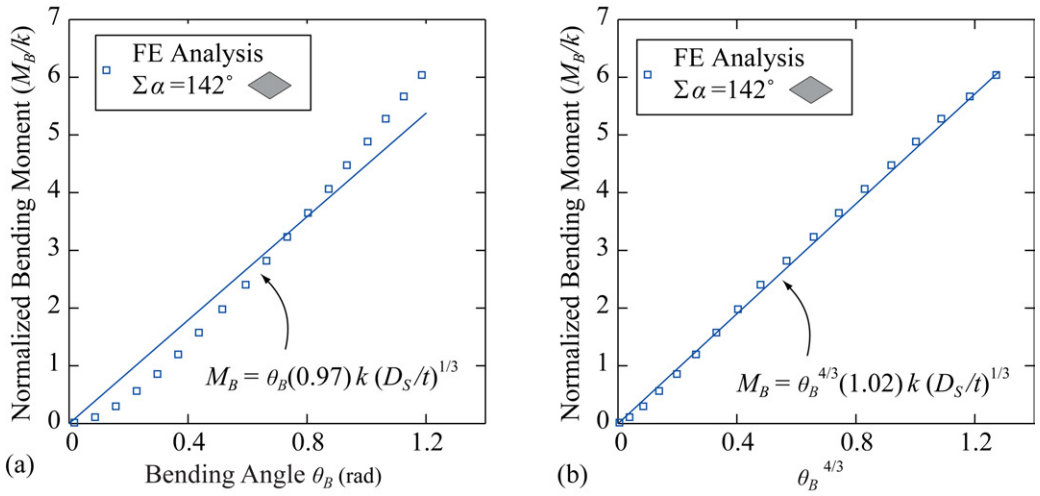

Figure 2.6: Bending moment of panel with respect to the bending angle. The FE analysis presented is the same as that for the $\Sigma\alpha = 142°$ panel in Figure 2.4. (a) The moment (M_B) vs. bending angle (θ_B) cannot be represented well with a linear fit. (b) The moment (M_B) scales almost linearly with the bending angle raised to the power of 4/3 ($\theta_B^{4/3}$).

The equation is suitable for panel geometries in the range of $\pi/2 < \Sigma\alpha < \pi$, which would satisfy most origami structures.

For the large displacement analyses ($\theta_B > \ 23° \approx 0.4$rad), we observe the same global behaviors as previous research (Lobkovsky et al., 1995). The bending becomes restricted along the short diagonal D_S (Figure 2.4 (b)). In this case, tensile forces develop over the sheet's surface, and flexural deformations become restricted to a small area focused at the bending ridge. In Figure 2.6 we verify that, for large displacements, the bending moment scales reasonably well with $\theta_B^{4/3}$. This behavior differs from a linear hinge and, in contrast, the restrained panel becomes stiffer with larger bending angles (Figure 2.4 (e)). For large displacements, stiffness is not significantly affected by the panel geometry and boundary conditions, which is similar to observations in previous research (DiDonna, 2002; Witten, 2007). The bending moment for large displacements can be approximated as

$$M_{BL} = \theta_B^{4/3}(1.0)k\left(\frac{D_S}{t}\right)^{1/3} = \theta_B^{4/3}(1.0)\frac{Et^3}{12(1-\nu^2)}\left(\frac{D_S}{t}\right)^{1/3}, \tag{2.6}$$

which includes the increasing stiffness with higher angles of θ_B.

We can further use Equations 2.5 and 2.6 to inform not only the bar and hinge models, but also other phenomenological models aimed at simulating the structural behaviors of origami.

As an example, we can use the small deformation relations to define each of the stiffness components in the diagonal matrix $\mathbf{K}_B$ (see Equation 3.1) as

$$K_{BS} = (0.55 - 0.42\frac{\Sigma\alpha}{\pi})k\left(\frac{D_S}{t}\right)^{1/3}. \tag{2.7}$$

Large displacement nonlinear cases will require an alternative formulation.

The N5B8 model can be used to capture both small and large displacements. Because two rotational hinges are used on each diagonal of the panel, half of the appropriate stiffness ($K_B/2$) is placed on each rotational constraint. The deformed shape in (Figure 2.4 (c)) is obtained by using Equation 2.7 to define each angular constraint with the corresponding diagonal (D_S or D_L). This allows for the central node to deform downward and the deformed shape looks similar to the FE approximation where there is bending along both diagonals. This approach also provides a good approximation for the displaced shape with large displacements because bending occurs primarily about the short diagonal, which is more flexible. Unfortunately, Equations 2.5 to 2.7 assume panel bending in only one direction, thus the stiffness of the N5B8 model is lower when both diagonals are defined with these approximations. A better stiffness approximation is obtained when the short diagonal is defined based on Equations 2.5 to 2.7, and the long diagonal is defined to be about 100 times stiffer. This adaptation provides a reasonable representation of panel bending stiffness and the deformed shapes consist of bending about the short diagonal. Future studies could be pursued to define both the short and long diagonals in a manner that would capture an accurate deformed shape and stiffness simultaneously.

2.2.2 The effect of panel geometry on bending stiffness

In this section, we explore the influence of the geometry and skew on the bending stiffness of panels. The restrained rhombus panel presented in Figure 2.4, is used as a base case for four geometric variations: *Case A* - Change D_S, and keep D_L constant; *Case B* - Change D_L, and keep D_S constant; *Case C* - Change D_L and D_S, and keep the panel area (A) constant; *Case D* - Change D_L and D_S, and keep panel corner geometry $\Sigma\alpha$ constant. Cases A, B and C induce a variation of the panel corner geometry $\Sigma\alpha$ which is calculated as

$\Sigma\alpha = \alpha_1+\alpha_2+\alpha_3+\alpha_4 = 4\alpha_1 = 4\arctan(D_S/D_L)$. Cases A, B, and D induce a change in the panel area $A = D_L * D_S/2$. For these analyses we calculate a normalized bending stiffness of the sheet as $K_B = M_B/\theta_B/k$. The results for small and large displacement cases are shown in Figure 2.7. The bending stiffness for small displacement scales well with the geometric parameter $\Sigma\alpha$. As is later shown in Figure 2.8, we have found that this parameter provides a good correlation for different types of panel skew. An elongated panel with $\Sigma\alpha = 0.6\pi$ ($D_L \approx 2D_S$) would have about double the stiffness of a square panel with $\Sigma\alpha = \pi$. This large difference in stiffness occurs because the non-square, elongated geometry limits double curvature, and instead the bending energy becomes concentrated at the corners of the short diagonal. This phenomenon also occurs with skew and is represented in Figure 2.8 (a). The stiffness scales roughly with the length to thickness ratio as $(D_S/t)^{1/3}$ when the geometric parameter $\Sigma\alpha$ is held constant. The results for large deformations in Figure 2.7 (g)-(j) show that the geometric parameter $\Sigma\alpha$ does not have a significant influence on the bending stiffness and the stiffness scales primarily with the length to thickness ratio as $(D_S/t)^{1/3}$.

We also explore the geometric effect of skewed panels by performing the same bending analysis with panels of different geometries and a constant short diagonal D_S. In Figure 2.8, we show seven different geometries, with Cases 1-3 using a rhombus geometry similar to Figure 2.4, and Cases 4-7 using a modified geometry derived from the *minimal ridge* case where $\Sigma\alpha = 0$ (Witten, 2007). The geometric parameter $\Sigma\alpha$ for Cases 1-3 is modified by changing the length of the long diagonal D_L. Cases 4-7 are modified by increasing the angles α starting from the minimal ridge case. The bending stiffness for small displacements is highly dependent on the corner geometry $\Sigma\alpha$. When the panel is a square it experiences double curvature with uniform bending energy over the entire area of the panel. The system is stiffer when the panel shape is more skewed, elongated, or the corners of the short diagonal are more obtuse (e.g. Case 3 or Case 6). The stiffer cases occur because bending becomes restricted at the obtuse corners and double curvature is limited. For the large displacement cases the skew and geometric parameter $\Sigma\alpha$ do not have a significant effect. In these cases bending is restricted to the short diagonal of the panel, thus the elongation and skew of the panel have little effect on the global stiffness.

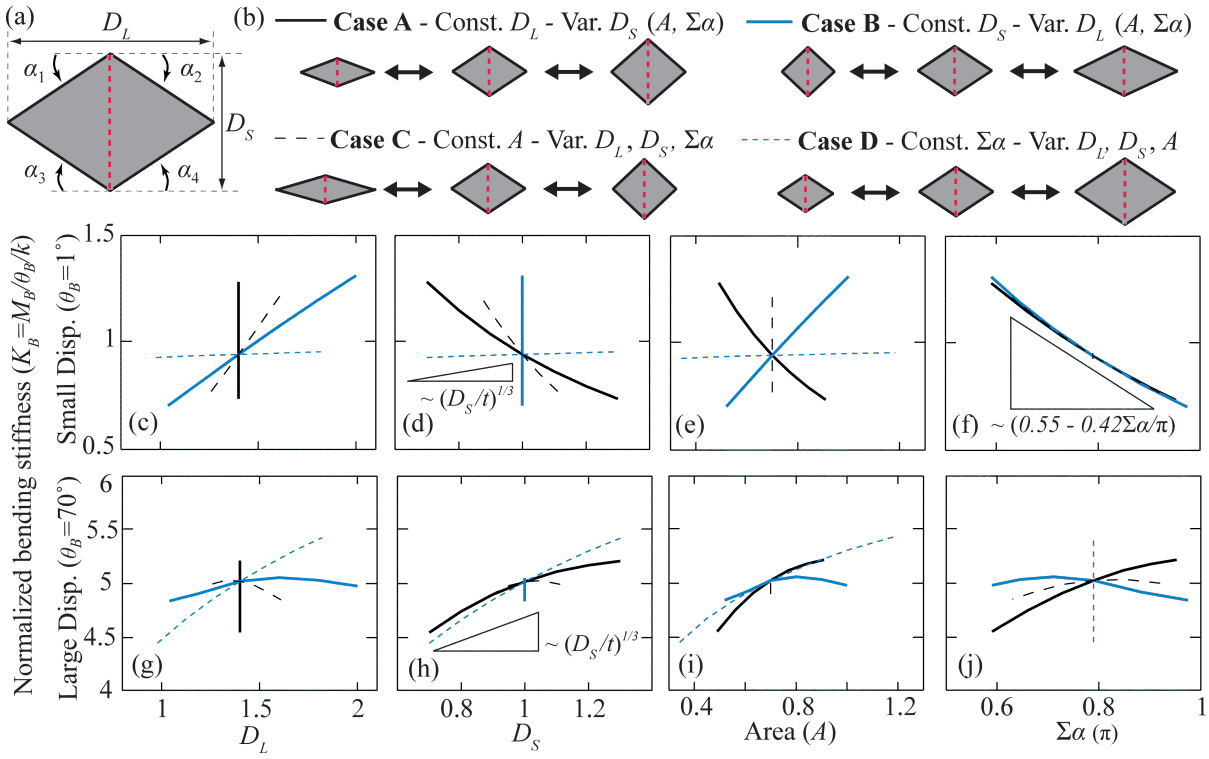

Figure 2.7: Influence of panel geometry variations on the bending stiffness of the panel. (a) Reference geometry of a single panel. (b) Four cases where the geometric parameters are varied (i.e. D_L, D_S, A, and $\Sigma\alpha$). In each case, one variable is kept constant while the other three are varied. (c)-(f) Normalized bending stiffness vs. geometric parameter for small displacement bending ($\theta_B = 1°$). Stiffness scales roughly as $(0.55 - 0.42\Sigma\alpha/\pi)$. The case where $\Sigma\alpha$ is constant scales roughly as $(D_S/t)^{1/3}$. (g)-(j) Normalized bending stiffness vs. geometric parameter for large bending displacement ($\theta_B = 70°$). Stiffness scales roughly as $(D_S/t)^{1/3}$.

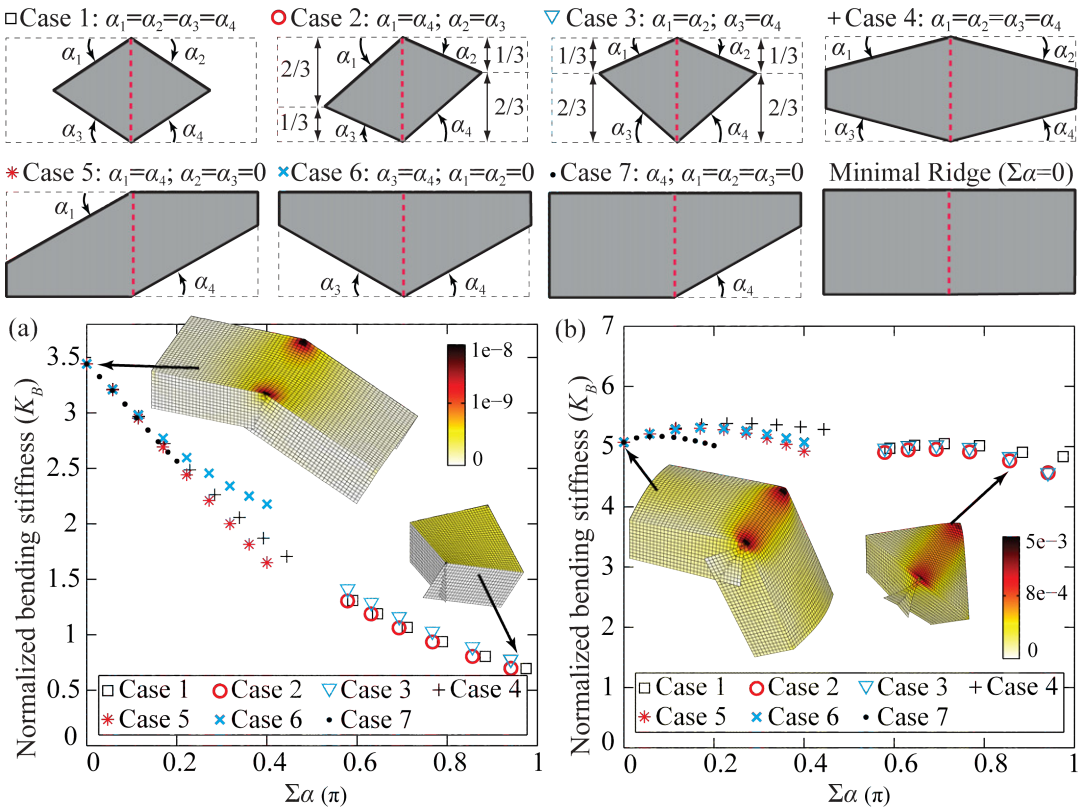

Figure 2.8: Influence of panel skew on bending stiffness. The panels with different skewed configurations are quantified by $\Sigma\alpha = \alpha_1 + \alpha_2 + \alpha_3 + \alpha_4$. Normalized bending stiffness vs. panel corner geometry ($\Sigma\alpha$), for (a) small displacement bending ($\theta_B = 1°$) and (b) large displacement bending ($\theta_B = 70°$). Skew has an influence on the bending stiffness for small displacements, but not for large displacements.

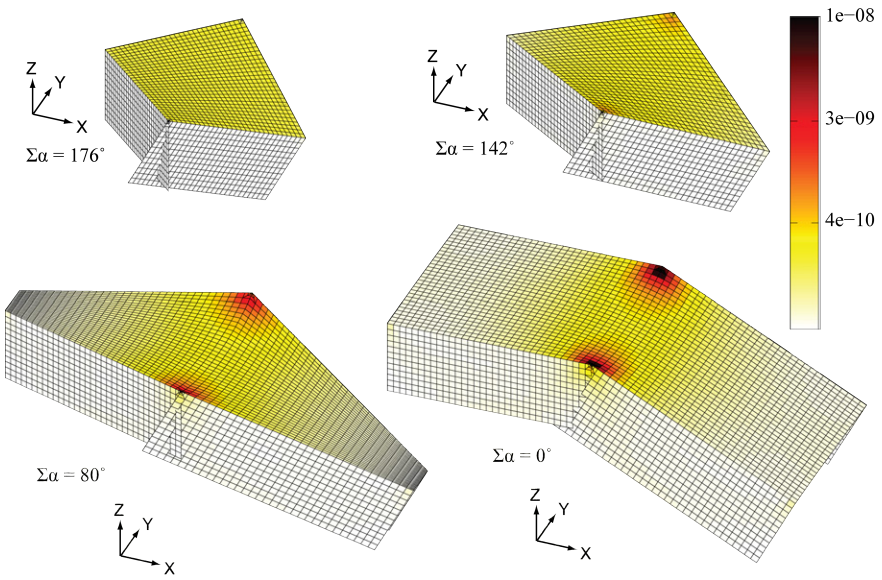

Figure 2.9: Energy distribution on thin restrained panel sheet for a small displacement bending ($\theta_B = 0.1°$). The four cases have different panel corner geometries ($\Sigma\alpha$), and a single scale is shown for the energy distributions. The square panels (high $\Sigma\alpha$) have a uniform energy distribution with bending in both directions. The elongated panels (low $\Sigma\alpha$) have energy concentrated at the panel corners and bending occurs primarily in the Y direction. The displaced shapes are scaled by 300.

2.2.3 Geometric influence on panel energy distribution

In this section, we explore the energy distribution for different bent panels. The energy distributions can help us to better understand the reasons for the stiffness scaling properties with respect to geometry. In Figure 2.9, we show the deformed shapes and energy distributions of four restrained origami panels with different geometries ($\Sigma\alpha$). The panels are bent about the short diagonal with a small applied displacement ($\theta_B = 0.1°$). The energy distribution results for these analyses are summarized in Table 2.1 with energies organized based on the finite element behaviors. The behaviors are shown in Figure 2.10 and are grouped into in-plane and out-of-plane behaviors. In-plane behaviors include stretching in the two global directions (N_X and N_Y), and shear (S_{XY}). Out-of-plane behaviors include bending shears (S_X and S_Y) and bending moments in the two directions (M_X and M_Y), as well as twisting moment (M_{XY}). The table only shows the energy of the top restrained sheet.

Although, we perform a large displacement analysis with updated geometry, the displacements are small and we can observe double curvature bending in the thin sheets. For the more square panels, there is double curvature bending and an even distribution of energy

Table 2.1 Energy distribution of four different thin panels with restrained edges when bent by $\theta_B = 0.1^\circ$

(a) Total energy distribution per element behaviors

		Σα = 176°	Σα = 142°	Σα = 80°	Σα = 0°
In-plane	N_X	1.32E-11	4.85E-11	9.55E-10	8.38E-09
	N_Y	1.75E-11	1.95E-11	2.70E-10	5.47E-10
	S_{XY}	8.01E-12	3.53E-11	2.85E-10	2.80E-09
Out-of-plane	S_X	3.18E-09	5.28E-09	3.41E-08	2.23E-07
	S_Y	3.04E-09	3.62E-09	1.75E-08	1.03E-07
	M_X	5.19E-07	6.89E-07	1.21E-06	3.08E-06
	M_Y	5.17E-07	6.62E-07	8.38E-07	2.17E-07
	M_{XY}	4.90E-10	3.86E-08	4.05E-07	1.41E-06
	Total	1.04E-06	1.40E-06	2.51E-06	5.04E-06

Largest ... Smallest

(b) % of total energy per element behaviors

		Σα = 176°	Σα = 142°	Σα = 80°	Σα = 0°
In-plane	N_X	0%	0%	0%	0%
	N_Y	0%	0%	0%	0%
	S_{XY}	0%	0%	0%	0%
Out-of-plane	S_X	0%	0%	1%	4%
	S_Y	0%	0%	1%	2%
	M_X	50%	49%	48%	61%
	M_Y	50%	47%	33%	4%
	M_{XY}	0%	3%	16%	28%
	Total	100%	100%	100%	100%

Largest ... Smallest

throughout the panel surface. The elongated panels have energy concentration at the short diagonal corners and the curvature in the X direction is higher than that in the Y. The influence of panel geometry on curvature and bending energies can be observed from Table 2.1 (b). The restricted deformation for the elongated (or skewed) panels explains the increased stiffness observed in Figure 2.8 (a). The increase in the twisting, and shear energies for the elongated panels (Table 2.1 (b)) occurs because twisting is required to transit from the conical curvature at the corners to the double curvature at the center of the sheet.

The adjacent restraining panels for the small displacement simulations do not have a significant amount of energy (Figure 2.9). Significant stretching and shear forces (and energies) do not occur for the small displacement analyses because the deformation can be primarily accommodated through bending of the top panel. Because there is a high concentration of energy at the corners of the sheet, adding holes there would likely reduce the stiffness for the skewed panels but less so for the square panels. Therefore, the observed effect that stiffness is higher for elongated and skewed panels, would likely not be as significant in practical applications.

Figure 2.11 shows the deformed shapes and energy distributions of the four restrained panels for a large applied displacement ($\theta_B = 70^\circ$). The energy distribution results for these FE analyses are presented in Table 2.2. The deformed shapes and energy distributions are somewhat similar for all four cases. Deformation primarily occurs as bending along the short diagonal (i.e. bending in the X direction) with energy concentrations at the ends of the diagonal. Stretching and shearing occur for all cases with energy being transferred to

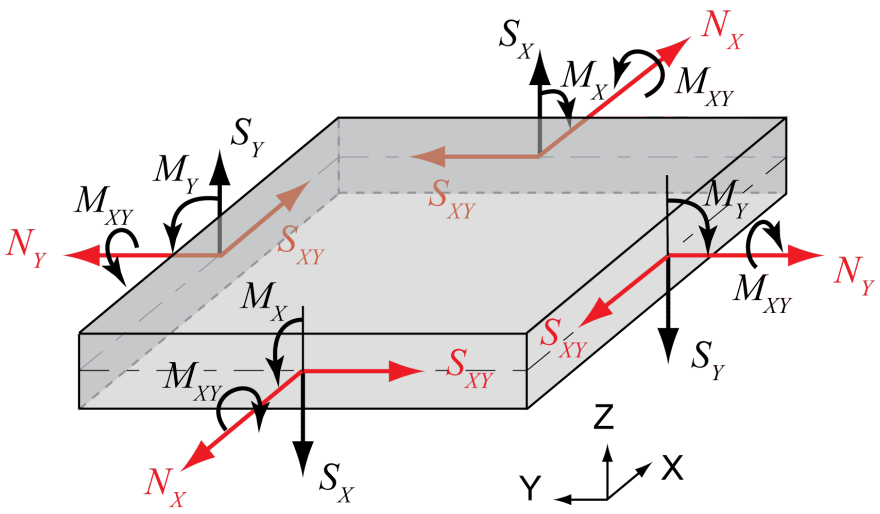

Figure 2.10: In-plane and out-of-plane behaviors on a thin shell element used in the FE model. The in-plane behaviors shown in red include stretching (N_X and N_Y), and shear (S_{XY}). Out-of-plane behaviors shown in black include bending shears (S_X and S_Y), bending moments (M_X and M_Y), and twisting moment (M_{XY}).

the adjacent restricting panels. The energies presented in Table 2.2 only represent the top restrained sheet, and not the adjacent sheet material. The square panel geometry leads to higher stretching and shear energies as the cone at the corner of the diagonal becomes sharper with higher curvature ($\approx 25\%$ in-plane energy for $\Sigma\alpha = 176°$ vs $\approx 8\%$ for $\Sigma\alpha = 0°$). Although the total energy in the top sheet for elongated sheets is higher, the higher stretching for square sheets leads to higher energy in the adjacent panels and thus an overall similar bending stiffness for all geometries (Figure 2.8 (b)). These results agree well with other literature in the field that explores the large displacement behavior of thin sheets (e.g. Lobkovsky et al. (1995); DiDonna (2002); Witten (2007)).

We have found that, for large displacement bending, it is important to either use the same materials at the side panels or to use symmetric boundary conditions to restrain the top sheet (e.g. as in Lobkovsky et al. (1995)). If we use side panels with a much higher or infinite stiffness, there is a significant overestimation of the panel bending stiffness. This increase occurs because the stretching and shearing at the corners is additionally restrained, and the in-plane energies start to govern the system behavior. In reality, these in-plane energies would not be as high because they would be mitigated by stretching and bending in adjacent panels.

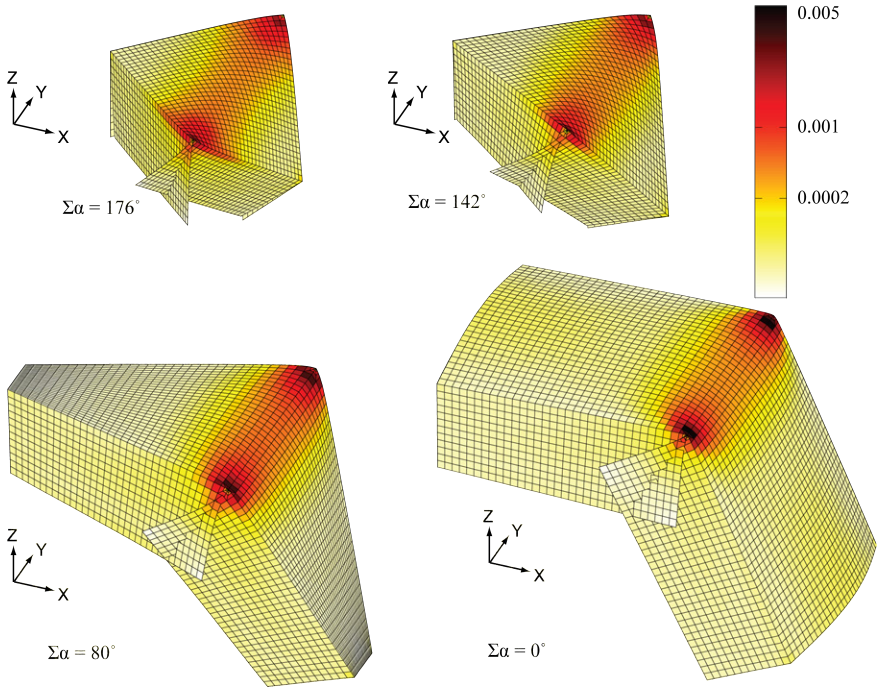

Figure 2.11: Energy distribution on thin restrained panel sheet for a large displacement bending ($\theta_B = 70°$). The four cases have different panel corner geometries ($\Sigma\alpha$), and a single scale is shown for the energy distributions. The deformed shapes and energy distributions are similar for all cases with bending and energy concentrated along the short diagonal.

Table 2.2 Energy distribution of four different thin panels with restrained edges when bent by $\theta_B = 70°$

(a) Total energy distribution per element behaviors

		Σα = 176°	**Σα = 142°**	**Σα = 80°**	**Σα = 0°**
In-plane	N_X	1.57E-01	8.68E-02	1.04E-01	8.67E-02
	N_Y	1.75E-01	2.28E-01	1.81E-01	1.04E-01
	S_{XY}	9.92E-02	1.10E-01	1.02E-01	4.77E-02
Out-of-plane	S_X	6.51E-03	7.30E-03	1.88E-02	4.22E-02
	S_Y	8.93E-03	8.52E-03	1.17E-02	2.44E-02
	M_X	1.04E+00	1.80E+00	2.21E+00	2.10E+00
	M_Y	3.37E-01	1.87E-01	1.47E-01	2.93E-01
	M_{XY}	1.91E-02	4.35E-02	1.56E-01	3.40E-01
	Total	1.84E+00	2.47E+00	2.93E+00	3.03E+00

Largest ... Smallest

(b) % of total energy per element behaviors

		Σθ = 176°	**Σθ = 142°**	**Σθ = 80°**	**Σθ = 0°**
In-plane	N_X	8%	4%	4%	3%
	N_Y	9%	9%	6%	3%
	S_{XY}	5%	4%	3%	2%
Out-of-plane	S_X	0%	0%	1%	1%
	S_Y	0%	0%	0%	1%
	M_X	57%	73%	75%	69%
	M_Y	18%	8%	5%	10%
	M_{XY}	1%	2%	5%	11%
	Total	100%	100%	100%	100%

Largest ... Smallest

2.3 Bending along prescribed fold lines

Fold lines (or hinges) between two origami panels, is where bending is intended to occur for the kinematic folding of origami (see right column of Figure 2.1). With modern applications of origami in engineering, the fold lines can be created in many different ways and from a variety of different materials. A basic method for creating a fold is to *crease* the material by using a die crease, perforating the sheet, or etching into the material. Creasing and folding the sheet causes permanent localized damage, which leads to a more flexible fold line (similar to a folded cardboard box). Fold lines can be engineered into *composite* system where a flexible material is used at the fold line, while stiff material is used at the panels. Composite origami can be created using additive manufacturing of multiple materials or by sandwiching flexible materials between stiff panels. For large scale origami, physical *hinges* are often used to facilitate motion between stiff panels with finite thickness. The characterization, modeling, and behavior of the fold lines has been a wide topic of study, and there is not a one single approach that can be used for all origami structures and systems. In this work, we provide a summary of the crease type folds and quantify their stiffness in scalable terms. The behavior of the composite and hinged origami would likely be dependent on the specific design, and scalable stiffness properties can be explored on an individual basis.

When performing detailed modeling of fold lines, it is possible to include a finite fold width (Peraza Hernandez et al., 2016), or to account for an offset that accommodates hinges and the material thickness (Edmondson et al., 2014; Chen et al., 2015). However, for most origami, the fold width can be considered negligible, and the fold is assumed to lie on the center of the adjacent panels. We make these assumptions for our model, and we are able to simulate the bending moment behavior of the fold line by connecting adjacent panels with a rotational hinge. In this chapter, we use a linear elastic bending moment behavior at the fold lines, however the model can be adapted to capture nonlinearity (e.g. Giampieri et al. (2011), Mentrasti et al. (2013b)). Origami with creased fold lines can have highly nonlinear behavior, while those with hinges may involve friction slip-stick type phenomena.

2.3.1 Stiffness characteristics of creased fold lines

We assume that the behavior over the length of the fold line is constant, and that the bending moment for the fold can be obtained from $M_{FL} = \theta_F K_{FL}$ where the factor K_{FL} represents the rotational stiffness of the fold line. The subscript $_L$ indicates that this is the *local* folding behavior over the infinitesimal small width of the fold, and that the behavior of the adjacent panels is not included. In Section 2.3.2, we discuss the interplay between the fold and adjacent panels and provide a stiffness scaling approach for the global fold behavior. Based on previous research (Lechenault et al., 2014; Pradier et al., 2016), we can expect K_{FL} to scale with the length of the fold line (L_F) and the bending modulus of the thin sheet (k). We can obtain the following equation for the localized stiffness of the fold line

$$K_{FL} = \frac{L_F}{L^*} k = \frac{L_F}{L^*} \frac{Et^3}{12(1-\nu^2)}, \tag{2.8}$$

where a length scale factor L^* (in units of length, e.g. m) defines the relative stiffness of the fold based on the material, fabrication, and geometric properties. The length scale factor L^* is assumed to increase with the thickness of the sheet (Lechenault et al., 2014), however, there is currently no physical basis for determining the length scale, other than from experimental data. Here, we follow the same methodology and use L^*, however, we acknowledge that future research may bring about alternative methods to quantify the local fold stiffness.

To better understand realistic values of L^*, we explore published experimental research on creased fold lines and summarize our findings in Table 2.3. The experiments consist of the following: 1 Beex and Peerlings (2009); 2 Huang et al. (2014); 3 Lechenault et al. (2014); 4 (Mentrasti et al., 2013a); 5 (Nagasawa et al., 2001); 6 (Nagasawa et al., 2003); 7 (Nagasawa et al., 2008); 8 (Pradier et al., 2016); and 9 (Yasuda et al., 2013). Table 2.3 documents the material properties, testing direction for the paper based samples, the creasing type and the general bending behavior. Several of the experiments crease and cycle the fold before testing (3,8,9) and in one case the thickness is partially cut or a dash cut is performed through the thickness (4ab). In the remainder of the cases (1,2,4c,5,6,7), a die crease mechanism is used and a virgin loading (folding) of the sample is tested. From the experimental results, we find the initial stiffness of the fold line with respect to the bending

Table 2.3 : Experimental results of fold line testing

#	Paper	Material	Crease Type	Direction	E (GPa)	t (mm)	K_{FL}/L_F (Nm/m/rad)	L^* (mm)‡	Comment
1	Beex and Peerling 2009	Laminated paperboard	Die crease - V	MD	1.3†	0.9	1.72-11.5	7.7 - 52	Elasto-plastic response affected by creasing depth.
2	Huang et al. 2014	Multi-ply layered paperboard A	Die crease - V	MD	4.4†	0.383	0.9 - 2.1	11-25	Elasto-plastic response affected greatly by creasing depth. The creasing direction (MD/CD) and the material properties of different plys (samples A,B,C) can influence behavior.
				CD	1.5†		0.32 - 1.1	7.2-25	
		Multi-ply layered paperboard B		MD	4.5†	0.39	0.7 - 1.8	14-36	
				CD	2.6†		0.5 - 1.4	10-29	
		Multi-ply layered paperboard C		MD	4.6†	0.332	0.4-1.4	11-40	
				CD	1.9†		0.25 - 0.8	8-26	
3	Lechenault et al. 2014	Mylar sheets	Folded by hand and weight - C	N/A	4	0.13	0.029	28	Essentially elastic response for large angle variations. Behavior depends on origami length scale.
					4	0.35	0.27	60	
					4	0.5	0.5	94	
4	Mentrasi et al. 2013	Paperboard	a. Cut - C/V	U	3.5*	0.4 - 0.44	0.041-0.095	222-667	Essentially elastic response.
			b. Dash cut - C/V		3.5*	0.4	0.38-0.73	29-55	Elasto-plastic response.
			c. Die crease - V		3.5*	0.4 - 0.44	0.16-0.69	30-133	Response can vary significantly.
5	Nagasawa et al. 2001	Paperboard	Die crease - V	MD	3.5*	0.44	2.6-3.7	7.6-11	Elasto-plastic response, peak strength was affected by creasing but stiffness was not.
6	Nagasawa et al. 2003	Paperboard	Die crease - V	MD	3.5*	0.46	0.5-5.4	5.9-64	Elasto-plastic response affected greatly by creasing depth. The stiffest cases correspond to no creasing.
				CD	3.0*	0.46	0.3-2.9	9.5-91	
7	Nagasawa et al. 2008	Paperboard	Die crease - V	MD	1.6	0.37	1.6-4.7	1.6-4.8	Elasto-plastic response affected greatly by creasing depth. Aluminum coating increases stiffness in non creased cases.
				CD	1.05		0.7-2.8	1.8-7.1	
		Paperboard coated with aluminum foil		MD	1.6		1.6-5.2	1.6-4.8	
				CD	1.05		0.7-3	1.7-7.1	
8	Pradier et al. 2016	ECF woodfree pulp uncoated paper	Folded by hand and weight - C	MD/CD/45°	4 MD	0.129	0.042	19	Essentially elastic response with stiffening when fold opens. Direction (MD/CD) does not influence behavior significantly.
9	Yasuda et al. 2013	Paper	C	U	2.9†	0.27	0.106	50	Linear behavior with stiffening when fold reaches closed state.

Notes:

Crease type: V - virgin folding of material C - material is pre-folded and cycled or pre-cut

MD - Machine (grain) Direction CD - Cross-machine (parallel) direction

U - Unknown information

† Value interpolated from results presented in paper

* Value assumed for typical paper/paperboard

‡ Except for ref. #3, the authors computed the L^* values

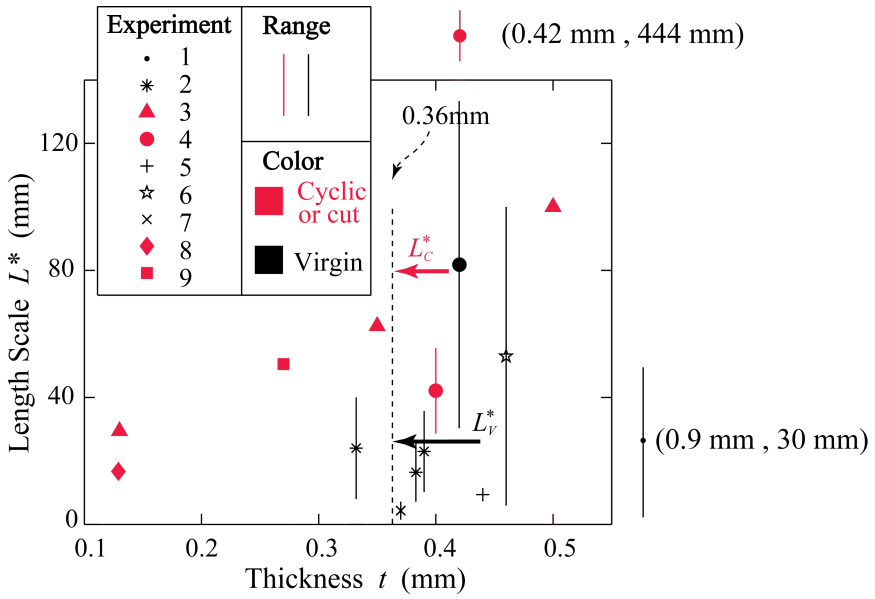

Figure 2.12: The length scale L^* with respect to the thickness for the experiments in Table 2.3. The red (gray in B&W) points are cases where the crease is cycled or pre-cut. The black points represent cases where a virgin loading is applied to a die crease. The distribution of L^* from the different experiments does not show a strong correlation with thickness, and likely material, fabrication and other properties have a more significant influence. We show representative values of the length scale for the virgin (L_V^*) and the cyclic (L_C^*) tests for a material thickness of 0.36 mm. Two outliers from the experiments (experiment 1 and 4a) are represented off the plot with the numerical value of the central points (t,L^*).

angle (in radians) and normalize by the fold length to obtain a normalized stiffness K_{FL}/L_F (in units of Nm/m/rad). Most cases where a virgin loading is performed exhibit a highly nonlinear elasto-plastic type of response, and for our calculations we only use the initial stiffness at the beginning of the experiment. For each set of experiments a range of values of the length scale are calculated as $L^* = 1/(K_{FL}/L_F/k)$. The bending modulus (k), uses thickness of the tested material (t) and the recorded elastic modulus (E) where available. The value of E is assumed for typical materials if not available from the experimental data, and we assume that the Poisson's ratio is $\nu = 1/3$ for all cases. In some of the studies the range in L^* resulted from sample variability (4,5,8), while in other studies the range in L^* can be attributed to the creasing penetration depth (1,2,6,7). Cases with deeper creasing typically result in more damage to the material and a more flexible fold line (higher values of L^*); experiments 1, 5, 6, and 7 contain some samples where no creasing is performed.

To show the variability in fold stiffness, in Figure 2.12 we plot the length scale L^* with

respect to the thickness for the nine tested specimens. The cases where cyclic loading or cutting is performed tend to have higher length scales indicating a more flexible fold line. The cases where only the virgin loading is recorded (1,2,4c,5,6,7) would likely have much higher length scales (be more flexible) if the fold is cycled or the entire loading curve is considered. The results from Lechenault et al. (2014) (tests 3) show a trend that L^* increases with thickness, however, globally it appears that the material, fabrication, and fold properties have a much larger effect on L^*. We do not fit the data, but as a point of reference, we pick two points to show: 1) flexible folds typical for origami with cutting and cyclic loading ($L^*_C = 80$ mm), and 2) a high stiffness estimate of folds with little creasing or virgin loading ($L^*_V = 25$ mm). Future experiments can provide improved estimates for the scaling of L^* with respect to thickness, and other fold characteristics.

2.3.2 Scalable stiffness parameters for fold lines

The results in the previous section provide insight on the behavior of fold lines, where the localized stiffness can be considered a function of fold length divided by a length scale (L_F/L^*). The length scale is believed to increase with thickness of the materials thus providing a scalable connection to real parameters. We can use these scale independent definitions for the fold stiffness in the bar and hinge model, as well as other simplified approaches. However, as currently presented, Equation 2.8 can result in an unrealistically high fold stiffness as L^* approaches zero. An infinite stiffness may be realistic on a local scale (e.g. when there is no fold), however the global stiffness of the fold would be limited by the flexibility of adjacent panel material.

In Figure 2.13, we explore how the local fold stiffness and adjacent material behave for different L^*. We use 30 mm panels, with a thickness of 0.36 mm to allow a length to thickness ratio of ≈ 100 for the short panel diagonals ($D_S = 35.87$ mm). This thickness is also close to many of the experiments presented in Table 2.3. We use a FE model where the panels and adjacent panels are simulated with shell elements. In the FE model, the localized fold line is simulated using collocated nodes that are joined in the three Cartesian directions. A rotational spring is placed at each pair of collocated nodes to simulate the local stiffness of the fold line (i.e. Equation 2.8).

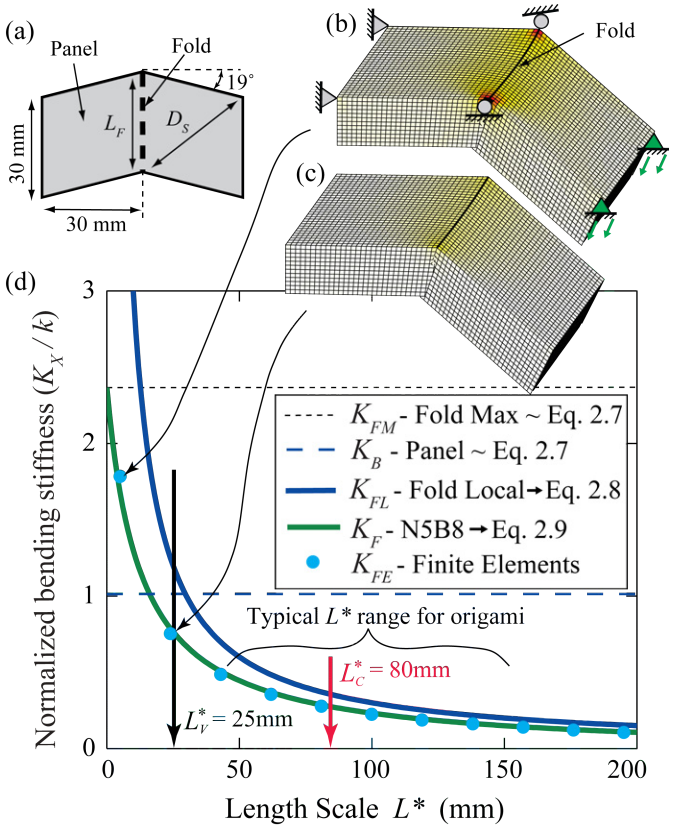

Figure 2.13: Bending of a fold line that connects two restrained panels with $t = 0.36$ mm. Large displacement analyses are performed with $\theta_F = 40°$. (a) Schematic of the fold and the two skewed panels with a geometry parameter of $\Sigma\alpha = 142°$. (b) Bending of a FE model where the localized fold line is much stiffer than adjacent material ($L^* = 5$ mm). Double curvature bending occurs similar to a sheet with no fold line. (c) Bending of the system where the localized fold line is stiffer than most origami ($L^* = 25$ mm). Bending occurs primarily at fold line. (d) The normalized bending stiffness of the fold and the adjacent panels. The maximum and panel stiffness (K_{FM} and K_B) are calculated with different variables (from Equation 2.7), while the fold stiffness (K_{FL} and K_F) is plotted for different L^* values (from Equations 2.8 and 2.9 respectively). We show representative values of the length scale for the virgin (L_V^*) and the cyclic (L_C^*) tests.

We perform a large displacement analysis where the fold is bent to $\theta_F = 40°$, and we calculate the bending stiffness similar to before. We normalize the stiffness by k, and compare different fold definitions and the adjacent panel (K_B calculate from Equation 2.7). In a case where an unrealistically high stiffness is used for the fold (Figure 2.13 (b)), the system deforms similar to the minimal ridge case presented in Section 2.2.2. Thus, we introduce a *maximum* fold stiffness K_{FM} that represents the stiffness of adjacent panel material. We assume the case of a minimal ridge and calculate K_{FM} with Equation 2.7 where we substitute L_F for D_S and we assume $\Sigma\alpha = 0$. Considering that the localized fold and the adjacent material act in series, we calculate a combined fold stiffness as

$$K_F = 1/(1/K_{FL} + 1/K_{FM}). \tag{2.9}$$

The introduction of K_{FM} limits the maximum stiffness of the fold when L^* is low (Figure 2.13 (d)). The value of K_{FM} is not important for the analysis, and we find that the N5B8 model provides a reasonable estimate for fold stiffness when either half or double the value of K_{FM} is used. Bending of the adjacent panels typically has a higher stiffness than the fold line ($K_B > K_F$) for the typical origami range (realistically large values of L^*). In extreme cases where a fold is intentionally restricted from folding ($L^* < L^*_V$), the entire fold assembly may be about two to three times stiffer than the adjacent panels. Thus, if the panel to fold stiffness ratio is used for evaluating system behavior, we believe that a range of $K_F/K_B = 1/20$ to 3 would provide a realistic estimate. The ratio may change slightly for different thickness of the material or L/t ratios.

Equation 2.9 can be used to define the fold stiffness in different bar and hinge models, as well as other phenomenological models where fold lines are simplified to a rotational hinge (e.g. Qiu et al. (2016)). We use a FE model and the N5B8 model to explore the asymmetric bending of a fold and adjacent panel where only one side of the panel is displaced downward (Figure 2.14). The connectivity of the fold line in the N5B8 model can be performed in two ways where the panel corners (outside) and/or the panel central node (inside) are connected to the fold element (see legend in Figure 2.14 or see Figure 3.4 for details). When only outside or inside connectivity is used, half of the stiffness in Equation 2.9 is distributed to each rotational constraint. If all four fold components are used, a quarter of the stiffness is

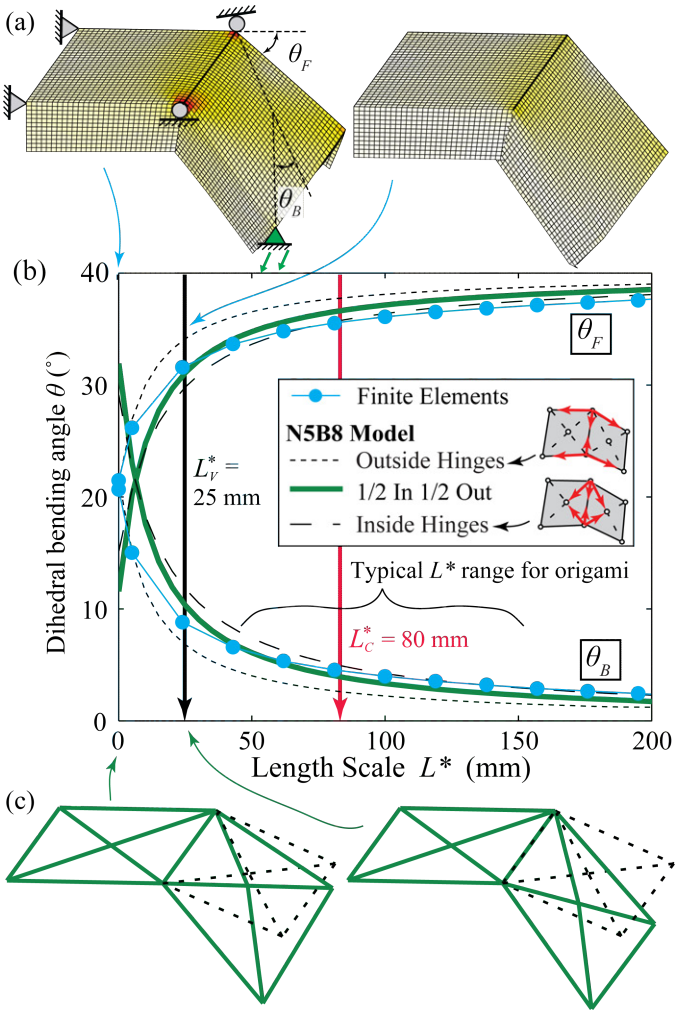

Figure 2.14: Asymmetric bending of the fold system from Figure 2.13. (a) Bending of a FE model with folds stiffer than typical origami ($L^* = 1$ mm left and $L^* = 25$ mm right). When the fold stiffness reaches realistic origami stiffness values ($L^* > 25$ mm) bending occurs primarily along the fold. (b) The folding angle of the fold (θ_F - top) and the adjacent panel (θ_B - bottom) with respect to the length scale parameter (L^*) for a FE model and different stiffness distributions in the N5B8 model. (c) Fold and panel bending simulated with the N5B8 model. We show representative values of the length scale for the virgin (L_V^*) and the cyclic (L_C^*) tests.

distributed to each constraint. The N5B8 model is able to capture the deformed state of the system relatively well regardless of the connectivity used (when considering most realistic values of L^*). Using only outside connectivity (which is the only option for N4B5 and N4B6 models) tends to slightly overestimate fold bending, and underestimate panel bending. For all further analyses we use both the inside and outside connectivity as it seems to provide the best estimate for the deformed shape of typical origami.

2.4 Concluding remarks

This chapter explores stiffness scaling of origami with an objective to inform the properties of the bar and hinge model that is discussed in more detail in Chapter 3. The bar and hinge model can capture three fundamental origami behaviors: 1) stretching and shearing of thin sheet panels, 2) bending of the panels, and 3) bending of fold lines. We explore the influence of panel geometry on the origami stiffness, and provide a study on the fold line stiffness characteristics. We create phenomenological relations to quantify stiffness of the different origami behaviors. All of these newly determined relations are scale dependent and incorporate material properties of the system. Thus many of the behaviors have been explored in the context of origami. The findings from this chapter could be used to inform the bar and hinge model, as well as other future origami models. A summary of the findings is presented here:

- All three of the origami stiffness behaviors captured in the N5B8 model can incorporate length scale effects, thickness (t), Elastic Modulus (E), Poisson's ratio (ν).
- For in-plane loading, the N5B8 model simulates tensile stiffness of the panel well, but it overestimates the shear stiffness. It provides a reasonable estimate of stiffness for square and skewed panels. The N5B8 model can capture isotropic material behavior.
- Panel bending stiffness can be defined to scale based on the width to thickness ratio as $(D_S/t)^{1/3}$ and with the bending modulus of the sheet k (suggested by Lobkovsky et al. (1995)).
- The out-of-plane panel bending stiffness for small displacements is highly dependent on panel geometry and skew ($\Sigma\alpha$). Skewed or elongated panels tend to be more stiff than square panels as they restrict double curvature over the surface.

- Alternative formulations for panel bending may be used for large displacement bending of panels, because the stiffness scales with $\theta_B^{4/3}$ (behavior first discussed by Lobkovsky et al. (1995)). The panel geometry does not significantly influence stiffness for large displacements.
- Further research can provide insight on how the N5B8 formulation may be adapted to capture the stiffness transition from small to large displacement panel bending (i.e. from Equations 2.5 and 2.6).
- Fold line stiffness can be defined to scale with the fold length L_F, the bending modulus of the sheet k, and a length scale parameter as $1/L^*$, (first suggested by Lechenault et al. (2014)). The length scale parameter is believed to scale with thickness, but also depends strongly on material, fabrication, and geometric characteristics of the fold.
- For origami structures fold bending is expected to dominate, and a panel to fold stiffness ratios of $K_F/K_B = 1/20$ to 3 are expected to be realistic.

CHAPTER 3

BAR AND HINGE MODELS FOR THE ANALYSIS OF ORIGAMI

Simulating the elastic stiffness and estimating deformed shapes of origami systems is important for conceptualizing and designing practical engineering structures. In this chapter, we explore a simplified bar and hinge model that can simulate essential behaviors of origami. The model simulates three distinct behaviors: stretching and shearing of thin sheet panels; bending of the initially flat panels; and bending along prescribed fold lines. The model is simple and efficient, yet it can provide realistic representation of stiffness characteristics and deformed shapes. It can be adapted for different analytical problems and can be used to model a variety of three dimensional origami structures. The simplicity of this model makes it well suited for the growing community of origami engineers, and its efficiency makes it suitable for practical problems such as optimization and parametrization of geometric origami variations. In this chapter we introduce the model and provide examples of how it can be used to study origami. Chapter 2 is closely related to this work as it explores stiffness scaling of origami and provides information to define the parameters for the model.

3.1 Introduction

The field of *origami* has grown in the past years as it offers novel solutions to problems in both science and engineering. Applications can range in scale and discipline from micro-robotics to deployable architecture. A typical origami consists of flat thin sheet *panels* (or facets) that are interconnected by *fold lines* (or hinges). There are many important aspects in the design and fabrication of origami systems that influence their general behavior and function. The geometry of the fold pattern determines the flat and rigid foldability of the system, the different ways in which origami can be folded, as well as the structural stiffness. The material and specific components used to make the origami can influence the kinematics, stiffness, and reliability of the origami. As the field of origami has grown, so have the theoretical, analytical, and fabrication techniques that allow for the successful simulation and implementation of novel folding solutions.

Characterizing the elastic and inelastic behavior of origami has become important for evaluating the feasibility and practicality of these systems. Recently, various approaches have emerged to model origami behaviors which may be grouped into three categories that vary in complexity and generality: 1) Analytical solutions for elasticity problems related to origami have been developed where typically a unit cell or a portion of the pattern is explored empirically, e.g. Hanna et al. (2014), Qiu et al. (2016), Brunck et al. (2016). These analytical approaches are typically suited for one specific origami pattern and cannot be readily used for other origami systems; they also often assume that deformation only occurs as folding along the prescribed fold lines. 2) A bar and hinge method where panel in-plane deformations are restrained using bars elements while bending of panels and folds is modeled using rotational hinges, e.g. Schenk and Guest (2011), Wei et al. (2013). 3) Numerical methods, and particularly, finite element (FE) methods where the system is discretized in a detailed fashion, e.g. Schenk et al. (2014a), Lv et al. (2014), Gattas and You (2015b), Peraza Hernandez et al. (2016). The FE approach often provides higher accuracy, however, it tends to be computationally expensive, and depending on the discretization technique may not be suitable for studying patterns with different geometries. In this chapter, we develop and explore a variation of the bar and hinge model that provides for scalable and isotropic modeling of origami. To show the practicality of the model, a real origami deformed by a physical load and a corresponding bar and hinge simulation are presented in Figure 3.1.

The chapter is organized as follows: Section 3.2 discusses basic ideas for modeling origami and introduces the bar and hinge formulation used in this work. In Section 3.3, we show examples of how eigenvalues can be used to study origami, while in Section 3.4 we use static analyses to characterize the structures. Section 3.5 provides a discussion on the model including its advantages and limitations, and Section 3.6 provides concluding remarks. Note that Chapter 2 discusses the basic behaviors of origami, and provides parameters to effectively model the stiffness.

3.2 Model variations and formulation

A typical origami consists of flat thin sheet *panels* (or facets) that are interconnected by *fold lines* (or hinges). The specific fold pattern and geometry have a large influence on

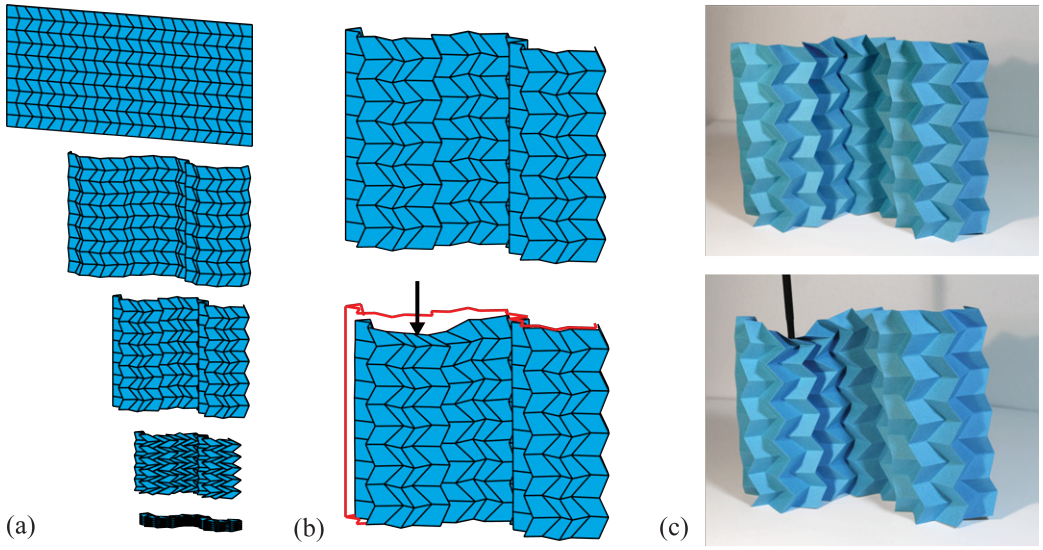

Figure 3.1: A Miura-ori pattern with a modified curved geometry. (a) Folding kinematics of the origami. (b) and (c) Initial (top) and deformed (bottom) shapes of the origami from a point load applied at the top, while the bottom of the structure is restrained vertically. (b) structural simulation with the bar and hinge model and (c) physical model of the origami.

both the folding behavior and the mechanical characteristics of the folded structure. In this chapter, we apply the bar and hinge approach to rigid foldable origami that can fold through a kinematic motion where panels remain flat and deformation occurs only at the fold lines. The in-plane behavior of panels, the bending of panels, and the folding along fold lines can be treated as three distinct behaviors. Contributions from this work and the bar and hinge model could be further adapted for non-rigid foldable patterns where the panels bend to allow the origami to fold. We also limit our study to system where the thin sheets are continuous and no cuts are present. We expect that with further study and modification the bar and hinge models could be adapted for kirigami where cuts are present and sections of the sheet are removed.

Although, we only explore the model for rigid foldable and continuous systems, this nevertheless allows for a tremendous variety of different origami geometries that can be explored and parametrized. Continuous rigid origami are the most common for practical application, because they are easier to manufacture, actuate, and deploy. The bar and hinge model can be used to analyze both flat foldable and non-flat foldable origami. The model is also suitable for both developable and non-developable origami (origami that can be folded and developed starting from a flat sheet). The bar and hinge approach can be used in the study of origami

tubes, or cellular systems where multiple origami are stacked and assembled together. The model may also be used for the analysis of non-folding origami-like structures made of thin sheets (e.g. boxes and cartons).

The geometric versatility, the simplicity, and the efficiency are the main motivation behind the bar and hinge model. The approach is suitable for a wide range of origami structures and can analyze the origami at different stages of deployment. It is possible to parametrize the origami and explore the influence of geometry on the structural properties. The simplicity of the model is useful in understanding the behavior of origami and adjusting the model for different analyses or different origami structures. Because only four or five nodes are used per panel, the bar and hinge model is much more efficient than any discretized FE approach. Over the last several years bar and hinge models have been used for various studies, and the model has evolved to provide more functionality and improved quality of analyses.

3.2.1 Evolution of bar and hinge models

Bar and hinge models vary in formulation and implementation. One of the earliest implementations is that by Schenk and Guest (2011) where four bars are placed on the perimeter of the panel and one bar is placed along the shorter diagonal of the panel. The model has four nodes and five bars, thus we designate this base of model as N4B5 (Figure 3.2). It has become popular to use the bar and hinge model with an energy approach to find the deformed shape of the structure (Bridson et al., 2003; Wei et al., 2013; Narain et al., 2013). The energy approach has been modified and has been used to provide fundamental studies on origami (Silverberg et al., 2014; Dudte et al., 2016). The N4B5 model has also been formulated based on elasticity and kinematics of solid state lattice systems (Evans et al., 2015). Another approach by Fuchi et al. (2015a) uses frame elements instead of bars, and includes rotational degrees of freedom to enhance the flexibility of the model at the fold lines. This model can potentially capture more local bending and torsion behaviors in the origami, but the formulation becomes more complex and the number of DOFs increases significantly. *All of these approaches assume that the in-plane behavior and scalability of stiffness can be neglected.* Inspired to overcome some of the limitations of the conventional N4B5 bar and hinge models, Filipov et al. (2016b) presented a N4B6 model that again has

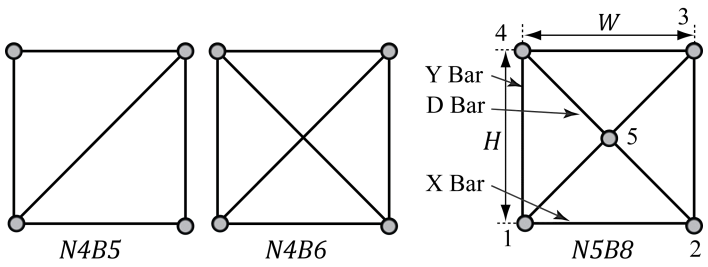

Figure 3.2: Evolution of the bar and hinge models, where different orientations of bars and nodes are used to simulate the in-plane behavior of origami panels. The frame of bar elements can be used as one element to model the in-plane behavior for an entire origami panel. The added complexity from the N4B6 and N5B8 models makes it possible to include scalability, isotropy, accuracy and more functionality to the model. The N4B5 model is from Schenk and Guest (2011), the N4B6 is from Filipov et al. (2016b), and the N5B8 is introduced in this work.

four nodes, but has an extra bar in the system and thus the frame becomes indeterminate for in-plane loading (Figure 3.2). By defining the bar properties, the model incorporates scaling effects and material properties. The indeterminate frame provides symmetric and isotropic response for in-plane loading. The model uses elastic modulus (E), Poisson's Ratio (ν), and thickness of the origami (t) along with length parameters to obtain scalable system behavior. One limitation of the N4B6 model is that, because of the crossed bars, large panel bending (large displacements) cannot be easily accommodated. Here, we introduce a modified approach where a node is incorporated at the connection of the panel diagonals. This model has five nodes and eight bars (N5B8), and is able to combine the benefits of both the N4B5 and N4B6. Approaches that have were aimed at modeling origami and thin sheets have also been formulated with scenarios where in-plane stiffness. Some approaches for modeling of origami and thin sheets have also been formulated to account for in-plane stiffness using triangular finite elements (Resch and Christiansen, 1971; Phaal and Calladine, 1992a). These approaches would lead to non-isotropic behavior for stretching and shear (see comparison in Section 2.1).

3.2.2 Model formulation for the bar and hinge approach

In this section we describe the numerical modeling of thin sheets in origami systems. A previously established model (Schenk and Guest, 2011) is used as a basis, and several improvements are discussed. We incorporate scaling effects for the structure and make the

panel stiffness dependent on the thickness (t), the elastic modulus (E), and Poisson's ration (ν) of the material. The formulation for fold modeling is also updated, and a ratio is used to relate the bending stiffness of panels to the bending stiffness of a fold. The model provides an improved basis for origami stiffness simulation, while keeping the formulation simple and modeling the origami components (panels and folds) as individual elements. The simplicity of this model makes it a good option for origami optimization, but we also acknowledge that it is not an ideal substitution to a detailed finite element (FE) model composed of nonlinear shell elements. The stiffness matrix ($\mathbf{K}$) for the origami structure incorporates stiffness parameters for 1) panels *stretching* and *shearing* ($\mathbf{K}_S$); 2) panels *bending* ($\mathbf{K}_B$); and 3) *folding* (bending) along prescribed fold lines ($\mathbf{K}_F$). The global stiffness matrix is constructed as follows:

$$\mathbf{K} = \begin{bmatrix} \mathbf{C} \\ \mathbf{J}_B \\ \mathbf{J}_F \end{bmatrix}^T \begin{bmatrix} \mathbf{K}_S & \mathbf{0} & \mathbf{0} \\ \mathbf{0} & \mathbf{K}_B & \mathbf{0} \\ \mathbf{0} & \mathbf{0} & \mathbf{K}_F \end{bmatrix} \begin{bmatrix} \mathbf{C} \\ \mathbf{J}_B \\ \mathbf{J}_F \end{bmatrix}, \tag{3.1}$$

where the compatibility matrix ($\mathbf{C}$) and Jacobian matrices ($\mathbf{J}_B$ and $\mathbf{J}_F$) relate the stiffness of elements to the nodal displacements as discussed in detail. Each node has three degrees of freedom (DOFs), x, y and z displacement, and the stiffness matrix is of size ($n_{DOFs} \times n_{DOFs}$), where n_{DOFs} is the total number of DOFs in the system.

3.2.3 Bar formulation for bar and hinge models

Each of the bars in the indeterminate frame (N5B8 frame in Figure 3.2) are defined to result in an isotropic and scalable behavior of the entire panel. A general formulation for bar elements is used where an equilibrium matrix ($\mathbf{A}$) relates internal bar forces ($\mathbf{t}$) to nodal forces ($\mathbf{f}$); a compatibility matrix($\mathbf{C}$) relates bar nodal displacements ($\mathbf{d}$) to bar extensions ($\mathbf{e}$); and a diagonal matrix ($\mathbf{K}_S$) relates the bar extensions to the local forces. The formulation can be written in three linear equations as

$$\mathbf{At} = \mathbf{f}, \qquad \mathbf{Cd} = \mathbf{e}, \qquad \mathbf{K}_S\mathbf{e} = \mathbf{t}. \tag{3.2}$$

Using the static-kinematic duality that $\mathbf{C} = \mathbf{A}^T$, the linear system for stretching and shear of the panels can be rewritten and is represented as the first row of Eq. 3.1. For definitions of the bar stiffness parameters (K_S) see Section 2.1.1. When constructing the full model of the origami structure, the bar frame is used essentially as a single element to model the in-plane behaviors of the panel. At fold lines, where two panels are connected, there will be two bars in the same location and connecting to the same nodes.

3.2.4 Rotational hinges for out-of-plane bending

Early implementations of the bar and hinge model use two triangular segments connected by an angular constraint along one diagonal to model the global out-of-plane displacement of the panel (Figure 3.3 (a)). The choice of the diagonal does not influence the displacement pattern for small displacements (Schenk and Guest, 2013), but typically the shorter diagonal (with triangular segments 1-2-3 and 1-3-4) used to better match the expected real world behavior. For the N5B8 model we have one additional degree of freedom out-of-plane at node 5. The panel is divided into four triangular segments with bending possible about both diagonals. For each panel four angular constraints are used to restrict bending between the adjacent triangular segments (Figure 3.3 (b)). Each angular constraint, F, is formulated separately based on the dihedral bending angle(s), θ_i, which can be calculated by using cross and inner products of the vectors $\mathbf{a}$, $\mathbf{b}$, $\mathbf{c}$ and $\mathbf{d}$ from the nodal coordinates of the panel $\mathbf{p}$. This constraint is defined as

$$F = \sin(\theta_i(\mathbf{p})), \tag{3.3}$$

and the corresponding Jacobian for panel bending, $\mathbf{J}_B$, is calculated as

$$d\theta_i = \frac{1}{\cos(\theta_i)} \sum \frac{\partial F}{\partial p_i} dp_i = \mathbf{J}_B \mathbf{d}, \tag{3.4}$$

where $\mathbf{d}$ are the displacements of the panel nodes. The second row of Equation 3.1 incorporates panel bending stiffness where each element in the diagonal matrix $\mathbf{K}_B$ corresponds to the bending stiffness for an angular constraint. The specific parameters used to define the bending stiffness K_B are discussed in Section 2.2.

The bending definition here is the same as that used by other researchers (Schenk and

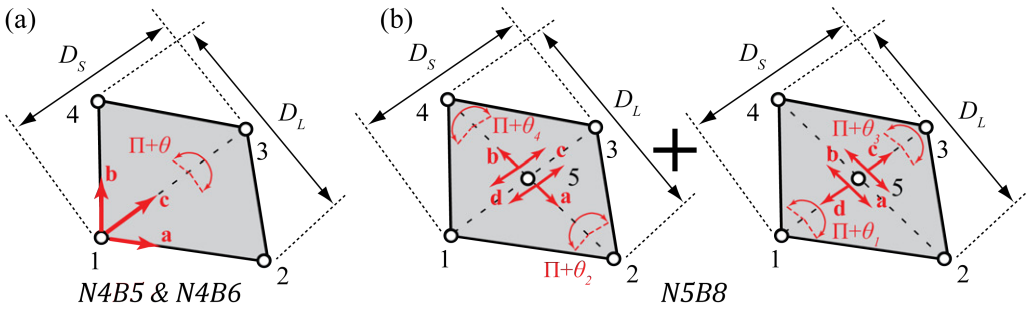

Figure 3.3: Placement of rotational hinges in the different bar and hinge models. The hinges provide stiffness for out-of-plane deformations of the panels.

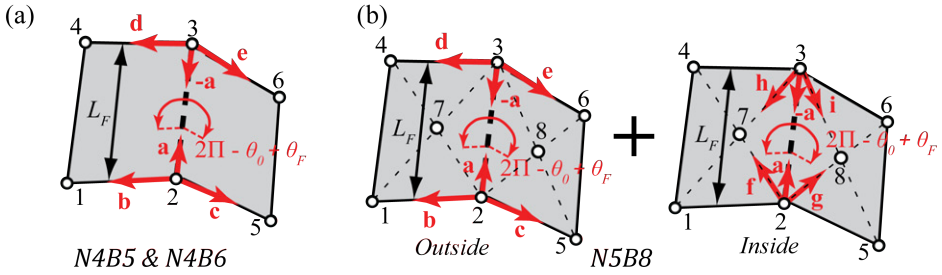

Figure 3.4: Placement of rotational hinges to capture the fold line stiffness. The N5B8 model can include both the outside and inside fold lines to better distribute stiffness onto the adjacent panels.

Guest, 2011; Phaal and Calladine, 1992b). Although the N5B8 model allows for bending in both directions, in Section 2.2 we discuss that this poses a problem for accurately capturing the stiffness. We make a modification to restrict bending about the long diagonal by making those rotational hinges about 100 times stiffer. This modification is not necessary for large displacement results, however using it allows for an accurate representation of panel bending stiffness, thus we use it for both small and large displacement cases. The deformed shapes with this modification consist of bending about the short diagonal only, and thus the N5B8 model is essentially reduced to a N4B5 model for panel bending. Future studies could be pursued to define both the short and long diagonals in a manner that would capture an accurate deformed shape and stiffness simultaneously. The accurate displaced shape for small displacements would include bending along both diagonals (see Section 2.2.1).

3.2.5 Rotational hinges for fold line bending

The folds are modeled in a similar fashion to the bending of panels. Realistic origami behavior does not allow for out-of-plane displacements along fold lines due to the restrictive nature of the perpendicularly oriented sheets. Thus, it is sufficient to use this simplified approach where the origami fold is modeled as a rotational hinge along an edge. A schematic of the fold model contains a fold spanning nodes 2 and 3 connecting two panels (1-2-3-4 and 2-5-6-3) (Figure 3.4). In the N4B5 and N4B6 models the angular constraint formulation (Section 3.2.4) is used to formulate two independent fold elements from the two vector sets: (1) **a**, **b**, and **c** and (2) **-a**, **d**, and **e**. We call these the *Outside* hinges as they connect the corner nodes of the panel. The initial fold angle (θ_0) represents the origami at a static and unstressed state. This angle could be different for different folds on the origami, and can be calculated using basic geometric relations for each chosen configuration. Here, the angle θ_F represents a rotation away from the initial static configuration.

The N5B8 model can use an additional set of *Inside* rotational constraints that connect to the central node: (3) **a**, **f**, and **g** and (4) **-a**, **h**, and **i**. The two inside angular constraints will have the same fold angle and are not influenced by panel bending, however the outside hinges could have different fold angles when panel bending is involved. The different fold angles can occur for all three variations of the bar and hinge model. In Section 2.3.2, we explore the interaction between fold and panel bending, and we show that using only inside or only outside hinges can provide a reasonable estimate for stiffness and displaced shape. However, if both inside and outside hinges are used in the N5B8 model, the fold line stiffness can be better distributed throughout the panel and a better estimate can be obtained for the deformed shape. The bending stiffness of the fold lines is discussed in detail in Section 2.3.2.

3.3 Eigenvalue analysis of origami systems

The bar and hinge method provides a basic system for global structural analysis of origami type systems. In this section, we show how the model can be used for both conventional structural analysis, as well as analyses methods suited specifically to origami. The bar and hinge framework can also be readily modified and can be used in ways beyond what is

presented in these examples.

3.3.1 Kinematic folding of origami

The basic implementation of the bar and hinge model can be used to study the folding characteristics of an origami pattern or structure, and subsequently perform folding operations. The mathematics on foldability of origami, and the folding kinematics are an advanced topic of study which involves the pattern geometry and the three dimensional motions that occur through folding (e.g. Huffman (1976); sarah-marie Belcastro and Hull (2002a); Hull (2012); Tachi and Hull (2016)). Rigorous analytical approaches for defining the folding kinematics are often limited to patterns with one or a few vertices and are cumbersome to compute. The bar and hinge model can provide a simple method to explore foldability of a pattern in mechanical and physical terms.

Because the panel and fold bending are treated separately in the model, it is possible to separate these behaviors and obtain information about the global folding characteristics from the stiffness matrix $\mathbf{K}$. One approach, as discussed by Schenk (2011) is to consider the null space of the combined compatibility matrix and Jacobian matrix for panel bending. This null space is equivalent to the stiffness matrix where the contribution of fold lines is not included (last row of Eq. 3.1 is removed). A more general approach is to make the fold lines much more flexible than the panels by using a L^* that is unrealistically high (e.g. 10000). Making the fold stiffness low makes the kinematic folding to be the preferred (most flexible) method of deformation, and still allows for bending to occur along the panel diagonals. The eigenvalue approach can be more forgiving in detecting possible fold patterns, as the null space approach may not show a fold pattern if the updated geometry has a small error. The eigenmodes also simultaneously provide feedback into the global stiffness and behavior of the system (e.g. they show the most flexible method of folding. Finally, the eigenvalue method can be useful at showing bifurcation points where the system can be reconfigured.

Having defined the geometry of the origami pattern in a completely flat or three dimensional state, it is possible to explore folding motions by obtaining the eigen properties of the stiffness matrix. In Section 3.3.2, we discuss an alternative approach where mass of the structure is also considered. We obtain the eigenvalues λ_i and corresponding eigenmodes $\mathbf{v}_i$

of the stiffness matrix $\mathbf{K}$ based on the linear equation

$$\mathbf{K}\mathbf{v}_i = \lambda_i \mathbf{v}_i. \tag{3.5}$$

The eigenvalues are arranged in an incremental order (i) and represent the elastic energy that would deform the structure into a shape represented by the corresponding eigenmode. The system is analyzed with no supports, and thus the first six eigenmodes require no energy and represent rigid body motion of the origami (three displacements and three rotations in space). We omit these six modes, and begin studying the subsequent modes that require elastic deformation. The most flexible eigenmodes (lowest elastic energy) represent deformations where folding occurs along fold lines. As the eigenmodes become stiffer folding of the panels also begins to occur, and the much stiffer eigenmodes include stretching and shearing of panels.

At times, it is also possible to have two or more eigenmodes with eigenvalues of the same magnitude. This may happen with symmetric structures that have symmetric eigenmodes. Alternatively, during optimization or a parametric analysis we can see "mode switching" when the value (and thus order of eigenvalues) are switched. In Figure 3.5 (a), we use the eigenmodes to find five rigid folding motions that can be performed on a Miura-ori patterned sheet. The top horizontal folds of the Miura sheet have a sector angle of $\alpha = 70°$, while the bottom have $\alpha = 55°$. The folding direction is shown by mountain and valley fold assignments, and all of the patterns can be reversed (i.e. valley folds become mountain and vice versa). These fold patterns are found after one folding iteration (see next paragraphs). Eigenmode 9 represents the traditional folding motion for the Miura-ori sheet where all folds of the pattern are engaged. The other folding motions shown in eigenmodes 7, 8, 10 and 11 are also valid rigid folding motions where bending occurs only at the fold lines and the panels remain completely flat. Eigenmode number 12 and higher require bending of the panels. When bending of the panels is considered, it is possible to find folding motions that do not follow rigid folding definitions. Allowing folding to occur throughout the sheet has been used to design origami based mechanisms (Fuchi et al., 2015b, 2016) where the origami can fold starting from a flat state, but is not rigid or flat foldable.

The eigenmode analysis can also be used as a numerical method to perform the kinematic

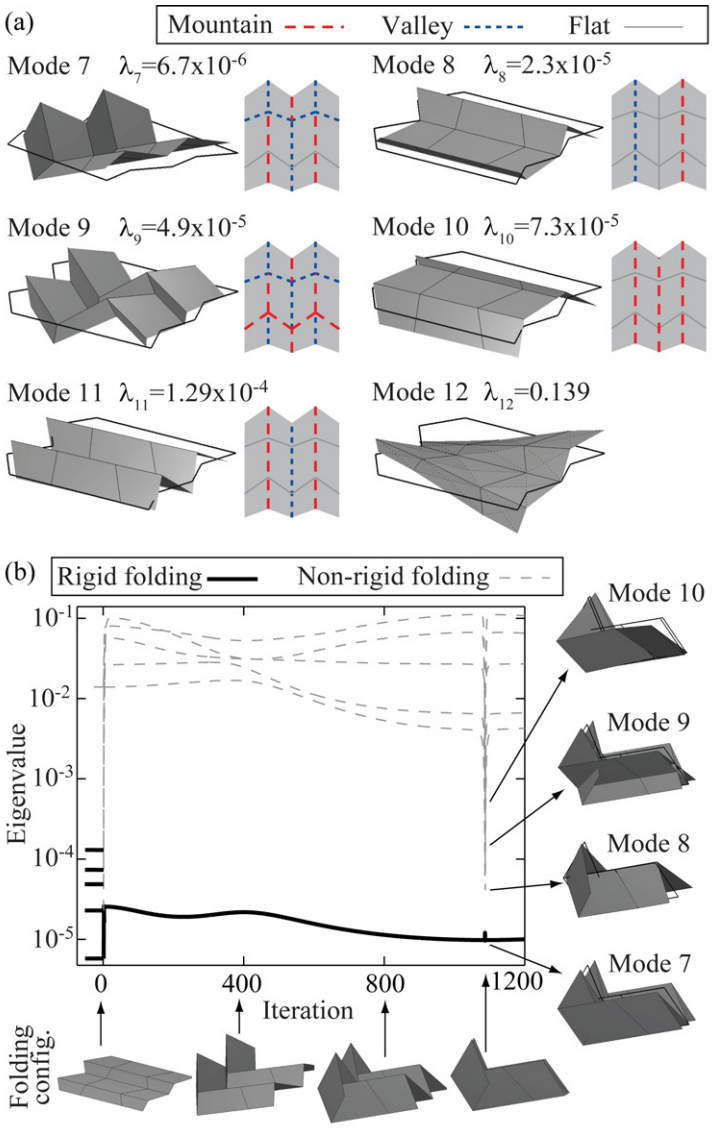

Figure 3.5: Folding kinematics of a Miura-ori pattern with folds of different sector angles. (a) Eigenmodes 7-11 of the flat sheet show five valid rigid folding motions with corresponding mountain and valley folds. The deformed modes are shown after one iteration of the folding algorithm, and thus they limit global deformations where bending of both folds and panels occurs. Although eigenmode 9 is typically the prescribed folding motion for Miura-ori sheets, it is not the only possible way in which the sheet can be folded. Eigenmode 12 represents a global bending of the sheet which is not a rigid folding mode (λ is orders of magnitude higher). (b) An iterative approach is used to fold the sheet based on the rigid folding motion in Mode 7. A jump in eigenvalues occurs after the first iteration because when the sheet starts folding into a rigid motion it can no longer deform globally with both fold and panel bending. When the system reaches another flat state at 1100 iterations, other folding motions are enabled, some with self intersection.

rigid folding of the origami. Using an analytical approach for folding is particularly useful for more complicated fold patterns that have non-repetitive fold vertices (e.g. Tachi (2009a); Gattas et al. (2013); Dudte et al. (2016)). The kinematic folding can be performed by iteratively updating the nodal locations by adding increments of a chosen eigenmode (and corresponding rigid folding pattern). The folding can be performed by correcting geometric errors using the Moore-Penrose pseudo-inverse (Tachi, 2009c), or using Newton-Raphson iterations with a sufficiently small (e.g. 1/1000) increments of the eigenmode. When we perform folding of the structure we assume that the folds move freely, and the structure is unstressed after folding. In other words, forces and stresses do not accumulate at the fold lines after the kinematic motion.

In Figure 3.5 (b), we show the kinematic folding following the seventh eigenmode as a chosen fold pattern. At the first step there is a jump in eigevalues. The value of λ_7 increases because the origami enters a rigid folding mode, and the seventh mode becomes self-restricting as global fold and panel bending is no longer possible in the newly folded configuration. Eigenvalues $\lambda_8 - \lambda_1 1$ increase by several orders of magnitude. The initial kinematic motions are no longer possible and the eigenmodes switch shape to new motions with global system bending (similar to the initial mode 12). As the folding is performed, the origami reaches another flat state, and the eignvalues drop again. At that point, it is possible to explore other folding motions that are made capable by the newly folded geometry. The order of eigenvalues can change as the kinematic folding is performed, so it is often necessary to track the eigenmode that corresponds to the chosen folding pattern. Tracking of the x^{th} eigenmode can be achieved by finding the i^{th} eigenmode that minimizes $|\mathbf{v}_i^{j+1} \pm \mathbf{v}_x^j|$, for the updated geometry at step $j+1$. The same results could be obtained by obtaining the minimum dot products between the initial eigenomode and eigenmodes of the updated configuration. With the current formulation the model does not account for self-intersection of the panel elements and can thus suggest unrealistic folding scenarios. In future work, the bar and hinge method may also be adopted to study the folding patterns and kinematics of *multi-DOF origami* that has more than four folds per vertex and can result in multiple folding motions (Xi and Lien, 2015).

The eigenmode and eignvalue approach for folding an origami structure has the benefit that it can identify different folding patterns, and can subsequently perform the entire folding

kinematics. Other folding methods typically require a pre-determined fold pattern to follow (Tachi, 2009c). The eigenvalue approach can also identify points during the folding sequence where the structure can be folded in different ways. Overall, the eigenvalue approach is similar to exploring the null space of a stiffness matrix where no folds are included. However, using some fold line stiffness with the eigenvalue approach can also provide some benefits. It can help in differentiating folding patterns that are stiff and flexible. It also simultaneously shows non-rigid folding motions which are useful for the structural characterization of the origami.

3.3.2 Band-gap analysis of origami systems

Previously, natural eigenvalues and eigenvectors have been used to analyze a wide range of problems in science and engineering. They have been used to study quantum mechanics (Atkins and Friedman, 2011), climate (Jun et al., 2008), electrical power systems (Marszalek and Trzaska, 2005), and many other mathematical models. The eigenvalues and eigenmodes of the stiffness matrix discussed in Section 3.3.1 can provide significant information about the structural characteristics of the system. For example, Schenk and Guest (2011) use these analyses to evaluate how the structural behavior of Miura-ori and egg-box patterns is affected by changing the relative stiffness between panel bending and fold lines. Alternatively, it is possible to incorporate the mass matrix of the structure ($\mathbf{M}$), and use the linear dynamics system of equations

$$\mathbf{K}\mathbf{v}_i = \lambda_i \mathbf{M}\mathbf{v}_i, \tag{3.6}$$

to find λ_i and $\mathbf{v}_i$. We construct the mass matrix $\mathbf{M}$ by distributing 1/5 of the panel mass to each of the panel's nodes, however more advanced shape function approaches can be used to distribute the mass of the panel. Including mass in the analysis can be beneficial for performing scale dependent studies, comparing different systems, and exploring the dynamic properties of the system.

In Figure 3.6 we use the eigenvalues and eigenmodes that incorporate mass to compare the behavior between an eggbox pattern and an origami tube. The eggbox pattern is curved with repetitive panels that have sector angles $\alpha = 62.9°$,$117.1°$,$69.3°$,$110.3°$ and the left

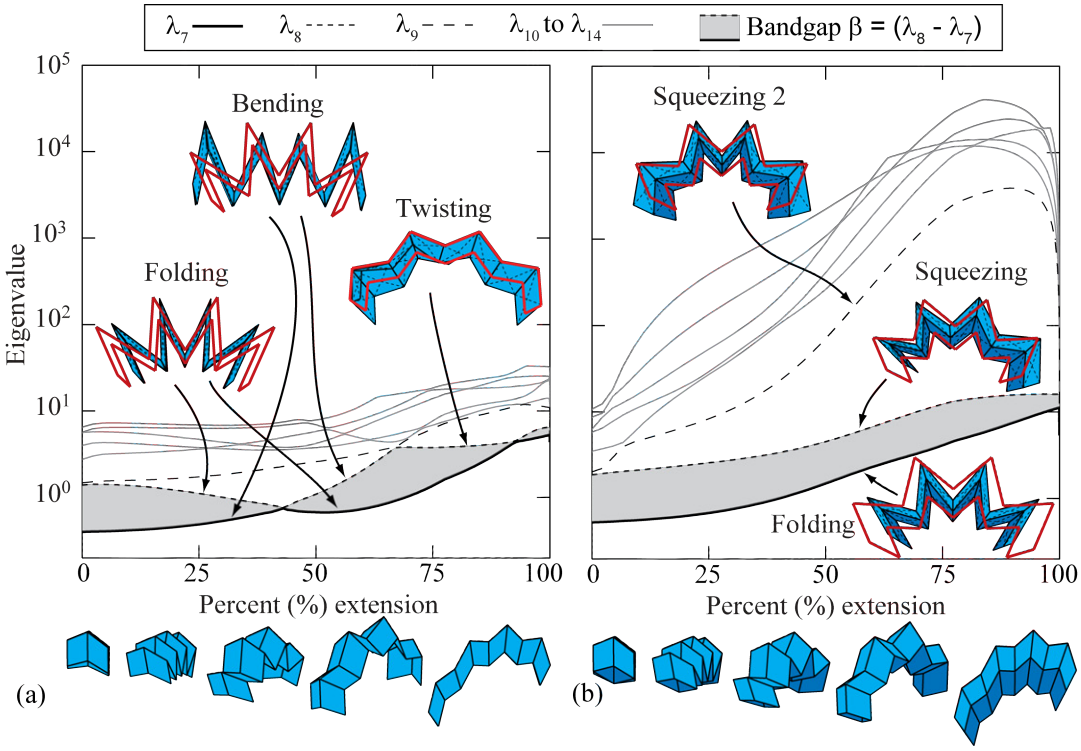

Figure 3.6: Eigenvalues vs. configuration (% extension) of (a) a curved eggbox form and (b) a tube with the top section identical to (a). The deformation modes of the eggbox are more flexible than the tube and switch at different configurations. The tube has a continuous bandgap for different configurations indicating that it requires less energy to deploy the structure than to deform it in other ways (e.g. twisting).

panel dimension is a unit value of 1 (Xie et al., 2015a). The model is defined with arbitrary dimensions, although realistic values can also be used. The panels have a thickness of $t = 0.01$ ($L/t \approx 100$), and mass of $\rho = 1$. The model uses a Young's Modulus $E = 10^6$ and fold lines are defined with $L^* = 40$. The magnitude of the eigenvalues 7-14 for the eggbox are relatively low, indicating that the most flexible ways to deform the structure (folding, bending, and twisting) require only deformation of the fold lines and panels. As the structure is extended, there is mode switching, meaning that depending on the configuration, it may be easier to deform the structure in different ways.

In Figure 3.6 (b) the eggbox is closed on the bottom to create a rigid foldable tube (Tachi, 2009b) that has a symmetric cross-section with all edges having a dimension of 1. Because mass is used with this analysis, it is possible to compare the results between the eggbox and the tube. When additional panels are added, both the stiffness and mass scale linearly with the change in material. Thus any change in the eigenmodes and eigenvalues can be

attributed to the change in geometry. When the second part of the tube is added, the magnitude of the seventh eigenvalue does not change drastically, however mode switching does not occur any longer, and the lowest eigenmode corresponds only to the folding and unfolding motion. Deforming the structure in bending and twisting is stiffer than for the eggbox, and the eight eigenmode becomes a squeezing type of motion where one side folds and the other unfolds. The ninth and subsequent eigenvalues are substantially stiffer and engage the panels in stretching and shear.

A *bandgap* ($\beta = \lambda_8 - \lambda_7$) separates the seventh and eight eigenvalues throughout the extension of the structure. This separation means that it is always more flexible for the system to be deployed than to be deformed in another fashion. The work in Chapter 4 shows that coupling multiple tubes can be used to substantially increase the structural bandgap. The system becomes easy to deploy yet it is stiff in all other directions and can be used as a cantilever. Analyzing the bandgap between the seventh and eight eigenvalues is particularly important for origami, because it informs whether the origami is capable of deploying easily per design or if other motions are possible.

Band-gaps are especially important in structures, because they define a region of frequencies where the structure avoids dynamic resonance (or does not have natural energy modes). Beyond origami, they have been used in optimizing the photonics of piezocomposite materials, in creating vibration-free environments, and for constructing energy harvesting devices (Gonella et al., 2009; Rubio et al., 2011; Vatanabe et al., 2014). bandgaps in acoustics have lead to using disruptive properties of metamaterials to prevent the passage of sound and limiting acoustic interference (Huang and Sun, 2010; Ahmed and Banerjee, 2013). Typically it is of interest to maximize a bandgap such that the structure would not experience natural resonance in that case, however at other times it may be beneficial to preserve a bandgap for a given set of parameters.

In addition to the bandgap, another measure that can be used for the analysis of origami structures has been the ratio between the seventh and eighth eigenmodes λ_8/λ_7 (Filipov et al., 2016b). This ratio may provide a more theoretical benchmark for the origami, but it could be potentially misleading. For example, if the seventh eigenvalue is reduced, the ratio λ_8/λ_7 would increase and would indicate a more useful and stiff structure. However, the entire change in the ratio can be driven by the lowest eigenmode which could approach zero

when the stiffness of the folds is reduced (the ratio λ_8/λ_7 would approach infinity). Thus when using the ratio, a structure could seem stiff when in fact it is only easy to fold and unfold. The bandgap on the other hand provides a physical measure that is not affected by extremeley low values of λ_7.

Finally, the bar and hinge model and Eq. 3.6 could also be used to find the circular natural frequency ($\omega_i = \sqrt{\lambda_i}$) or the natural period ($T_i = 2\pi/\omega_i$) of the structure. These parameters could be used to investigate the dynamic characteristics and behavior of the system (e.g. if they are to be used as mechanical systems subject to vibration). More advanced analyses that incorporate the mass and stiffness of the structure could explore nonlinear dynamic response using numerical time-iterating schemes.

3.4 Static analysis of origami systems

Static analyses are important for understanding specific deformations of structures and understanding their stiffness characteristics. Static analyses are useful when a specific application of origami is explored. For example, if we choose to use an origami tube system as a beam or cantilever we can use the static analyses to understand the structural characteristics specifically for that application. For these types of analysis we would provide supports that make the structure at least statically determinate - at least 6 DOFs would be restrained for the three dimensional analysis. Indeterminate analyses with more restraints can also be performed with the same methodology. Loads can be applied at unrestrained nodes and the system displacement $\mathbf{u}$ can be calculated from the linear function

$$\mathbf{F} = \mathbf{K}\mathbf{u}, \tag{3.7}$$

where $\mathbf{F}$ is a force vector, and $\mathbf{K}$ is the stiffness matrix.

This type of analysis is also useful to characterize the stiffness of different origami structures for loads applied in the three Cartesian coordinates. For example, we would apply a load of $F_X = 1$ either on one point or distributed on a portion of the origami. Then, we use Equation 3.7 to find the system displacements, and we calculate δ_X to be the mean X direction displacement of the loaded nodes. The characteristic X direction stiffness for the

origami would then be calculated as $K_X = F_X/\delta_X$. The results for stiffness obtained from this approach would be consistent with the units of the stiffness matrix and would be in units of force per length (e.g. N/mm).

3.4.1 Cantilever deformation analysis

In this section, we present a cantilever analysis of an eight-sided reconfigurable polygonal tube that is introduced in Chapter 6 (a similar analysis is performed in Section 6.7). We perform the analysis on the structure with the N5B8 model, and compare the results to a discretized FE model (FE model detailed in 4.2.3). Both models are defined with the unit dimensions based on the definitions in Chapter 6. The panels have a thickness of $t = 0.01$ units ($L/t \approx 50 - 100$), Poisson's ratio of $\nu = 1/3$, Young's Modulus of $E = 10^6$, and fold lines are defined with $L^* = 40$.

One end of the cantilever is fixed and a uniformly distributed load is applied on the other end. We perform static, linear elastic, small displacement analyses of the structures when they are deployed to 95% extension. Figure 3.7 (a) and (b) show the displaced shapes obtained with the N5B8 and FE models when a load is applied in the Y direction and the structure is in configuration I. We find the characteristic stiffness for each of the six possible configurations (I - VI), when the tubes are deployed to 95% extension. The characteristic stiffness is calculated orthogonal to the X axis, in a combination of the Y and Z directions. In other words, we rotate the load in the $Y - Z$ plane and find a corresponding stiffness K_{YZ} that represents the cantilever.

Both the N5B8 and the FE model provide similar displaced shapes and radial plots depicting the K_{YZ} stiffness. However, the N5B8 model overestimates the global stiffness of the polygonal tube by as much as 160%. This significant difference is partly due to the overestimation in shear stiffness of the origami panels, and also because the N5B8 model cannot capture localized deformations.

The large ovals in the radial plots (configurations I and V) indicate a relatively higher stiffness in most directions. Each of the cross-section configurations has a different direction (in $Y - Z$) where it has a lower or higher stiffness. This phenomenon indicates that the tube geometry has a high influence on the anisotropy of the tube structures. Both the N5B8

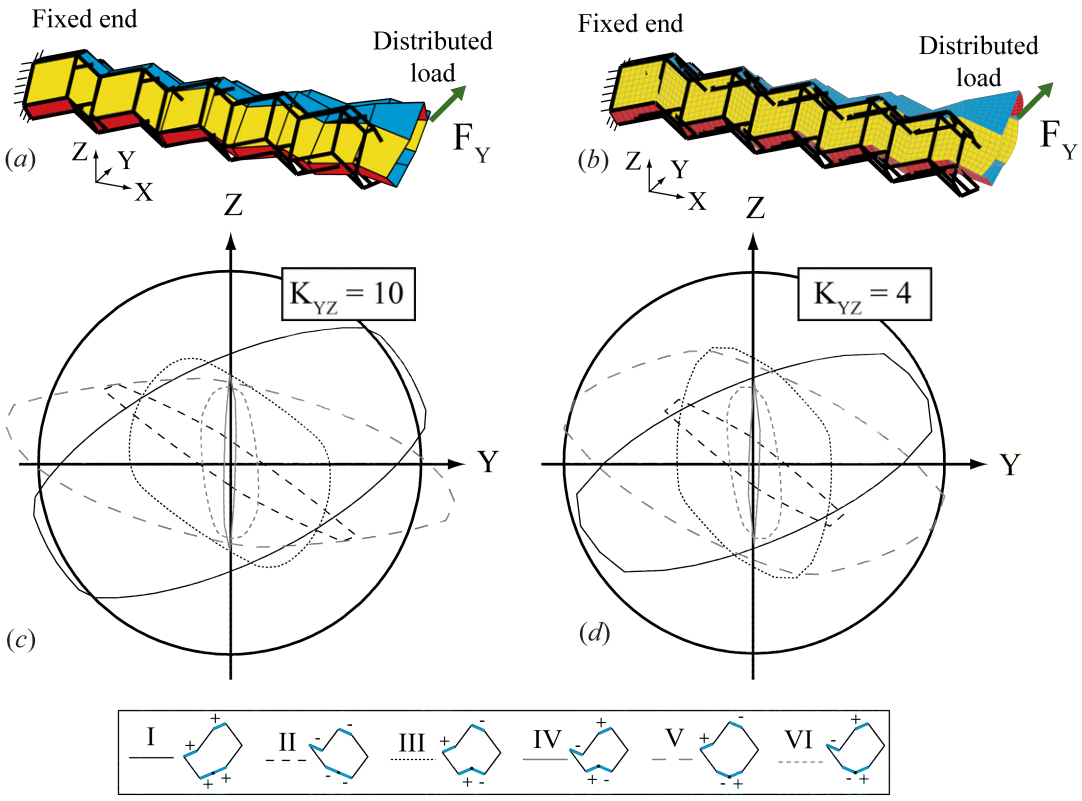

Figure 3.7: Structural analysis of cantilevered reconfigurable tube. (a) and (c) are performed with the N5B8 model while (b) and (d) are performed with a discretized FE model. The displaced shapes presented in (a) and (b) appear similar but are scaled to have the same maximum displacement and do not represent stiffness. (c) and (d) are the tube stiffness for different loading directions in the $Y - Z$ plane represented as a radial plot. The stiffness for the six possible tube configurations (I - VI) are shown when the system is at 95% extension. The N5B8 and FE plots show similar behaviors but the stiffness estimated by the N5B8 model is higher.

and the FE model predict the same type of anisotropy related to geometry (i.e. the oval shapes look similar for both models). The global influence of geometry is accurately captured by the bar and hinge model. *Although the bar and hinge model does not provide accurate quantitative results, it provides good qualitative and comparative analysis of different origami geometries.*

Furthermore, some local behaviors are not captured by either model. For example, both models use the same definition for linear fold line stiffness and both models assume zero thickness of the origami. These local phenomena may have some influence on the system behavior, however the geometric configuration (I - VI) is likely the most important factor that influences the global stiffness.

3.4.2 Characteristics of origami inspired materials

In recent years origami has been shown to have a tremendous potential for creating materials with unique properties (Schenk and Guest, 2013; Silverberg et al., 2014; Lv et al., 2014; Cheung et al., 2014; Filipov et al., 2015a). The origami materials are often composed of repetitive cells, and the global system can have anisotropy, negative Poisson's ratios, high stiffness to weight ratios, high energy dissipation and other properties useful for engineering application. The characteristics of origami metamaterials may also be tuned by reconfiguring the structure. The analysis of the metamaterials is often performed as local unit cell exploration aimed to characterize the mechanical properties of the system. When a larger material specimen is to be investigated the bar and hinge model can be a useful tool that can characterize behavior and explore geometric and other specimen variations. The mechanical properties of the origami system depend on the fold pattern, fold angles, material properties, material thickness and other properties which can be easily scaled and parametrically explored using the bar and hinge model.

In Figure 3.8 we use the N5B8 model to study the mechanical properties of the interleaved tube cellular material explored by (Cheung et al., 2014) and inspired by the Flip-Flip origami (Yenn, 2000). The panels are rhombi with sector angle of $\phi = 2\arctan(\sqrt{2}/2) \approx 70.53°$. For this analysis, we use panels with unit dimensions (height = width = 1), thickness of $t = 0.01$ units, a Poisson's ratio of $\nu = 1/3$, Young's Modulus of $E = 10^6$, and the fold lines are

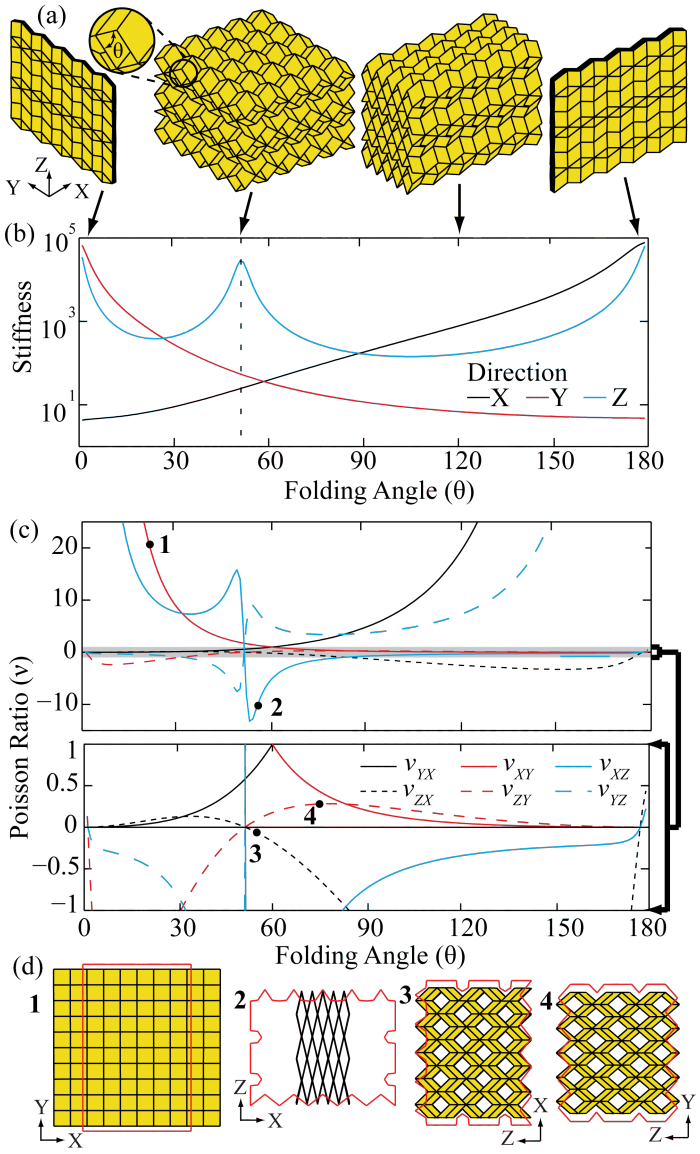

Figure 3.8: Structural linear elastic analysis of interleaved tube cellular material. (a) Four folding states of the cellular material; the system can fold flat in both the X and Y directions. (b) Stiffness of the material in three directions at different folding states. (c) The analytical Poisson's ratio (ν) simulated with the bar and hinge model. (d) Four deformed states of the structure when compressed at different configurations and in different directions. Cases 1 and 4 have positive ν, Case 3 has $\nu \approx 0$ and Case 2 has a negative ν. These results are based on infinitesimally small displacements, and would differ for large displacement simulations.

defined with $L^* = 10$. For this metamaterial simulation we use a low length scale factor L^* that represent folds that are about as stiff as the panels. This behavior would be realistic for a metamaterial created through additive manufacturing where the fold lines are not explicitly defined.

We perform a static analysis on the assemblage by applying a uniform load at both the bottom and top of the system. The characteristic stiffness for each direction is calculated based on the mean displacement of the loaded surfaces. Figure 3.8 shows that the stiffness of the assemblage can be tuned by changing the configuration. The maximum stiffness in the X and Y directions is obtained when the structure becomes flattened in the opposite plane (e.g. in the $Y - Z$ plane for X loads). In the Z direction the stiffness has three maxima, with the intermediate on occurring at a deployed symmetric state. We also show that the Poisson's ratio in the three Cartesian directions can be tuned with reconfiguration. We calculate the Poisson's ratio as a resultant of the Y displacement with respect to a load applied in the X direction as $\nu_{yx} = -(dy/l_y)/(dx/l_x)$, where dy and dx are the displacements in the two directions and l_y and l_x are the corresponding initial lengths of the metamaterial. Due to the kinematic deformation motion of the origami assemblage, the material can take on Poisson's ratios that are much larger or smaller than conventional materials. Extremely high or low Poisson's ratios can be achieved for infinitesimally small displacements at some configurations (Figure 3.8(c,d)).

3.5 Discussion

We discuss the advantages of bar and hinge models in general and, in particular, the advantages associated with the N5B8 model. Afterwards, we discuss the limitations of of those models and present an outlook on future developments.

3.5.1 Advantages of bar and hinge models

- The bar and hinge models are simple to understand, implement, modify and use. This makes them valuable to the growing community of origami researchers and enthusiasts.
- The models distill structural behavior of origami into three intuitive components: 1)

bending of creases, 2) bending of flat panels, and 3) stretching/shearing of the paper. This makes the model and methodology especially useful when describing structural behaviors of different origami systems.

- The simplicity and versatility of models allows us to explore and show some of the more intricate behaviors of origami (e.g. Section 3.3.1).
- The bar and hinge models use few nodes per each panel and are thus much faster than a discretized FE approach.
- The speed and versatility of the models makes them suitable for various extensions such as: *i)* Parametric variations for geometric design; *ii)* Optimization of cellular origami type structures; *iii)* Large displacement simulations; *iv)* Exploring the effect of different nonlinear fold line models.

3.5.2 Advantages of the specific N5B8 model

- The N5B8 model is scalable as it includes length and thickness (t) to define the stiffness and mass of the system.
- The model can approximate in-plane stretching and shearing for both regular and skewed panels. Although shear stiffness is overestimated, the model behaves similar to expected trends when skew is incorporated.
- In-plane behaviors exhibit symmetry and isotropy which is not possible with N4B5 models.
- Mass can be distributed more realistically in the N5B8 model than in the N4B5 and N4B6 models.
- Stiffness parameters now include material properties E and ν.
- The N5B8 model can effectively differentiate a deformed shape where bending of both panels and fold lines occurs. The model can distribute stiffness to fold lines and approximate deformed shapes well.
- The model is simple and efficient while allowing for a surprising level of detail and accuracy.

3.5.3 Limitations

- The bar and hinge model cannot capture localized effects accurately.
- This and most other origami modeling techniques neglect the effect of thickness (e.g. localized stress concentration at vertices).
- Stiffness for shearing of the panels is overestimated in comparison to the stretching and bending deformations.
- The model is currently only capable of simulating origami with quadrilateral panels.
- Bar and hinge models are not currently available in easy to use software packages and are thus not easily accessible for wide-spread use.

3.5.4 An outlook on future developments

- Developing a generalized bar and hinge implementation that can model non-quadrilateral panels. Origami patterns can be constructed with polygonal panels, and both in and out-of-plane formulations would need to be revised. The generalized geometry could be adapted to simulate non-rigid foldable panels.
- An in-depth verification of the panel bending stiffness and global behaviors can be performed by comparing eigenvalue analyses with a detailed FE model. The N5B8 model can be formulated to capture double curvature in the panel for small deformations.
- The model can be further verified, validated, and calibrated against experimental findings.
- Enhanced in-plane formulations could be explored to improve the stiffness approximation for shear of the panels.
- The panel bending definitions can be refined to better capture stiffness and to allow for bending along the long diagonal which may be necessary for some large displacement analyses.
- The N5B8 formulation may be adapted to capture the stiffness transition from small to large displacement panel bending (i.e. from Equations 2.5 and 2.6 in Chapter 2).
- The fold line formulation could be enhanced to incorporate nonlinear material characteristics of fold lines bending.
- Fold and panel bending formulations could be adapted to prevent bending with $\theta >$

180°, as this type of bending would result in self-intersection.

- Panels that are not restrained with orthogonal panels on all four sides may experience different bending characteristics and stiffness; an extension of the study in Section 2.2 could give more information on these behaviors. Findings could be used to adapt the model for kirigami type systems.
- The bar and hinge method could be modified to explore adhesive or other connectivity between different origami components. Preliminary work exploring connectivity between two tubes is shown in Chapter 4.
- Bar and hinge methods could be used to consider localized structural effects. For example, high loads that would lead to buckling could be detected and predicted using the model.

3.6 Concluding Remarks

This chapter discusses bar and hinge models for the mechanical and structural simulation of origami type systems. We introduce a bar and hinge model where five nodes and eight bars (N5B8 model) are used to simulate the in-plane stiffness of origami panels. Rotational hinges are used to simulate the out-of-plane bending of the panels, as well as the moment-rotation behavior of prescribed fold lines. The model parameters incorporate realistic material characteristics, and the model is formulated to provide a scalable, isotropic, and realistic system behaviors. The bar and hinge models have various applications for the characterization and design of origami type structures and systems. Folding pattern characteristics and kinematic rigid folding can be performed using eigenvalues and eigenmodes of the stiffness matrix. When mass is incorporated with the eigen-analysis, it can provide a scalable basis for comparing the mechanical characteristics of origami structures. Static analyses can be used for stiffness characterization of origami inspired deployable structures or mechanical metamaterials. The bar and hinge model cannot capture localized phenomena of origami, but has the benefits that it is versatile, efficient, and adaptable for a wide range of applications. The bar and hinge model can be a useful analytical and design tool that facilitates practical application of origami in science and engineering.

CHAPTER 4

TAILORING STIFFNESS BY COUPLING ORIGAMI TUBES

Thin sheets have long been known to experience an increase in stiffness when they are bent, buckled, or assembled into smaller interlocking structures. In this chapter, we introduce a unique orientation for coupling rigidly foldable origami tubes in a "zipper" fashion that substantially increases the system stiffness and permits only one flexible deformation mode through which the structure can deploy. The flexible deployment of the tubular structures is permitted by localized bending of the origami along prescribed folds lines. All other deformation modes, such as global bending and twisting of the structural configuration, are substantially stiffer because the tubular assemblages are over-constrained and the thin sheets become engaged in tension and compression. The zipper-coupled tubes yield an unusually large eigenvalue bandgap that represents the unique difference in stiffness between deformation modes. The enhanced mechanical properties, versatility, and adaptivity of these thin sheet systems can provide practical solutions of varying geometric scales in science and engineering.

4.1 Introduction

Introducing folds into a thin sheet can restrict its boundaries, cause self-interaction, and reduce the effective length for bending and buckling of the material (Lobkovsky et al., 1995; Vliegenthart and Gompper, 2006; Cambou and Menon, 2011; Witten, 2007). These phenomena make thin sheets practical for stiff and lightweight corrugated assemblies (Côté et al., 2006; Yokozeki et al., 2006); however, such systems tend to be static, i.e., functional in only one configuration. For creating dynamic structures, origami has emerged as a practical method in which continuous thin sheet panels (facets) are interconnected by prescribed fold lines (creases). Existing origami patterns and assemblages can easily be deployed, however they tend to be flexible and need to be braced or locked into a fixed configuration for a high stiffness to weight ratio to be achieved (Schenk and Guest, 2013; Heimbs, 2013; Cheung et al., 2014; Gattas and You, 2015a). The zipper-coupled system is different because it is

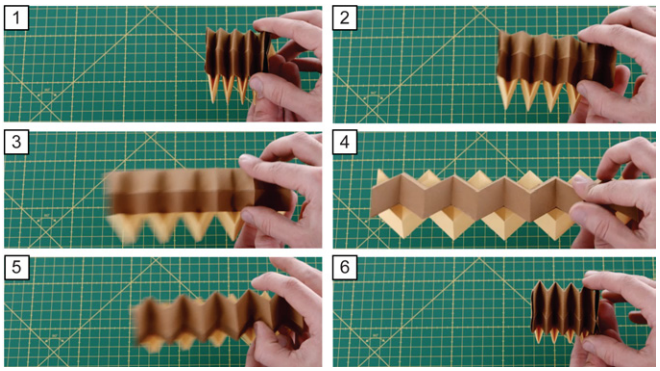

Figure 4.1: Deployment and retraction sequence of a "zipper"-coupled tube system. This origami has only one flexible motion through which it can deform, and thus it is deployed by actuating only on the right end.

stiff throughout its deployment without having to be locked into a particular configuration.

Origami principles have broad and varied applications, from solar arrays (Campbell et al., 2006; Zirbel et al., 2013) and building façades (Del Grosso and Basso, 2010) to robotics (Felton et al., 2014), mechanisms in stent grafts (Kuribayashi et al., 2006), and DNA sized boxes (Andersen et al., 2009). The materials and methods used for fabricating, actuating, and assembling these systems can vary greatly with length scale. On the micro scale, metallic and polymer films, or more often, layered composites consisting of stiff and flexible materials, can be folded by inducing current, heat, or a chemical reaction (Gracias et al., 2002; Peraza-Hernandez et al., 2014). Large scale origami structures can be constructed from thickened panels connected by hinges, and can be actuated with mechanical forces (Zirbel et al., 2013; Hoberman, 2010; Tachi, 2011). The kinematic motion, functionality, and mechanical properties of the origami are governed largely by the folding pattern geometry. For example, rigid origami systems are defined as those having a kinematic deformation mode in which movement is concentrated along the fold lines, while the panels remain flat (Huffman, 1976; Hull, 2012). Among various rigid folding patterns, the Miura-ori has attracted attention for its folding characteristics (Mahadevan and Rica, 2005; Miura, 2009), elastic stiffness properties beyond rigid folding (Schenk and Guest, 2011; Wei et al., 2013), geometric versatility (Tachi, 2009a; Gattas et al., 2013), and intrinsic material-like characteristics (Silverberg et al., 2014; Lv et al., 2014).

The zipper-coupled tubes introduced here are derived from the Miura-ori pattern, and can

undergo the same type of rigid kinematic deployment. All other deformations are restrained as they require stretching and shear of the thin sheets. Thus, the structure is light, and retains a high stiffness throughout its deployment. It has only one flexible degree of freedom, and can be actuated by applying a force at any point (Figure 4.1). To explore the zipper tubes' unique mechanical properties, we introduce concepts of eigenvalue bandgaps and cantilever analyses to the field of origami engineering. Zipper assemblages can be fabricated with a variety of materials and methods. We envision applications of these assemblages will range in size from micro-scale metamaterials that harness the novel mechanical properties, to large-scale deployable systems in engineering and architecture.

The chapter is organized as follows: first, in Section 4.2 we discuss the stiffness properties of basic Miura-ori tubes. Section 4.3 introduces possible methods for coupling the origami tubes and discusses the unusual behavior of the zipper coupled tubes. In Section 4.4, we explore the origins of the enhanced zipper stiffness. In Section 4.5, we study the influence of tube geometry on the eigenvalue bandgap. Section 4.6 discusses cantilever analyses of zipper and other coupled tubes. Cellular variations are discussed in Section 4.7, and Section 4.8 shows further geometric variations of the zipper tubes. Section 4.9 concludes this chapter.

4.2 Stiffness properties of Miura-ori tube structures

4.2.1 Basic definitions for rigid and flat foldable origami tubes

The Miura-ori pattern is composed of vertices connected with four folds and four panels. Rigid and flat foldability have been studied with some success in the past years. Flat folding at a single vertex was theorized by Kawasaki (1989) and Justin (1986), and more robust proofs and necessary conditions for flat folding have been shown in Bern and Hayes (1996); sarah-marie Belcastro and Hull (2002b,a). Proving rigid origami at a single vertex, was first shown using a Gaussian curvature approach in Huffman (1976). A simple presentation for rigid folding using spherical trigonometry and the spherical law of cosines is also presented in Hull (2012). Based on these approaches it is shown that a single four fold non-singular vertex will always be at least partially rigid foldable. Finally, some interesting generalizations, a study of entire rigid foldable patterns, and pattern degrees of freedom is discussed in Tachi

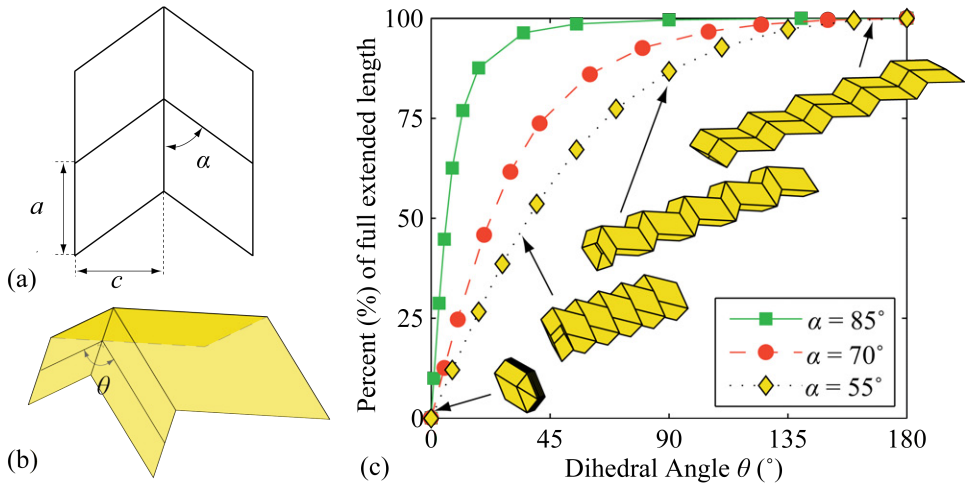

Figure 4.2: Construction of a rigid and flat foldable origami tube: (a) definition of a single Miura-ori cell, (b) folding definition for the Miura-ori cell, (c) dihedral angle θ vs. tube length as a percent(%) of the maximum extension length for tubes with $\alpha = 55°$, $\alpha = 70°$, and $\alpha = 85°$. The tube with $\alpha = 55°$ is shown folded at $\theta = 2°, 35°, 90°$, and $170°$.

(2010b).

In this chapter, we restrict our study to a simple subset of the origami tubes that is available in the literature. Figure 4.2 shows the definition of a Miura-ori cell in our study. The acute vertex angle α along with the dimensions a and c are sufficient to define the Miura-ori cell, and the dihedral angle θ can be used to define the folded configuration of the cell. The Miura-ori cell is then repeated, and reflected to create a tube. For example, Figure 4.2 (c) shows a tube that is 10 panels (5 cells) long and is folded in different configurations. The tube is flat foldable in both directions, and the total extended length of the tube L_{Ext} can be calculated as:

$$L_{Ext} = Nc\frac{\tan(\alpha)\sin(\theta/2)}{\sin(\alpha)\sqrt{1+\tan(\alpha)^2\sin(\theta/2)^2}} \tag{4.1}$$

where N is the number of panels repeating in the direction of c. The maximum (full) length (L_{Max}) that the tube can reach (when $\theta = 180°$) stays constant if the parameters c and N are fixed, and the total area of the panels will also remain constant if the parameters a and c are fixed. Figure 4.2 (c) shows how different structures ($\alpha = 85°; \alpha = 70°$;and$\alpha = 55°$) expand at different rates when related to the dihedral angle. Thus, it is also useful to consider the percentage of the the maximum extended length when comparing the configuration of different structures. The extension gives a physical definition that is easy to visualize and

gives a specific location of the current deployment of the structure.

4.2.2 Eigenvalue analysis of tube structures

In this chapter, we use the N4B6 model presented in Chapter 3. The model stiffness is defined based on preliminary estimates for the structural stiffness and does not incorporate all of the findings presented in Chapter 2. The bar element stiffness (K_S) for stretching and shearing is defined in the same manner as discussed in Section 2.1.1. The same bar area definitions are used, and thus the panels exhibit an isotropic and scalable behavior similar to the N5B8 model. Here, we define the panel bending stiffness of the panels to be the same regardless of panel geometry. We incorporate the phenomenon where the elastic energy scales as $k(D_S/t)^{1/3}$ where D_S is the length of the short diagonal of the panel, and k is the bending modulus of the sheet, defined as $k = Et^3/12(1-\nu^2)$. The panel bending stiffness is thus defined as

$$K_B = C_B \frac{Et^3}{12(1-\nu^2)} \left(\frac{D_S}{t}\right)^{1/3}, \tag{4.2}$$

where we use a scaling factor $C_B = 0.441$ that provides an approximate estimate for the panel stiffness. This approximation is about double of the more refined estimates obtained in Chapter 2, but is within a close and realistic range when compared to the panel stretching stiffness.

In this chapter, we also use an approximate method to define the fold bending stiffness as a ratio of the panel bending stiffness. We introduce a parameter R_{FP} to relate the stiffness between the bending of a fold with length $L_F = 1$ and the bending of a panel with a diagonal of $D_S = 1$. For the analyses, we assume that the folds are less stiff than the panels, and we use an arbitrary choice of $R_{FP} = 1/10$ based on visual observations of our physical models. In Section 4.3.3, we show that R_{FP} influences the magnitude of eigenvalues associated with fold bending, however, it does not influence the overall behavior and the qualitative results presented in the chapter. For our implementation, the stiffness for each of the two fold

elements (i.e. **a**,**b**,**c** and **-a**,**d**,**e** in Figure 3.4) is calculated similarly to Equation 4.2, as

$$K_F = R_{FP}\frac{L_F}{2}C_B\frac{Et^3}{12(1-\nu^2)}\left(\frac{D_X}{t}\right)^{1/3}, \tag{4.3}$$

where $D_X = 1$ units long, indicating a panel with short diagonal with of one unit. This function scales linearly with the fold length L_F and incorporates the ratio between fold and panel stiffness R_{FP}. These assumptions and the stiffness formulation are consistent with the findings presented in Chapter 2.

Eigenvalue analyses are used to study the stiffness and flexibility of the origami structures. The linear dynamics system is used to solve the underlying eigenvalue problem formulated as:

$$\mathbf{K}v_i = \lambda_i \mathbf{M}v_i, \;\; i = 1, ..., N_{dof} \tag{4.4}$$

where λ_i is the i^{th} eigenvalue and v_i is the corresponding eigen-mode of the structure. A base case of the analysis is shown in Figure 4.3 for a tube where $\alpha = 55^\circ$ and $N = 10$, and $a = c = 1$. The thickness of the material is $t = 0.01$, the Young's modulus is $E = 10^6$, the Poisson's ratio is $\nu = 1/4$, the density is $\rho = 1$, and the factor relating fold to panel stiffness is $R_{FP} = 1/10$. The first six eigen-modes correspond to rigid body motion of the structure in 3 dimensional space so they are omitted in our study. The linear elastic structure can be modeled at different configurations meaning that the starting configuration can be defined either with the dihedral angle (θ) or based on the percent extension of the (%) of maximum extended length that the tube can reach. For the majority of our analysis we will use the percent of the maximum extended length because this provides a more realistic representation of the physical configuration in which the structure is situated.

Performing the analysis in different configurations we can plot an eigenvalue spectrum (Figure 4.3 (a)) that shows the eigenvalues as a function of the configuration. Figure 4.3 (b) shows representative eigenmodes corresponding to the seventh to 10^{th} eigenvalues of the structure when deployed to 70% of the maximum extension length.The rigid folding motion corresponds to the seventh mode of the structure where the system can fold and unfold without deforming the panel elements, and thus deformation occurs primarily in the more

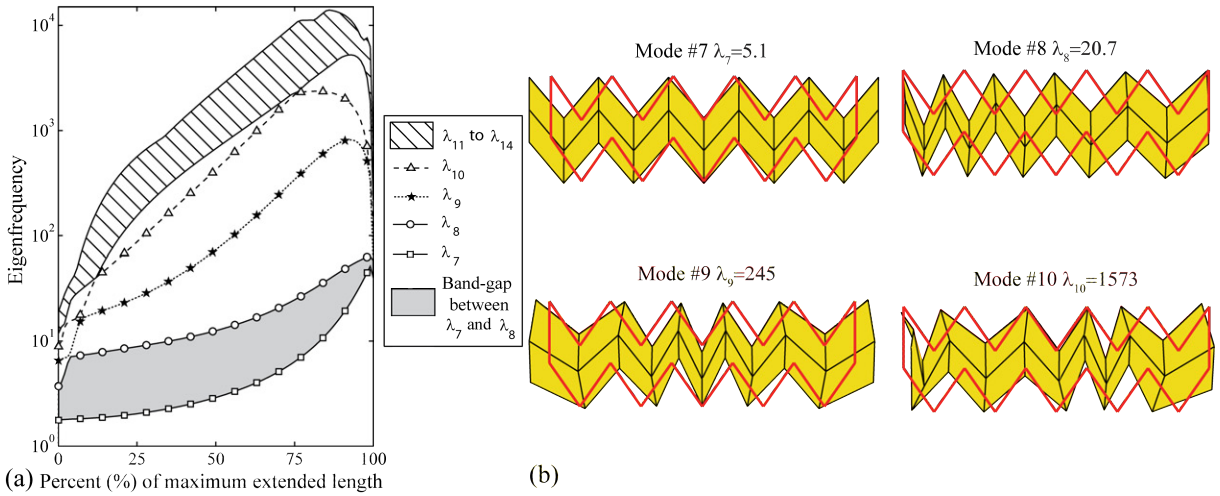

Figure 4.3: (a) Eigenvalue spectrum for the $\alpha = 55°$ tube structure through the extension ($0\% - 100\%$ of the maximum extension length), (b) normalized mode shapes #7 to #10 when tube is at 70% of the maximum extension length (undeformed outline in red).

flexible fold elements. The eighth mode is a type of "squeezing" mode, where one end of the structure is folded while the other end is unfolded. This mode results in bending of the fold and the panel elements, however, the panels do not stretch or shear, and thus the total energy is only slightly higher than that of the seventh eigen-mode. Subsequent modes contain stretching and shearing of the panels which require much higher energy than the bending deformations. Note that in Figure 4.3 (a) there is substantial mode switching for higher modes and at the extreme ends of the spectrum. The mode switching is a result of the changing geometry of the structure, for example, when the structure reaches a nearly flattened state $\theta \approx 180°$, bending of the structure globally becomes easier than folding or squeezing of the structure.

Figure 4.4 (a) shows the same spectrum as above, and also shows the effect of reducing the factor R_{FP} (Figure 4.4 (b)). Keeping all other parameters of the analysis the same, only the fold elements become, much more flexible, and the seventh and eighth eigenvalues drop. Since the seventh mode depends only on the fold elements, its eigenvalue drops more substantially and the gap λ_7 and λ_8 is effectively enlarged. In practice this type of behavior can be achieved through making the panels out of thick rigid material, while making the folds from thinner and more flexible material e.g. cloth. In Figure 4.4 (c) we show the behavior of the structure with the thickness reduced to $t = 0.001$, but all parameter are kept the

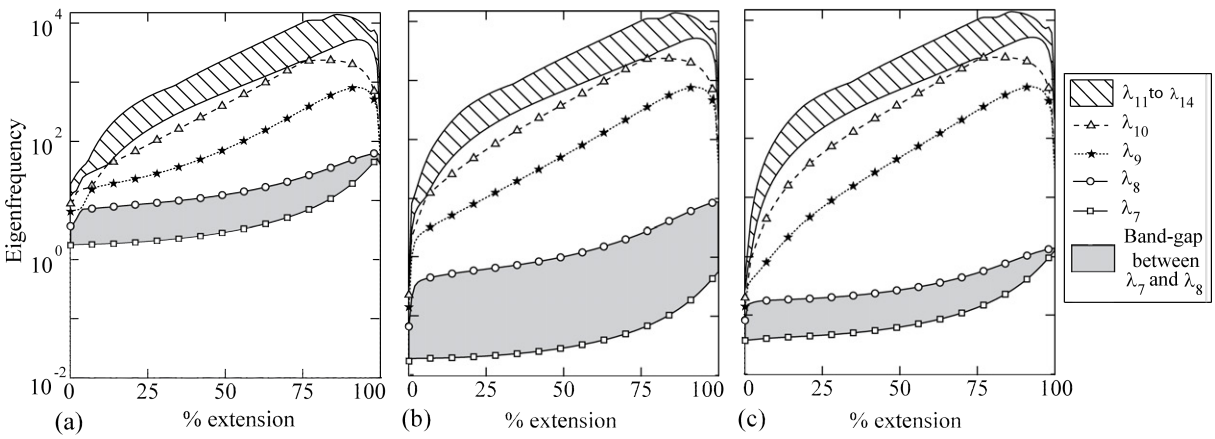

Figure 4.4: (a) Eigenvalue spectrum for the yellow tube structure ($\alpha = 55°$, $a = c = 1$, $N = 10$, $t = 0.01$, $E = 10^6$, $\nu = 1/4$, $\rho = 1$, and $R_{FP} = 1/10$) through the deployment (0%-100% extension), (b) eigenvalue spectrum for the structure now with $R_{FP} = 1/1000$, (c) eigenvalue spectrum for the structure now with $t = 0.001$.

same as before. Reducing the thickness of the material reduces the axial and shear stiffness linearly, but the bending stiffness of the panels and folds is reduced at a much higher rate with $t^{2\frac{2}{3}}$ (i.e. Equations 4.2 and 4.3). Due to this both the seventh and eighth eigenvalues drop substantially. Note that since the mass and axial/shear stiffness both vary linearly with the thickness, modes 9 and higher are not substantially influenced by this change.

Figure 4.5 shows the eigenvalue spectrum and the representative modes at 70% extension for a tube structure with a sector angle of $\alpha = 85°$ and all other properties kept the same as for the $\alpha = 55°$ tube. The eigenvalues for this structure are much lower for most extension lengths and mode switching occurs for the seventh and eighth eigenvalues even at intermediate configurations. At 70% extension the seventh eigenvalue is the global bending of the structure, this form of bending has low stiffness since at this configuration the structure is shallow. As one can see this type of bending requires more energy (higher eigenvalue) as the structure extends and takes on a more quadratic shape. The eighth mode corresponds to the rigid body folding and after the mode switching at about 80% extension, this becomes the seventh eigenmode. The ninth mode is a second degree manifestation of the bending mode where the structural deformation now has one point of zero curvature considering the deformation map globally. Mode 10 at the 70% extension length corresponds to the squeezing mode where one end is folded while the other end is unfolded.

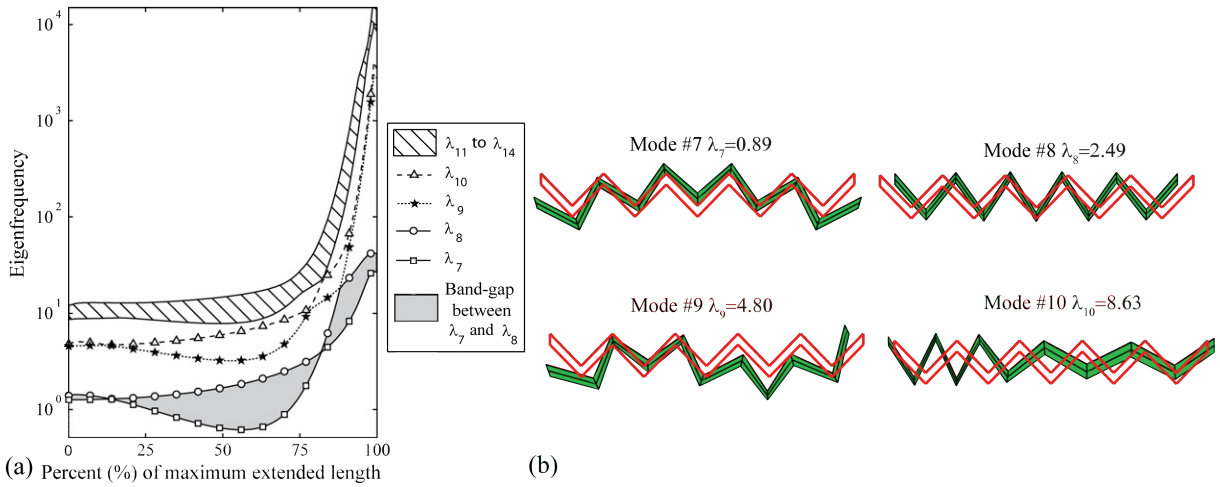

Figure 4.5: (a) Eigenvalue spectrum for the $\alpha = 85°$ tube structure through the extension ($0\% - 100\%$ of the maximum extension length), (b) normalized mode shapes #7 to #10 when tube is at 70% of the maximum extension length (undeformed outline in red).

4.2.3 Model verification

In this section, we verify and explore the benefits and shortcomings of the simplified model for elastic origami. We do this by comparing the results from the bar and hinge model to a detailed finite element (FE) shell model created using the software ABAQUS (Dassault Systemes Simulia Corp, 2010). Details of the FE implementation are shown in Figure 4.6 (a) for a single Miura-ori cell. For the FE model we discretize each panel into D segments in each direction, such that each panel will now be modeled using D^2 shell elements (for Figure 4.6 (a) $D = 5$). Standard S4 general-purpose square shell elements with finite membrane strains are used and are connected with one node at each corner. The S4 elements do not have hourglass modes in either the membrane or bending response of the element. The element has four integration locations, which makes it more computationally expensive, however, this also provides greater accuracy. The S4 element typically outperforms other shell elements (e.g. S4R) in cases where membrane or bending hourglassing may occur. A 3 dimensional model is built in FE, and thus each node has 6 DOFs 3 displacements and 3 rotations. The shell elements take into account all of the 6 DOFs at each of the attached nodes. Mass in the model is distributed based on the volume and the density ρ of the shell elements.

At the fold lines, overlapping (collocated) nodes are placed with one node on each of the

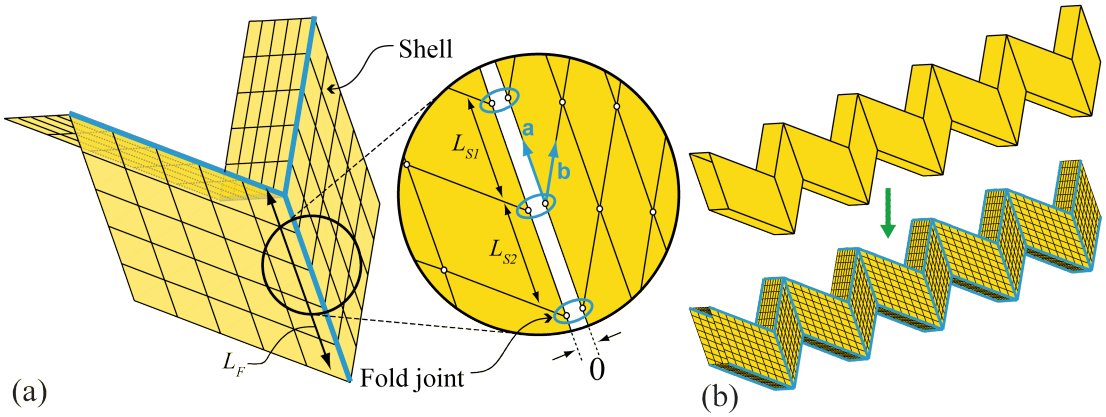

Figure 4.6: FE model used for verification (a) Miura-ori cell discretized with $D = 5$ elements for each panel, and cut-out showing local zero-length connectivity at fold lines. (b) Discretization of single tube with $D = 8$.

adjoining panels. These nodes, indicated on the cut-out of Figure 4.6 are then connected using a "JOIN" connection element that restricts the collocated nodes to remain in the same XYZ coordinates throughout the analysis. At the same location, the fold stiffness is modeled as an elastic rotational spring that resists rotations between the adjacent panels. The spring is placed locally on each pair of collocated nodes, and resists rotations about the local **a** vector shown on the cut out of Figure 4.6 (a). The stiffness of the fold is assigned based on the dimensions of attached shell elements as:

$$K_{F\,FE} = \frac{(L_{S1} + L_{S2})/2}{L_F} K_F(L_F) \tag{4.5}$$

where L_{S1} and L_{S2} are the lengths of the attached shell element parallel to the fold line, L_F is the length of the entire fold and the K_F is a function of stiffness based on the fold length and the standard material properties as defined in Equation (4.2). Equation (4.5) distributes the stiffness of the fold (as calculated for the bar and hinge model) based on the tributary length of the shells elements used. Naturally, collocated nodes that are at the end of a fold or at a vertex will only have one adjacent shell element and thus the stiffness will be based only on $L_{S1}/2$ or $L_{S2}/2$.

In the FE model bending stiffness of the shell elements is estimated based on the thickness (t), the Poisson's ratio (ν), and the elastic modulus (E). For small deformations (and

eigenvalue analysis) the shells are assumed to exhibit double curvature bending, and thus the stiffness of the shells is less than if we were to use a single curvature bending definition.

The yellow tube with $\alpha = 55^\circ$ and $a = b = 1$ presented in Section 4.2.2 is used for comparing the bar and hinge, and FE models. The tube properties are defined as previously, i.e. $t = 0.01$, $E = 10^6$, $\nu = 1/4$, $\rho = 1$, and $R_{FP} = 1/10$. A discretized tube model with $D = 8$ (Figure 4.6 (b)) is formulated in the FE model as shown above and a natural eigenfrequency extraction is performed. The eigenfrequency spectrum for the FE model and the bar and hinge model is presented in Figure 4.7 (a). The mode shapes for the FE model when analyzing the tube at 70% extension are shown in Figure 4.7 (b). At 70% of the maximum extension length the mode shapes from the FE model are identical when considering the global deformation of the structure. The seventh mode is the rigid body folding, the eighth is the global squeezing mode, and the ninth and tenth modes are the same squeezing type modes that require stretching and shear of the panels. The magnitude of the eigenvalues λ_7 and λ_8 from the FE and the bar and hinge models are about equal (within 5% difference) for most of the extension spectrum. The fold lines have the same amount of stiffness for the bar and hinge and the FE models, and since the rigid body folding requires deformation primarily in the flexible fold lines then it is to be expected that λ_7 will be the same for both models. The squeezing deformation mode requires bending of the folds and bending of the panels and since these are again defined to behave in a similar fashion, then λ_8 is similar for both modeling approaches.

The eigenvalues λ_9 and λ_{10} are lower in magnitude for the FE than the bar and hinge model, but they follow the same general trend over the extension length. The difference in magnitude for these eigenvalues can be attributed to the localized deformations and stress concentrations that can be evaluated with the FE discretization, but cannot be captured using the bar and hinge model. For example in mode #9 the Miura-ori cell in the middle of the tube experiences bending, stretching, and shear localized at the vertex. The FE model can capture the localized effects and individual shell elements can deform more than others. On the other hand in the simplified model stretching shear and bending can only be captured as global phenomena over the entire panel. In a sense this is the same problem that occurs with finite element meshes that are not discretized sufficiently. The stiffness is over estimated, and with element refinement we are able to achieve a more realistic solution

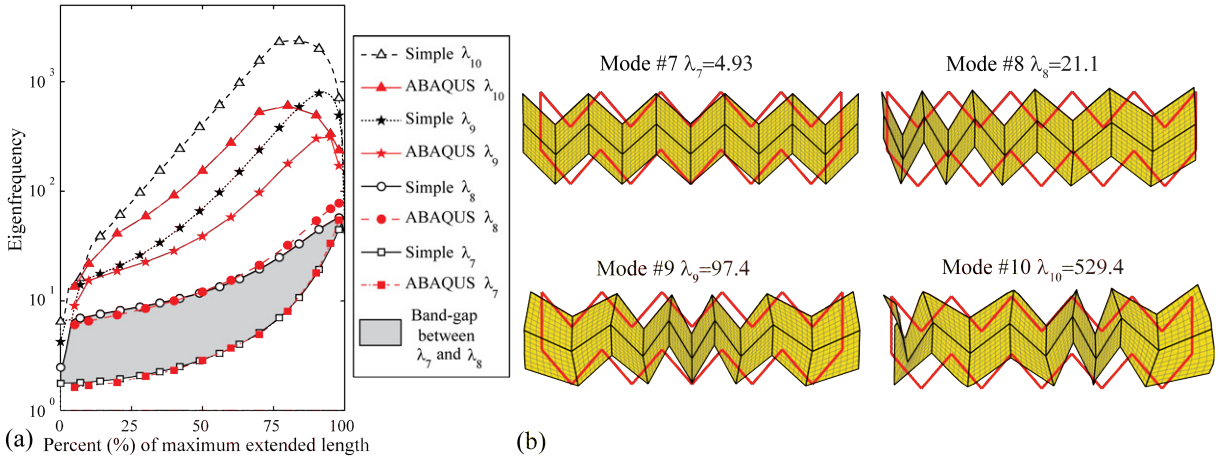

Figure 4.7: (a) Eigenvalue spectrum from bar and hinge and FE analyses for the $\alpha = 55°$ tube structure through the extension ($0\% - 100\%$ of the maximum extension length), (b) normalized mode shapes #7 to #10 of the FE tube model when tube is at 70% of the maximum extension length (undeformed outline in red).

This FE verification allows us to better understand when the bar and hinge model is sufficient vs. when it may provide misleading or inaccurate results. We can also better appreciate some of the advantages and disadvantages of the simplified model.

4.3 Coupling of two tubes

Stacking of the tube structures can be performed in a variety of ways while maintaining the rigid and flat foldability. Figure 4.8 shows three variations in which these origami tubes can be combined. The zipper type coupling (Figure 4.8 (a)) involves rotating one of the tubes about the x axis and placing two opposing faces of the tubes adjacent to each other. This can be repeated in the z direction and the flat and rigid foldability of the system will be preserved. However, if zipper coupling is performed in the z and the y directions simultaneously, then the structure will only be flat foldable in one direction, and will self intersect if folded in the other direction. The aligned coupling (Figure 4.8 (b)) is performed by simply translating a structure in the y or z direction and aligning the parallel faces of the two tubes together. This can be repeated in both the z and y directions infinitely and the structures will preserve flat and rigid foldability. In the presented form, both the zipper and the aligned coupling configuration allow the structure to go from a flat folded stowed

configuration (when $\theta = 0°$) to a flat configuration when the structure is fully deployed (when $\theta = 180°$). Figure 4.8 (a) and (b) each use two tubes where the sector angle is $\alpha = 55°$, however, these types of coupling remain rigid and flat foldable even when we use tubes where α is different for each of the coupled tubes. Finally, the internal tube coupling is similar to the stacked Miura-ori configurations shown by (Schenk and Guest, 2013). This type of tube coupling requires an internal tube that specifically conforms to the geometry of the external tube, and the entire system can only extend up to the point where the internal tube becomes flat in the $x-y$ plane ($\theta = 180°$ for the internal tube). We can define all of the internal tube dimension (a_I, b_I, and α_I) if we decide the maximum extended length of the internal tube (EXT_I)to be a fraction (EXT_I/EXT_E) of the maximum possible extended length of the external tube (EXT_E). Then:

$$c_I = \frac{EXT_I}{EXT_E} c_E \tag{4.6}$$

$$a_I = \frac{a_E * \cos(\alpha_E)}{\sqrt{1 - (EXT_I/EXT_E)^2 * \sin(\alpha_E)^2}} \tag{4.7}$$

and

$$\alpha_I = \sin^{-1}\left(\frac{EXT_I}{EXT_E}\sin(\alpha_E)\right) \tag{4.8}$$

where a_E, a_E, and α_E are the dimensions of the external tube. Finally, the different stacking types can also be used together, for example, we can stack tubes in the zipper fashion in the Z axis, and can simultaneously stack more tubes in the aligned fashion in the Y direction.

4.3.1 Zipper coupled tubes

The different types of tubes (e.g. α), and the type of tube coupling can have a significant effect on the structural behavior of the entire system. The thin origami sheets are composed of a system of panels inter-connected by prescribed fold lines. The panels are much thinner in comparison to their length, so they are much more flexible for bending out-of-plane than they are for stretching or shearing in-plane. The prescribed fold lines can be created by perforating the base material or by placing individual hinges to connect the panels, and are assumed to be more flexible in relation to the bending of the panel. The material properties

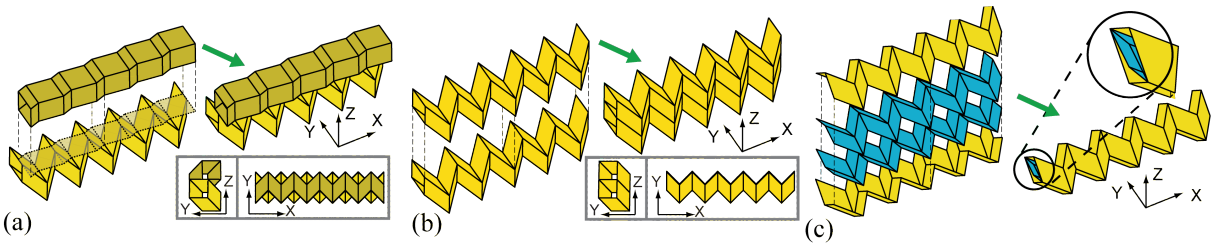

Figure 4.8: Basic configurations for coupling Miura-ori tubes. (a) Zipper coupled tubes. A tube is translated and rotated in the $Y - Z$ plane until the opposing faces of the two tubes align. For clarity a different shade is used for one of the zipper tubes, but both tubes are identical to the previous definitions. (b) Aligned coupled tubes. A tube is translated in the $Y - Z$ plane and coupled with the tube in the initial configuration. (c) Internally coupled tubes inspired by Schenk and Guest (2013). External tube is the same as in before, and the internal tube parameters are defined so that it reaches a flat configuration when the external tube is at 80% extension.

of the tubes are the same as those used in Section 4.2.2, namely the thickness of the material is $t = 0.01$, the Young's modulus is $E = 10^6$, the Poisson's ratio is $\nu = 1/4$, the density is $\rho = 1$, and the factor relating fold to panel stiffness is $R_{FP} = 1/10$.

Figure 4.9 shows the structural behavior of a single sheet, a single tube and the zipper coupled tubes. The eigenvalues, are plotted vs the percent of the maximum extended length that the structure can reach, and representative deformation modes are shown for each structure when it is extended to 70% of the maximum length. A single Miura-ori sheet (Figure 4.9 (a)) is quite flexible and can bend, and twist in a variety of configurations. The schematic modes #7 and #8 of the single sheet exhibit a global bending in two directions. These deformation modes are primarily a product of the panels and the folds bending. In mode #9 we can observe the rigid folding mode, where only the folds deform, and the panels remain essentially flat through the deformation. Finally, mode #10 represents a global twisting of the sheet. When observing the eigenvalues plotted vs. the configuration, we can see that the eigenvalues change, and that there is mode switching, meaning that depending on the configuration, it may be easier to bend or twist the structure in different ways. For practical purposes, we would typically prefer that the eigenfrequency corresponding to the rigid body folding to be low, meaning it is easy to fold and unfold the structure, while subsequent eigenfrequencies are high, meaning it is difficult to bend and twist the structure. This would mean that the rigid body folding corresponds to eigenvalue #7 and subsequent eigenvalues are higher, thus creating a bandgap between (λ_7 and λ_8). A structure with a

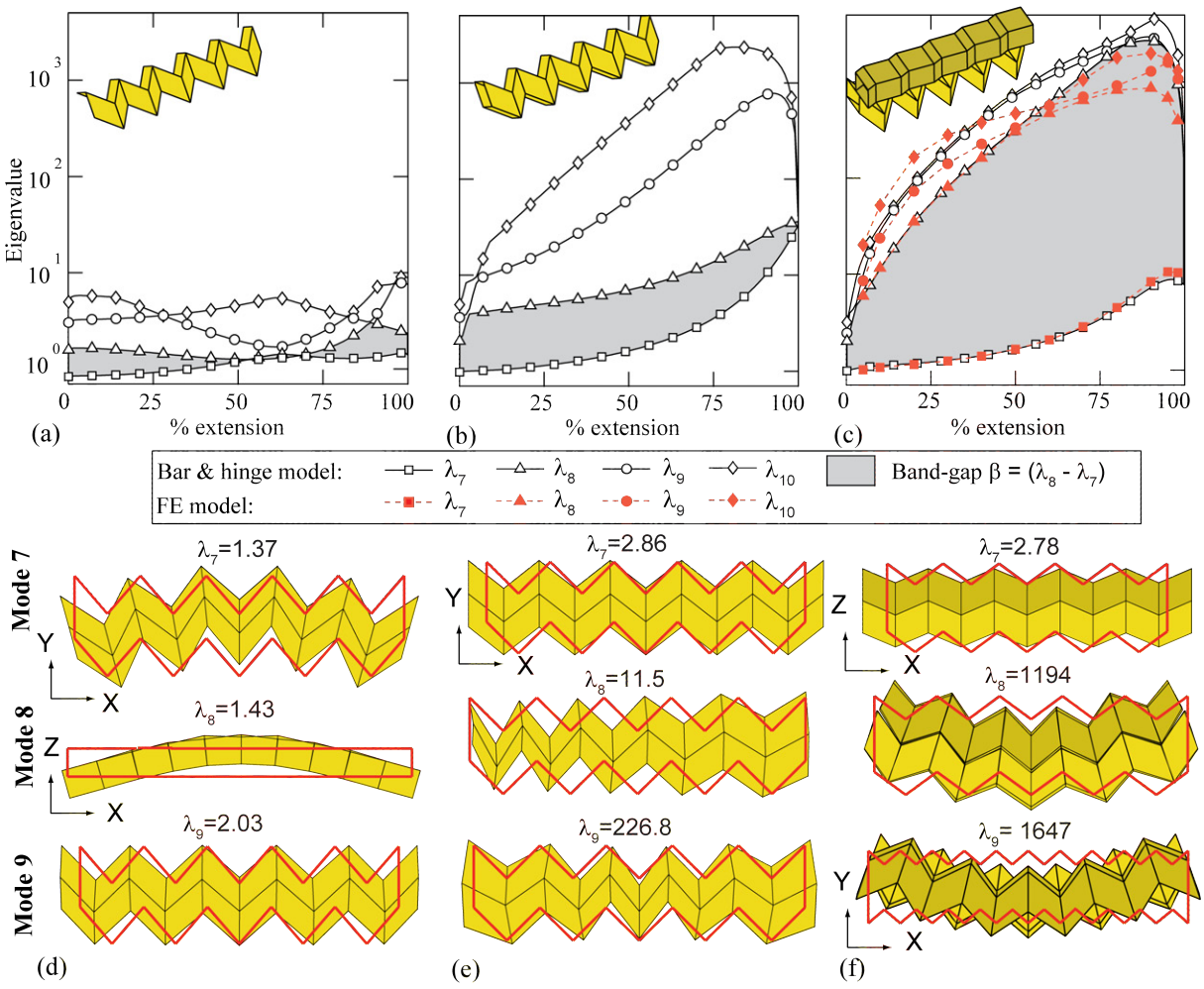

Figure 4.9: (a) to (c) Eigenvalue vs. the structural configuration (% extension) for the sheet, single tube and zipper coupled tubes respectively. The FE model verification is only shown for the zipper coupled tubes. (d) to (f) seventh, eighth, and ninth deformation eigen-modes when structures are at 70% extension (undeformed outline in red).

large bandgap would be flexible and easy to deploy, yet it would be stiff for other external loadings. A trivial method to achieve a larger bandgap is to make the panels much stiffer in relation to the folds (i.e. the factor R_{FP} is reduced), as this would restrict the structure to deploy based on the prescribed rigid body folding. Alternatively, Figure 4.9 (b) and (c) show how the bandgap can be created and increased simply by combining the thin sheets.

When in a tube configuration the rigid folding motion corresponds to the seventh mode of the structure where the system can fold and unfold without deforming the panel elements, and thus deformation occurs primarily in the more flexible fold elements. The eighth mode, is a type of "squeezing" mode, where one end of the structure is folded while the other end

is unfolded. This mode results in bending of the fold and the panel elements, however, the panels do not stretch or shear, and thus the eigenvalue is only slightly higher than that of the seventh eigen-mode. Subsequent modes contain stretching and shearing of the panels which requires much higher energy than the bending deformations. The tube has a continuous bandgap between (λ_7 and λ_8), while mode switching occurs at the extreme configurations (fully folded or fully unfolded) and for the higher modes. The continuous bandgap means that it would always be easier to deploy the structure than it would be to twist it or bend it in another configuration. A problematic point however, is that the eigenvalue corresponding to the squeezing mode (λ_8) is only slightly higher than the rigid body folding eigenfrequency (λ_7). As such, the structure is prone to squeezing when loads are applied to one of the ends: e.g. if the tube is used like a cantilever, or if a one tries to deploy the entire structure by controlling only one end. Mode #9 of the structure is another manifestation of the squeezing mode, except here the structure is unfolded at the two ends and is folded in the center. This deformation requires some stretching and shear of the panels, so the ninth eigenvalue is higher. Similarly, the tenth mode requires more energy since it is a global bending of the structure meaning that one side will be in compression and the other in tension.

The aligned and the internal tube coupling configurations are also prone to the squeezing deformation modes, and the bandgap is not increased as discussed in Section 4.3.4. However, when coupling the tubes in the zipper fashion we observe an unusual behavior, in that the coupled structure has a substantial bandgap between the rigid body folding and subsequent eigenmodes. At a 70% extension the rigid-body folding mode has an eigenvalue of $\lambda_7 = 4.99$ while the subsequent, squeezing mode has an eigenvalue of $\lambda_8 = 1203$ that is roughly two hundred and fifty times larger. The next two modes require a global bending of the structure, which requires stretching and shear of the material and thus higher energy. When comparing the single tube and the coupled tubes, the magnitude of the eigenvalues λ_7 changes only slightly. This occurs since we double the mass of the system and we also introduce twice the number of elements, and thus both the total element stiffness and total mass scale linearly. Therefore, any change in the eigenvalues can be attributed to changes in the stiffness caused from the coupling, because the mass will always increase linearly with the number of tubes coupled.

In Figure 4.10, we use the FE model presented in Section 4.2.3 to perform energy analy-

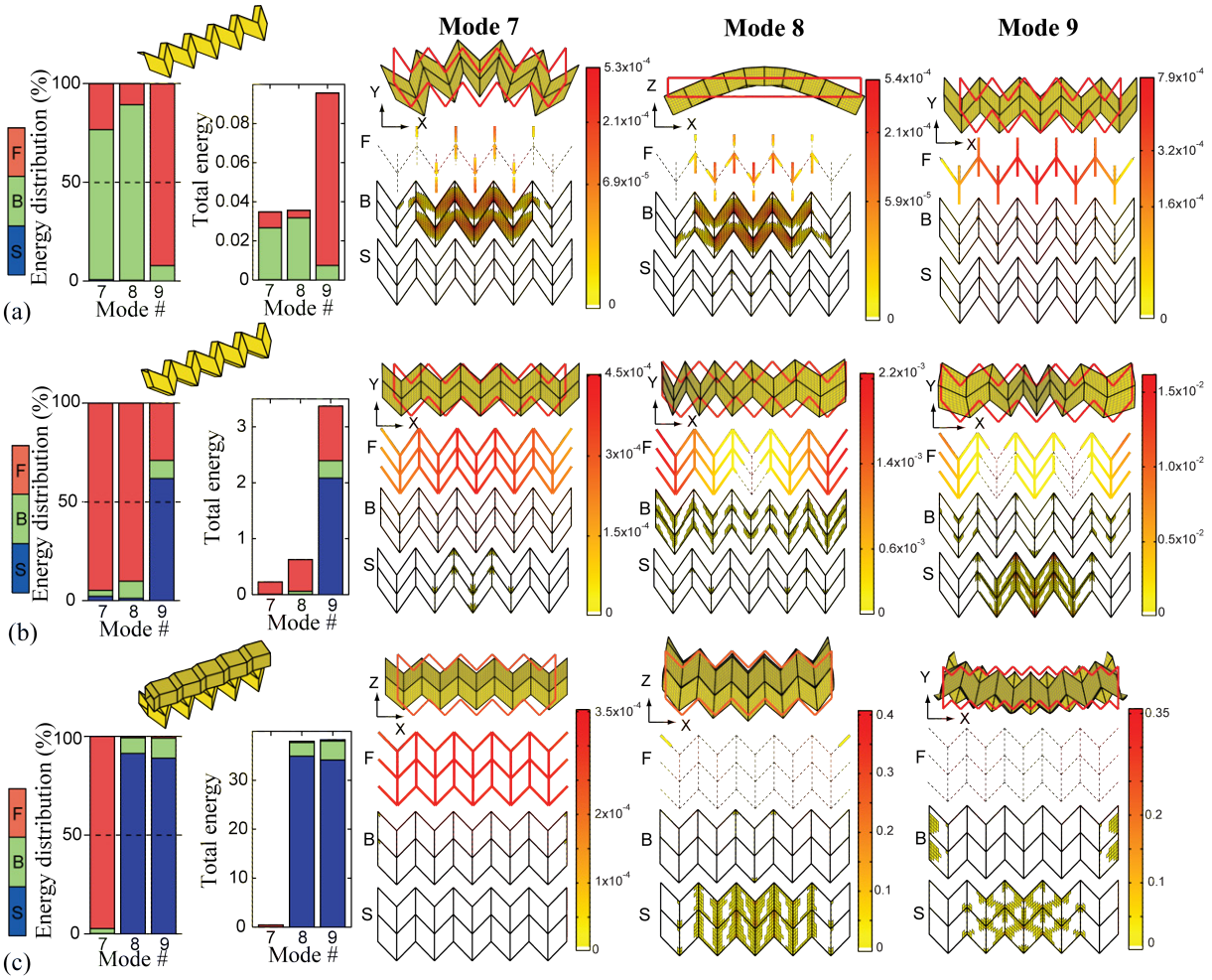

Figure 4.10: (a) to (c) Eigen-mode energy of the sheet, the single tube and the zipper coupled tubes respectively, using the FE model. Energy distributions (as a percentage and as a total amount) are presented in stacked bar graphs indicating energy in the different sets of components (i.e. fold bending (F), panel bending (B), and panel stretching (S)). The energy within the structure is shown by relative shading of elements to show concentrations of energy. The color scale indicates the magnitude of energy.

ses for the Miura-ori sheet, the single tube, and the zipper-coupled tubes. To connect the zipper tubes in the FE model we first find the ten planes where the panels of the two tubes connect. We then identify the nodes that are adjacent to both tubes, and connect these nodes to the respective planes using tie elements. The energies are calculated based on the structural deformation for the normalized mode shapes (Figure 4.9(d-f)). Percentage distribution between the different sets of element deformations (i.e. fold bending, panel bending, and panel stretching/shear), and the total energy for each mode are shown. The total energy for eigenvalues of the single sheet are relatively low, because deformations consist of localized bending in panels and folds. The distribution of energy for the seventh and eighth deformation modes (Figure 4.10 (a) Mode 7 and 8) illustrate that bending occurs in the central panels and folds while the remainder of the structure remains unstressed. As expected, the bending energy in the panels is highest at the vertices, where the curvature approaches infinity (Lobkovsky et al., 1995; Cerda et al., 1999). These energies are relatively low, while the eighth and ninth modes of the zipper-coupled tubes require much more energy, because the thin sheets are engaged in stretching and shearing. The rigid folding modes, ninth for the sheet, and seventh for the tube structures, primarily engage the fold lines in bending as previously expected. The ninth mode of the sheet and the seventh mode of the tube represent a rigid folding motion where bending is primarily concentrated in the folds and the panels remain essentially flat throughout the deformation (Figure 4.9(d-f))

4.3.2 Coupling elements for zipper tubes

In the bar and hinge model, the coupling of the zipper structures is realized by inserting coupling elements that restrict relative movement between the adjacent panels of the two tubes. These coupling elements can be thought of as an adhesive joint between the adjacent faces of the tube. The relative local coordinates (X' and Z') are different for the odd and even panels of the structure (Figure 4.11). The X' coupling elements restrain relative movement between panels along the length of the tube (relative to the local X' axes) and the Y' coupling elements restrain differential orthogonal movement in the $Y'(= Y)$ axis. The X' and Y' coupling elements are formulated using a compatibility relation where bar elements

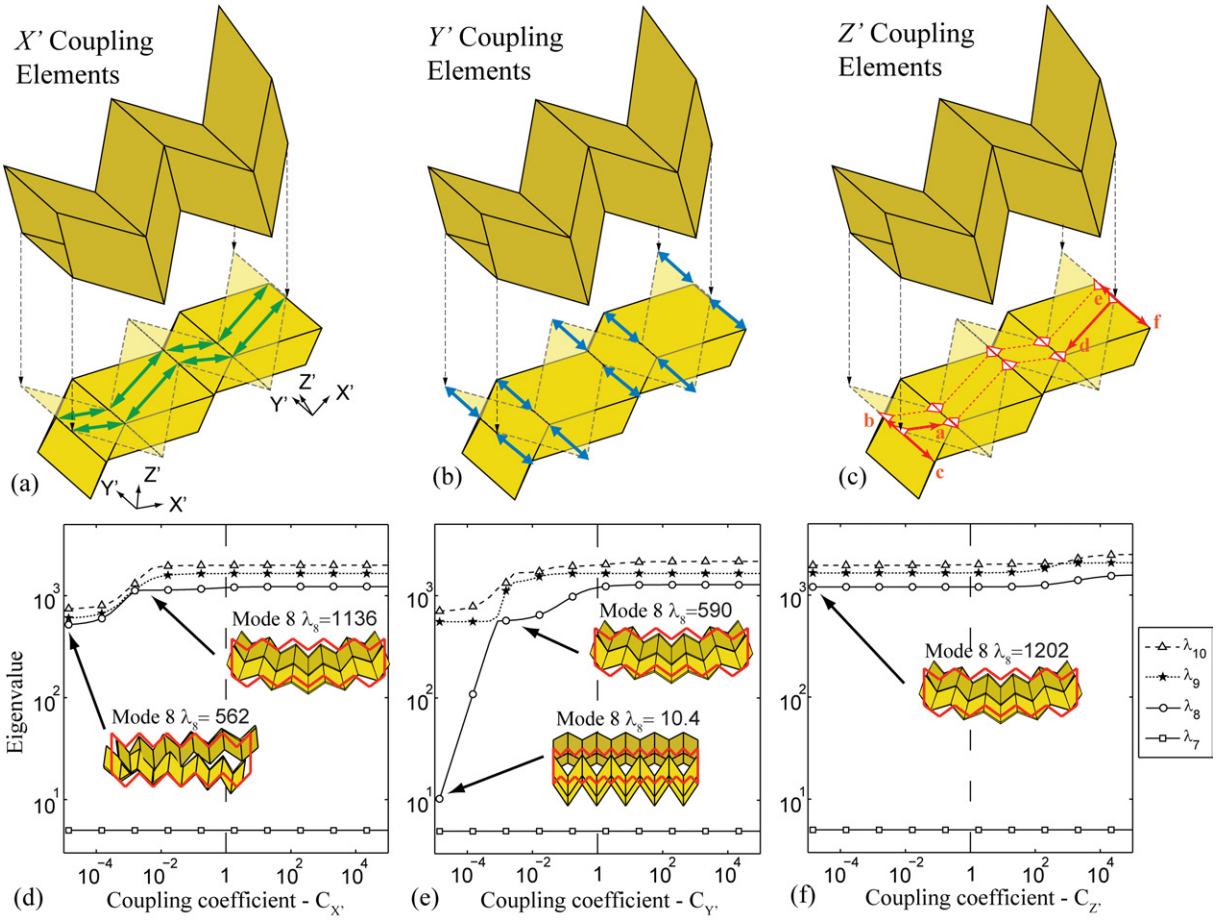

Figure 4.11: Configuration of (a) X', (b) Y', and (c) Z' coupling elements for a segment of zipper coupled tubes. The local axes are shown for the left most and right most panels. Only representative coupling configurations are shown for the Z' coupling elements. The sensitivity of the system eigenvalues vs. magnitude of each of the coupling coefficients (d) $C_{X'}$, (e) $C_{Y'}$, and (f) $C_{Z'}$ while the other coupling coefficients remain at a value of 1.

are used to restrain relative movement between two nodes. The stiffness for the coupling elements is defined as:

$$K_{X'} = C_{X'}\frac{EA}{L} = C_{X'}\frac{E0.5t}{1}, \tag{4.9}$$

and

$$K_{Y'} = C_{Y'}\frac{EA}{L} = C_{Y'}\frac{E0.5t}{1}, \tag{4.10}$$

where E is the Young's modulus, and t is the thickness of the thin sheet, and the coupling coefficients ($C_{X'}$ and $C_{Y'}$) can be used to vary the total stiffness of the coupling elements. When these coupling coefficients are set to 1, each coupling element has the same axial

stiffness as a 0.5 unit wide, 1 unit long, and t thick piece of panel material. Finally, Z' coupling elements are used to prevent nodes which lay on the same plane (on a panel), from moving out-of-plane (in the relative Z' direction). The Z' coupling elements are defined in the same fashion as the out-of-plane rotational stiffness for folds and panel bending. Here, we consider a node on one of the zipper tubes that overlaps a panel on the opposite tube, indicated as a red/white triangle in Figure 4.11 c. A rotational hinge element is constructed which restricts out-of-plane movement between each of these overlapping nodes and the 3 corresponding nodes on the opposing tube. For clarity, only two sample corresponding node sets are illustrated in Figure 4.11 (c). The vectors groups (**a**, **b** & **c**) and (**d**, **e** & **f**) can be used to define the rotational hinge for each set. The stiffness for each of these rotational hinges is defined as:

$$K_{Z'} = C_{Z'} C_B \frac{Et^3}{12(1-\nu^2)} \left(\frac{1}{t}\right)^{1/3}, \tag{4.11}$$

where the parameters are the same as the panel definition in Equation 4.2, and the coupling coefficient $C_{Z'}$ can be used to vary the total stiffness of the coupling elements. With this formulation, the stiffness of each Z' coupling element is equal to the stiffness of a panel element with a diagonal length, D_S, of 1. Since the equation for $K_{Z'}$ is based on bending of the thin sheet, the value of this stiffness is substantially lower than that of the X' and Y' coupling elements.

The sensitivity of the model eigenvalues vs. the magnitude of each of the coupling coefficients, is explored for the zipper coupled tubes deployed to 70% extension (Figure 4.11). The rigid folding mode (λ_7) of the coupled tube is not affected by any of the coupling elements, i.e. it is neither easier nor harder to fold and unfold the structure due to the coupling. When the coupling coefficient $C_{X'}$ is substantially reduced (lower than 10^{-2}), the eighth and subsequent eigenvalues experience a drop in magnitude from approximately 1200 to approximately 500. This drop occurs because the tubes are not restrained in the relative X' direction, and thus the eighth mode switches to a deformation mode in which the tubes begin to separate. Due to the presence of the Z' coupling elements, the magnitude of this eigenvalue remains relatively high even when $C_{X'} = 10^{-5}$ ($\lambda_8 = 560$ vs. $\lambda_8 = 20.7$ for a single tube). When decreasing the value of the $C_{Y'}$ coupling coefficient, there is a more significant effect on λ_8 and the subsequent eigenvalues. The eigenvalue corresponding to bending

reduces to $\lambda_8 = 590$, when $C_{Y'} = 10^{-3}$, and experiences a mode switch for lower coupling coefficients. When $C_{Y'}$ is substantially reduced, the tubes are free to slide apart in the Y direction. The $C_{Z'}$ coupling coefficients on the other hand have essentially no influence on any of the eigenvalues. This is due to the zig-zag geometry of the tubes, which causes the axial members to restrain global out-of-plane movement between the two tubes. In other words, the Z' coupling elements can be removed and the tubes would still be effectively connected. When any of the coupling coefficients are increased past a value of 1, there is negligible increase in the eighth and subsequent eigenvalues of the structure.

When changing the value of the vertex angle α, or the maximum extension length of the zipper coupled tubes, there is little change in the sensitivity of the different coupling elements, however the general trends remain. The tubes are effectively coupled when the coupling coefficients are about equal to 1. The X' and Y' coupling elements have a higher influence on the coupling and maintaining a large bandgap ($\beta = \lambda_8 - \lambda_7$), while the Z' coupling elements have little influence on the eigenvalues.

4.3.3 Sensitivity of model and analysis

In Figure 4.12 we show differences in scaling of eigenvalues, for the tube and zipper-coupled tubes, with respect to different model parameters. The seventh eigenvalue for both the single and the zipper-coupled tubes corresponds to the rigid folding mode, in which deformation primarily occurs as bending of the prescribed folds (Figure 4.10). The eighth mode for the single tube corresponds to squeezing, in which bending occurs in the fold and panel elements. However, the eighth mode for the zipper-coupled tubes requires stretching and shearing of the thin sheet, which requires much more energy than bending, and results in drastic differences for the scaling of eigenvalues.

All eigenvalues (λ_7 and λ_8 for both systems) scale proportionally with the Young's Modulus E (i.e. doubling E, doubles the eigenvalue), and inversely proportionally with the material density ρ (Figure 4.12 (a,b,e,f)). This is expected because E scales the stiffness proportionally, and ρ scales the mass proportionally in equation $\mathbf{K}v_i = \lambda_i \mathbf{M}v_i$. Scaling of other parameters, however, does not necessarily influence all eigenvalues proportionally. When changing the sheet's thickness, t, its stretching/shearing stiffness and the system's

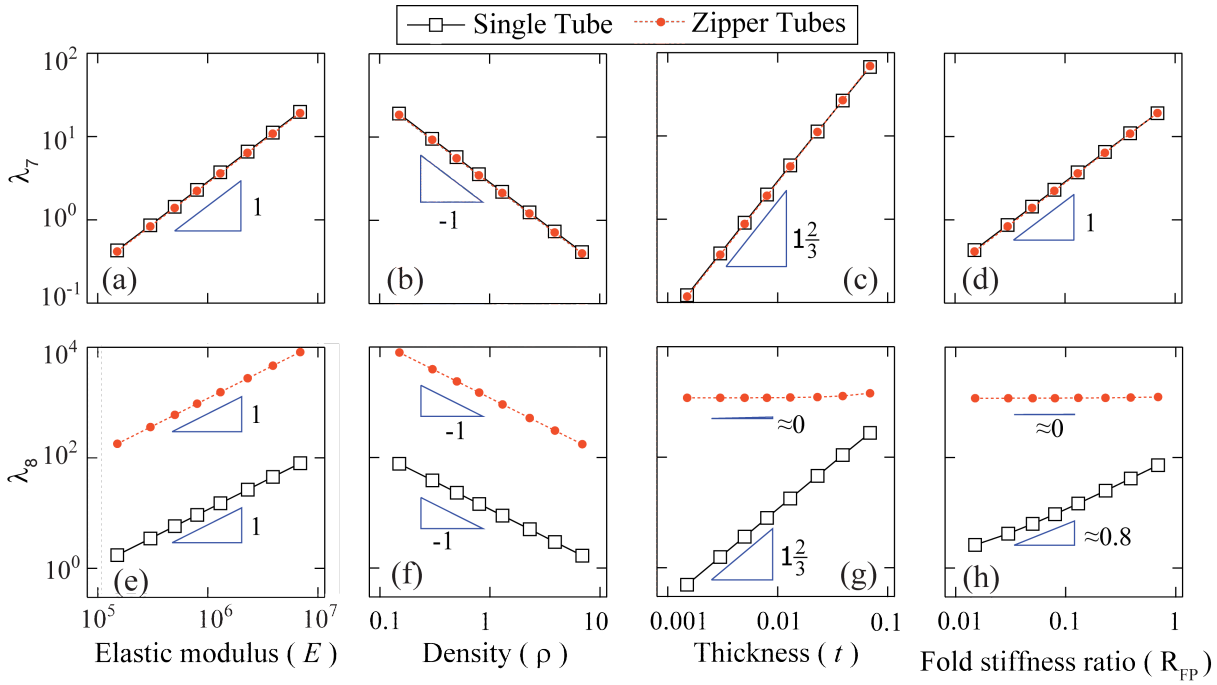

Figure 4.12: Eigenvalue sensitivity for a single tube and the zipper-coupled tubes. (a-d) Scaling of λ_7 with respect to E, ρ, t, and R_{FP}. (e-h) Scaling of λ_8 for the same cases. These relations directly govern the scaling sensitivity of the bandgap.

mass scale proportionally (i.e. scaling with 1). On the other hand, the bending stiffness for both the panels and the folds scale as 8/3 based on Equations 4.2 and 4.3. Therefore, when scaling the thickness, the eigenvalues scale as 5/3 for both tubes' rigid folding modes (λ_7) and the single tube's squeezing mode (λ_8) (Figure 4.12 (c) and (g)). The eighth eigenvalue for the zipper-coupled tubes does not change because both mass and stretching/shear stiffness scale proportionally (both are defined by t). When scaling the fold stiffness ratio, R_{FP}, λ_7 scales proportionally for both structures, λ_8 scales as 0.8 for the single tube, and λ_8 remains constant for the zipper tubes (Figure 4.12 (d) and (h)). The system behaviors that lead to these scaling relations are complemented by the energy distributions shown in Figure 4.10.

In summary, the Young's Modulus E and material density ρ directly scale all system eigenvalues, while the material thickness t and fold stiffness ratio R_{FP} scale eigenvalues influenced by panel and fold bending. The scaling of different parameters does not cause mode switching and the order of eigen-modes remain the same as shown in Figure 4.9. Scaling different

parameters can change the quantitative results (e.g. magnitude of λ_7), however it does not influence the qualitative results presented here. The eighth eigenvalue for the zipper-coupled tubes remains substantially higher than the seventh, ensuring a large band-gap ($\beta = \lambda_8 - \lambda_7$) regardless of the parameter values used. The results presented in this paper are independent of length scale, making the zipper-coupled tubes applicable across scales.

4.3.4 Aligned and internally coupled tubes

The eigenvalue vs. configuration plots and representative eigen modes at 70% extension are illustrated for the zipper, aligned, and internally coupled tubes in Figure 4.13. Aligned and internal coupling of tubes is much simpler to formulate than the zipper coulpled cases. The nodes of these coupled tubes conveniently fall in the same location for these tubes. Therefore, the same DOFs are used for both tubes, and only one of the overlapping nodes is used in the model. This approach is stiffer than the element based approach used for the zipper coupling tubes. The behavior of the aligned coupled tubes for λ_7 and λ_8 is almost identical to that of the single tube, and again this can be attributed to the fact that when tubes are coupled we double the mass of the system, and we simultaneously add an identical set of elements to the system. Mode #9 is a similar squeezing as that in the single tube but the eigenvalue has doubled. In Mode #10 the aligned coupled tubes bend in the X-Y axis which is in contrast to the single tube which bends in the Y and the diagonal between the Y and Z axes. The eigenvalue increase can be attributed to the linear coupling.

Figure 4.13 (b) shows the behavior of the internal coupled tubes which can only extend up to 80% of the external tube maximum extension, since at that point the internal tube will become completely flat. The coupling configuration also influences the modal behavior of the structure, as compared to a $\alpha = 55°$ tube used alone. The rigid body folding and the squeezing mode are still λ_7 and λ_8 respectively, however at larger deployment configurations (60 to 80% of the maximum extension length) these eigenfrequencies increase significantly. At 80% extension length $\lambda_7 = 280$ in contrast to the single or other tube coupling configurations where λ_7 reaches values of about 45 at most. At the 80% extension length the internal tube is essentially flat and it is difficult for the structure to deform in the prescribed rigid

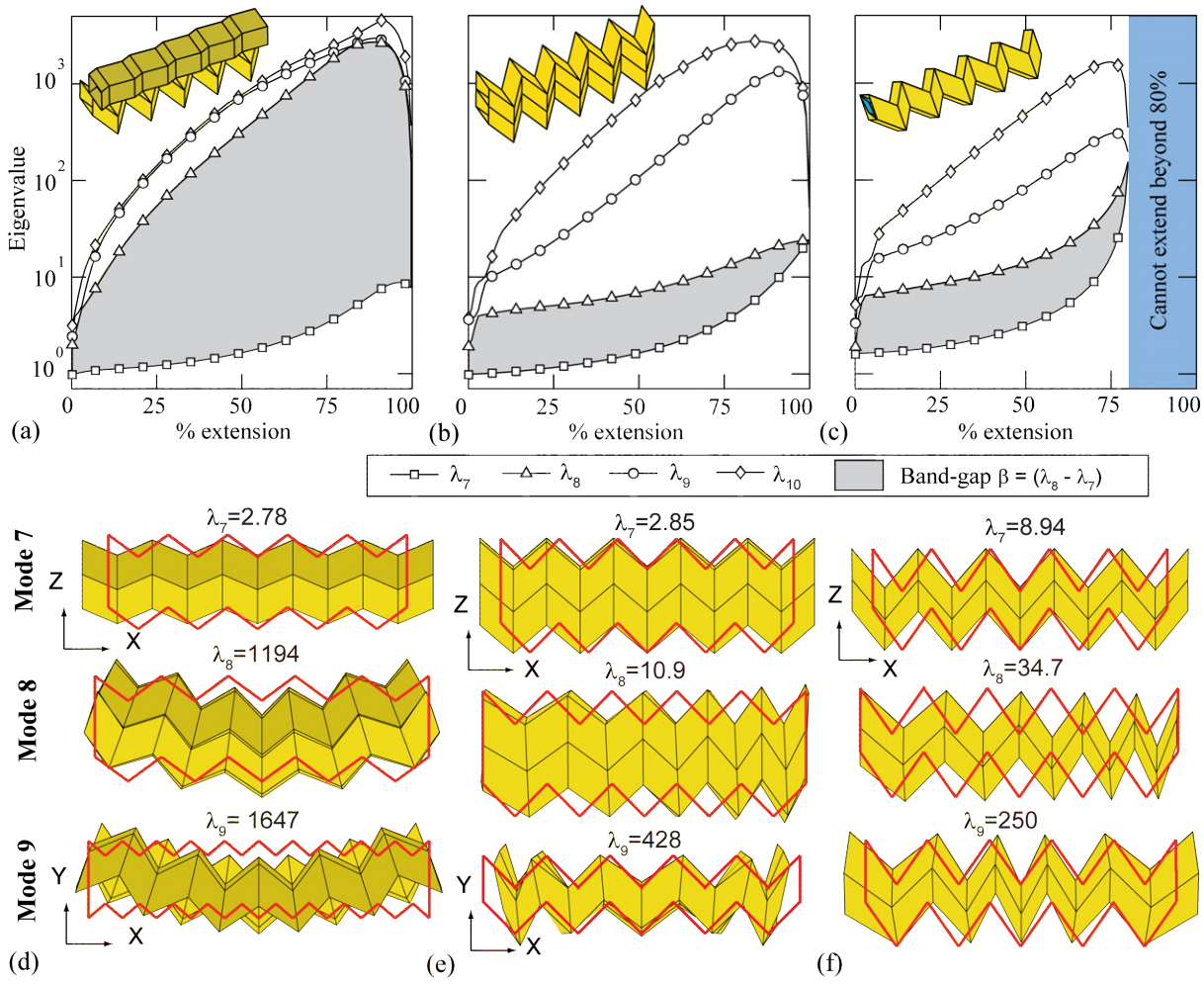

Figure 4.13: Eigenvalue comparison for the different coupling assemblies. (a) to (c) Eigenvalue vs. the structural configuration for the zipper, aligned, and internally coupled structures respectively. (d) to (f) seventh, eighth, and ninth deformation eigen-modes when structures are at 70% of the maximum extension length (undeformed outline in red).

folding mode. In other coupling configurations the eigenvalues typically drop rapidly at high extension configurations since the structure becomes essentially flat ($\theta = 180°$) and is thus easy to bend. The large increase of λ_7 for the internally coupled tubes could be useful for systems that would need to lock and stay in a deployed configuration.

4.4 Origins of the zipper coupling effect

When two tubes are coupled into a zipper geometry the folding kinematics remain unrestricted, however there is a significant increase in stiffness for other deformation motions. The thin sheet panels become engaged in tension and shear for other deformations and there are no other global motions that engage primarily fold and panel bending. In Figure 4.14, we show the deformation associated with the squeezing of different tubes. The squeezing of the single tube is the second most flexible mode of deformation, so we explore why this motion is not possible with the zipper coupled tubes. The squeezing requires continuous bending of the panels from one end of the tube to the other, and this essentially leads to type of rotation of the panels over the length of the tube (Figure 4.14 (b)). All squeezing deformations in Figure 4.14 are shown with the near side of the tube unfolding (approaching a flattened state) and the far side folding (approaching a collapsed tube). When coupled tubes go through squeezing, it is necessary that the ends of both tubes go through the same type of folding or unfolding motion (e.g. the near end of both tubes is unfolding). For aligned tubes (Figure 4.14 (d)) the squeezing motion in the two tubes is compatible. The coupled side of both aligned tubes rotates in the same direction and there is no separation between the deformed modes. On the other hand, the zipper coupled tubes (Figure 4.14 (c)) have a non-compatible motion when squeezing. The coupled side of the tubes rotate in opposite directions, and there is differential movement between the two tubes.

Another way of exploring the source of the large band-gap increase, is to investigate the squeezing deformation mode as it is restrained by the new geometry. We perform an eigenvalue analysis on two tubes arranged in a zipper coupling fashion, when the stiffness of all coupling elements is substantially reduced ($C_{X'} = C_{Y'} = C_{Z'} = 0.0005$). In this scenario the tubes can simultaneously undergo the squeezing deformation mode where the tubes fold on the left side and unfold on the right (Figure 4.15 (a-c)). However, this motion

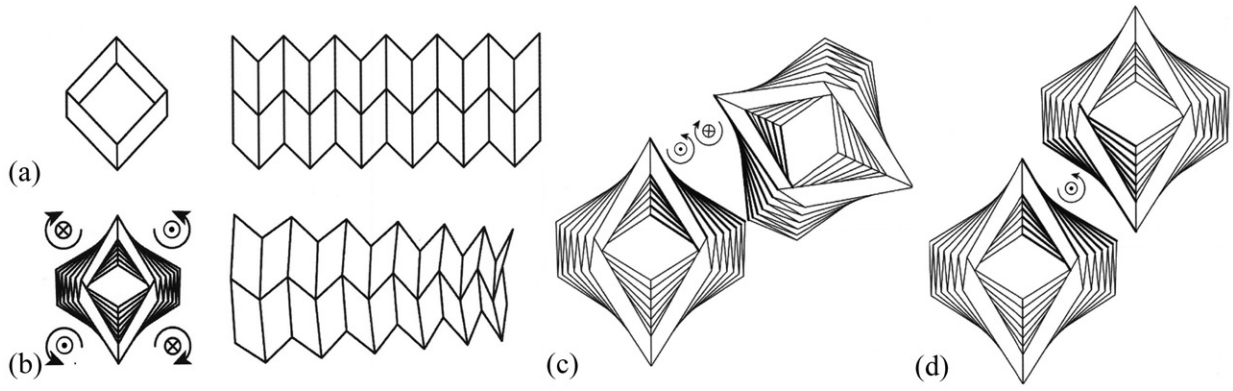

Figure 4.14: Tube with squeezing deformations (image from Filipov et al. (2015b)). (a) Undeformed configuration of a single Miura-ori origami tube. (b) Squeezing of a single tube, with panel rotations indicated on each side of the tube. The cross section view shows the near side unfolding - into a flat sheet; and the far side folding - into a collapsed tube. (c) Squeezing of two tubes that are oriented in a zipper coupling configuration. The coupled surfaces on the two tubes rotate in different directions. (d) Squeezing of two tubes oriented in an aligned direction. The coupled surfaces rotate in the same direction and remain compatible.

is incompatible for an effectively coupled zipper system. On the left side, the first vertex of the bottom tube moves downward (point I on Figure 4.15 (a)), while the first vertex on the top tube moves upward (point II on Figure 4.15 (b)) and vice versa on the right side. This transverse motion between the two tubes can be quantified by tracking the distance between adjacent panel-edge center points on the two tubes (Figure 4.15 (d)). In an undeformed (or effectively coupled) system the distance between adjacent edge center points is uniform at 0.7 units. The squeezing of the loosely-coupled system results in separation on the left side (distance increases up to 0.9 units), and a closing on the right side (distance decrease down to 0.5 units). In an effectively coupled zipper system these in-plane motions are restrained, and it would be necessary to stretch and shear the thin sheet to achieve a squeezing type deformation.

4.5 Influence of tube geometry on eigenvalue bandgaps

As it is briefly discussed in Section 4.3 it is possible to couple tubes where the geometry of the individual tubes is different e.g. the sector angle α or the panel height a do not need to be the same for the two coupled tubes. Furthermore, as we showed in Section 4.2.2 tubes

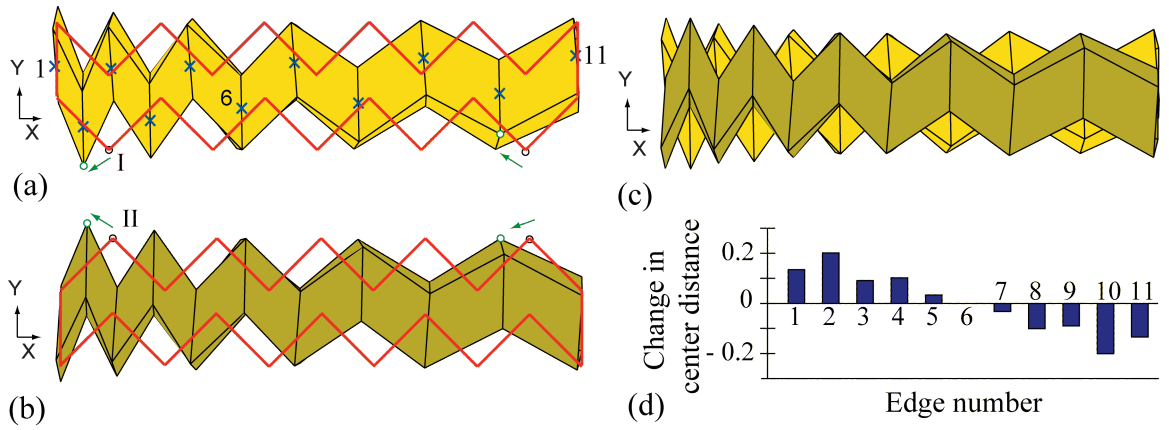

Figure 4.15: Squeezing deformation of zipper-coupled tubes when the coupling coefficients are reduced to $C_{X'} = C_{Y'} = C_{Z'} = 0.0005$. (a) Top view of only the deformed bottom tube with an outline of its initial configuration. The x-marks indicate the panel-edge center points on the side of the tube which is attached. (b) Only the deformed top tube. (c) The squeezing deformation of the zipper-coupled assembly with low coupling. (d) Change in the distance between the panel-edge center points of the two tubes. Initial distance before deformation is 0.7 units for all locations; the squeezing results in separation on the left side and closing on the right side of the coupled tubes.

of different geometries have different characteristics at different deployment configurations, and thus it may be useful to couple different geometry tubes. Here we study two tubes with different α in the zipper coupled configuration, and we investigate how the bandgap between (λ_7 and λ_8) is influenced by the different geometries. Firstly, in 4.16 we can see the different eigenvalue response achieved by coupling different tubes. The $\alpha = 55°$ yellow tube is coupled with a $\alpha = 70°$ red tube (Figure 4.16 (a)) and also with a $\alpha = 85°$ green tube (Figure 4.16 (b)). The ($\alpha_A = 55°$ - $\alpha_B = 70°$) tube combination has a large gap for the lower extension lengths, while the ($\alpha_A = 55°$ - $\alpha_B = 85°$) tube combination only has a large bandgap for some of the higher extension lengths. The gap in the ($\alpha_A = 55°$ - $\alpha_B = 85°$) combination is substantially larger than that of either a $\alpha = 55°$ tube or a $\alpha = 85°$ tube alone. This property could be of benefit if for example one needs to use the $\alpha = 85°$ tube due to its geometric (i.e. it results in a square tube with a direct opening), but would like to have a bandgap through the entire deployment sequence which was not possible for the single $\alpha = 85°$ tube (Figure 4.5).

Next we study the response of different zipper tube pairs by performing a parametric study on the sector angles α_A and α_B of the tubes. Figure 4.17 shows the bandgap between (λ_7 and

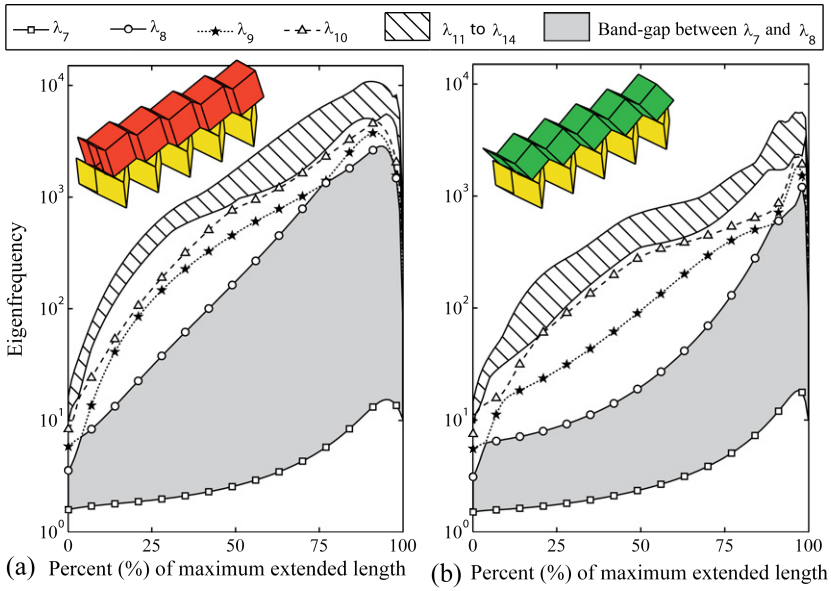

Figure 4.16: Eigenvalue response of zipper coupled tubes with different geometries: (a) $\alpha_A = 55°$ yellow tube coupled with a $\alpha_B = 70°$ red tube, and (b) $\alpha_A = 55°$ yellow tube coupled with a $\alpha_B = 85°$ green tube.

λ_8) of the α_A and α_B zipper coupled tubes when they are analyzed at three different extension lengths. In Figure 4.17 (a) the zipper tube combinations are analyzed at a configuration of 50% of the maximum extension length, and the ($\beta = \lambda_8 - \lambda_7$) bandgap is plotted for the different tube pairs. Coupling two identical tubes with $\alpha_A = \alpha_B = 51°$ results in the highest gap for zipper coupled tubes at the 50% of the maximum extension length configuration. For higher extension length configurations (80% in Figure 4.17 (b) and 95% in Figure 4.17 (c)) the sector angles of the tube pairs with maximum bandgap are higher and this is similar to the single tube behaviors e.g. $\alpha = 85°$ tubes experience low bending eigen modes in low extension configurations. For all of the extension lengths the maximum bandgap occurs when two of the same tubes are coupled together ($\alpha_A = \alpha_B$). This is interesting since it shows that there is no benefit in coupling two different tubes even for different system configurations. Finally, the value of the actual bandgap tends to be higher for configurations at a higher extension length.

The response was studied for lower extension lengths as well, and the zipper coupled tubes that resulted in the maximum gap ranged from pairs $\alpha_A = \alpha_B = 42°$ for near 0% extension to $\alpha_A = \alpha_B = 87°$ for 99% extension. This however does not give an encompassing answer to

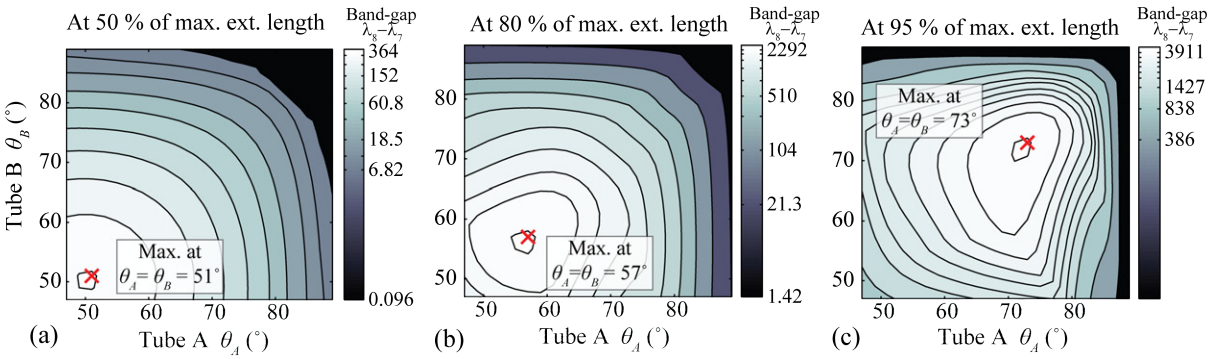

Figure 4.17: The bandgap ($\beta = \lambda_8 - \lambda_7$) for zipper coupled tubes pairs α_A and α_B at configurations (a) 50%, (b) 80%, and (c) 95% of the maximum extension length.

what tube geometries are best to use to achieve a large bandgap. To capture the cumulative tube response for different configurations, we can study the integral of the bandgap between (λ_7 and λ_8). For each tube pair α_A and α_B, we take an integral over the extension length as:

$$\int_{\%EXT=0\%}^{\%EXT=100\%} \beta = \lambda_8 - \lambda_7 \tag{4.12}$$

The value of this integral is plotted for the different tube pairs in Figure 4.18. This figure, similar to those showing the bandgap at a single extension length is also symmetric, and the maximum integral of the bandgap vs. extension length occurs for a tube pair of $\alpha_A = \alpha_B = 60°$. Furthermore, Figure 4.18 shows the maximum integral of the bandgap that can be achieved when one of the tube sector angles (α_A) is initially prescribed. This way a designer that would like to use a specific tube can choose the geometry (α_B) of the second tube so that the structure has the maximum possible bandgap for different configurations.

4.6 Structural cantilever analysis

Coupled tube systems can be applicable as deployable cantilever structures, when restrained on one end (Figure 4.19). A mechanism can be used to deploy the system or to fix it on one end for practical utilization . In this configuration the tube systems exhibit behavior similar to that of an I beam, wherein the second moment of area (or area moment of inertia) is increased by distributing material away from the centroid. The aligned and internally coupled tube systems often experience squeezing type deformation when loaded on one end,

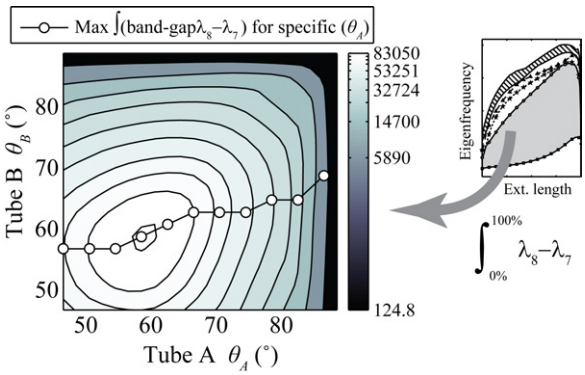

Figure 4.18: The integral of the bandgap ($\beta = \lambda_8 - \lambda_7$) over the extension length, for different tube pairs α_A and α_B.

whereas the zipper coupled tubes experience a more uniform deformation (Figure 4.19).

The support and loading conditions for the cantilevers are shown in Figure 4.20. At the supported end, all nodes are fully fixed (X,Y,and Z displacements). A total load of 1 is distributed on the other end of the structure, by placing 1/8 of the load at each of the 8 nodes. Double the load (1/4), is placed on the collocated nodes occurring in the aligned and internally coupled systems. The fixed end of the cantilevers may also be constrained in a different fashion, so that a mechanism could be used to fold and deploy the entire structure. Figure 4.20 (g) to (i) shows a new constraint pattern, where a mechanism is used to control the rigid folding mode of the system. When the mechanism is contracted the structure will deploy, and when it is extended the structure will fold. When the length of the mechanism is fixed, the cantilever will behave much like if the support is fully fixed.

We compute the stiffness in different directions for the coupled tube structures, and normalize it with respect to the total material used in the system (Figure 4.21 (a-f)). The stiffness of the structures is calculated for the three Cartesian directions for different extension configurations (Figure 4.21 a-c). The distributed loads are applied for each individual case, and the resultant displacements (Δ_X, Δ_Y, and Δ_Z) are calculated from the linear function $\mathbf{F} = \mathbf{K}\Delta$, where $\mathbf{F}$ is a force vector, and $\mathbf{K}$ is the stiffness matrix from Equation 3.1. A quantitative stiffness is then calculated as $K = F/\delta = 1/\delta$ based on the maximum system displacement ($\delta = \max(\Delta)$) in the direction of the applied load.

The results for stiffness presented here show the general system behavior, and are in consistent units of force per length (e.g. N/mm). A realistic length scale and elastic modulus

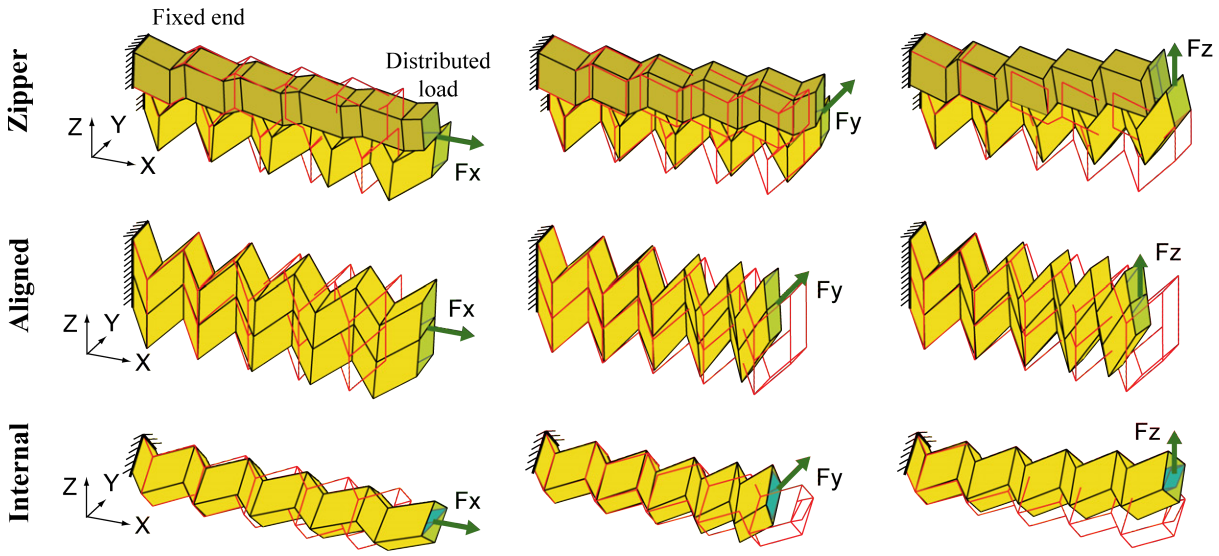

Figure 4.19: Zipper, aligned and internally coupled tubes used as cantilevers. Initial (red line) and deformed geometry of the structures at 70% extension when the left end is fixed and a uniform load is applied on the right end. The deformed shapes are scaled so the maximum displacement for each case is equal to the panel height ($a = 1$), and do not necessarily represent stiffness.

can be substituted to find quantitative results for the cantilevers.

The stiffness for different directions of load application, orthogonal to the X axis, is also investigated, by rotating a load in the $Y - Z$ plane. At three different configurations (40%, 70%, and 95% extension), the stiffness for each structure is calculated, and presented as a radial plot showing the direction of load application (Figure 4.19 (d-f)). The structure is analyzed with the same constraint and load distributions, and only the direction of the load vector (equating to 1) is rotated in the $Y-Z$ plane. The aligned and internally coupled tube systems demonstrate anisotropic behavior, wherein one loading direction (in the $Y-Z$ plane) displays high stiffness, whereas the zipper coupled tubes tend to be stiff for all directions of loading (Figure 4.19 (d-f)).

4.7 Cellular systems

Cellular origami can permit self-assembly of engineered hierarchical materials (Côté et al., 2006; Fratzl and Weinkamer, 2007), whose mechanical properties depend on the micro-structure geometry. The structural stiffness and energy absorption properties of cellular origami can be optimized to complement and improve naturally-occurring materials (Gibson

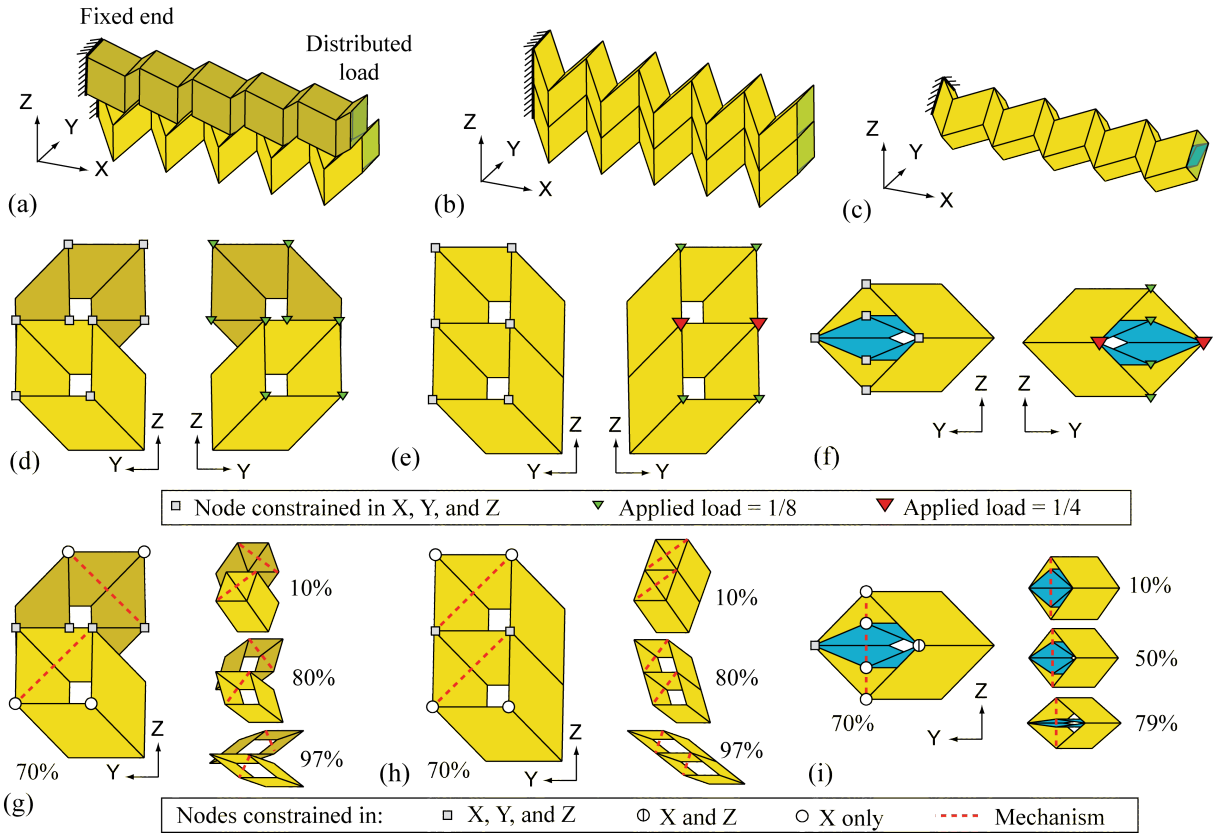

Figure 4.20: Support and loading conditions of origami cantilever structures. (a) to (c) Initial configurations for the zipper, aligned, and internally coupled structures respectively. (d) to (f) Support conditions (left), and loading conditions (right), used in the analyses of the three cantilever systems. The total load of 1 is distributed by placing 1/8 of the load at each of the 8 nodes, while double the load (1/4), is placed on collocated nodes occurring in the aligned and internally-coupled systems. (g) to (i) Support conditions (left) for the cantilevers, if a mechanism is installed to deploy the system. Cantilever configurations (right) for different levels of system extensions/contractions.

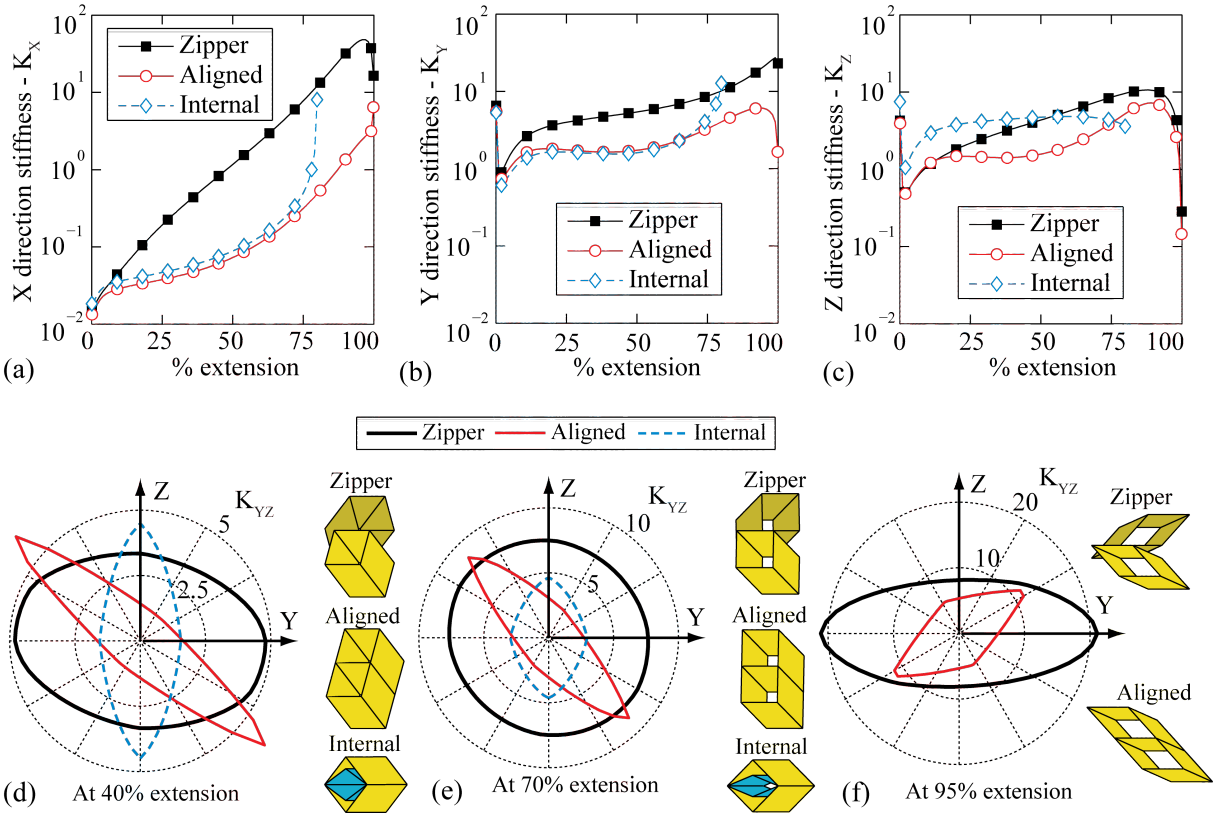

Figure 4.21: (a) to (c) The stiffness (force/length) of the cantilevers in the three Cartesian directions. The internally coupled tube cannot extend beyond 80% extension of the external tube. (d) to (f) The stiffness for loads in the $Y - Z$ plane represented as a radial plot at extensions of 40%, 70%, and 95% respectively. Stiffness is shown as distance from the origin.

et al., 2010). Zipper-coupled tubes can be integrated with aligned or internal coupling to create layered foldable assemblages (Figure 4.22). Structures that incorporate zipper coupling inherit the large band-gap, while also retaining properties from the other coupling techniques (e.g. space filling from aligned or locking from internal coupling). In Figure 4.22 (b-e), we study a zipper/aligned metamaterial consisting of 36 developable tubes constructed with square unit cross-sections, projections of $\phi_Z = \phi_{YT} = -\phi_{YB} = 35^\circ$ and six equivalent segments of $l_1 = l_2 = l_i$. For the analysis, we use the N4B6 model and the same parameter as discussed in Section 4.2.2. For these analyses the fold to panel stiffness ratio is set to $R_{FP} = 1$, to simulate an assemblage constructed by additive manufacturing (Figure 4.22 (f-g)). Origami metamaterials created with 3D printing do not fold like traditional origami, but possess novel characteristics such as the single flexible mode of zipper coupling.

We analyze the assemblage in Figure 4.22 by applying symmetric uniform forces (summing to 1) on opposing faces of the system, and calculate the compression stiffness as $K = F/\delta = 1/\delta$ where δ is the mean total displacement in the direction of loading. We reconfigure the structure based on the folding kinematics and analyze the model at different extensions. The analysis is performed with the folds not accumulating stresses during the reconfiguration. Because of the zipper geometry, the system is primarily flexible in the X direction at lower extensions (0-70%), and in the Y direction at higher extensions (70-100%). The peak in the Y direction stiffness (at 96.4% extension) corresponds to a bifurcation point, where the tube cross-section is square, and can transition to a different rhombus depending on the direction of folding. In addition to the stiffness, the deformation characteristics of the material are also anisotropic. The perceived Poisson's ratio is negative in the Y direction when compressed in X, while it is positive in the Z direction when compressed in Y (Figure 4.22 (c-d)). The structure is substantially stiffer in the Z direction, and deformations do not follow the kinematic folding mode. In Figure 4.22 (f-g), we show how additive manufacturing can be used to create cellular metamaterials with characteristics inherited from the zipper tubes.

4.8 Other variations

In this section, we briefly discuss other possible methods for coupling origami tubes. We show several physical models that were used for demonstrating the new mechanical characteristics

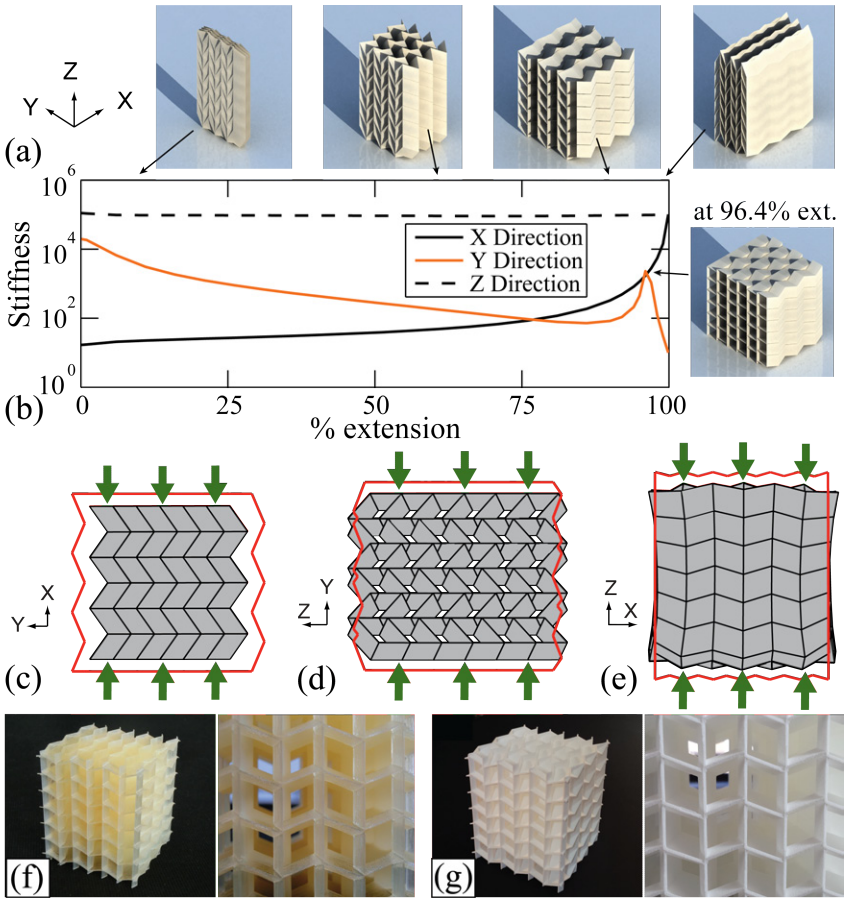

Figure 4.22: Cellular origami metamaterial consisting of 36 tubes arranged as zipper in the horizontal Y direction and as aligned in the vertical Z direction. (a) Kinematic folding sequence of the assemblage. (b) Compression stiffness of the metamaterial in the three Cartesian directions vs. extension. (c-e) Initial (red line) and deformed geometry of the assemblage at 90% extension for uniform compression tests in the X, Y, and Z directions respectively. The deformed shapes are scaled so the mean displacement of the loaded surfaces is equal to the panel height ($a = 1$) and do not represent stiffness. (f-g) Metamaterial prototypes constructed with additive manufacturing, cannot undergo the full folding motion in (a), but inherit the anisotropic mechanical properties of the cellular zipper assemblages. In (f) a soft metamaterial made with Digital Light Processing of an AR-M2 transparent resin with a wall thickness of 0.09 mm can be deformed by hand. In (g) a polyamide (PA 2200 material) assemblage with a wall thickness of 0.8 mm was created by Selective Laser Sintering and is substantially stiffer.

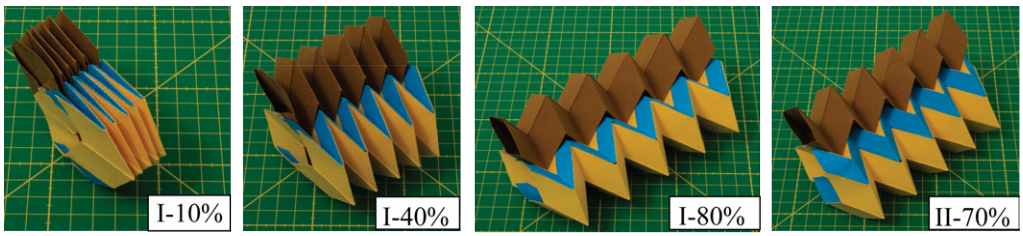

Figure 4.23: Physical prototype of Zipper coupling of a reconfigurable tube with a polygonal cross-section. The six-sided pilygonal tube has two possible shapes (I and II). Generalizations of the Miura-ori sheets can be employed to create a variety of tubular structures with varying polygonal geometries.

and for showing the kinematic folding of the different assemblages. The origami assemblages were created from perforated paper that is folded and adhered together. The Miura-ori sheets were created from 160 g/m^2 paper by perforating along the fold lines with cuts of length 0.5 mm spaced evenly at 1 mm intervals. Because each tube cannot be developed from a single flat piece of paper, it is assembled by connecting two Miura-ori sheets. One of the sheets is constructed with perforated tabs at the edge, which can be folded and attached with standard paper adhesive to a mirror image Miura-ori sheet. When connecting two tubes into either the zipper or aligned assemblage, the adjacent facets are adhered together on the coupling surface.

4.8.1 Zipper coupling of tubes with different cross-sections

In Figure 4.23, we show the extension and reconfiguration of a physical polygonal tube coupled with a developable tube in the zipper orientation. The internal (blue) panels of the polygonal tube are defined to reach a flat configuration when external panels (yellow) are at 80% extension. The structure is only flat foldable in one direction, but the internal folds (in blue) can change their polarity, and can reconfigure the overall structural shape. In Chapter 6, we perform a detailed study on the possible variations of polygonal tubes that can be created. The cross-sections of the polygonal tubes can have many different geometries, and many of the tubes can also be reconfigurable.

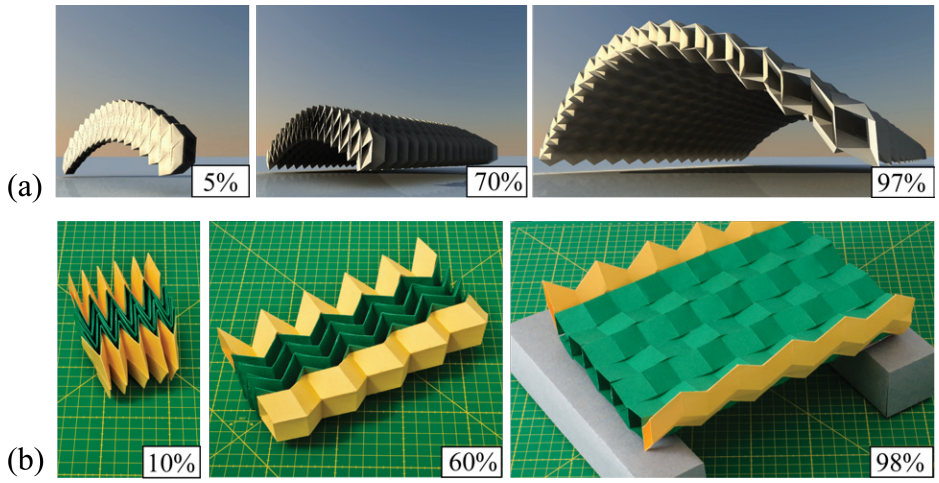

Figure 4.24: Variations of horizontally coupled tubes. Approximate percentage of extension shown. (a) Deployable architectural canopy with a high out-of-plane stiffness for transformable building design. (b) Bridge structure from zipper -coupling tubes of different geometries. The structure is flat foldable in two directions and stiff for out-of-plane bending.

4.8.2 Coupling of tubes in multiple directions

There are numerous ways in which rigid foldable tubes can be defined, combined, and coupled. The arch in Figure 4.24 (a) is designed with thirty two alternating tubes with $\phi_Z = \phi_Y$ varying between 32° and 6°. All tubes have panels with dimensions $a = c = 0.3$ m and are 32 segments long. All tubes are coupled in the zipper orientation. The projection angles $\phi_Z = \phi_Y$ are calculated so the overall cross-section follows a smooth planar curve (e.g. $\alpha = 32°, 6°, 30°, 7°, 28°, 8°$ for the first six tubes). This structure covers an area of 8.1×9.3 m with a 2.6 m rise when deployed to 97% extension, and can fold down to a size of $5.1 \times 0.8 \times 1.3$ m at 5% extension. The prototype bridge in Figure 4.24 (b) is constructed with a distinct deck and parapets . When deployed the bridge structure is stiff in bending and can allow for traffic to pass, this could be useful for disaster relief in areas that have lost road access or could be used to construct new temporary bridges when there is a need. Two tubes with $\phi_Z = \phi_Y = 35°$ (yellow) and six with $\phi_Z = \phi_Y = 5°$ (green). All tubes have square cross-sections with sides of 25 mm, segment lengths of 25 mm and ten segments. Zipper coupling is continued in one direction only, where each tube is coupled on two opposite faces. The system remains rigid and can fold down completely flat in two different planes. The structure has a high out-of-plane stiffness.

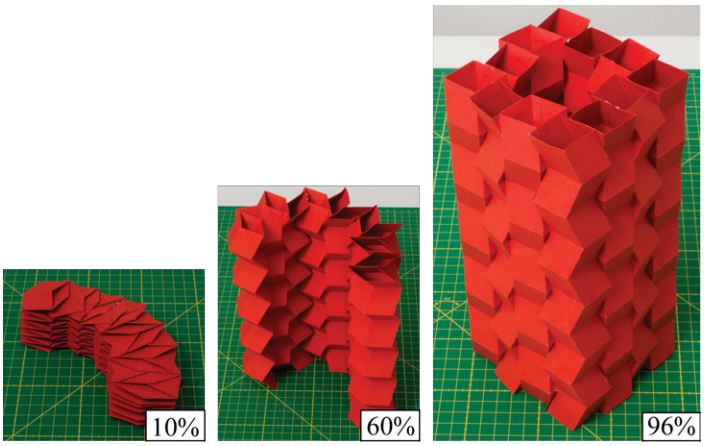

Figure 4.25: Extension (percent deployment) of structure that interlocks into a fully conforming shape. Each edge of the structure is composed of four tubes coupled in a zipper orientation.

If the zipper coupling is repeated in more than one direction, the structure will self-interlock during the deployment, creating a stiff array of coupled thin sheets (Figure 4.25). The side of the the self-interlocking structure can be composed of any number of zipper coupled tubes together (of same θ). Furthermore, the interlocking structure does not necessarily need to have a square final cross-section (four segments of zipper coupled tubes), but can be any radially symmetric shape with n sides as long as there is no self intersection. The structure will interlock when an angle (γ) between the two faces on the $Y-Z$ cross-section the Miura-ori cell are at $\gamma = 360°/n$. Thus the structure will interlock at an extension of:

$$Ext. = 100\% \frac{\sqrt{1-\cos(\gamma/2)^2/\sin(\theta)^2}}{\sin(\gamma/2)}. \tag{4.13}$$

The tube presented in Figure 4.25 have projection angles of $\phi_Z = \phi_Y = 25°$ square cross-sections with sides of 25 mm, segment lengths of 25 mm and ten segments (red tubes). Zipper coupling continued in one direction for each side of the structure. The tubes at the corners have zipper coupling in orthogonal directions (i.e. on two adjacent faces of the tube). The system is flat foldable in one direction, and interlocks into a stiff conforming assembly at an extension of 96.3%.

4.8.3 Local geometric variations

There are other methods for coupling and combining tubes beyond what is covered here (e.g. stacked sheets (Schenk and Guest, 2013) or interleaved (Cheung et al., 2014)), and perhaps, more methods will be discovered in the future. In this section, we briefly discuss local variations that can be made to the zipper coupled tube systems. One local variation is to only couple specific portions of a tube. The long tube in Figure 4.26 has zipper-coupling only in the middle portion to restrict the global squeezing and bending of the system. The ends remain uncoupled, allowing for a rigid connection to the outside edge while still permitting the system to fold and unfold. Applications would be to use these types of tubes as actuators or deployable booms. Origami has already been used and tested for theses applications, and is again especially suitable due to the pre-configured small stowing configurations (Martinez et al., 2012; Schenk et al., 2014b; Fernandez et al., 2014). Gases or liquids could be pumped in at one of the ends and can lead the structure to deploy. The zipper coupling in the middle section of the actuator is also beneficial, since it prevents localized squeezing to occur in the middle of the actuator and it also reinforces the structure for out-of-plane loadings.

Finally, using available techniques for thick origami (Hoberman, 2010; Tachi, 2011), we can create structures of thick panels adjoined with physical hinge elements. With these techniques cost-effective materials (e.g. thin wood panels with metal hinges) can be used to create large structures that can be easily deployed, but possess large global stiffness from the zipper-coupling framework (Figure 4.26 (b)). The thickened tubes have panel dimensions $a = 80$ mm, $c = 40$ mm, and the thickness is $t = 5$ mm on the thin and $t = 10$ mm on the thick part of the panels. A technique of cutting out material is adopted, allowing the structure to fold down completely to the minimal feasible thickness of $2Nt = 80$ mm. The structure cannot extend to 100% extension because intersection of the thick material will occur.

4.9 Concluding remarks

This chapter explores single origami tubes and introduces a new approach for coupling tubes together in a zipper fashion. We explore the unique mechanical characteristics of the coupled systems through eigenvalue and structural analysis. The zipper coupling configuration

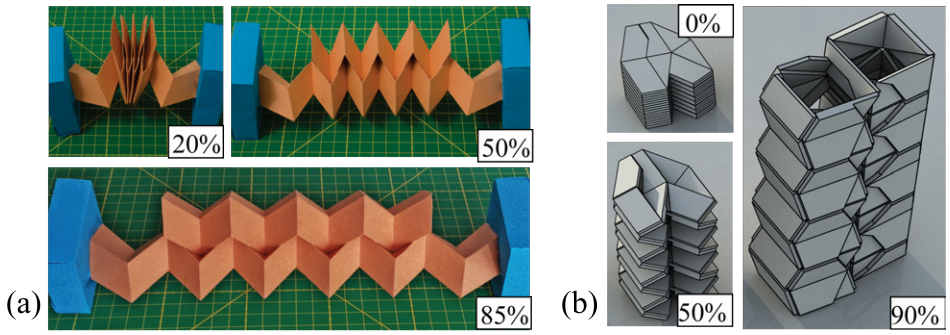

Figure 4.26: Local variations for possible future extensions of coupled tube structures. Different stages of deployment are shown with approximate percentage of extension. (a) Actuator system from zipper coupling of two tubes of different length. The edges of the long tube are restrained, but squeezing can occur on the uncoupled sections allowing the system to fold. (b) Computer visualization of zipper tubes from thick material (thick origami).

results in a large bandgap between the the rigid body folding (seventh) mode and subsequent squeezing and bending modes (eighth and larger). The origami tubes engage the thin sheets in tension, compression, and shear for any deformation mode that does not follow the kinematic deployment sequence. Therefore these systems are easy to deploy yet are stiff for any other motion. The increase in stiffness of the eighth mode is several orders of magnitude with the zipper coupling. This increase is much larger than could be achieved with other coupling methods or with variations in the fold pattern geometry.

The zipper tubes increase the structural stiffness while still maintaining the rigid and flat foldability of the origami. These properties are especially appealing because the structures can be stowed in small spaces, they can be constructed of panels and hinges and can extend into stiff practical structures. The zipper structure is analyzed as a deployable cantilever where one end is constrained and can be actuated with a deployment mechanism, while the other end of the cantilever can resist perpendicularly applied loads. The cantilever is useful between 30 to 90% of its extension length, because at that range it can be deployed easily and it is stiff in other directions. We also explore variations to the coupled tube geometry, and show possible local and general coupling variations. The tube could be used to create a variety of cellular assemblages that can have tunable stiffness and other enhanced mechanical characteristics. In Chapter 5, we discuss how the zipper-coupled origami tubes can be generalized to create assemblages that have flat tops and are curved to create new functional forms.

As origami becomes more widely used in science and engineering, the coupled tube assemblages will serve as an important component that allows flexible deployment while simultaneously retaining a high global stiffness. The zipper tubes could be useful for large scale applications such as buildings or space structures, and potentially at much smaller scales such as in micro robotics or metamaterials. Further study of the hierarchical system properties with respect to fabrication, scale, and materials will be needed to inform potential applications. Extensions and refinements of this work could improve stiffness to weight ratios, impact energy dissipation, and other mechanical properties.

CHAPTER 5

DEPLOYABLE CANOPIES AND ROOFS WITH HIGH OUT-OF-PLANE STIFFNESS

In this chapter, we develop a generalized definition for coupled tube systems such that they can be created with different cross-sections and can take on curved profiles. We explore how geometry affects stiffness and present a methodology to create usable slab, arch, and roof type structures. We find that the deployable systems have a high out-of-plane stiffness when at an extended configuration, however the cross-sectional geometry significantly influences stiffness during deployment. Typically structures that have a more zig-zagged initial geometry can have a reasonably high stiffness during deployment.

5.1 Introduction

In Chapter 4, we introduce the idea of zipper coupled tubes and explore their stiffness characteristics. We show that this new type of coupling can provide unique structural properties where the structure is easy to deploy yet it is substantially stiffer for any type of bending, twisting or other deformation mode. In Chapter 4, we focus primarily on one specific geometry of origami tubes that is symmetric and developable. In this chapter, we explore the geometry variations of coupled tubes, building upon the interesting characteristics of the zipper coupled systems.

Varying the geometry of the tubes can be used to tune and tailor the stiffness and other structural characteristics of the tubes. Additionally, geometric versatility can open up additional capabilities and advantages of the origami tubes, such as reconfigurability where the structure can be folded and re-folded in different ways. Varying the geometry of the structures is also particularly important when aiming to apply the origami tubes to specific applications. For example, it is possible to create tubes that would be curved or that could have a continuous flat surface when deployed. It is also possible to use the tubes as inflatable systems that can be actuated through internal pressures, or to use them as cellular metamaterials with unique characteristics. Changing the geometry can allow a designer greater versatility to enhance functionality and aesthetics of the deployable system. This versatil-

ity can also be used for improving structural properties of the system such as strategically increasing the stiffness in specific directions.

In this chapter, we introduce a generalized projection method to create the coupled origami tubes. This method is an extension of the generalized surface approach discussed by Tachi et al. (2015) to create coupled tube systems that have a non-straight profile (e.g. see deployable canopy in Figure 5.1). In addition to curved coupled systems in this work, we discuss cross-section variations of the tube systems, such that, straight tubes can be constructed with two distinctly different tubes. We use eignevalues to verify the rigid foldability of the coupld tubes and we show that tubes can be made reconfigurable. The kinematics show that depending on the tube geometry, some tubes can have two distinct folding paths.

We explore the stiffness of the coupled tubes through three point bending tests, and investigate the influence of projection and cross-section geometry on stiffness. We study the stiffness of the systems not only at a fully deployed state, but at intermediate states of deployment as well. An increase in stiffness from zipper coupling can be observed, and we find that tubes that are more zig-zagged tend to have a higher out-of-plane stiffness during deployment.

Using the generalized approach, we construct tubes with flattened tops that could be aesthetically pleasing and functional for applications such as deployable slabs, decks, walls, bridges or walkways. We also explore possible extensions of such systems into non-straight variations. In particular, we explore tubes that can deploy into conventional roof types including gable, barn (gambrel), and arched shapes. We explore the stiffness of the different variations and show that they can be stacked in sequence to form a deployable surface.

The chapter is organized as follows: Section 5.2 discusses a generalized projection approach for defining the geometry of single and coupled tube structures. In Section 5.3 we explore the kinematics, rigid foldability, and geometric properties that limit the generalized coupling definitions. Section 5.4 discusses how the geometric properties affect stiffness of coupled tubes. Section 5.5 explores the stiffness of slabs and beams with a flat top surface, and gives insight to how different cross-sections affect stiffness. Deployable roof and arch systems are discussed in Sections 5.6, and Section 5.7 provides concluding remarks.

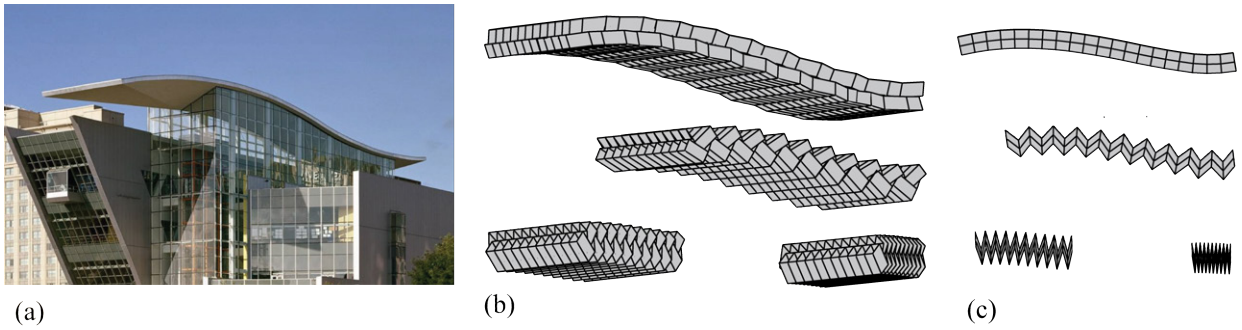

Figure 5.1: Canopy structures. (a) The roof of the Connecticut Science Center by Csar Pelli & Associates (image from Woodruff and Brown (2009)). Deployment sequence of a curved canopy constructed with zipper coupled origami tubes shown in (b) isometric and (c) side views.

5.2 Generalized projection definition for single and coupled tubes

We introduce a simplified projection based technique to define the geometry of the origami tubes. In this chapter, we use cross-sections that are simple squares or rhombuses (four equal edges). However, the techniques and concepts presented here can be extended to any type of parallelogram cross-section. Tubes with a parallelogram cross-sections would be flat and rigid foldable, and also allow for the valid and effective coupling of multiple tubes (as discussed in Section 5.2.2). In Chapter 6, we extend the projection methodologies to tubes with arbitrary polygonal cross-sections. These tubes can be flat and rigid foldable, however the polygonal cross-sections could limit some of the coupling capabilities presented in Section 5.2.2.

5.2.1 Origami tubes with quadrilateral cross-sections

We start by constructing a tube cross-section in the $Y - Z$ plane. We define the rhombus cross-section such that all sides have a unit length (1). The bottom of the cross-section is placed to be parallel with the Y axis, and an angle of θ counterclockwise from the Z axis defines the rotation of the cross-section into a rhombus. We use two angles ϕ_Y and ϕ_Z to guide the direction of the projection. The angle ϕ_Y relates the projection from the X towards the Y axis, while the ϕ_Z angle relates the projection from the X towards the Z axis (see Figure 5.2). For a *straight* tube, we project the cross-section in the X direction onto a projection plane that remains parallel to the $Y - Z$ plane. We use a *segment length*

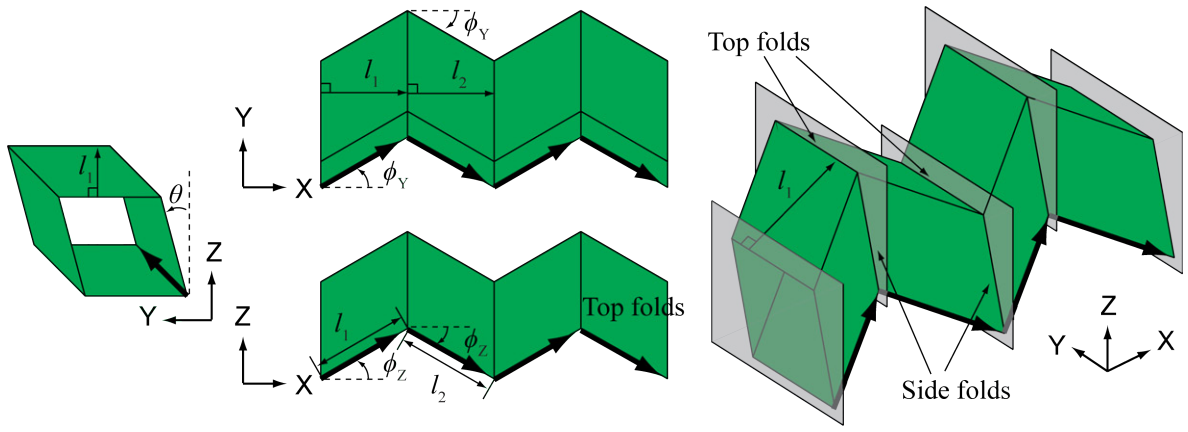

Figure 5.2: Generalized projection approach to define a *straight* tube inspired by the Miura-ori pattern. The tube is constructed by starting with a cross-section in the $Y-Z$ plane and projecting the cross-section in the X direction. The rhombus cross-section has unit (1) dimensions and is defined by an angle θ. The projection is guided by the angles ϕ_Y and ϕ_Z with respect to the X axis. The cross-section is projected by a distance l_i in the $X-Z$ plane. The tube in this figure has dimensions $\phi_Y = 30°$; $\phi_Z = 30°$; $\theta = 15°$, and $l_1 = l_2 = l_i = 1$.

parameter l_i to define the distance between the i^{th} and the $i+1^{\text{th}}$ projection plane where the first plane is at $X = 0$ and defines the initial cross-section. The segment length l_i is defined in the $X-Z$ plane only. Thus the distance between projection planes in the X direction can be calculated as $l_i \cos(\phi_Z)$. This definition is later important for coupling of multiple tubes.

This projection creates a new cross-section that again lies only in the $Y-Z$ plane and is parallel with the initial cross-section when looked at from above ($X-Y$ plane). The corresponding edges of the two cross-sections are connected with thin origami sheets creating a system of fold lines and panels. At the subsequent projection plane, we mirror the tube locally, or in other words we use the opposite projection angles to find the subsequent projection ($-\phi_Y$ and $-\phi_Z$). This mirroring ensures flat foldability of the origami tube. In Figure 5.2 we show a basic tube generated using this projection scheme. For subsequent discussions we define fold lines at the projection planes as either top/bottom folds or as side nodes. The *top/bottom* folds are the folds that are symmetric to the Y axis, while *side* folds are rotated θ from the Z axis. The projection lengths can be varied, and as long as the projection planes remain in the $Y-Z$ plane, we characterize this set of tubes as *straight*.

When a square cross-section is used, and the angles ϕ_Y and ϕ_Z are equal ($\phi = \phi_Y = \phi_Z$),

this projection approach generates the same tubes as those discussed previously in Chapter 4. In this scenario the panel sector angle is $\alpha = \pi - \phi$, the panel height a is the cross-section dimension, and the panel width c is $l_i \cos(\phi)$. These tubes can be developed from two flat sheets folded into a Miura-ori pattern. Although the entire system is not developable, we call these tubes to be *partially developable* meaning that parts of the tube are developable. With this projection approach it is also possible to construct the same tube by using different parameters. For example, a rhombus cross-section where $\theta \neq 0$ and $\phi_Y \neq \phi_Z$ could be used to create the same partially developable tubes from Chapter 4, but just in a different configuration. As a reference see the kinematics of the tubes in Section 5.3.

The tube projections do not need to be straight and it is possible to create a wide variety of *curved* (or non-straight) origami tube structures. Curved tubes can be constructed by projecting onto planes that are rotated. In this chapter, we focus on tubes that can be coupled and thus we limit the projections to rotate only in the $X - Z$ plane. In Chapter 6, we show some other possible projection methodologies that can be used to create tubes that curve in three directions or that do not necessarily follow the same mirroring approaches. In Figure 5.3, we show a tube where the i^{th} projection plane is rotated in the $X - Z$ plane by an angle ϵ_i. The rotation occurs about the bottom of the newly projected bottom edge of the cross-section. In other words, the bottom edge of the cross-section is translated by $l_i \cos(\phi_{Zi})$ in the X direction and $l_i \sin(\phi_{Zi})$ in the Z direction; and the projection plane is rotated about this new line (which is parallel to the Y axis). The tube is again mirrored locally about the projection plane, and the projection angle ϕ_Z is updated based on the projection plane rotation, e.g. $\phi_{Z2} = \phi_{Z1} + 2\epsilon_2$.

The imposed symmetry from mirroring ensures that all vertices will be locally flat foldable (Tachi, 2009a). Moreover, due to the global symmetry and rigid foldability of the tube, the kinematics do not result in intersection and the tube is globally flat foldable. We verify the flat foldability and the kinematic properties in more detail in Section 5.3.

5.2.2 Coupling of two tubes

In this section, we use the generalized projection scheme to construct two tubes that are coupled along a common *coupling surface*. With the projection methodology it is possible

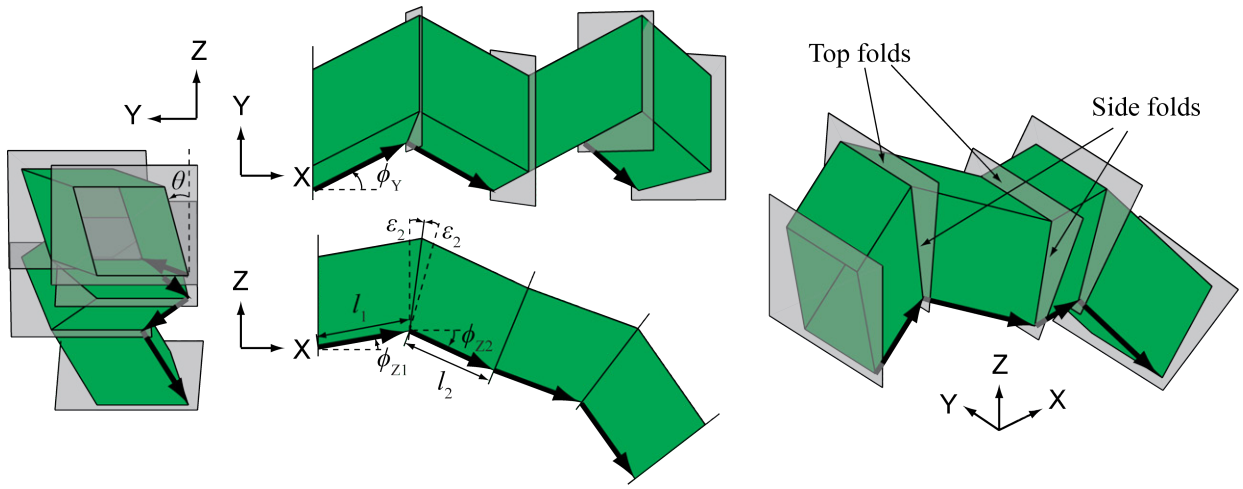

Figure 5.3: Generalized projection approach to define a *curved* (non-straight) tube. The tube is constructed by starting with cross-section in the Y-Z plane and projecting the cross-section in the X direction. Subsequent projection planes can be rotated in the X-Z plane by an angle ϵ. The distance between projection planes l_i is measured along the bottom of the tube in the X-Z plane. The tube in this figure has dimensions $\phi_Y = 30°$; $\phi_{Z1} = 10°$; $\theta = 15°$; $\epsilon_2 = \epsilon_3 = \epsilon_i = 7.5°$, and $l_1 = l_2 = l_i = 1$.

to construct the aligned and zipper tubes discussed previously; but also a larger variety of curved and non-symmetric coupled tubes. The curved tubes employ the symmetry plane definitions introduced by Tachi et al. (2015). We first discuss the basic geometric definition of the coupling of tubes and only note what are valid coupled systems that can allow for the kinematic folding of the systems. The kinematics of the different tube systems are discussed in more detail in Section 5.3.

In Figure 5.4 we show a schematic of two tubes that are generated using the same cross-section and projection technique discussed above. We designate the tubes as a *top* (T) and a *bottom* (B) tube depending on their location along the Z axis. The two tubes always follow the same coupling surface defined by the projection in the $X - Z$ direction, however, it is possible for the tubes to have different cross-sections and different Y projections. The Y projections are defined by ϕ_{YT} and ϕ_{YB}, while the cross-section rotations are defined by θ_T and θ_B, for the top and bottom tubes respectively. The angles ϕ_Y and θ are measured counterclockwise from the X and Z axes respectively. With this definition the bottom tube shown in Figure 5.4 has a negative ϕ_{YB} and a negative θ_B.

The definitions can be extended similar to before, with the segment length l_i varied at

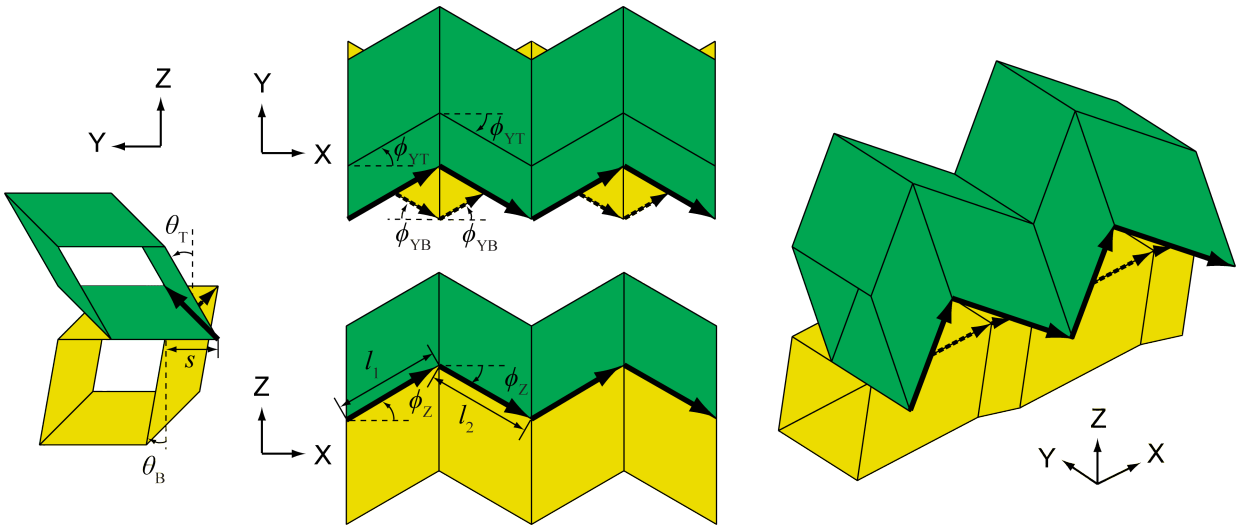

Figure 5.4: Geometric definition of a zipper coupled tube system. Two separate tubes are constructed by projecting the cross-section in the X direction. The *top* (T) and *bottom* (B) tube can have different projection angles in the Y direction (ϕ_{YT} and ϕ_{YB}) and can also have different cross-sections (θ_T and θ_B). The two tubes must have the same projection characteristics in the Z-X plane (angles ϕ_Z and lengths l_i). The zipper tube system in this figure has dimensions $\phi_{YT} = 30°$; $\phi_{YB} = -30°$; $\phi_Z = 30°$; $\theta_T = 30°$; $\theta_B = -10°$ and $l_1 = l_2 = l_i = 1$.

different segments, so long as l_i is measured at the coupling surface and is the same for both tubes. Changing the segment length does not affect foldability of the tube. The coupled tubes can be made curved similar to Figure 5.3 where an angle ϵ_i is used to rotate the projection plane for both tubes. For non-straight zipper coupled tubes (i.e. $\epsilon_i \neq 0°$) to be valid and foldable ϕ_{YT} must equal $-\phi_{YB}$ and θ_T must equal $-\theta_B$. The other alternative is an aligned coupled system where $\phi_{YT} = \phi_{YB}$ and $\theta_T = \theta_B$. The kinematics and foldability of the curved tubes are explored in the next section. Finally, it is also possible to couple tubes in multiple directions and create systems of coupled tubes as discussed further in Sections 5.5.

5.3 Folding kinematics of tube variations

In this section, we discuss the general kinematic properties of the Miura-ori tubes and the variations of coupled tubes. Origami patterns with four folds per vertex are one-DOF folding mechanisms, where the entire geometry of the folds and panels can be calculated from a single variable such as one of the fold angles (Hull, 2012). In a generic case, if

additional and arbitrary constraints are added to the system, the system will become an *over-constrained* mechanism and will no longer be rigidly foldable. However, there exist ways to add additional components (and constraints) such that the origami system maintains the rigid folding mechanism.

Origami patterns such as the Miura-ori use repetition to connect multiple one-DOF vertices into a system that preserves the rigid foldability (the entire system remains a one-DOF folding origami). More advanced origami structures such as the Miura-ori tube use symmetry to connect multiple patterns together while maintaining rigid folding properties (Tachi, 2009b). In Chapter 4, we showed that it is possible to couple multiple tubes together, and while this coupling does not restrict rigid foldability it restrains the origami from flexible motions that engage panel bending. Coupling and adding compatible components to origami system is a non-trivial task.

In Tachi et al. (2015), we explore the two basic geometric families of allowable coupling methods for the rigid foldable origami tubes. These families allow for compatibility between the coupled structures to permit the rigid folding motion. The two families are: (1) Coupling on an *arbitrary straight or curved surface* where the fold lines are parallel and mirroring is used between the bottom and top tubes to ensure rigid foldability; (2) Coupling on a *flat developable surface* with non-symmetric fold lines, with arbitrary fold angles calculated to preserve rigid folding motion (Tachi et al., 2015). The basic zipper coupled tube in Chapter 4 belongs to both families, (i.e. they use a straight and developable surface). The generalized approach used in this chapter, makes use of the first family, where we use an arbitrary coupling surface (defined by ϕ_Z and ϵ). We then enforce symmetry on the top and bottom of the structure by limiting the cross-section and projection variations (i.e. $\phi_{YT} = -\phi_{YB}$ and $\theta_T = -\theta_B$).

5.3.1 Verifying folding kinematics with eigenvalue analyses

The kinematics of folding an origami vertex with four fold lines can be computed using analytical approaches (Huffman, 1976; Hull, 2012; sarah-marie Belcastro and Hull, 2002b,a) or numerical methods (Tachi, 2009c; Schenk, 2011) (see Section 3.3.1). Subsequently the folding of the entire system can be performed by changing a fold angle in one vertex, calculating

the other angles in the vertex, and cycling through the adjacent vertices of the fold pattern until all fold angles, and the new geometric shape are calculated. These methodologies can be used for rigid foldable sheets or tubes where the initially flat panels remain flat throughout the folding sequence, and deformation occurs only by rotation along the fold lines. An issue that arises with some of these approaches is that they cannot detect if a system is not rigidly foldable and may thus give misleading results from a folding simulation. For example, they may simulate a folding motion where the panels stretch or bend and are not noticed graphically by the user. Also, these analytical approaches are not typically suited to capture fold reversal where a fold may switch from a mountain to a valley fold.

In this chapter, we perform all of the kinematic folding using an eigenvalue approach suggested by Schenk (2011) and discussed in more detail in Section 3.3.1. With the eigenvalue approach we can check different origami structures if they are rigidly foldable as we perform the folding simulation. Although eigenvalue analysis cannot guarantee the rigid foldability of the system it can determine the number of (infinitesimal) rigid folding motions and can capture reconfiguration in the tubes.

We perform an eigenvalue analysis of the individual tube or the coupled tube system and can detect if the system is rigid foldable based on the magnitude of the eigenvalues. For these analyses we set the stiffness of fold lines to be 10^{-6} the stiffness of the panels. We evaluate the systems with no constraints and explore the seventh eigenvalue which is the first to engage the elastic deformations of the system. If the seventh eigenvalue (λ_7) is low ($<\approx 10^{-4}$), the system is rigid foldable and deformation occurs only at the fold lines. However if λ_7 is relatively high ($>\approx 10^{-1}$) the eigenmode deformation also engages the panels in bending, stretching and/or shear.

In Figure 5.5, we show the eigenvalues and eigenmodes of six different coupled tube structures. Three of the coupled systems are straight tubes and three are curved tubes. The eigenvalue analyses show that the straight tubes are foldable regardless of the cross-section and the projection angle. The seventh eigenvalues for these cases are six orders of magnitude lower than the eight eigenvalue ($\lambda_7 << \lambda_8$). From the curved origami cases, only one case is rigid foldable, while in the two other cases the seventh and eight eigenvalues have magnitudes that are only two orders of magnitude apart. The example verifies that relative symmetry is needed between the top and bottom tube if the system is to be curved and

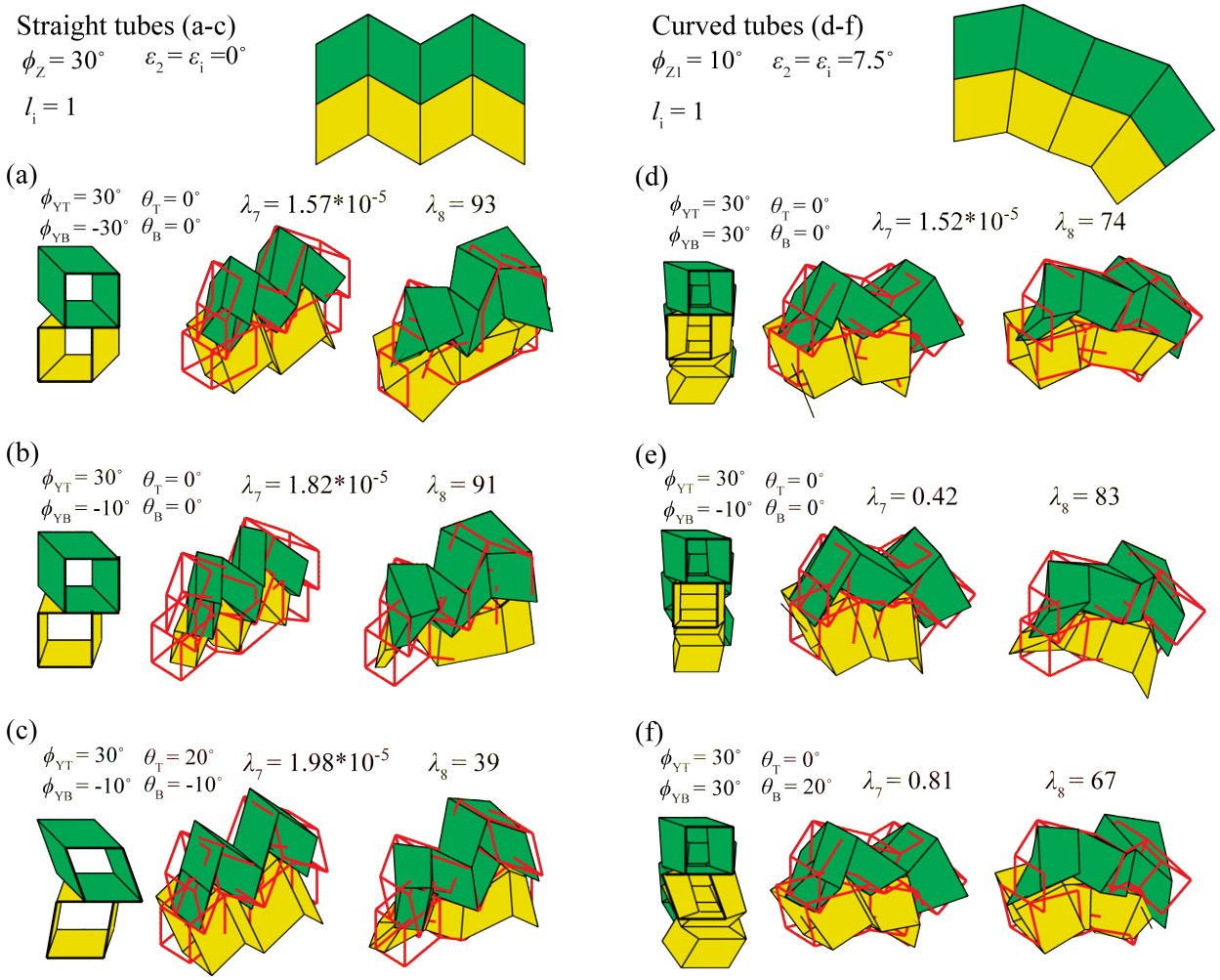

Figure 5.5: Eigenvalues and eigenmodes of coupled origami tubes. Low eigenvalues ($<\approx 10^{-4}$) represent rigid folding motions of the origami, while high ones ($>\approx 10^{-1}$) represent bending and stretching of the origami sheets. Each subfigure contains a schematic cross-section, definition parameters, isometric view, eigenmode 7 and eigenmode 8. (a-c) straight origami tubes. (d-e) curved origami tubes. (a and d) Equivalent top and bottom projection and cross-section. (b and e) Equivalent top and bottom projections, but different top and bottom cross-sections. (c) Different top and bottom cross-sections, and different top and bottom projections. (f) Equivalent top and bottom cross-sections, but different top and bottom projections.

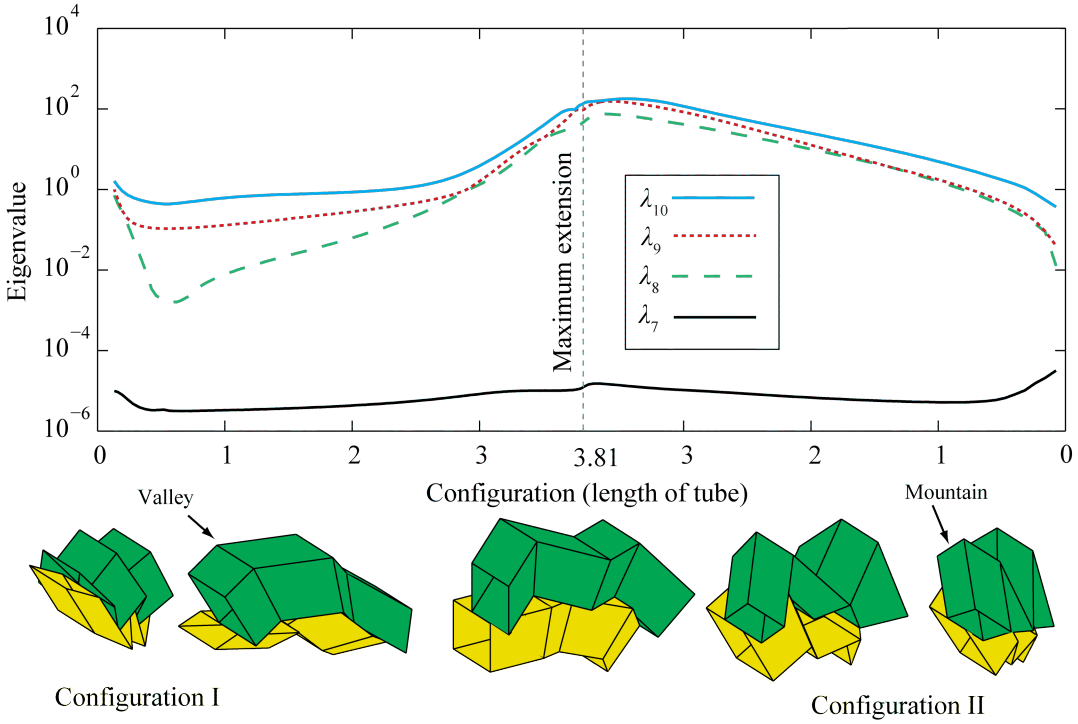

Figure 5.6: Eigenvalues of coupled curved tube with respect to length of the system (measured at the coupling surface on the two farthest ends). The configuration is represented as the tube length, and we use both an increasing and decreasing horizontal axis to represent the reconfiguration of the tube structure. When the tube reaches a maximum length at 3.81 the top and bottom folds switch from mountain to valley folds and the structure folds down.

rigid foldable. We have verified that zipper tubes where $\phi_{YT} = -\phi_{YB}$ and $\theta_T = -\theta_B$ are rigid foldable however, non-symmetric curved zipper cases where $\phi_{YT} \neq -\phi_{YB}$ or $\theta_T \neq \theta_B$ are not rigid foldable. The verification with eigenvalues presented here is not a proof of the kinematic compatibility between these systems. More thorough studies on the kinematics would be needed to prove these cases and to show other possible coupling variations beyond what is presented here and in Tachi et al. (2015).

5.3.2 Reconfiguration kinematics of generalized tubes

Having verified the rigid foldability of the origami tubes, we can also use the eigenvalues to perform the finite folding motion and reconfiguration of the coupled origami. In Figure 5.6, we show the folding sequence along with the eigenvalues versus configuration for the origami tubes shown in Figure 5.5(d). Because the seventh eigenvalue does not increase drastically,

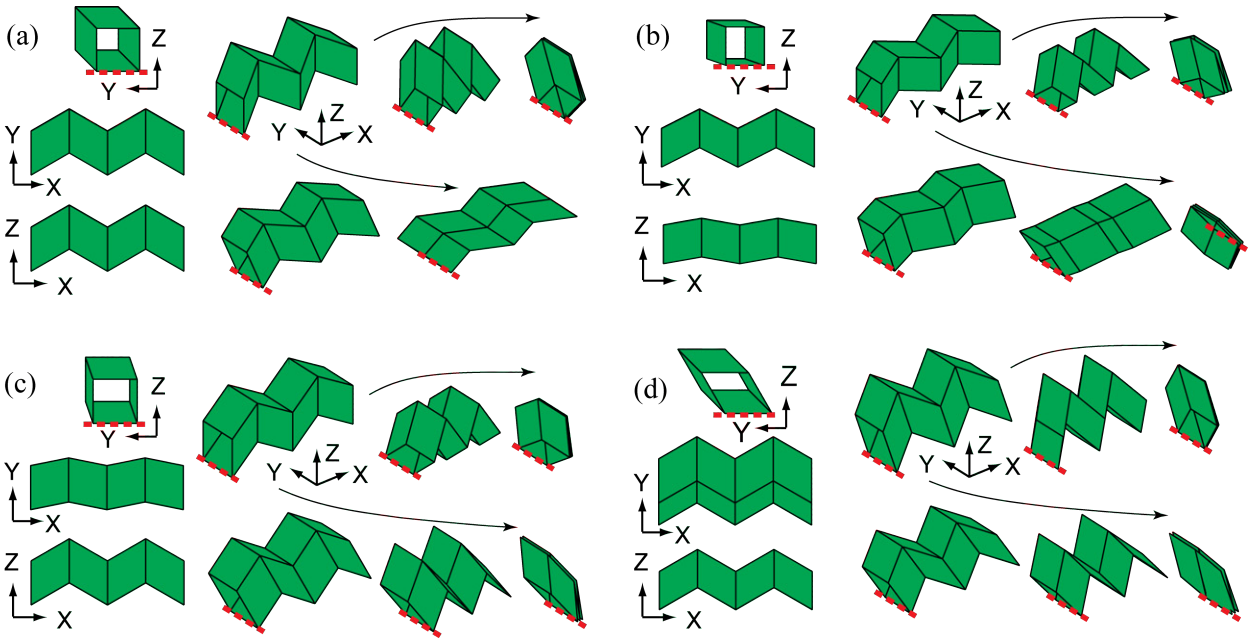

Figure 5.7: Initial geometries (left) and folding kinematics (right) of different rigid foldable tubes. A thick dotted line parallel to the Y axis is shown as a reference for all configurations. (a) Tube created with $\phi_Z = \phi_Y = 30°$ and a square cross-section. This tube is partially developable and flat foldable. Tubes shown in (b) - (d) are not partially developable, but are flat foldable and can fold down through two different kinematic motions. (b) Tube with $\phi_Z = 10° < \phi_Y = 30°$; the tube reconfigures when the fold on the top and bottom surface change from mountain to valley folds. (c) Tube with $\phi_Z = 30° < \phi_Y = 10°$; the tube reconfigures when folds on the sides change from mountain to valley folds. (d) Tube with $\phi_Z = \phi_Y = 30°$ and a rhombus cross-section ($\theta = 30°$), this tube follows kinematics similar to (c).

the system does not become significantly stiffer or more difficult to fold. In other words, it can fold through the entire sequence and does not cease to be rigid foldable.

Figure 5.6 shows the eigenvalues of the structure for the entire folding sequence of the tube, which involves (1) an extension to full deployment - Configuration I, (2) a *switching* reconfiguration at a full deployment length of 3.81, and (3) another extension through which the system can retract - Configuration II. The reconfiguration in this structure occurs when the top and bottom sheets reach their full extensions, at this point the top and bottom folds *switch* from being mountain to valley folds and vice versa. The structure can follow two distinct folding paths and we can also note that the eigenvalues change somewhat for these two folding paths. We discuss the influence that each of these folding motions have on the structural stiffness characteristics in Section 5.5.1.

The folding kinematics and reconfiguration characteristics of the coupled tubes is directly influenced by the characteristics of each of the two coupled tubes. It is useful to investigate the kinematics of individual tubes first to understand how the geometric definitions affect the global kinematics. In Figure 5.7 we show the kinematics of four origami tubes with different projection angles and cross-sections. When a square cross-section is used with $\phi_Y = \phi_Z$ we create a partially developable tube that can fold into a fully deployed and flat state in the $X - Y$ axis (bottom right of Figure 5.7(a)). This tube has only one folding sequence that preserves the tubular shape. When the tube reaches the completely flattened state in the $X - Y$ axis the tube can reconfigure, but the system can reconfigure into multiple different folding motions similar to a basic Miura-ori pattern (see Figure 3.5). Tube variations created with the projection methodology that are not partially developable cannot reach a flat state in the $X-Y$ plane (see (b)-(d) in Figure 5.7). However, these non partially developable tubes also have the reconfigurable type of kinematics observed in Figure 5.6 where the structure can extend and retract through two different motions.

Origami tubes with square cross-sections and $\phi_Z < \phi_Y$ reconfigure with the top and bottom fold lines switching (Figure 5.7(b)). On the other hand, tubes with square cross-sections and $\phi_Z > \phi_Y$ reconfigure with the side fold lines switching (Figure 5.7(c)). Changing the cross-section also influences the global kinematics in similar ways, with an increase in θ tending towards side folds switching (Figure 5.7(d)), and a decrease in θ tending towards top/bottom folds switching. The projection and cross-section effects can counteract each other and it is possible to construct a partially developable tube with $\phi_Z < \phi_Y$ and $\theta > 0$. For example, one of the folded configurations in Figure 5.7 (a) could be the initial geometry of a tube (defined with $\phi_Z < \phi_Y$ and $\theta > 0$)

5.3.3 Reconfiguration kinematics of coupled tubes

When two tubes are coupled, it is possible to have different types of reconfiguration occur with either one or both of the tubes reconfiguring. The deployment sequence and kinematic properties are determined by the geometry of each tube's projection and cross-section. The coupled tubes reconfigurations have many of the same characteristics as those shown in Figure 5.7. If we assume that the cross-sections of both tubes are square, then possible

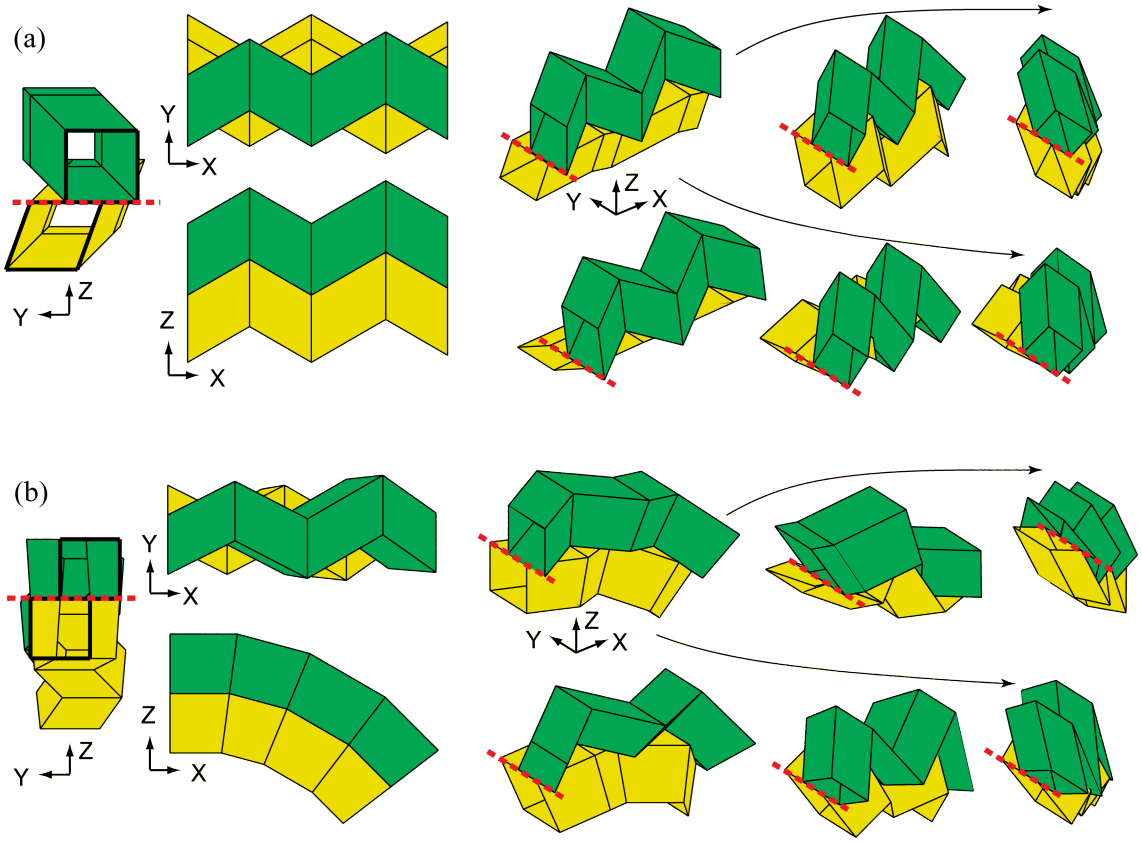

Figure 5.8: Initial geometries (left) and folding kinematics (right) of two zipper coupled tubes. A thick dotted line parallel to the Y axis is shown as a reference for all configurations. (a) Straight zipper tube with $\phi_{YT} = -\phi_{YB} = -30°$; $\phi_Z = 30°$; $\theta_T = 0°$ and $\theta_B = -20°$. Because of the rhombus cross-section, the side folds of the bottom tube switch leading to two different folding motions (similar to Figure 5.7 (d)). (b) Non-straight tube with $\phi_{YT} = -\phi_{YB} = 30°$; $\phi_Z = 0°$; $\theta_T = \theta_B = 0°$; $\epsilon_2 = \epsilon_3 = \epsilon_i = 7.5°$. Because $\phi_Z < \phi_Y$ the top and bottom folds can switch leading to two different folding motions (similar to Figure 5.7 (b)). The length of the projections for both zipper tubes is not constant: $l_1 = l_2 = l_4 = 1$ and $l_3 = 1.2$.

reconfiguration kinematics can be grouped into four categories:

1. No switching - $\phi_Z = \phi_{YT} = -\phi_{YB}$ - When all projection angles are equivalent (or negative and equal magnitude) both tubes are partially developable and the system can reach a flat state in the $X - Z$ plane (same as Figure 5.7 (a)).

2. Top/bottom folds switch - $\phi_Z < \min(\phi_{YT}, -\phi_{YB})$ - If the Z projection is the smallest of the three, then the top and bottom folds of both tubes reconfigure (see Figure 5.8 (b)).

3. Side folds of one tube switch - $\phi_{YT} < \min(\phi_Z, -\phi_{YB})$ or $-\phi_{YB} < \min(\phi_Z, \phi_{YT})$ - If one tube has a Y projection smaller than the Z projection, the side folds of the tube with the smallest Y projection will reconfigure (see Figure 5.8 (a)).

4. Side folds of both tubes switch - $\phi_{YT} = \phi_{YB} < \phi_Z$ - Both tubes have equivalent Y projection angles (or negative and equal magnitude), each tube can reconfigure independently at its side folds when the system reaches a fully deployed state.

The kinematics of two common coupled tube cases are shown in Figure 5.8. When the cross-sections are changed into rhombuses the switching cases remain the same as the four discussed above, but the projection angles alone would not determine the case. For tubes that have curvature, it is possible to have multiple cases occur over the length of the tube. The tube shown in Figure 5.8 (b) has a curve with all top and bottom folds reconfiguring simultaneously. If the curvature of the system is varied, it is possible that only one portion of the tubes' folds would be able to flatten (in a position for a switch). Such a tube would only have one folding motion.

5.4 Stiffness of tube variations

In this section, we evaluate the tube stiffness using static analyses to evaluate the influence of the tube geometry. We use the N5B8 model introduced in Chapter 2 with the stiffness characteristic enhancements introduced in Chapter 3. We use arbitrary dimensions and material properties that are within a realistic range. For most of the dimensions of the origami structures we use unit dimensions (1), for example the cross-sections and projection dimensions are 1. The thickness of the material is defined as $t = 0.01$ such that the length to

thickness ratio is generally $L/t \approx 100$. We use an arbitrary elastic modulus of $E = 10^6$ and a Poisson's ratio of $\nu = 1/3$. The fold line stiffness is defined with a length scale parameter of $L^* = 4$ which would result in a panel to fold stiffness ratio of about $K_F/K_B \approx 1/5$ (similar to a length scale of $L^* = 120$ mm for the 30 mm panels in Figure 2.13). All tubes investigated in this section are straight and have ten segment lengths of $l_1 = l_2 = l_i = 1$.

5.4.1 Static analysis of two coupled tubes

In the following static analyses, we investigate the bending characteristics of two coupled tubes using a three point bending test. We perform an analysis where the tube ends are closed off with thin sheet panels, and are thus restricted from folding. The coupled tube is supported on both ends, while it is free to expand lengthwise and orthogonally. A perpendicular load is applied at the middle of the tube in the Z direction, and a second test is performed in the Y direction. We distribute a unit load ($F_Z = 1$ or $F_Y = 1$) to the middle nodes of the beam, and we calculate the displacement in the direction of loading (Δ_Z and Δ_Y respectively). Subsequently, a representative stiffness of the structure for the Z direction can be calculated as $K_Z = F_Z/\Delta_Z = 1/\Delta_Z$.

In Figure 5.9, we show static analysis for three beams defined by the geometric properties discussed in Section 5.2.2. Two of the tube systems specifically correspond to the zipper and aligned tubes discussed in Chapter 4. The third tube is an intermediate beam where the top tube is the same, but the bottom tube has a shallower Y projection ($\phi_Y = -10°$). The deformed shapes, show that the aligned tubes have some squeezing type motions occurring, where the middle of the tube is unfolding and the entire system is elongating. The other two scenarios have more uniform deformed shapes. Although the folding and unfolding of the systems is restrained the squeezing likely has an influence on the structural stiffness.

The vertical (K_Z) and horizontal (K_Y) stiffness versus configuration of the structure, are shown in Figure 5.9 (d) and (e) respectively. The configuration of the tube is presented as the current length of the tube. When the aligned and zipper tube extend fully they lay flat in the $X - Y$ plane, reaching the maximum length of the flattened coupling surface (10 units). On the other hand, the intermediate tube can only reach a length of 8.9, at which point its side folds switch, and the structure retracts. This leads the system to have two

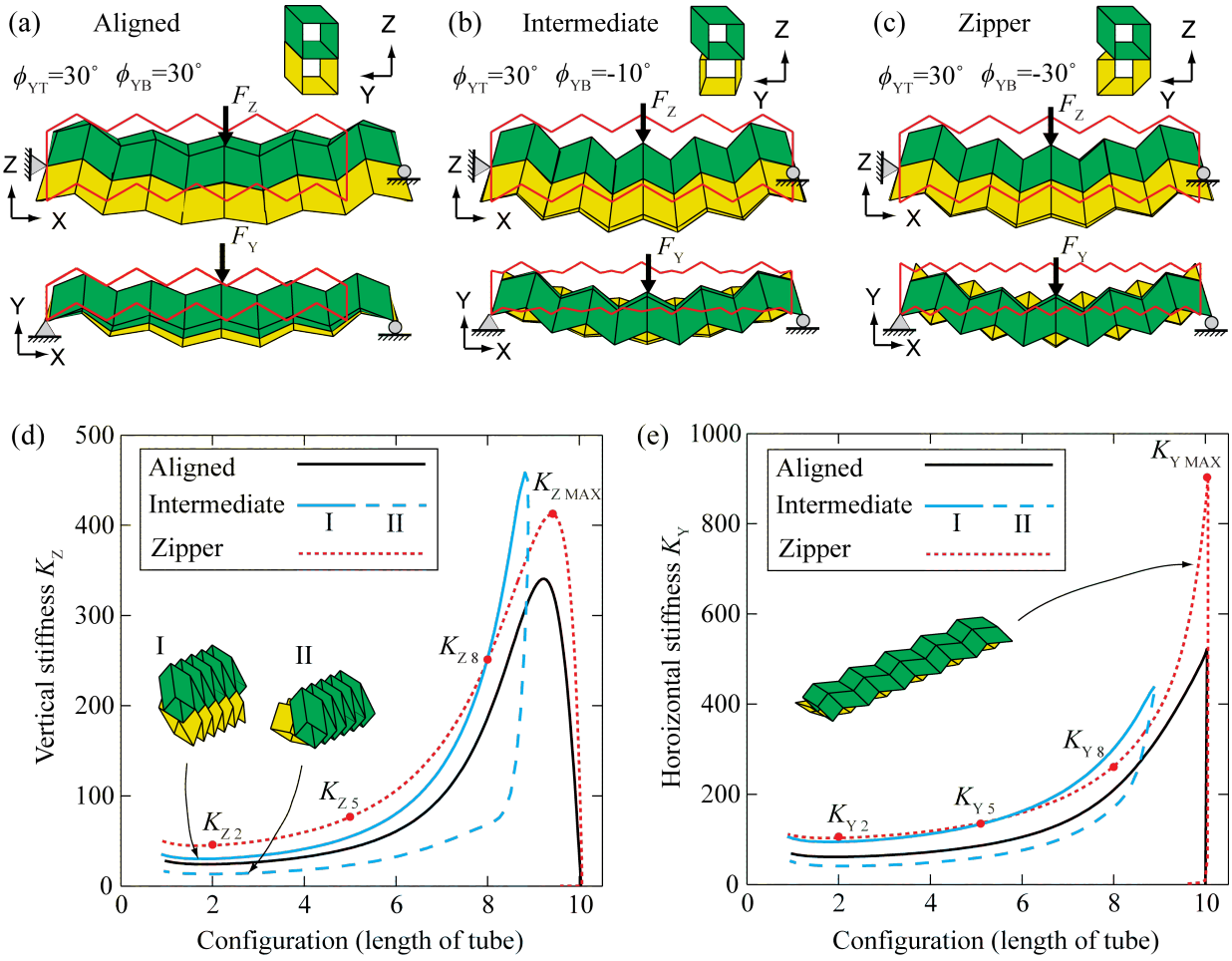

Figure 5.9: Static analysis of origami tube beams. Tubes are subjected to a three point bending test where the ends are restrained from folding and a load is applied in the middle of the beam . Initial (red outline) and deformed geometry for Y and Z direction tests of the (a) aligned ($\phi_{YT} = \phi_{YB} = 30°$), (b) intermediate ($\phi_{YT} = 30°$, $\phi_{YB} = -10°$) and (c) zipper tube ($\phi_{YT} = -\phi_{YB} = 30°$). The deformed shapes are scaled so that the maximum displacement is equal to the cross-section width (=1) and do not necessarily represent stiffness. (d) Stiffness in the vertical direction (K_Z) versus folding configuration (length of structure). The intermediate tube has a different stiffness for the two folding directions (I versus II). (c) Stiffness in the horizontal direction (K_Y) versus folding configuration (length of structure). Stiffness values of interest for the zipper tube are indicated (e.g. K_{Y5} horizontal stiffness at length 5).

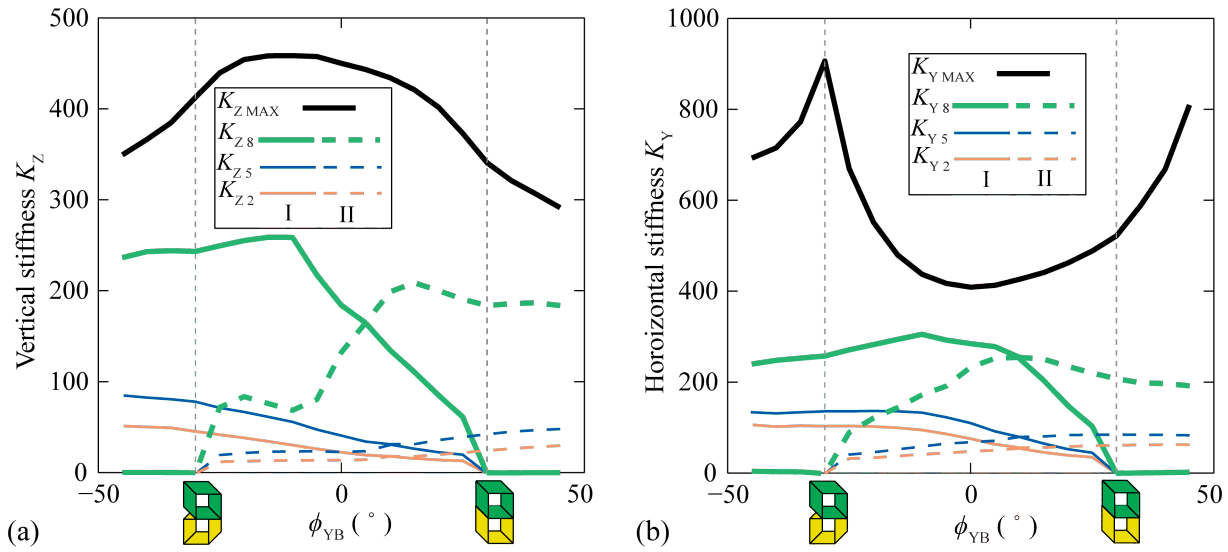

Figure 5.10: Influence of the bottom tube geometry on stiffness at different points of deployment. The vertical (a) K_Z and horizontal (b) K_Y stiffness are presented for different values of ϕ_{YB}, while ϕ_{YT} and ϕ_Z are kept constant. The peak stiffness (K_{MAX}) and stiffness at different points of the configuration are shown (e.g. K_{Y5} horizontal stiffness at length 5). The zipper coupled tubes with $\phi_{YB} \approx 30°$ have higher stiffness in Y and Z than other coupling geometries.

separate curves for stiffness, that each correspond to one of the folding sequences (I or II). In most scenarios the zipper coupled tubes had a higher stiffness than the other two tubes, except around the maximum extension of the intermediate tube. At that point the lower tube ($\phi_Y = -10°$) has a square cross-section and is able to brace the structure in both directions.

To more generally compare different structures we use points of interest on the stiffness curves for each direction of testing. For vertical stiffness analyses, we obtain the points K_{Z2}, K_{Z5}, K_{Z8}, and K_{ZMAX}, representing the stiffness at configuration lengths of 2, 5, 8, and the maximum vertical stiffness at any configuration. Figure 5.9 (e) shows that the maximum stiffness may at times provide misleading results. At a configuration length of 10 both the aligned and zipper tubes have a maximum horizontal stiffness (K_{YMAX}), but at this configuration the systems are flat in $X-Y$, and have no stiffness in the Z direction, so they may not be usable. Similarly, although the intermediate tube has the highest K_{ZMAX}, its vertical stiffness is about $1/4^{\text{th}}$ the stiffness of the zipper tubes when at configuration length of 2 in the II folding sequence.

In Figure 5.10, we use the stiffness points of interest for the tubes to compare the influence

of the lower tube projection angle (ϕ_{YB}). The projection angles $\phi_{YT} = 30°$ and $\phi_Z = 30°$ are kept constant while projection of the bottom tube ϕ_{YB} is changed. Overall, zipper type of coupling where $\phi_{YB} < 0°$ has a higher stiffness than the aligned coupled tubes where $\phi_{YB} > 0°$. The peak vertical stiffness is for an intermediate tube ($\phi_{YB} \approx -15°$), and the peak horizontal stiffness is for the zipper tube ($\phi_{YB} = -30°$). At intermediate points of deployment 2, 5, and 8, tube systems near the zipper configuration ($\phi_{YB} \approx -30°$) have high stiffens in both the Z and Y direction.

The stiffness of both deployment paths are shown in Figure 5.10. Typically the same path has a higher Z and Y stiffness, path I for the zipper type tubes and path II for the aligned type tubes. The higher stiffness folding sequence typically has more "open" tubes with a higher cross-sectional area and bending modulus (see Figure 5.9 (d)). In cases beyond the intermediate range $\phi_{YB} < -30$ and $\phi_{YB} > 30$, the top tube controls the maximum extension of the system as it flattens completely in the $X - Y$ plane. We only consider one path of deployment for these cases, however it is also possible to refold the system where the partially developable tube is folded in an accordion fashion. This second folding sequence would be substantially more flexible than the original.

Comparing Figure 5.10 (a) and (b), it is interesting that both the maximum and intermediate stiffness in the Y direction is typically higher than that in the Z direction. Typically one would expect a higher stiffness in the Z direction because the combined bending modulus of the two tubes is greater. However, as we noted earlier the maximum stiffness in the Y direction is often due to a case where system comes close to flattening and panels lie close to the $X - Y$ plane. At intermediate points, the coupling plane, as well as the corresponding top and bottom planes, are kept perpendicular to the $X - Z$ plane; these perpendicularly placed elements have high shear stiffness and thus increase the stiffness for loads applied in the Y direction.

In Figure 5.11, we show the effect of different projection definitions on the coupled tubes structural stiffness. For clarity, we only show the folding path that provides higher stiffness (i.e the maximum K_{Z5} from paths I and II is shown). We use the zipper tube as a base where $\phi_Z = \phi_{YT} = -\phi_{YB} = 30°$, and we use a variable ϕ_{VAR} to change different parameters in the the tube geometry. We use four different cases: **Case 1** - $\phi_{VAR} = -\phi_{YB}$ which varies the bottom tube projection, resulting in the same variation as shown in Figure 5.10; **Case 2**

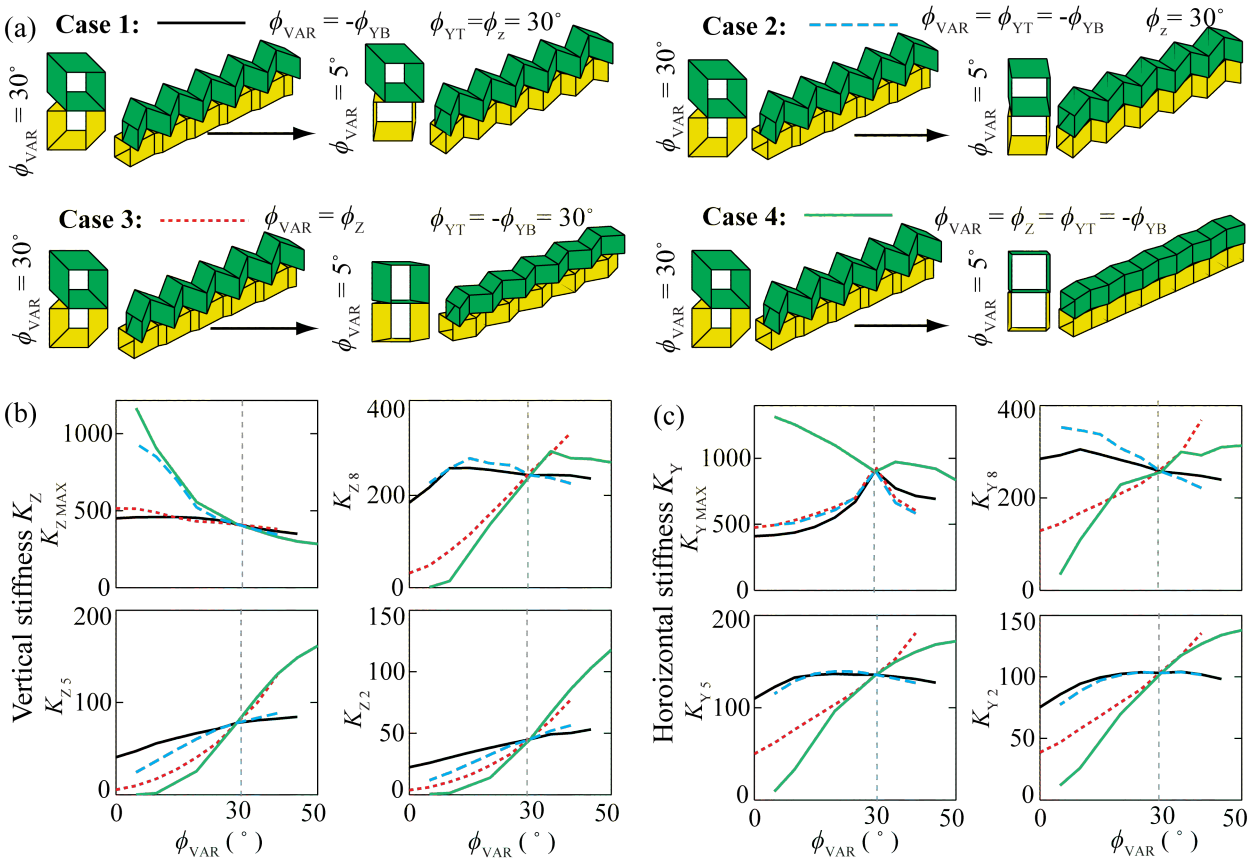

Figure 5.11: Influence of projection angles to the zipper tube stiffness. (a) Four cases that depict variations of the projection angles. Case 1 is the same as that presented in Figure 5.10 . A variable ϕ_{VAR} is used to vary a single or multiple projection angles for each case. For example, in Case 4 all projection angles are varied as $\phi_{VAR} = \phi_Z = \phi_{YT} = -\phi_{YB}$, thus these tubes are all partially developable. (b) Vertical stiffness presented as the peak stiffness (K_{ZMAX}) and at different points of the configuration (e.g K_{Z5} vertical stiffness at length 5). (c) Horizontal stiffness presented as the peak stiffness (K_{YMAX}) and at different points of the configuration (e.g K_{Y5} horizontal stiffness at length 5).

- $\phi_{VAR} = \phi_{YT} = -\phi_{YB}$, the top and bottom tubes' Y projections are varied symmetrically; **Case 3** - $\phi_{VAR} = \phi_Z$, only the Z projection of the coupling surface is varied; and **Case 4** - $\phi_{VAR} = \phi_Z = \phi_{YT} = -\phi_{YB}$, all projections are varied together, and the systems are always partially developable.

Figure 5.11 (b) shows that the maximum vertical stiffness (K_Z) can typically be increased by making the tubes more square and less zig-zaged (by reducing ϕ_{VAR}). This increase in especially pronounced in Cases 2 and 4 where as ϕ_{VAR} approaches zero, and the cross-sections have elements that lie close to the Z direction. However, as ϕ_{VAR} approaches zero the vertical stiffness at deployment configurations (especially lengths of 2 and 5) is significantly decreased. In other words, tubes that are more zig-zaged and have higher ϕ_{VAR} can have high vertical stiffness during the deployment sequence (e.g. Case 4 with $\phi_{VAR} > 30°$ at length 2). In horizontal direction the maximum stiffness occurs for tubes that can completely flatten in the $X-Y$ plane (i.e at $\phi_{VAR} = 30°$ and all tubes in Case 4). The horizontal stiffness during deployment follows similar trends to the vertical, where typically more zig-zaged tubes are stiffer.

5.5 Flat deployable beams and slabs

In this section, we investigate the zipper type tubes with the intention to make them better suited for practical applications. We explore the stiffness of beams that when fully deployed have a flat top. This property would be useful in creating deployable slabs, decks, walls, and other structures. Having a flattened surface could be aesthetically pleasing, and it would be functional for applications such as bridges or walkways. We perform the same type of three point bending analyses to evaluate the stiffness in the Y and the Z directions.

First, we investigate straight tubes defined with a Z projection of $\phi_Z = 0°$ with ten segment lengths of $l_1 = l_2 = l_i = 1$. The tubes are defined such that in their initial configuration they are fully deployed and have a flat top surface. Because the tubes are straight we have freedom to have non-symmetric top and bottom tube projections and cross-sections. We have verified that increasing the ϕ_Y projections can increase the stiffness during deployment (see Figure 5.11), so here we explore the influence of the cross-section variations. We keep the Y projections the same ($\phi_{YT} = -\phi_{YB} = 30°$), and vary the cross-section angles with a

parameter θ_{VAR}.

Figure 5.12 presents three cross-section variations: **Case 1** - $\theta_{VAR} = -\theta_B$, only the bottom tube cross-section is varied; **Case 2** - $\theta_{VAR} = \theta_T = \theta_B$, the top and bottom cross-sections are rotated in the same direction; and **Case 3** - $\theta_{VAR} = \theta_T = -\theta_B$, the top and bottom cross-sections are rotated in opposite directions, (appear mirrored about $Y-X$). All cross-section variations reduce the peak vertical stiffness (K_{ZMAX}) of the system, but they increase the stiffness during deployment. In particular, Case 3 substantially increases the vertical stiffness at intermediate deployment configurations. In the horizontal direction, Case 2 reduces the intermediate stiffness while Case 3 increases the stiffness for all deployment configurations. Case 3 where the tube cross-sections are rotated in opposite directions would likely be the best design alternative for slab type systems where a flat surface is needed. This system would provide a high orthogonal stiffness during deployment, and would not substantially reduce the peak vertical stiffness.

5.5.1 Influence of profile geometry on stiffness properties

In this section, we explore the influence of reconfiguration and profile geometry on the stiffness at various points of deployment. In Figure 5.13, we compare the stiffness and kinematics of three tubes with different Z projections and cross-section geometries (all tubes have the same Y projection $\phi_{YT} = -\phi_{YB} = 30°$). The first tube is a ***Zipper*** tube, identical to the tube presented in Figure 5.9 (c) - $\phi_Z = 30°$. The second case is a tube with a ***Flat*** top and square cross-sections - $\phi_Z = 0°$. The last case is a tube with a flat top and a ***Skewed*** cross-section - $\theta_T = -\theta_B = -30°$. The results for the second and third cases are presented as points on the graphs in Figure 5.12.

The kinematic motion of the three cases presented in Figure 5.13 are different. The zipper coupled tube does not reconfigure and follows essentially one continuous motion from a folded system in $Y-Z$ to a flattened system in $X-Y$. Over most of the motion the zipper tubes have a wide and deep profile (i.e. section view in $X-Z$). Due to this cross-section the structure typically has higher vertical and horizontal stiffness when compared to the other two structures.

The flat top system with a square cross-section is initially defined at a fully deployed

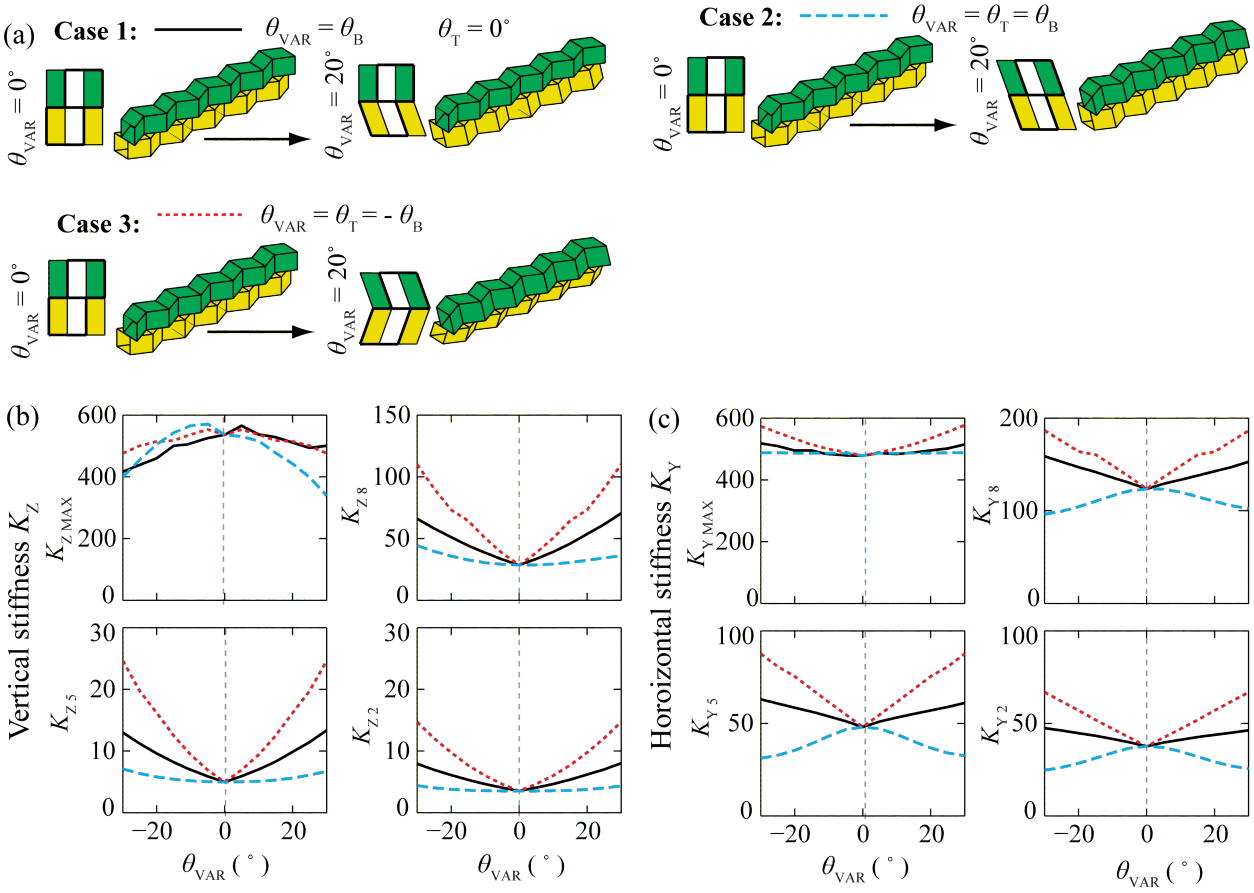

Figure 5.12: Influence of cross-section geometry on stiffness for zipper tubes where the top surface is flat ($\phi_Z = 0°$). (a) Three cases that depict variations of the cross-section angles. (b) Vertical stiffness presented as the peak stiffness (K_{ZMAX}) and at different points of the configuration (e.g K_{Z5} vertical stiffness at length 5). (c) Horizontal stiffness presented as the peak stiffness (K_{YMAX}) and at different points of the configuration (e.g (K_{Y5}) horizontal stiffness at length 5). Case 3 where the cross-section is mirrored about the Y axis presents a significant increase in stiffness during the deployment sequence.

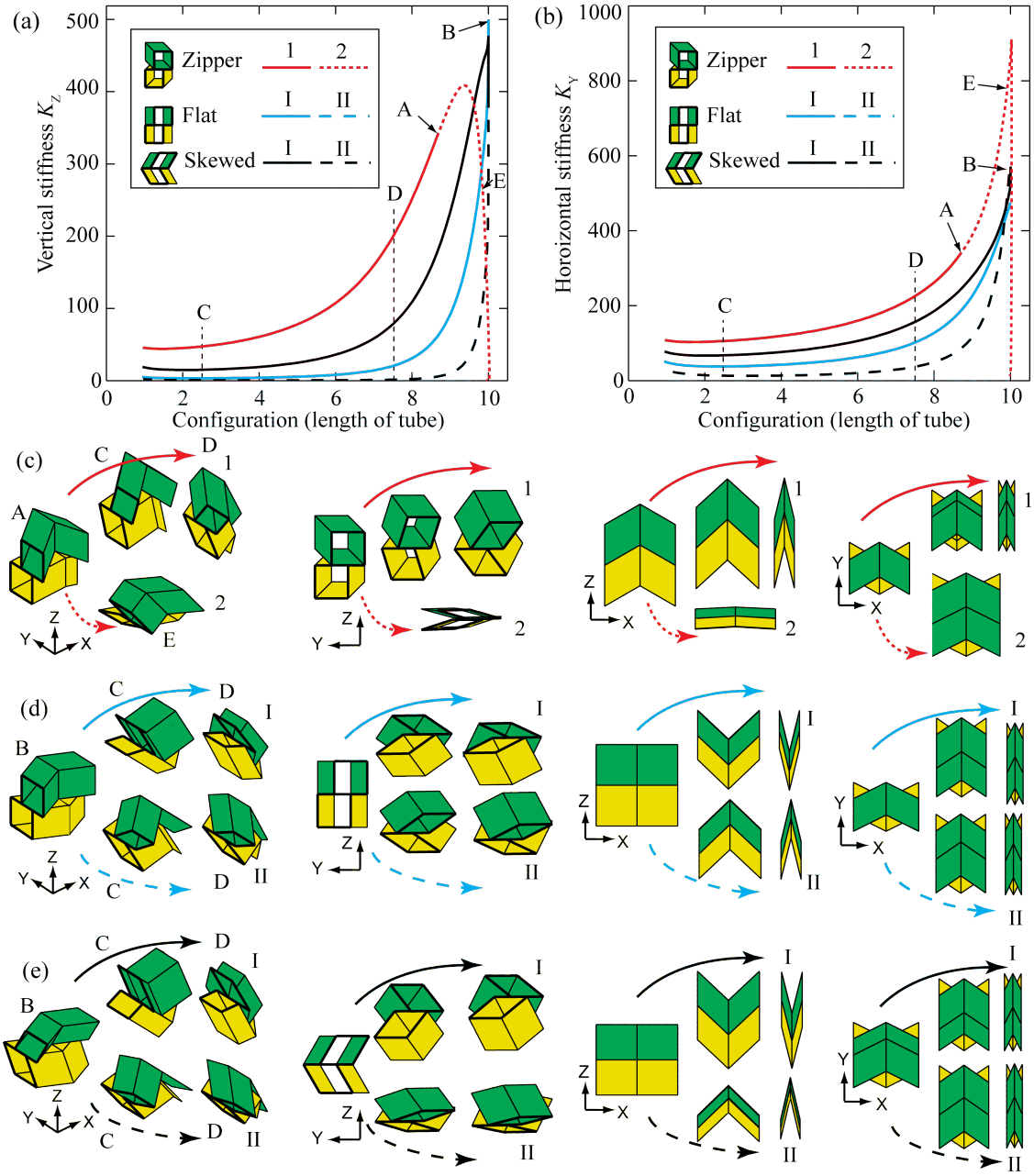

Figure 5.13: The influence of profile geometry on beam stiffness. *Zipper* coupled tubes ($\phi_Z = 30°$); tube with a *Flat* top and square cross-section; and a tube with a flat top and a *Skewed* cross-section ($\theta_T = -\theta_B = -30°$) are compared. The horizontal projection is the same for all three cases ($\phi_{YT} = -\phi_{YB} = 30°$). (a) Vertical and (b) horizontal stiffness of straight tubes with ten segment lengths. Solid and dotted lines are used to show the kinematic motion starting from the initial state. Isometric and section views depicting the motion of unit cells of (c) Zipper, (d) Square, and (e) Skewed tubes. The views are shown at initial configurations (A and B), as well as 2.5 (C), 7.5 (D), and 9.9 (E) deployment.

state. When fully deployed it has the highest vertical stiffness because the side panels are orthogonal to the applied load. The structure can retract in two symmetric motions. The vertical stiffness for these two motions is the same, and it is close to zero when the system approaches a stowed configuration (length ¡ 6). The profile (in $X - Z$) of the tube is more shallow than the zipper, and it approaches a triangular, accordion-like shape when stowed.

The skewed cross-section system has two different reconfiguration motions. Motion I has a deeper profile (in $X - Z$) and higher stiffness in both the horizontal and vertical directions. The profile through motion I deployment is deeper and wider than the tube with a square cross-section, however shallower than the zipper tube in the same configurations. Motion II has a narrow profile in $X - Z$ and low out-of-plane stiffness. Although the cross-section in the Y direction is deep (section $Y - X$ in Figure 5.13 (e)), the structure is flexible in the horizontal direction. This flexibility is because the structure can deform similar to a folding hand fan for Y direction loading (i.e. imagine moments in Z applied to the section in $X - Z$).

The observations from Figure 5.13 show that deeper profiles in the $X - Z$ direction lead to higher stiffness in both directions. This behavior can be explained by looking at the system as a three dimensional beam where a deeper section leads to a higher bending modulus. The deployable structures are stiffest when they are close to fully deployed. At deployed configurations their cross-sections are open and they behave like deep beams. When retracting all tubes become more flexible because their profile approaches more of a triangular wave and accordion-like shape. The narrow profiles and triangular geometry lead to lower bending stiffness. Finally, reconfigurable tubes (such as the skewed tube) can be designed to have one motion of high out-of-plane stiffness.

5.6 Roof systems from coupled tubes

In this section, we investigate the stiffness of different roof geometries that can span a distance and provide a clearance. First we compare three roof shapes and explore the influence of increasing clearance on total stiffness. In the next section, we explore arch systems and evaluate if changing the cross-sectional properties leads to similar effects as those observed for straight beams above.

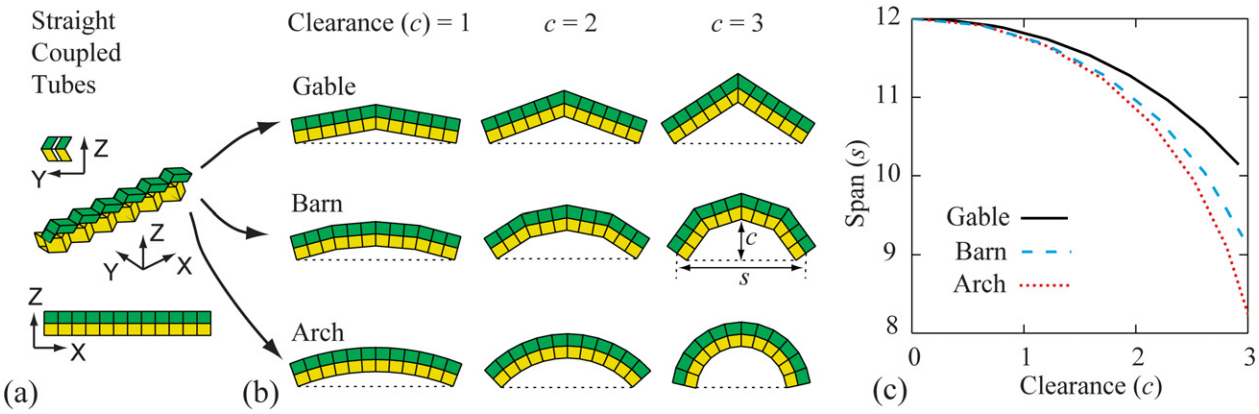

Figure 5.14: Geometry of different deployable roof structures. (a) Straight tube with a skewed cross-section that is used as an initial basis for the modified roofs. (b) Gable, barn (gmabrel), and arch roof structures shown with increasing clearance - c from left to right. (c) The clearance versus the span for the different structures. The length of the coupling surface is the same for all geometries and this leads to the different clearance to span relations.

We study gable, barn (gambrel), and arched shaped roof structures. All systems are created with an initially flat top (Z projection of $\phi_Z = 0°$) and with skewed cross-sections ($\theta_T = -\theta_B = -30°$). The tubes have twelve segments with a constant segment length of $l_1 = l_2 = l_i = 1$. The gable roof is constructed with two straight tube sections and with one cross-section rotation in the middle of the span ($\epsilon_7 \neq 0$). By increasing the cross-section plane rotation, we increase the clearance and reduce the span of the structure. The barn (gambrel) roof consists of four straight tube sections, with three equivalent plane rotations ($\epsilon_4 = \epsilon_7 = \epsilon_{10} \neq 0$). The arch is defined with the projection plane rotated equivalently over the length with $\epsilon_2 = \epsilon_3 = \epsilon_i$. Schematics and the span versus clearance relations for the three structures are shown in Figure 5.14.

We explore the stiffness of the roof structures using a three point bending test similar to that done in previous sections. The analysis is linear elastic and we only explore small deformations of the structures. In Figure 5.15, we show the vertical stiffness of the roof structures with respect to their deployment. Because all structures have different dimensions we show intermediate stiffness with respect to the maximum span dimension, for example $K_{Z1/4s}$ corresponds to the vertical stiffness when the deployment is at quarter span. For clarity, we do not show the horizontal stiffness because in practice multiple tubes will be sequentially coupled together and will have a high horizontal stiffness (see Section 5.6.2).

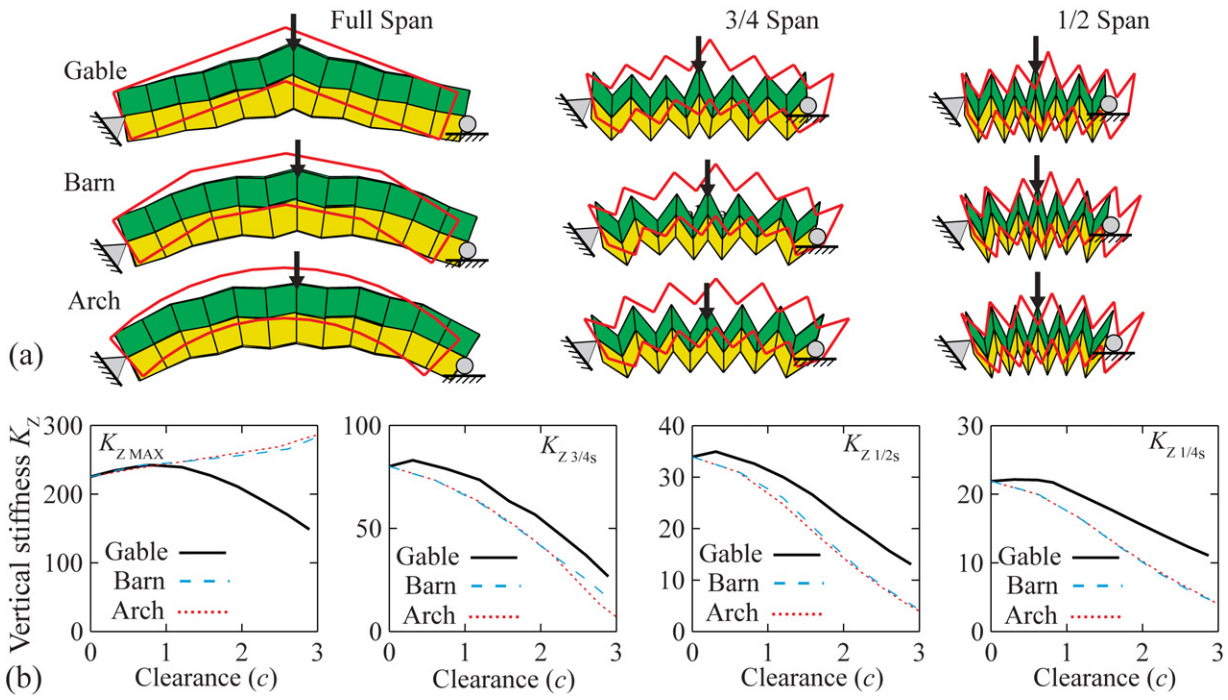

Figure 5.15: Static, linear elastic analysis of the gable, barn (gambrel), and arch roofs. (a) Deformed shapes for the three roofs with a clearance of two (2) shown at configurations of full span, three quarters span, and half span. Initial shape is shown with a red outline, and deformed shapes are scaled so that the maximum displacement is equal to one twelfth of the span ($s/12$) and do not necessarily represent stiffness. (b) Vertical stiffness of the roof structures shown with respect to the clearance - c. The dimensions of the structures change with increasing clearance, thus stiffness is shown at different configurations defined as portion of span (i.e. K_{ZMAX} - peak stiffness - typically at full span; stiffness at three quarters span $K_{Z3/4s}$; at half span $K_{Z1/2s}$; at quarter span $K_{Z1/4s}$. Peak stiffness increases for the barn and arch roof as they become more curved (higher clearance), however the intermediate stiffness decreases for clearence for all cases.

As the clearance of barn and arch systems is increased they have a higher maximum vertical stiffness K_{ZMAX}. This increase is likely because the curved geometry better distributes the in-plane loads from the load to the support. Curved geometries are well known to be efficient at carrying vertical loads between two supports (e.g. Tyas et al. (2011)). When loaded at a fully deployed state the structures experience a spread with the two ends moving apart. If both ends are fixed, the maximum stiffness would likely be much greater. The gable has a lower peak stiffness for a clearance higher than about 1, this may be due to the observed spreading behavior.

All three roof systems have a peak stiffness near their full deployment, and the vertical stiffness is much lower in intermediate deployment stages (similar to the behavior of straight tube structures). In the intermediate deployment stages the vertical stiffness decreases with increased clearance. We believe this effect to be similar to the influence of cross-section changes discussed in Section 5.5.1. The curved geometry leads to a more accordion-like geometry during deployment. The gable roof tends to have a higher stiffness during deployment, this is likely because the cross-section projection is only rotated in one point. In practice, the gable geometry presented here may pose problems as high stress concentrations would develop at the apex of the gable.

5.6.1 Cross-sectional influence on curved arch stiffness

In this section, we explore the influence of cross-section geometry on the stiffness of the curved arch structure. The arch is defined as before with the projection plane rotated equivalently over the length with $\epsilon_2 = \epsilon_3 = \epsilon_i = 4°$. We use twelve equal segment lengths of $l_1 = l_2 = l_i = 1$, and thus the structure makes approximately a quarter circle. The tubes are defined such that in their initial configuration they are fully deployed and have a flat top surface (the surface is curved, but all folds are mountain and are equivalent thus we classify it as flat). Because the tubes are curved the projections and cross-sections need to be defined as $\phi_{YT} = -\phi_{YB}$ and $\theta_T = -\theta_B$.

In Figure 5.16 we show the stiffness analysis of two different arches. Arch A has square cross-sections and shallow projections ($\phi_{YT} = -\phi_{YB} = 20°$), on the other hand, Arch B has sharper projections and skewed cross-sections. Both arches can fold and unfold through

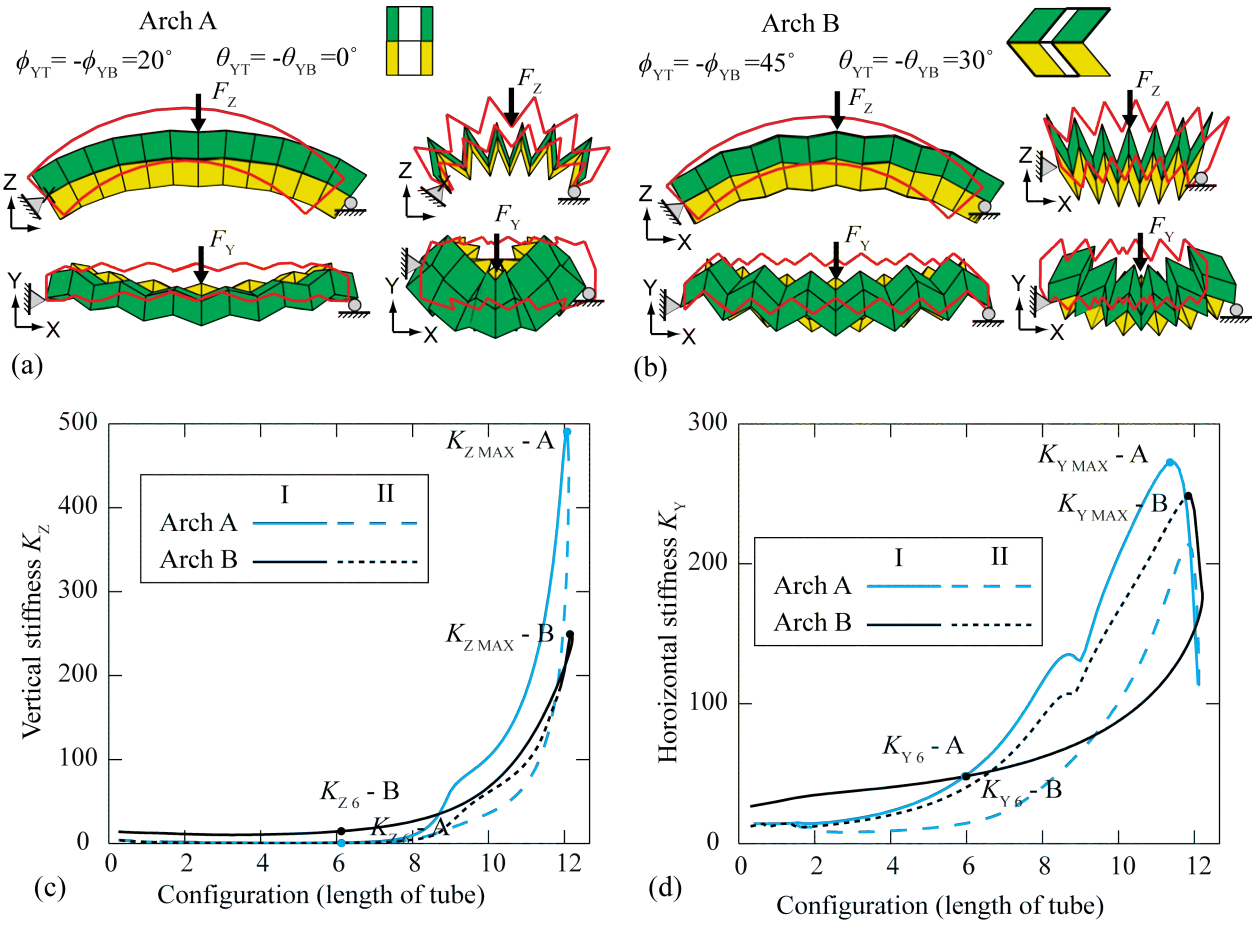

Figure 5.16: Static, linear elastic, small deformation analysis of arched tubes. The arches are shown at both fully deployed states and at a configuration of length 6. Initial (red outline) and deformed geometry for Y and Z direction tests of the (a) Arch A ($\phi_{YT} = -\phi_{YB} = 20°$ and $\theta_T = -\theta_B = 0°$), (b) Arch B ($\phi_{YT} = -\phi_{YB} = 45°$ and $\theta_T = -\theta_B = -30°$). The deformed shapes are scaled so that the maximum displacement is equal to the cross-section width (=1) and do not necessarily represent stiffness. (d) Stiffness in the vertical direction (K_Z) versus folding configuration (length of structure). (c) Stiffness in the horizontal direction (K_Y) versus folding configuration (length of structure). Stiffness values of interest for the two tubes are indicated (e.g. K_{Y6} horizontal stiffness at length 6).

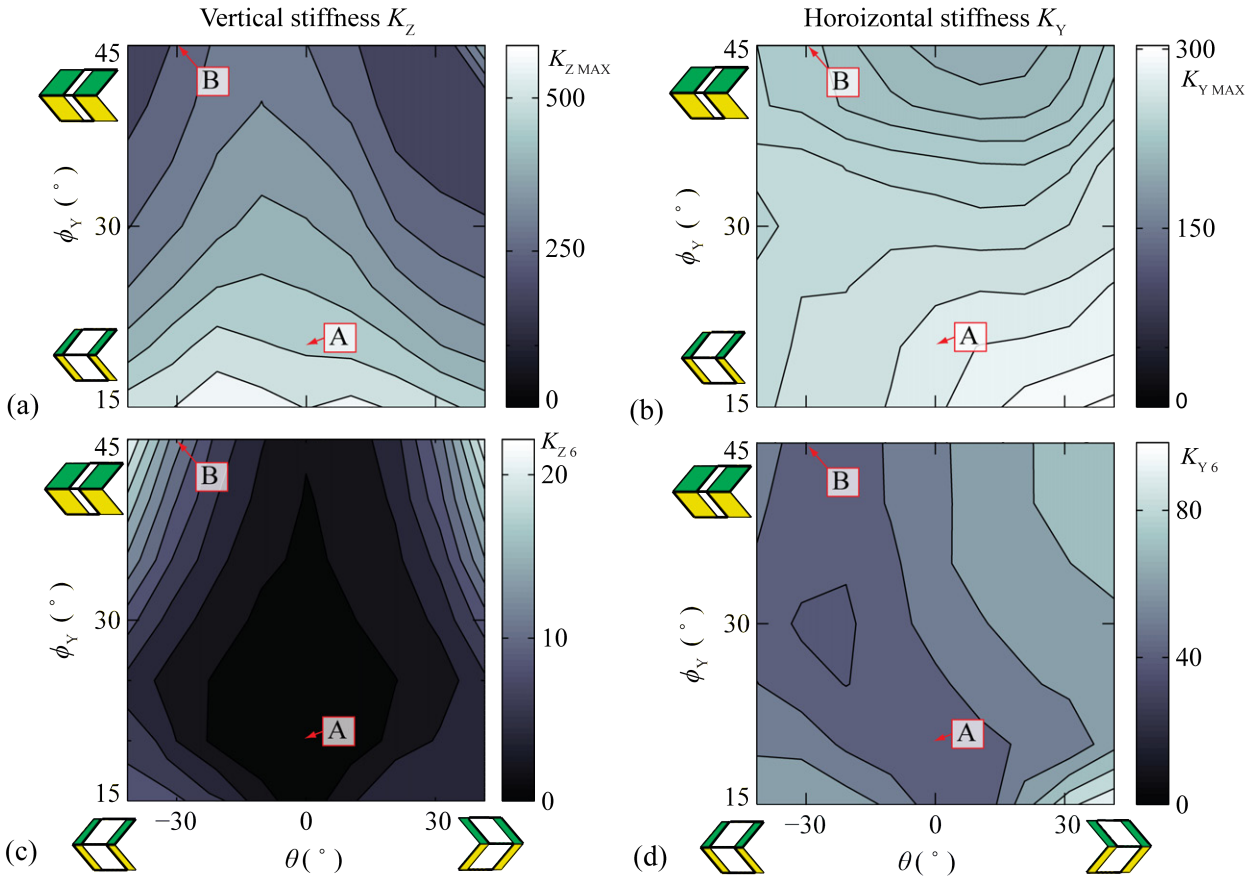

Figure 5.17: Influence of projections and cross-section geometry on stiffness for arched tubes where the top surface is flat ($\phi_Z = 0°$). The maximum stiffness and stiffness at a configuration of 6 are shown with respect to the cross-section rotation ($\theta = \theta_T = -\theta_B$), and the projection angle ($\phi = \phi_{YT} = -\phi_{YB}$). (a) K_{ZMAX}, (b) K_{YMAX}, (c) K_{Z6} (d) K_{Y6}. The magnitude of stiffness is shown using colorbars. Results on the stiffness of arch cases A and B discussed in Figure 5.16 are pointed out in the plots.

two different motions, and each motion has a different stiffness. The vertical stiffness of both systems reaches its maximum at the fully deployed state, and Arch A with the square cross-section has a substantially higher K_{ZMAX}. However, Arch A and one of the motions of Arch B have virtually no vertical stiffness during deployment. We measure the stiffness at an extension length of 6 (K_{Z6} and K_{Y6}). The deformed shapes of the stiffer configuration at an extension length of 6 are shown for the two arches in Figure 5.16 (a) and (b). Note that during deployment Arch B has a much deeper section and thus a higher stiffness.

Stiffness results for different projections and cross-sections are shown in Figure 5.17. The results from Arch A and Arch B are pointed out on the plots. The horizontal stiffness is not

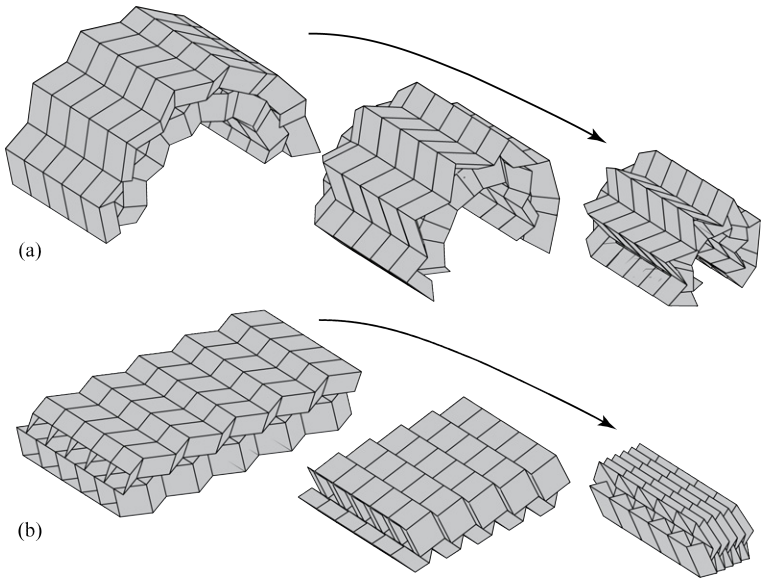

Figure 5.18: (a) Canopy system from repeated arches, and (b) Slab system from coupled and repeated tubes.

significantly influenced by the cross-section or projection. The maximum vertical stiffness (K_{ZMAX}) is high for square cross-sections with a less zig-zagged projection. However, higher stiffness during deployment can be achieved with rhombus cross-sections and more zig-zagged projections.

5.6.2 Continuous coupled systems

The coupled tube systems can be repeated in the Y direction without restricting foldability. By repetition, we can create slabs, decks, and canopy systems that are continuous and consist of multiple tubes in Y. With this additional bracing, the horizontal stiffness (K_Y) of the repeated tube systems would be much higher than discussed above. However the vertical stiffness would not be significantly increased. Therefore, to create slab and canopy systems that are stiff throughout their deployment, higher projection angles (more zig-zag) and rotated rhombus cross-sections should be used. In Figure 5.18 we show a concept of a deployable canopy and slab structures.

5.7 Concluding remarks

In this chapter, we provide a generalized framework for creating coupled origami tubes. We use an approach where a cross-section is projected onto corresponding projection surfaces. The framework allows for the construction of both straight and curved tubes that can have segments of different lengths, and their cross-sections can be varied. Depending on the cross-section projection properties the tubes could be partially developable meaning that parts of them could be made by folding a flat sheet. While other tubes could be reconfigurable meaning that they can deploy and retract through two different motions. The folding motions have different kinematics and could influence the stiffness of the tubes.

We explore the orthogonal stiffness of the coupled tubes by performing three point bending tests. We find that zipper coupled tubes have higher bending stiffness than aligned tubes, as was expected from Chapter 4. Tubes that are straighter and have square cross-sections typically have a higher maximum bending stiffness. However, these tubes are flexible during their deployment. Alternatively, tubes that are more zig-zagged and have rhombus cross-sections can have higher bending stiffness during their deployment at the cost of a slightly reduced maximum stiffness. These behaviors are also true for tube system that can deploy into a beam or slab with a flat top. For the flat top systems to maintain a high out-of-plane stiffness during deployment, the tubes need to have skewed cross-sections. We explore the stiffness of roof structures with a clearance including shapes of gable, barn (gambrel), and arch roofs. If constructed with a high clearance (higher curvature) the barn and arch systems have a high peak stiffness but reduced intermediate stiffness. Finally, we show that the coupled tube structures can be repeated sequentially to create slab or larger arched canopy structures.

CHAPTER 6

ORIGAMI TUBES WITH RECONFIGURABLE POLYGONAL CROSS-SECTIONS

In this chapter, we introduce and explore origami tubes with polygonal, translational symmetric cross-sections, that can reconfigure into numerous geometries. The tubular structures satisfy the mathematical definitions for flat and rigid foldability, meaning that they can fully unfold from a flattened state with deformations occurring only at the fold lines. The tubes do not need to be straight, and can be constructed to follow a non-linear curved line when deployed. *The cross-section and kinematics of the tubular structures can be reprogrammed by changing the direction of folding at some folds.* We discuss the variety of tubular structures that can be conceived and we show limitations that govern the geometric design. We quantify the global stiffness of the origami tubes through eigenvalue and structural analyses and highlight the mechanical characteristics of these systems. The two-scale nature of the present work indicates that, from a local viewpoint, the cross-section of the polygonal tubes are reconfigurable while, from a global viewpoint, deployable tubes of desired shapes are achieved. This class of tubes has potential applications ranging from pipes and micro-robotics to deployable architecture in buildings.

6.1 Introduction

Historically, origami has gained popularity in science and engineering because a compactly stowed or flat system can be folded into a transformable 3D structure with increased functionality. Folding structures can have practical applications ranging in scale and discipline from biomedical devices to deployable architecture. More recently, innovation with origami has pivoted on its capability to create programmable and re-programmable systems that can change shape, function, and mechanical properties. For example, Hawkes et al. (2010) created a sheet with pre-defined fold lines that can reshape autonomously into different three dimensional structures. Marras et al. (2015) showed that DNA can be folded to create nano-scale mechanisms with programmable mechanical function. Origami metamaterials that can be reconfigured, and whose mechanical properties can be tuned and tailored have also be-

come a popular subject of study (Fuchi et al., 2012; Schenk and Guest, 2013; Silverberg et al., 2014; Filipov et al., 2015a).

Thin walled origami tubes have been created by folding thin sheets, but they typically differ from the fundamental definitions of origami. In particular: entire origami tubes are not *developable*, meaning they cannot be created from a continuous flat sheet; and they require gluing or some other connectivity for creating the complete tube. Despite the higher complexity of manufacturing, origami tubes greatly extend the functionality of engineered thin sheet structures. For example, they can be be used as deployable stents in biomedicine (Kuribayashi et al., 2006), as inflatable structural booms for space structures (Schenk et al., 2013, 2014a), or as actuators and bellows (Martinez et al., 2012; Yasuda et al., 2013; Francis et al., 2014). Origami tubes have a self-constraining geometry that makes them suitable for energy absorption devices (Song et al., 2012; Ma et al., 2013; Ma and You, 2013; Gattas and You, 2015b). Stacking and coupling of origami tubes into more complex geometries can lead to stiffening of the system and enhanced mechanical characteristics (Schenk and Guest, 2013; Cheung et al., 2014; Filipov et al., 2015a; Li and Wang, 2015).

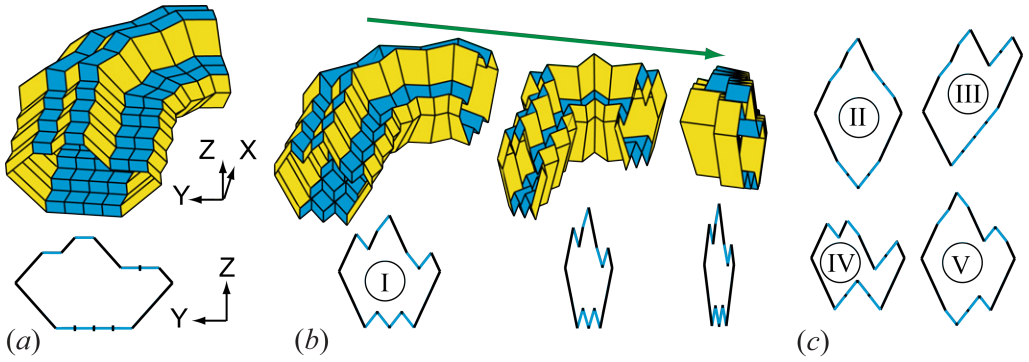

Figure 6.1: A reconfigurable origami tube with a polygonal cross-section. (a) The tube and cross-section shown at a fully extended state. (b) Folding sequence of the tube, where the cross-section is reconfigured using the four initially flat panels or *switches* ($n = 4$). (c) Four other possible cross-sections into which the tube can be reconfigured. Appendix B shows all 70 of the possible cross-section configurations.

A variety of origami inspired tubes exist including the Miura-Tachi polyhedron (Miura and Tachi, 2010; Yasuda et al., 2013; Yasuda and Yang, 2015), and variations inspired by the Yoshimura pattern (Tsunoda, Hiroaki et al., 2005). In this chapter, we explore and extend upon origami tubes that employ the Miura-ori pattern, that were first introduced by Tachi and Miura (Tachi, 2009b; Tachi and Miura, 2012). We generalize these into a new set

of polygonal cross-section tubes that possess the following properties and advantages:

1. Tube cross-sections can take a variety of polygonal shapes.
2. The cross-sections can be made reconfigurable to allow for programmable functionality.
3. A wide variety of new curved tubular forms are possible.
4. The tubes are compatible and can be coupled into a variety of assemblages.
5. The mechanical properties of the tubes can be tuned through reconfiguration.
6. Out-of-plane compression stiffness is enhanced similar to corrugated pipe systems.
7. The perimeter of the tubes is continuous, allowing for deployment by inflation and for the potential capability to carry liquids and gases.
8. Based on idealized zero-thickness kinematics, the tubes are *flat foldable* meaning that they can fold down to a completely flat state allowing for compact stowage.
9. These systems are *rigid foldable*, meaning the origami can fold and unfold with deformation concentrated only along the fold lines (creases), while the panels (facets) remain flat. This capability could allow the structures to be constructed with panels of finite thickness (Hoberman, 2010; Tachi, 2011; Chen et al., 2015), and to fold in a controlled motion.

Properties 1, 2, 3, 5, and 6 are possible with the new polygonal tube definitions presented herein. Some of the advantages are motivated by Figure 6.1 that shows a curved tube that can fold in a variety of different cross-sections. Appendix B shows all 70 of the possible geometries into which this tube can be reconfigured. The versatility, mechanical characteristics and reconfigurability of theses tubes could result in numerous applications as pipelines, architectural structures, robotic components, bellows, metamaterials, and other reprogrammable systems.

The chapter is organized as follows: Section 6.2 introduces the cross-sections, and Section 6.3 provides the full three dimensional definition for admissible polygonal tubes. Section 6.4 explains folding characteristics of the idealized tubes assuming zero-thickness. The system kinematics and reconfigurable characteristics of different tubes are discussed in Section 6.5. In Section 6.6 we extend the tubular definitions to cellular assemblages that can also be

reconfigured. In Section 6.7 we discuss the elastic modeling and explore the mechanical properties of the tubes through eigenvalue and structural analyses. Tubes with circular cross-sections are investigated in Section 6.8, and Section 6.9 gives an outlook for practical implementations and future extensions of the proposed systems. Section 6.10 provides a discussion and concluding remarks. The polygonal tubes discussed in this chapter were in a large part presented in a journal publication (Filipov et al., 2016a).

6.2 Cross-section definitions for polygonal tubes

The popular Miura-ori pattern has inspired the development of rigid foldable origami tubes discussed in several recent articles (Tachi, 2009b; Tachi and Miura, 2012; Miura and Tachi, 2010; Cheung et al., 2014; Filipov et al., 2016b, 2015a; Li and Wang, 2015). The cross-sections of these tubes are symmetric, with the most fundamental tube consisting of two equal symmetric Miura-ori strips placed opposite from each other. More advanced cross-sections follow isotropic, anisotropic, or star shaped cylindrical variations (Tachi, 2009b; Tachi and Miura, 2012; Miura and Tachi, 2010). In this work, we go beyond the previous tube variations and introduce a *translational symmetry method* to create a variety of polygonal shaped tubes. The basic cross-section variations for the polygonal tubes are defined in the $Y - Z$ axis, as demonstrated by Figure 6.2. For our definition, we divide the geometry of the cross-section into an upper (U) and a lower (L) *section*. The names of these two sections are only representative and their location may in fact be side by side as shown later in Figures 6.3 and 6.4. The two opposing sections of the tube have to be continuous and can be composed of $m \geq 2$ *edge groups*. The edge groups are identified by a unique slope angle θ, and denoted by a lower-case letter (a, b, c ...). The slope angle is taken clockwise from the Z axis of the cross-section, and has the admissible range of $-180° < \theta < 180°$. Each edge group on the upper section can be composed of $p \geq 1$ *edges*, and the corresponding lower edge group can be composed of $q \geq 1$ *edges*. The length of the i^{th} edge in the b edge group on the upper (U) section is denoted as b_{Ui}.

To create a valid cross-section, each edge group on the upper section must have a corresponding edge group on the lower section with the same total length and slope angle. This

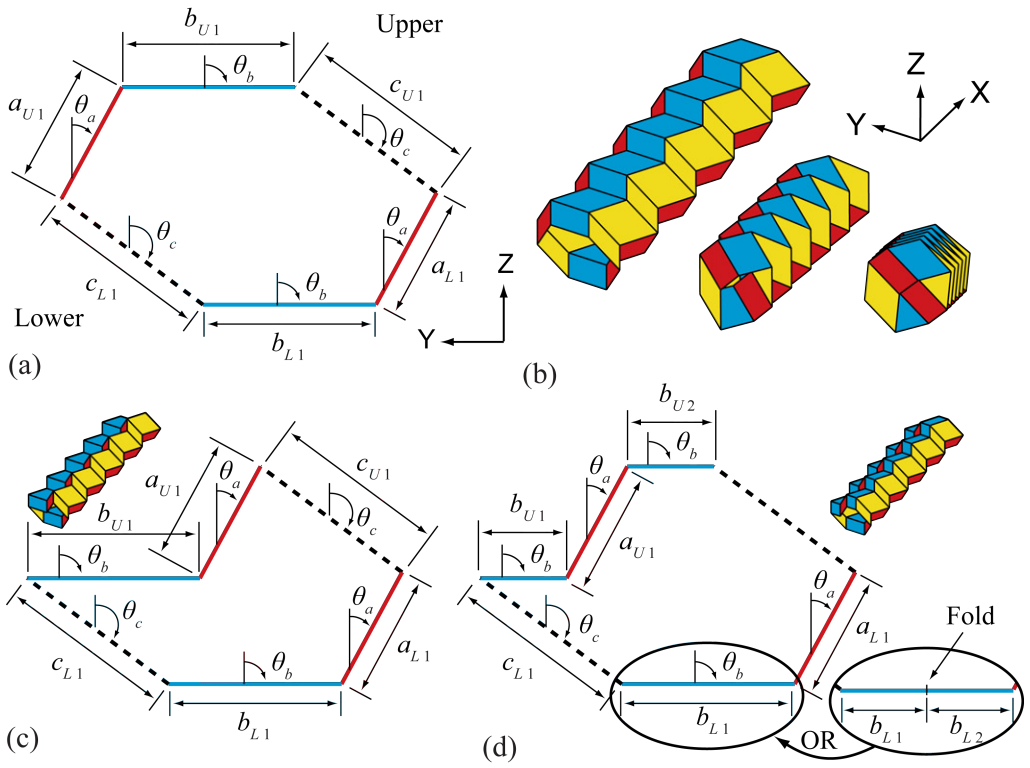

Figure 6.2: Valid cross-section definitions and basic variations. (a) Six-sided tube cross-section with $m = 3$ edge groups each having a unique slope angle θ. (b) Folding sequence of a tube created from the cross-section in (a). The cross-section corresponds to the fully-extended configuration. (c) Six-sided cross-section with the same edge groups as in (a), arranged in a different order. (d) The upper edge group b_U is divided in two ($p = 2$) and rearranged. The corresponding lower edge group b_L can be composed of a single, two, or more corresponding edges with an equal total length ($q \neq p$).

definition can be written mathematically as:

$$\sum_{i=1}^{p} a_{Ui} = \sum_{i=1}^{q} a_{Li}; \qquad \sum_{i=1}^{p} b_{Ui} = \sum_{i=1}^{q} b_{Li} \qquad \ldots \qquad \sum_{i=1}^{p} m_{Ui} = \sum_{i=1}^{q} m_{Li}, \tag{6.1}$$

This property ensures that the cross-section will be closed, thus creating a foldable origami tube with a continuous un-interrupted circumference. The logic of Equation 6.1 can also be though of as a sum of two groups (sections) of equal direction vectors (edge groups), segmented (into edges) and re-arranged to create the cross-section. The re-arrangement of the individual edges can be performed in any logical manner (e.g. Figure 6.2(c)), so long as the lower and upper sections do not intersect. As shown in Figure 6.2(d), when an edge group is segmented into several edges, the number of edges on the upper and lower sections

do not need to be the same (i.e. $p \neq q$). A non-trivial cross-sections with a negative θ is shown in Figure 6.3 and one with a complex outline is shown in Figure 6.4.

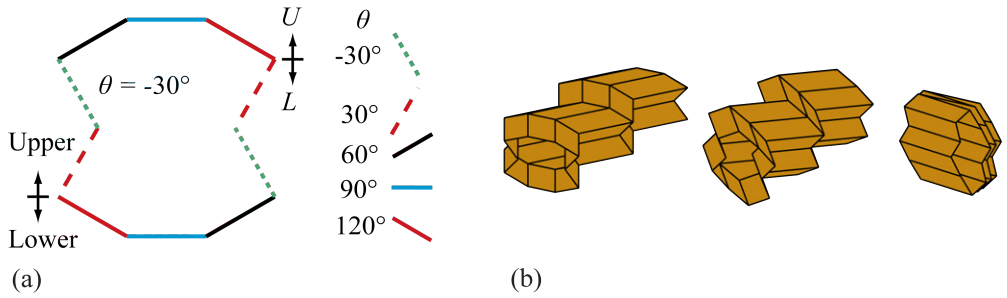

Figure 6.3: (a) Cross-section with a negative slope angle θ. (b) A tube with that cross-section shown fully extended, and folded to 95% and 10% extension.

The fundamental tube that was previously studied (Tachi, 2009b; Filipov et al., 2016b) is a unique case of the generalization proposed here. The tube is created from only four edges that are symmetric about the Y and Z axes; that is $\theta_B = 180° - \theta_A$, and the edge lengths are $a_{U1} = a_{L1} = b_{U1} = b_{L1}$. This tube can be fully flattened in the $X - Y$ plane and can also be folded into a flat state in the $Y - Z$ plane. However, as will be shown in Section 6.5, this most fundamental tube case is not reconfigurable. To create a reconfigurable tube, the cross-section must have at least three edge groups ($m > 2$) each with a unique slope angle θ. Although the slope angles can be arbitrary, in our work we define reconfigurable cross-sections with one edge group where $\theta = 90°$. When this cross-section is projected in the $X-Y$ plane per Section 6.3.1, the $\theta = 90°$ edge group will be completely flat. As defined, the tube is at a fully extended state (100% extension), because from this state the flat edge group can only fold down. When folding, the $\theta = 90°$ edges serve as programmable bits or *switches* to reconfigure the tube cross-section. The fold lines on the switch segments can change from mountain to valley folds and can reshape the geometry of the tube (see Section 6.5). A $m > 2$ cross-section that has no edge group with $\theta = 90°$, is not fully extended when initially defined, and the edges with θ closest to 90° serve as the switches.

6.3 Three dimensional profile definitions

In this section, we discuss the complete three dimensional definition of the tubes when a previously defined $Y - Z$ cross-section is used as a basis. The cross-section is projected in

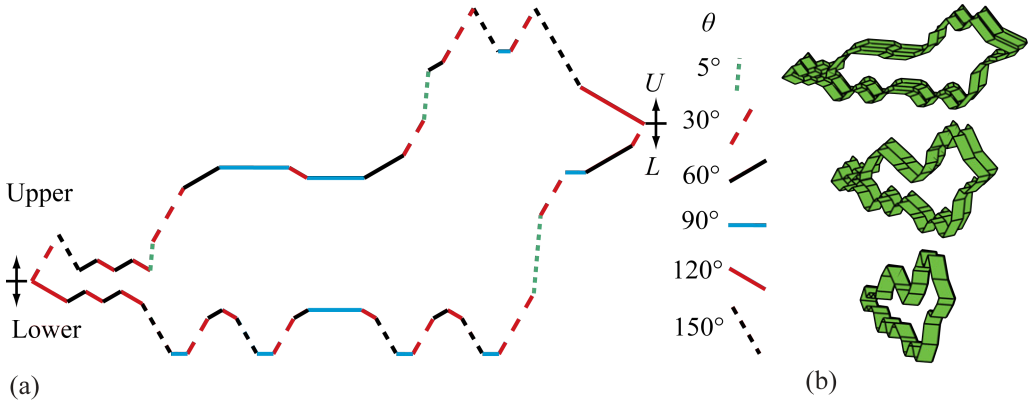

Figure 6.4: (a) An admissible cross-section with the shape of a dog, created with six different edge groups. The upper section has 22 edges, while the lower section has 29. (b) Dog tube fully extended, and folded to 95% and 10% extension.

$X-Y-Z$ space, to create a closed continuous tube. The tube definitions assume that the origami sheets have an infinitesimally small or zero-thickness. In practice, there is a technique that allows for thickness to be incorporated into the design of rigid foldable tubes (Tachi, 2011), however we do not take these details into account. In Section 6.3.1 we discuss the basic projection geometries that preserve the rigid and flat foldability of the polygonal origami tubes. *With these definitions the capability to reconfigure the cross-section is preserved allowing for a programmable system.* The projection discussed in Section 6.3.2 violates flat foldability conditions, but maintains rigid foldability and the programmable characteristics. The projection presented in Section 6.3.3 is the most geometrically unrestricted, but it restricts folding for non-square, non-symmetric tubes. The programmable characteristics of the tubes are discussed in Section 6.5, and the folding properties are summarized in Section 6.4.

6.3.1 Admissible projections for rigid and flat foldable polygonal origami tubes

The first geometric variation for the tubes is to project the the cross-section in the $X-Y$ plane with a constant projection angle as shown in Figure 6.5(a-d). The projection is defined by an angle ϕ and length l. This projection creates a new cross-section that again lies only in the $Y-Z$ plane and is parallel with the initial cross-section when looked at from above ($X-Y$ plane). The corresponding edges of the two cross-sections are connected with thin

origami sheets creating a system of fold lines and panels. A different projection angle ϕ can be used to create a distinctly different structure (Figure 6.5(b) and (c)). The length of individual projected segments can also be varied (Figure 6.5(d)). When the base projection with no length variation is used, all panels are parallelograms and are the same for each cross-section edge. The left vertex angle (α) of each panel (internal angle of the parallelogram) can be calculated as $\alpha_L = \arccos(-\sin(\theta) * \cos(\phi))$. For other more complex projections discussed herein we leave the geometric derivations to the reader.

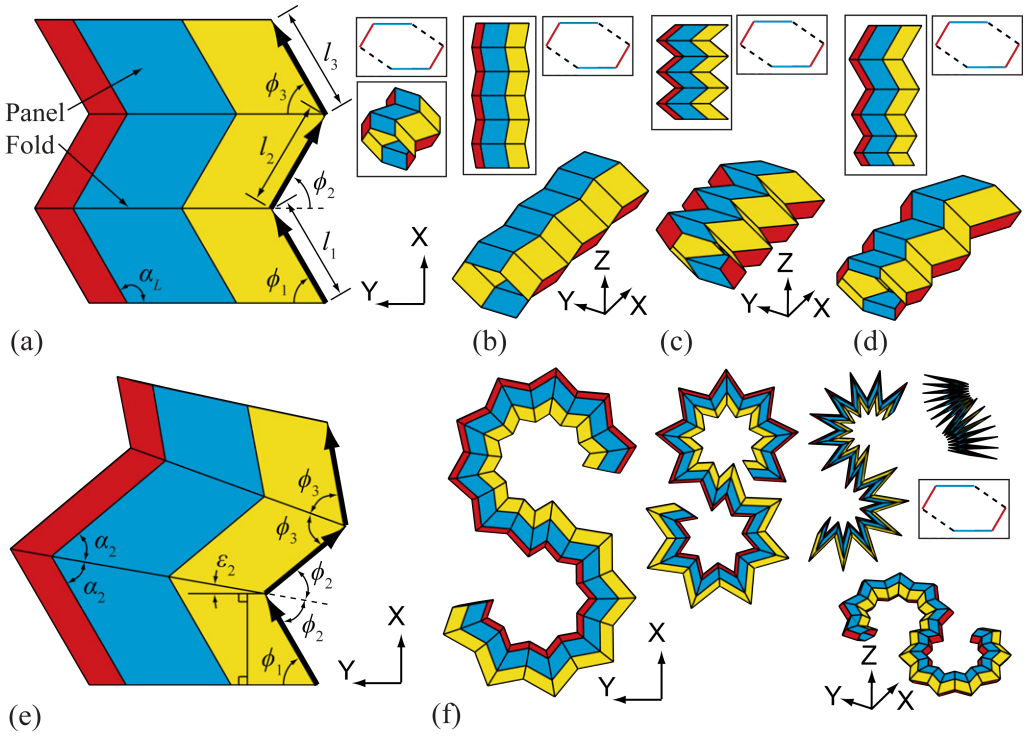

Figure 6.5: (a) Cross-section projection in the X-Y direction using a constant projection angle i.e. $\phi = \phi_1 = \phi_2 = \phi_3 = 60°$. (b) Constant $\phi = 80°$ projection. (c) Constant $\phi = 40°$ projection. (d) Constant $\phi = 60°$ projection, with lengths of segment i defined as: $l_i = 0.4 + 0.2 * i$. (e) Projection with angle variation. Symmetry between the cross-section and projection vector is preserved in the X-Y plane. (f) A rigid foldable S-shaped tube constructed by following symmetry rules in (g). All tubes of this figure use the cross-section in Figure 6.2 (a).

The basic type of projection is further extended by allowing an angle shift to occur, where the projection angles are not equal throughout (i.e. $\phi_1 \neq \phi_2 \neq \phi_3$...). Figure 6.5(e) shows the projection where the angle is varied in the $X-Y$ plane. Symmetry is enforced such that the adjacent vertex angles (α) about the cross-section are kept symmetric. This projection can be used to create an arbitrary geometry in the $X-Y$ plane that is flat and rigid foldable.

6.3.2 Projections for rigid, but non-flat foldable origami tubes

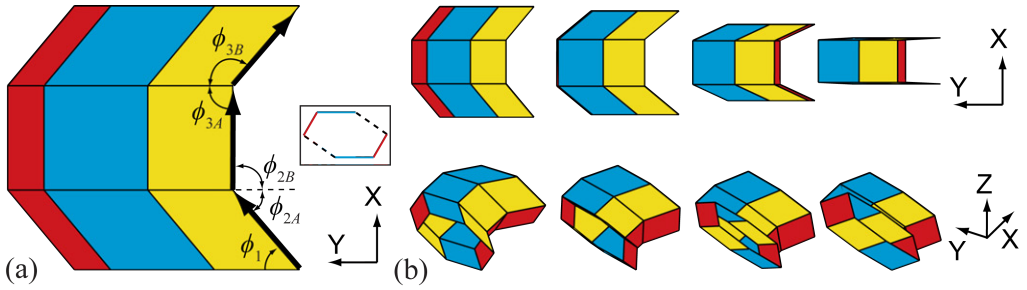

Figure 6.6: (a) Cross-section projection in the X-Y direction that does not preserve symmetry about the cross-section i.e. $\phi_{2A} \neq \phi_{2B}$. (b) The folding sequence of the non-symmetric projection shown in top and isometric views. The structure cannot fold completely flat.

Projection in $X-Y$ space can also be performed without following the symmetry about the cross-section. In Figure 6.6 we show a projection where the projection angles are $\phi_{2A} \neq \phi_{2B}$, and thus the adjacent vertex angles are also not symmetric. The system can undergo rigid folding, but in this case the folding sequence is restricted and the system cannot fold into a completely flat space (Figure 6.6(b) and Section 6.4).

6.3.3 Extended projections for origami tubes

The final form of projection discussed here is the most general, where the projection is performed arbitrarily in all three dimensions ($X - Y - Z$). The vector can be varied in all directions simultaneously, by using an angle ϕ to describe the projection vector in $X - Y$, and γ to vary the projection vector in $X - Z$. Symmetry of the projection is preserved, such that the adjacent vertex angles on opposing sides of a cross-section are equal. This symmetry can be visualized as mirroring the structure locally, which is shown using transparent planes in Figure 6.7(a-c). For the polygonal cross-section, when this projection is used, the resulting structure is not foldable, and so it is essentially no longer origami, but a static fully restrained structure (Section 6.4). However, if a simple symmetric cross-section is used, the structure remains rigid and flat foldable. When simple four sided tubes are projected in three directions, and the symmetry of the cross-section is preserved, this also ensures symmetry at all vertices (flat foldability) and symmetric kinematics on both sides of the tube (rigid foldability). The structure in Figure 6.7(d) follows an arbitrary spiral in

three dimensional space.

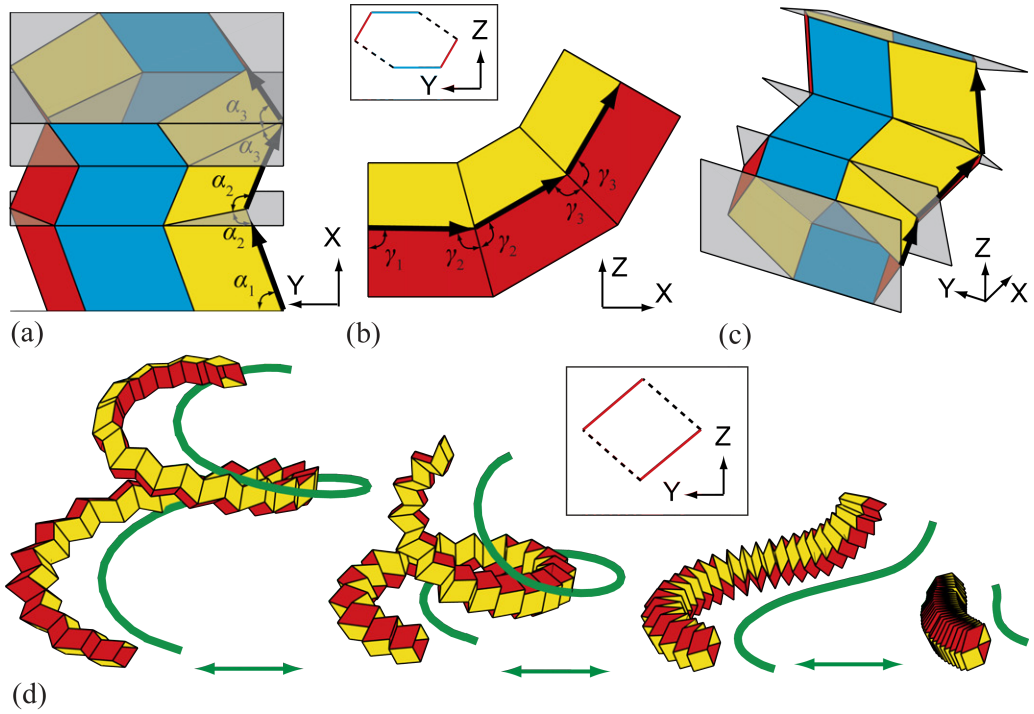

Figure 6.7: Cross-section projection varied in the X-Y-Z directions simultaneously while preserving symmetry of the structure about the cross-section. Projection of six-sided polygon shown in (a) top, (b) side, and (c) isometric views. This polygonal tube cannot fold. (d) Folding sequence of four-sided origami tube constructed by projecting along a spiral in three dimensional space. This tube is rigid and flat foldable.

6.4 Foldability of polygonal origami tubes

In this section we verify the developability, flat foldability and initial rigid foldability using the approach introduced by Tachi (Tachi, 2009a). We assume that the origami panels have an infinitesimally small or zero-thickness to satisfy the mathematical definitions. The origami tubes defined by Sections 6.2 and 6.3 contain a total number of n^{vert} internal vertices where four fold lines meet, and a number of n^{panel} four-sided panels. The folding characteristics of the origami can be explored by performing the following vector calculations for the vertices and panels:

$$\mathbf{c}^{\text{dev}} = \left[2\pi - \sum_{k=1}^{4} \alpha_{k,i} \right]_{n^{vert} \times 1} = \mathbf{0}, \tag{6.2}$$

$$\mathbf{c}^{\text{flat}} = \left[\sum_{k=1}^{4}(-1)^k \alpha_{k,i}\right]_{n^{vert}\times 1} = \mathbf{0}, \tag{6.3}$$

$$\mathbf{c}^{\text{planar}} = [\rho_j]_{n^{panel}\times 1} = \mathbf{0}, \tag{6.4}$$

where $\alpha_{k,i}$ represents the k-th vertex angle in the i-th vertex, and ρ_j represents the dihedral angle between the normals of two triangles that together create the j-th panel of the tube. The vector $\mathbf{c}^{\text{dev}}$ is of size $n^{vert} \times 1$, meaning that there is one entry for each of the vertices in the origami. When $\mathbf{c}^{\text{dev}} = \mathbf{0}$ for all vertices, then the origami is developable, meaning it can be created from a single flat piece of material. The origami tubes presented here have mostly non-developable vertices, and thus they cannot be folded from a single flat piece of material. However, some of the vertices may be developable and thus a portion of the tube may be constructed from an initially flat sheet (e.g. the single four-sided tube can be constructed from two flat sheets (Tachi, 2009b)). When $\mathbf{c}^{\text{flat}} = \mathbf{0}$, then all vertices of the origami are locally flat foldable meaning that, they can fold down to a flat 2 dimensional state. The definitions in Section 6.3.1 and 6.3.3 intentionally ensure symmetry when preforming a projection of the cross-section, thus they ensure that all vertices are flat foldable. However, in Section 6.3.2 where symmetry is not preserved, we lose the flat foldability ($\mathbf{c}^{\text{flat}} \neq \mathbf{0}$).

Equation 6.4 indicates that all panels are planar or flat for a given configuration. The dihedral angle (ρ_j) can be calculated using the four nodes on the corners of the panel, and will always equal 0 at the initial projected configurations defined using Section 6.3. Thus all tubes satisfy $\mathbf{c}^{\text{planar}} = \mathbf{0}$, however, this is only a necessary condition for rigid foldability and is not sufficient. For rigid foldability, folding along fold lines should permit the structure to transition between states while $\mathbf{c}^{\text{planar}} = \mathbf{0}$ is continuously satisfied. Analytical derivations of the kinematics and geometric characteristics of foldability (including rigid foldability) have been previously discussed (Huffman, 1976; sarah-marie Belcastro and Hull, 2002b,a; Hull, 2012), however these tend to be cumbersome for verifying the rigid foldability of complex origami systems.

The methodology used to perform kinematic folding in this chapter (Tachi, 2009c) performs well for patterns that are rigid foldable, but it fails if they are not. This deviation from rigid folding behavior is not intuitive and can be misleading. A more straightforward and intuitive method to check if a structure is rigid foldable, is to perform the eigenvalue analyses described

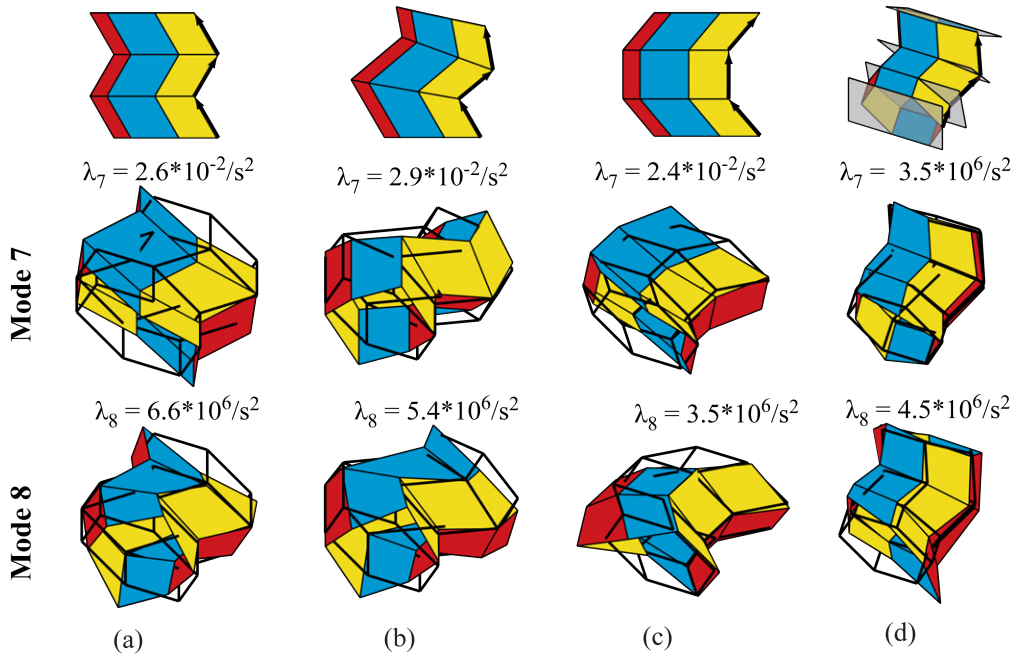

Figure 6.8: Schematic (top row), seventh mode (middle row) , and eighth mode (bottom row), of basic projection definitions. (a) Constant angle projection in $X-Y$. (b) Projection in $X-Y$ with symmetry enforced. (c) Projection in $X-Y$ without preserving symmetry. (d) Simultaneous projection in $X-Y-Z$. Low eigenvalues correspond to a soft, rigid folding mode of the origami.

in Section 6.7 with the fold stiffness (K_ρ) substantially reduced (e.g. to 10^{-7}) representing fold lines with no stiffness. In these analyses, the seventh and possibly higher eigenvalues will be near zero, indicating a rigid folding motion where a kinematic transition is permitted by folding along the fold lines. Subsequent deformation modes will indicate motions that are not rigi foldable and include other deformations in the origami. Figure 6.8 shows the eigenvalues and eigen-modes for the basic origami assemblies studied in this chapter. All cases except symmetric $X-Y-Z$ projection have a λ_7 that is low ($\approx 10^{-2}$), indicating a rigid folding motion. For the $X-Y-Z$ projection case, λ_7 is of much higher order indicating that bending of the panels must occur to deform the structure, and that the tube does not have a rigid folding mode. For the structures in Figure 6.8(a-c), λ_8 is substantially higher than λ_7 indicating that only one rigid folding motion exists, these systems can be classified as *one degree of freedom* for rigid folding.

In Figure 6.9 we show the eigenvalue and eigen-modes of the eight-sided tube with two switches ($n = 2$). Curiously, for this case, the system has three soft modes where the rigid folding can occur, and the tenth mode is the first to engage the origami panels in

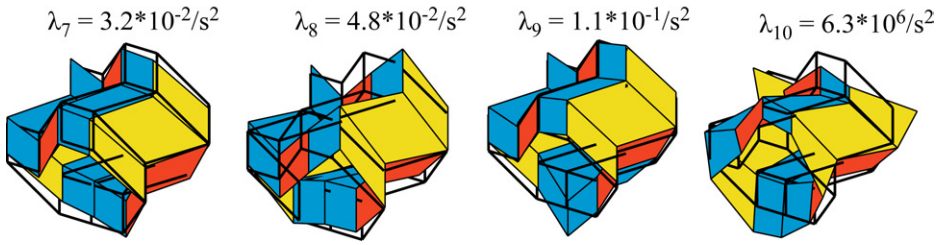

Figure 6.9: The seventh to tenth eigenvalues and eigen-modes of the eight-sided tube when it is at a fully extended state. Mode seven corresponds to configuration II and is the symmetric inverse to configuration I; Mode eight is corresponds to configuration IV and is symmetric to V; and Mode nine corresponds to configuration VI and is symmetric to III. Mode ten is the squeezing mode.

bending. These rigid folding modes each correspond to one of the system configurations shown in Figure 6.11, and each one of them also has a symmetric inverse that corresponds to another system configuration. These results indicate that the system has three non-symmetric degrees of freedom for rigid folding. However, once the structure enters one of the folding configurations (extension $< 100\%$), it behaves like a one degree of freedom system, where it only has a single flexible mode for rigid folding (Figure 6.14). This phenomenon of the eight-sided tube is similar to a flat sheet that can enter numerous different folding patterns when initially folded. Future, research could investigate differences in rigid folding configurations, the symmetric inverse eigen-modes, and the varying programmability possible with the polygonal tubes.

6.5 Kinematics in reconfiguring polygonal tubes

The folding of the tube can be preformed through an analytical (Huffman, 1976; Hull, 2012; sarah-marie Belcastro and Hull, 2002b,a) or numerical method (Tachi, 2009c), by changing a fold angle in one vertex, calculating the other angles in the vertex, and cycling through all of the vertices in the pattern until all fold angles, and the new geometric shape are calculated. Other methods that use the global properties of the structure (for example the eigenvalues) can also be used in an iterative folding scheme (Schenk2011b). Here, we use the numerical method in (Tachi, 2009c) to perform the kinematic folding, because with this method it is easier to specify a folding motion by assigning mountain and valley fold directions. In contrast to more simple tube structures, the geometry of the tubes presented here can be reconfigured, and thus picking a specific fold pattern is helpful. Figure 6.10 shows the

two basic geometry reconfigurations that can be obtained from the simple six-sided origami tube. The initially flat in $Y-Z$ segments, can be used as *switches* to change the structural geometry.

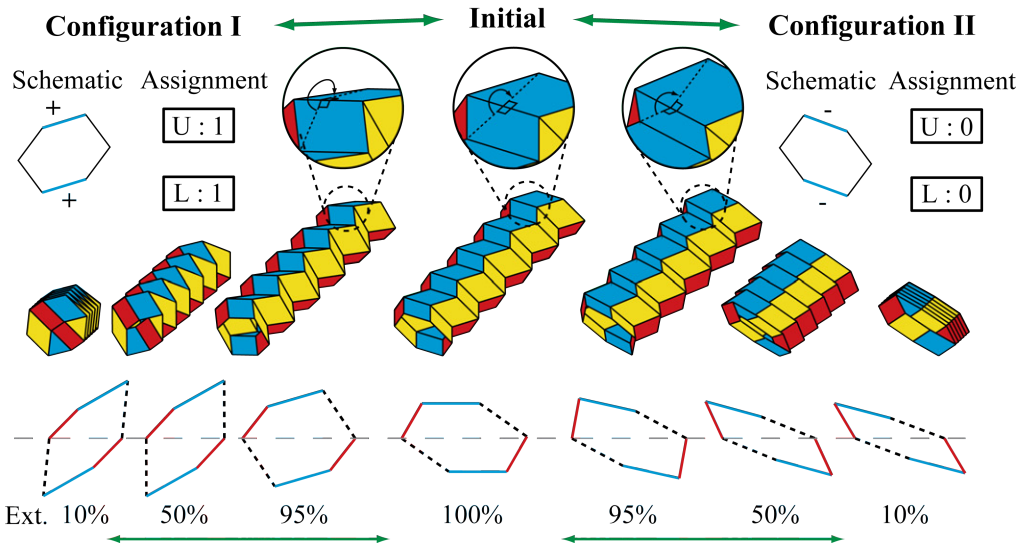

Figure 6.10: The six-sided tube can be folded into two different configurations by changing the polarity of folds (valley or mountain) on the single flat segment ($n = 1$). A cross-section schematic with positive or negative slopes is used to inform the fold assignment for the first/last fold ($0 =$ valley, $1 =$ mountain). The folded cross-sections of the two configurations are not symmetric because edge groups a and c in the cross-section definition are not symmetric (Figure 6.2(a)).

A binary system is used to inform the directional change in cross-section and new geometry. The upper and lower switches are defined as a 0 or a 1 and indicate negative or positive slope change in the cross-section respectively (*valley* or *mountain* fold respectively between the first and second panels). The assignment on the upper and lower segments must match to preserve the translational symmetry in Equation 6.1, thus if the [U: 1] then [L: 1] as well. In Figure 6.11(a) we extend these definitions to the eight-sided tube from Figure 6.2(d).

The eight-sided tube has two switches of equal length on both the upper and lower sections. The number of positive switches (1s) on the upper section has to correspond to the number of positive switches on the lower section of the tube. Thus the sum (k) of the L and U switches must match. Figure 6.11(a) shows the six possible switch variations for the eight-sided tube. The number of possible ways to reconfigure the upper section only, follows a

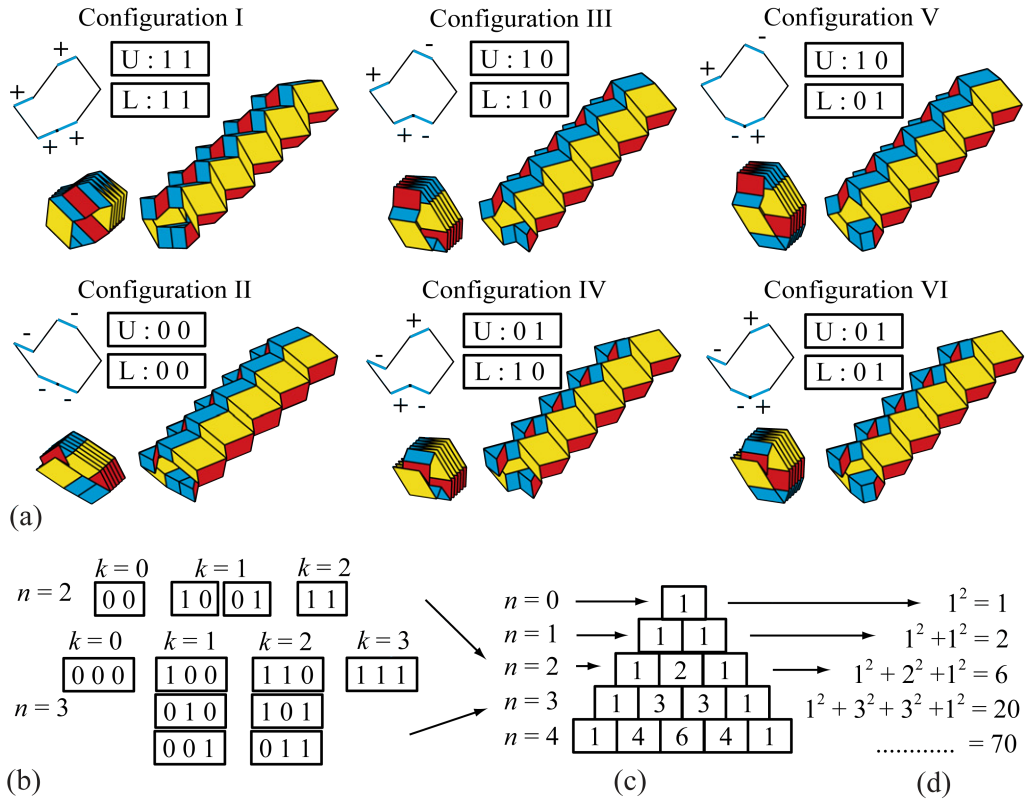

Figure 6.11: Variations in reconfiguring polygonal tubes. (a) An eight-sided tube with two equal length segments (switches) can reconfigure into six unique configurations. The three dimensional models are shown at 10% and 95% extension. (b) Possible switch variations for the upper section only, with $n = 2$ and $n = 3$ switches. The variable k corresponds to the sum of the of switch assignments. (c) A Pascal's triangle shows the number of variations for the upper section of the tube only. This is the binomial coefficient with n representing the rows and k the columns. (d) The total number of possible cross-section configurations. This is equivalent to the central binomial coefficient.

binomial coefficient as:

$$\left(\begin{array}{c} n \\ k \end{array} \right) = \frac{n!}{k!(n-k)!}, \tag{6.5}$$

where we have n available switches and we want exactly k of them to be positive. For example in Figure 6.11(a) there is only one possible way to reach a total of either $k = 2$ or $k = 0$, configurations I and II respectively. However, there are two possible ways to reach a total of $k = 1$, i.e. [U: 1 0] and [U: 0 1]. Because each variation of the upper section can be coupled with a corresponding lower section with the same polarity sum (k), we need to take the square of these possibilities, and sum them to find the total number of possible

variations for the cross-section. This results in the central binomial coefficient:

$$\sum_{k=0}^{n} \left(\frac{n!}{k!(n-k)!} \right)^2 = \frac{(2n)!}{(n!)^2}. \tag{6.6}$$

This function gives the total number of unique cross-section variations that can be obtained when folding a reconfigurable tube with n flat segments or switches. The possible upper section assignments for a $n = 2$ and $n = 3$ tube are shown in Figure 6.11(b). The number of possible upper section variations follow Pascal's triangle (Figure 6.11(c)), and the total number of possible configurations follow the central binomial coefficient (Figure 6.11(d)). The most basic, four sided tube cross-section (e.g. Figure 6.7(d)) has no switches ($n = 0$), and thus has only one possible cross-section configuration. On the other hand, the tube with four symmetric switches ($n = 4$) shown in Figure 6.1 can reconfigure into 70 distinct cross-sections. Appendix B of the thesis shows all 70 possible cross-section configurations that can be obtained from that tube.

6.6 Cellular extensions for reconfigurable origami tubes

The projection technique for creating polygonal tubes can be extended to creating cellular assemblages that have similar geometric characteristics. When the translational symmetry is used in the cross-section(s) and an admissible projection is followed to construct the three dimensional structure, the folding and reconfigurable characteristics remain similar to before. In Figure 6.12 we show two assemblages that use a constant angle projection, although it is possible to use more advanced curved projections as well. The cross-section in Figure 6.12 (a) is created by discretizing the cross-section into smaller sections. All of the internal cross-sections, as well as the global external cross-section, follow the translational symmetric rules in Equation 6.1. This assemblage can still be reconfigured as shown in Figure 6.10. In Figure 6.12 (b) we combine four tubes together, two of which have reconfigurable cross-sections. This assemblage can now be reconfigured into four different cross-sections, with configurations III and IV being rotationally symmetric. A variety of new assemblages can be constructed using these ideas, however the initial cross-sections cannot have overlapping components, and the kinematics of reconfigurations should be carefully analyzed.

When multiple tubes and cross-sections are reconfigured, it may be possible for different components to experience interaction or contact, and some of the reconfigurations may be obstructed.

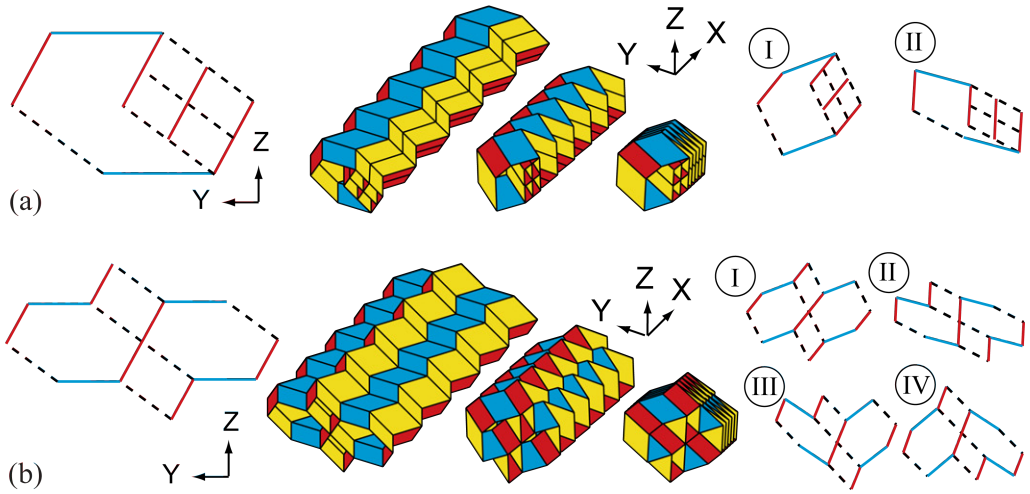

Figure 6.12: Cross-sections, isometric folding sequence and possible reconfigured cross-sections of cellular origami assemblages. (a) The basic six-sided polygon has four smaller parallelogram tubes inserted within. This assemblage has two possible configurations similar to before. (b) Assemblage consisting of two six-sided and two four-sided tubes together. This structure can reconfigure into four states.

Polygonal origami assemblages can be further enhanced by using different projection angles and projection directions, for the different tubes within the assemblage Filipov et al. (2015a); Tachi et al. (2015). The polygonal assemblages could be coupled in the zipper fashion to significantly stiffen the origami structures. Zipper coupling between the polygonal and regular square tube can be done on any of the polygonal tube faces. The assemblages can be generalized in numerous ways, but they also limit some of the projection directions that can be used to create the system Tachi et al. (2015). Furthermore, it is possible to introduce techniques for locking the origami configuration into a sandwich-like structure Schenk and Guest (2013); Gattas and You (2015a). These additions can enhance the structural rigidity of the systems, but can restrict the deployment and reconfigurable kinematics of the polygonal tubes. Future research can explore the numerous assemblage variations proposed and determine useful methods for enhancing the mechanical characteristics of the structures.

6.7 Elastic behavior of polygonal tubes

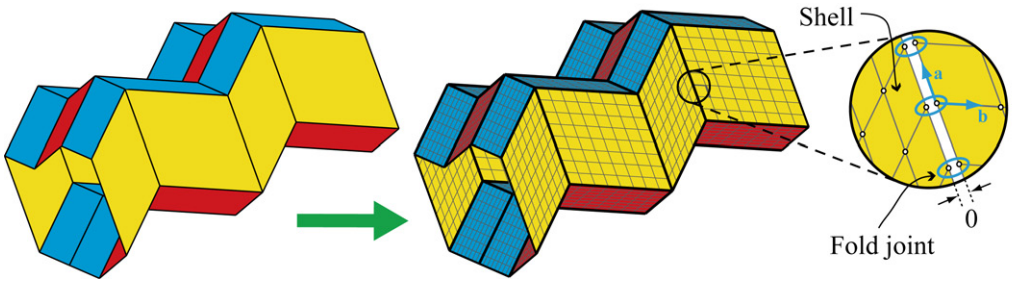

Figure 6.13: A portion of the eight-sided reconfigurable tube with the corresponding FE discretization. The inset shows the localized zero-length connectivity at the fold lines.

In this section, we explore the global mechanical characteristics of the tubes with a finite-element (FE) analysis software (Abaqus (Dassault Systemes Simulia Corp, 2010)). Each of the origami panels is discretized with 8×8 shell elements and the folds are modeled using rotational hinges as shown in Figure 6.13. The model uses standard S4 general purpose shell elements with finite membrane strains that are appropriate for the small deformation analyses of the thin sheet origami structures. We have also performed these analyses with the bar and hinge approach and we obtain similar qualitative results (see Figure 3.7 and Chapter 3). However, in this chapter, we use converged versions of the FE model to provide more quantitative results for the behavior. Quantitative estimates are required for comparing the origami tubes to analytical expressions for the behavior of uniform pipes in Section 6.8.

We model the eight-sided reconfigurable tube from Figure 6.2(d). The cross-section edges for the upper section have slopes of $[\theta_a, \theta_b, \theta_c] = [30, 90, 125]^\circ$, and lengths of $[b_{U1}, a_{U1}, b_{U2}, c_{U1}] = [0.5, 0.7, 0.5, 1]$ cm. The tube is ten segments long, and is created with constant projection of $\phi = 60^\circ$ and $l = 1$ cm. The configuration of the structure is defined based on the idealized zero-thickness rigid kinematics, however, to define the stiffness of the structure we assign a thickness of 0.1 mm which translates to roughly $L/t \approx 50 - 100$. The model does not however account for detailed effects of the thickness such as intersection that may occur when we attempt to fold an origami with finite thickness. Other model parameters are defined as Young's modulus $E = 5$ GPa, Poisson's ratio $\nu = 0.33$, and density $\rho = 650$ kg/cm^3. In reality the behavior and stiffness of the fold lines can depend on the material and fabrication used to make the origami. Here, we assume linear elastic folds where the stiffness for a

rotation of ρ radians is specified as $K_\rho = 0.0164$ N*cm/rad per one centimeter of fold line. The fold lines are assumed to be more flexible in bending than the panels, and thus K_ρ is specified to be one tenth (1/10) the bending stiffness of an origami panel with a diagonal length of one centimeter. The dimensions and units used here are chosen arbitrarily but within a realistic range to give qualitative insight to the origami behavior. Quantitative results for engineered origami systems could be obtained using known dimensions and material properties. The analytical model captures the elastic behaviors of origami type structures: 1) panels stretching and shearing, 2) panels bending, and 3) bending along prescribed fold lines. We have evaluated the mesh convergence for the tube when it is loaded as a cantilever later in this section. The 8×8 shell mesh approximates displacements within 4% of a significantly finer mesh discretized with 32×32 shell elements per panel. In this chapter, we use elastic and small displacement approximations for all analyses. Future research will be needed to understand localized behaviors in origami structures, as well as the large displacement behaviors which could be of significant importance.

We perform the eigenvalue analysis as discussed in Chapter 3 to evaluate the structural characteristics of the polygonal tubes. The eigenvalues (λ_i) are arranged in an incremental order (i) and represent the excitation frequencies that would deform the structure into the corresponding eigen-mode ($\mathbf{v}_i$). For the eight-sided reconfigurable tube the seventh eigen-mode follows the kinematic folding and unfolding of the structure (Figure 6.14(a-b)). The seventh mode has the least energy indicating that it is easiest to deform the structure by following the prescribed folding sequence. The eight mode is a squeezing mode, where one end of the tube is folding and the other end is unfolding. By changing the geometry or through tube coupling described in Chapters 4 and 5 it could be possible to substantially increase the band-gap $\lambda_8 - \lambda_7$, creating a structure that is easy to deploy, but is substantially stiffer for other deformations. The ninth mode of the structure is another manifestation of squeezing with the centre unfolding and the ends folding . The tenth mode is a localized mode, where the panels at the end of the tube fold. The ninth and tenth eigenvalues are substantially higher, meaning the structure is stiffer for these and other types of deformations.

Because the geometry of the system changes, the magnitudes of the eigenvalues also change with respect to the extension of the system. Extension here is defined as a percentage of the fully extended length. When the structure is at 0% extension it is completely folded

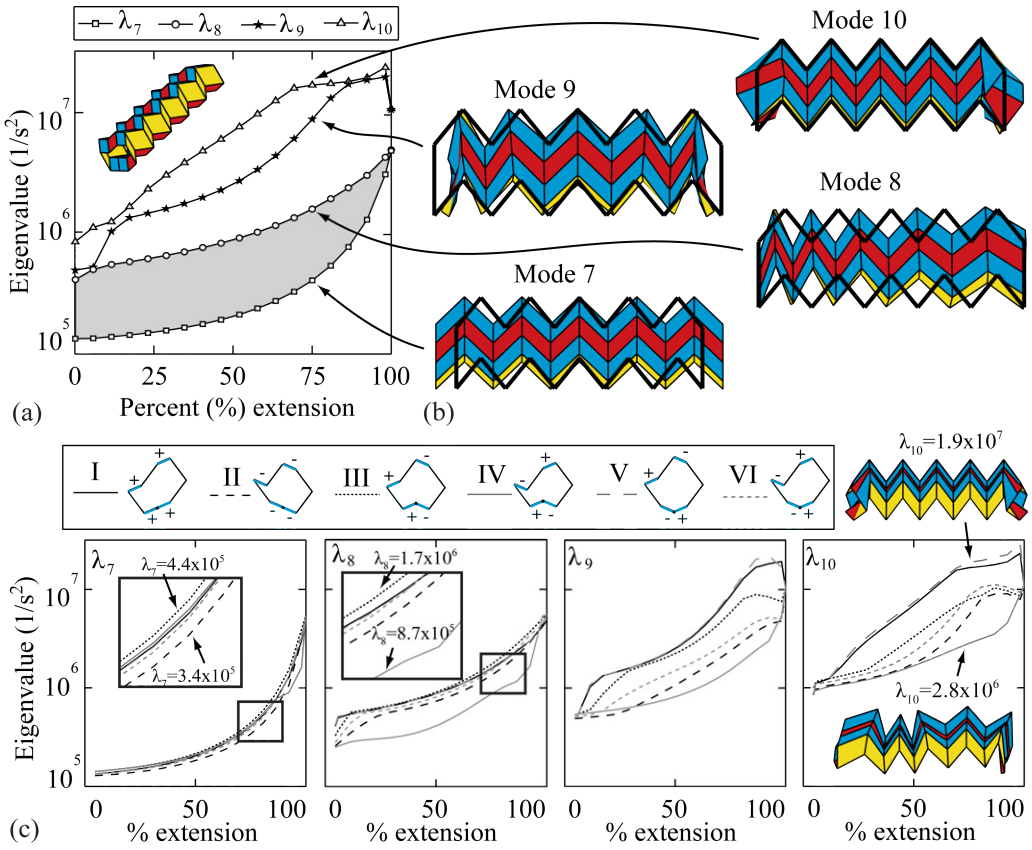

Figure 6.14: Eigenvalue analyses of eight-sided reconfigurable tube with two switches presented in Figure 6.11. (a) Eigenvalue versus the extension of the tube in configuration I. (b) Corresponding eigen-modes at 75% extension. (c) Eigenvalues seven through ten presented for each of the six possible geometric reconfigurations of the tube.

down, while at a 100% extension the switches flatten and the system can be reconfigured. The eigenvalues for rigid folding and squeezing remain essentially the same regardless of the folded configuration, although there are some small differences in magnitude. However, the ninth and tenth mode are greatly affected by the different folding configurations (Figure 6.14(c)). This is because the cross-sectional geometry has a higher influence in determining the more complex localized and global bending modes.

In Figure 6.15 we present a cantilever analysis of the eight-sided tube in different configurations. One end of the cantilever is fixed and a small uniformly distributed load (summing to a total of 0.001 N, e.g. $F_X = 0.001$ N) is applied on the other end. We perform static, linear elastic, small displacement analyses of the structures, with the main objective of exploring the global behaviors and anisotropy of the tubes. The system displacements (Δ_X, Δ_Y, Δ_Z) are calculated using the equation $\mathbf{F} = \mathbf{K}\Delta$, where $\mathbf{F}$ is a vector of forces. Subsequently, the

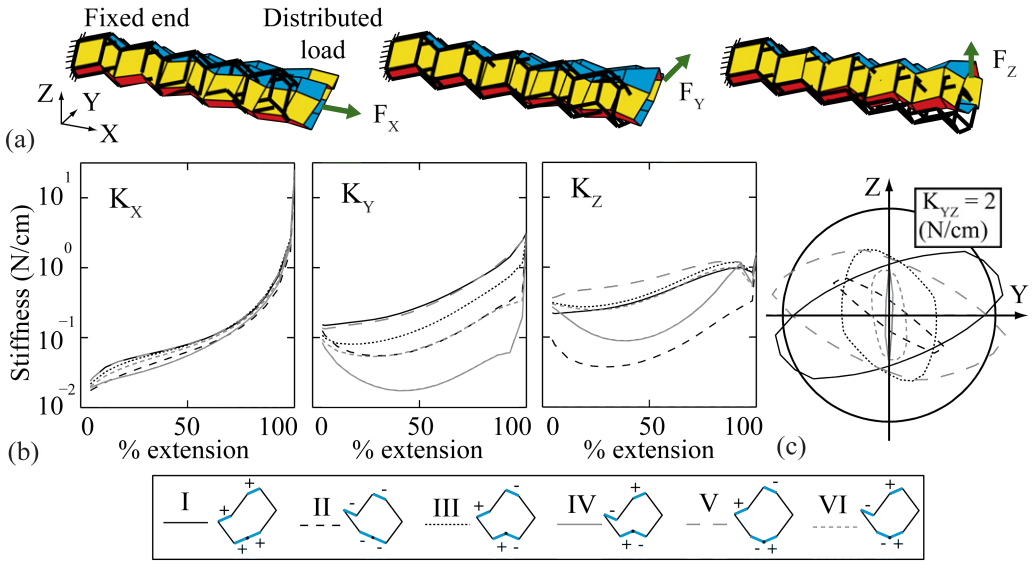

Figure 6.15: Structural cantilever analyses of eight-sided tube. (a) Representative deformed shapes scaled $\times 1000$ for the tube in configuration I at 95% extension. (b) The stiffness of different tube configurations in the three Cartesian directions with respect to the extension. (c) The tube stiffness for different loading directions in the $Y - Z$ plane represented as a radial plot. The tubes are at an extension of 95%.

system stiffness is calculated as $K_X = F_X/\delta_X$, where δ_X is the mean X direction displacement of the loaded nodes. A squeezing type deformation occurs for some of the loaded cases, and this is believed to result in lower stiffness than if the origami was engaged in stretching and shearing.

Different cross-section configurations, can have drastically varying stiffness characteristics, with up to an order of magnitude between different cross-sections (Figure 6.15 (b)). Typically, configurations I and V are the stiffest while configurations II and IV are the most flexible. We also show the stiffness perpendicular to the X axis, as a radial plot in Figure 6.15(c). The I and V configurations have large oval plots, meaning they have relatively higher stiffness in most directions. Each of the cross-sections also has a different direction (in $Y-Z$) where it has a lower or higher stiffness. This phenomenon indicates that the reconfigurable tubes have a highly adjustable anisotropy when used as cantilevers. The behaviors observed in this section show that the cross-section geometry can have a significant influence on the mechanical properties of the system. Thus, the reconfigurable polygonal tubes can be used to create highly tunable and adaptive structural systems. Detailed research is needed in this area to determine the influence of different cross-section geometries, as well as the tunability

achieved from each reconfiguration.

6.8 Cylindrical origami tubes

We explore a uniform circular pipe (made from a thin sheet) experiencing uniform out-of-plane loading and compare it with similar origami tubes. Figure 6.16(a) shows the pipe that is $L = 10$ cm long, loaded in space with symmetric out-of-plane distributed load equal to F/L. In this section, we use a total force of $F = 0.001$ N, and we assume linear elastic, small displacement behaviors. The radius of the pipe is $r = 2$ cm, and all other parameters (i.e. t and E) are the same as for the origami analysis in Section 6.7. An analytical solution for this problem is found using Castigliano's theorem where the pipe is simplified to a two dimensional bending of a thin beam (Section 6.8.1). The analytical solution matches well with a converged FE model where a uniform pipe is discretized with 120 shell elements along the diameter and 100 elements lengthwise. The total diametric deflection (δ_d), coaxial with the applied load, is found to be

$$\delta_d = \left(\frac{\pi}{4} - \frac{2}{\pi}\right) \frac{12Fr^3}{ELt^3} = 0.00286 \text{ cm}. \tag{6.7}$$

Subsequently, we perform similar analyses on the origami tubes with the same parameters, and dimensions defined to match the pipe as closely as possible. All cross-sectional edge lengths are defined as $2\pi r/N_{Edge}$ where N_{Edge} are the total number of edges on the circular tube. As such, the tube perimeter is the same as the analytical case. The edges are arranged in a symmetric fashion so that the cross-section becomes a regular polygon (Figure 6.16 (b)). Three cases with $N_{Edge} = 6$, 10, and 14 are used, such that there is a single flat segment in the initial configuration, meaning that the initial configuration is the fully deployed state. The number of panels in the X direction is chosen as 6, 8 and 12 for the three cases respectively, so that the structure is symmetric and the panels are approximately square. The projection angle defining the three dimensional shape is varied, and a consistent projection length is used so that the origami tube is $L = 10$ cm long in the fully deployed (same as initial) configuration. We perform a static analysis by loading the vertices on the top flat segment with a downward force, such that the edge vertices carry half the load of the internal vertices

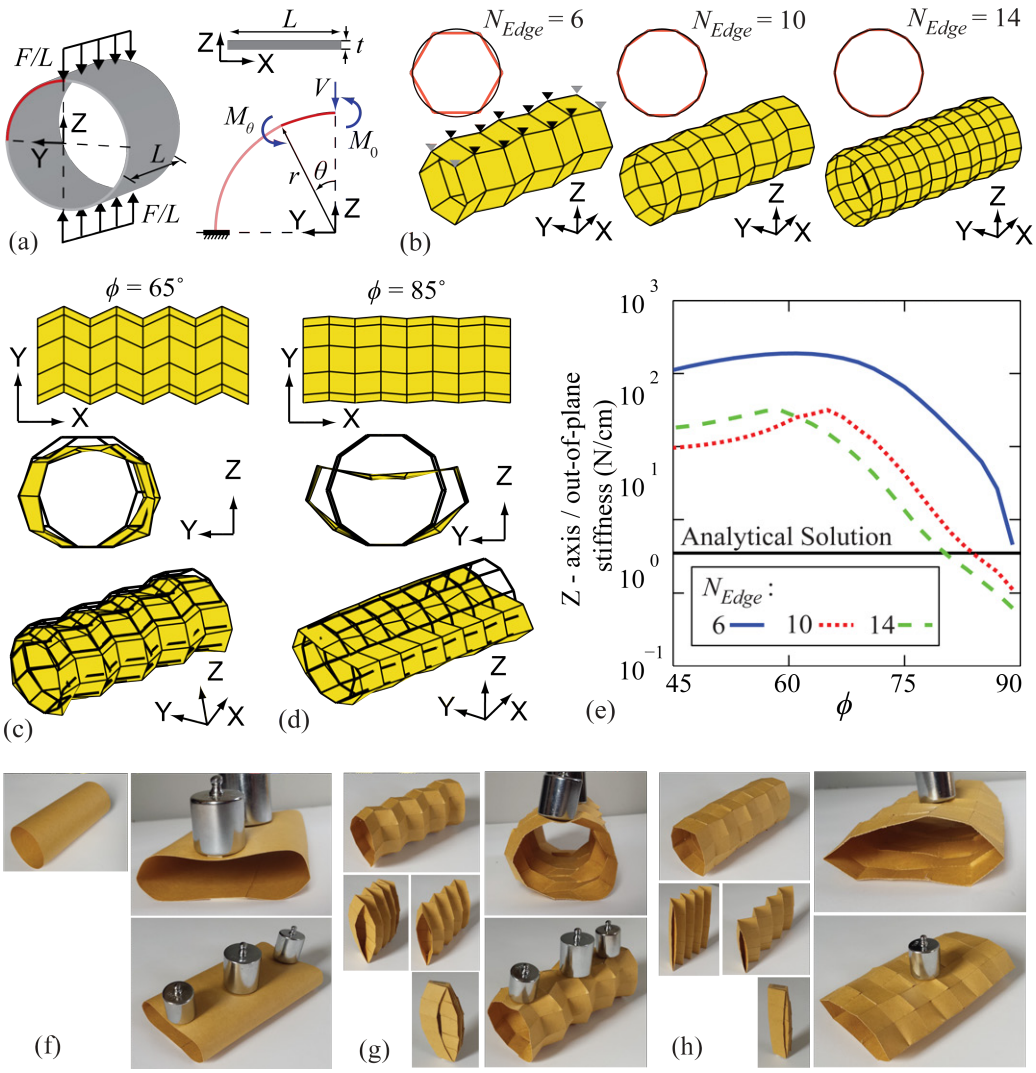

Figure 6.16: Out-of-plane compression on a pipe. (a) Problem definition and analytical approximations (Section 6.8.1). (b) Origami tubes with $N_{Edge} = 6$, 10, and 14. The origami tube cross-sections are overlayed with a $r = 2$ cm circle. The loading is only shown for the $N_{Edge} = 6$ tube. (c) A $\phi = 65°$ tube, and (d) a $\phi = 85°$ tube with $N_{Edge} = 10$. The top (X-Y) view is shown as a reference and the lower views show the deformed shapes. The deformed shapes are scaled $\times 10000$ for the stiffer $\phi = 65°$ tube and $\times 200$ for the more flexible $\phi = 85°$ tube. (e) The out-of-plane stiffness of tubes versus the projection angle ϕ. (f-h) Physical models of a uniform sheet, $\phi = 65°$, and $\phi = 85°$ tubes respectively, loaded out-of-plane with 400 grams. The $\phi = 85°$ tube is only loaded with one 100 gram weight due to the much larger deformation.

(grey versus black triangles in Figure 6.16 (b)). The loads are defined such that the total applied load sums to $F = 0.001$ N. The bottom vertices of the tubes are restrained in the Z direction, representing a symmetric loading similar to Figure 6.16 (a).

We use static, linear elastic, small displacement analyses to evaluate the mechanical prop-

erties of the origami tubes. Scaled deformed shapes of $N_{Edge} = 10$ tubes with two different projection angles are shown in Figure 6.16(c-d). The tube with $\phi = 65°$ is much stiffer and has an irregular deformed shape where panels bend and stretch. The tube with $\phi = 85°$ has a more regular deformed shape, similar to what we would expect from a thin pipe, and in this case, deformation occurs primarily by bending along the longitudinal fold lines. Stiffness with respect to the projection angle ϕ, of the tubes with different N_{Edge} is shown in Figure 6.16(e). The origami stiffness is calculated as in Section 6.7, and the analytical stiffness solution for the circular pipe is calculated as F/δ_d.

Similar to the deformed shapes, tubes with lower projection angles have lower displacement and are stiffer, while tubes with a projection angle close to 90° are more flexible because they permit folding along the longitudinally oriented fold lines. The origami tubes with projection angles between $\phi = 45° - 75°$ are stiffer than the analytical solution for a circular pipe. This behavior is similar to that of corrugated pipes and sheets (Briassoulis, 1986). Corrugated pipes have a higher stiffness for out-of-plane loadings, which makes them suitable for many applications such as culverts. The polygonal tubes may also have properties similar to the non-folding pseuo-cylindrical concave polyhedral (PCCP) shells inspired from the Yoshimura pattern (Miura, 1969, 2002). Due to their patterned nature, PCCP shells posses an increased buckling capacity for external hydrostatic pressures.

Polygonal tubes with more edges e.g. $N_{Edge} = 14$ have more fold lines along their cross-section perimeter, making them more flexible. The results are verified with physical models (Figure 6.16(f-h)). The stiffness of the fold lines R_{FP} factor, does not influence the deflection significantly for cases with lower projection angle $\phi < 75°$. However, for higher ϕ the fold lines are the primary location of deflections, and thus their stiffness greatly affects the tube stiffness.

6.8.1 Analytical solution for a pipe loaded out-of-plane

The exact analytical solution for the out-of-plane bending of a pipe can be calculated using Castigliano's theorem where we simplify the problem to a two dimensional bending of a thin curved beam. The theorem states that the displacement δ_q at the point where a load Q is

applied can be found by

$$\delta_q = \frac{\partial \mathbf{U}}{\partial Q} = \int_0^l \frac{M_x}{EI}\frac{\partial M_x}{\partial Q}dx, \tag{6.8}$$

where $\mathbf{U}$ is the elastic strain energy, M_x is the bending moment, I is the area moment of inertia, and x is the distance along the beam. By using symmetry, we only consider a quadrant of the pipe's cross-section which is loaded with a force $V = F/2$ (Figure 6.16(a)). The idealized thin beam has a width equal to the length of the pipe L (X direction), and a depth of t in the bending axis (perpendicular to X), resulting in the area moment of inertia $I = Lt^3/12$. A point along the beam is defined as a function of the angle θ, and the bending moment (M_θ) and the partial derivatives are calculated as

$$M_\theta = Vr\sin\theta - M_0, \qquad \frac{\partial M_\theta}{\partial V} = r\sin\theta, \qquad \frac{\partial M_\theta}{\partial M_0} = -1. \tag{6.9}$$

Using the theorem we can now calculate

$$\delta_{M_0} = \int_0^l \frac{M_x}{EI}\frac{\partial M_x}{\partial M_0}dx = \frac{1}{EI}\int_0^{\pi/2}(Vr\sin\theta - M_0) * (-1) * rd\theta = \left(\frac{\pi}{2}M_0 - Vr\right)\frac{r}{EI}, \tag{6.10}$$

$$\delta_V = \int_0^l \frac{M_x}{EI}\frac{\partial M_x}{\partial V}dx = \frac{1}{EI}\int_0^{\pi/2}(Vr\sin\theta - M_0) * r\sin\theta * rd\theta = \left(\frac{\pi}{4}Vr - M_0\right)\frac{r^2}{EI}. \tag{6.11}$$

By enforcing symmetry, the rotation at the unrestrained end of the beam will be $M_0 = 0$, and using Equation 6.10 we find that $M_0 = 2Vr/\pi$. Substituting M_0 into Equation 6.11, the total diametric deflection coaxial with the applied load is found to be

$$2\delta_V = 2\left(\frac{\pi}{4} - \frac{2}{\pi}\right)\frac{Vr^3}{EI} = \left(\frac{\pi}{4} - \frac{2}{\pi}\right)\frac{12Fr^3}{ELt^3}. \tag{6.12}$$

If we wish to find the total diametric deflection perpendicular with the applied load, we can use a fictitious load H applied horizontally at the free end of the curved beam, and use the same methodology to find

$$2\delta_H = 2\left(\frac{2}{\pi} - \frac{1}{2}\right)\frac{Vr^3}{EI} = \left(\frac{2}{\pi} - \frac{1}{2}\right)\frac{12Fr^3}{ELt^3}. \tag{6.13}$$

6.9 Practical considerations and extensions of reconfigurable origami tubes

In this section, we propose future research on the reconfigurable tubes to explore practical applications, considerations for physical fabrication, and non-linear behaviors that can extended capabilities. This section is meant to inform and motivate future research, rather than to provide a holistic discussion on the different topics.

6.9.1 Practical applications

The polygonal cross-section origami tubes discussed in this chapter open up a variety of applications in science and engineering. The continuous perimeter of the cross-sections could enable the tubes to be used in fluid flow applications. More traditional applications would involve primarily using these tubular origami as deployable pipe-like (Martinez et al., 2012; Schenk et al., 2013, 2014a) or bellow systems (Yasuda et al., 2013; Francis et al., 2014). These could have wide and varied applications including deployable pipes for construction, biomedical devices, or inflatable space structure components. The new projection definitions introduced in Section 6.3, provide a new capability where the origami tubes can follow a curved profile when deployed, versus the straight profile of previously introduced tubes. An instance taking advantage of this benefit, would be constructing a ventilation system, where the entire origami tube is deployed to carry air through a congested area, rather than connecting multiple straight and curved pipe segments. The properties studied in Section 6.8, show added benefits where the polygonal tubes have more stiffness for out-of-plane loading, than a conventional pipe with a constant cross-section. This property could allow for the deployable construction of culverts, or other pipes that need to carry large loads.

The programmable capability of the tube cross-sections offers novel applications where the structure can morph and adapt. The tubes can have an adaptable volume, surface properties, mechanical characteristics and more, simply through reconfiguring the polygonal cross-section. For example, components placed inside aircraft wing could be used to change the lift and drag properties of the wing for different stages of flight (Barbarino et al., 2011). The variable stiffness properties of the origami tubes discussed in Section 6.7 could allow for new devices in aerospace, mechanical, and civil engineering. Robotic components, such as the deployable and reconfigurable arm in Figure 6.17 could be designed to simultaneously

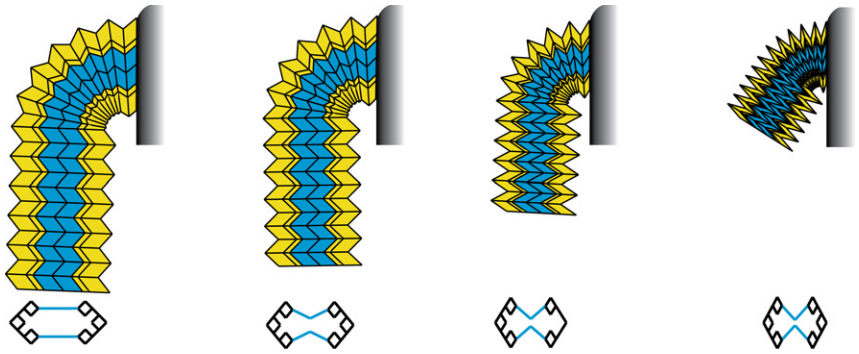

Figure 6.17: Potential application of origami tubes used as a robotic arm with reconfigurable components. The cross-section shown on the bottom reduces in area and could be used as a gripper when the tube is retracting.

fulfil multiple functions. A griper can be used with the reconfigurable cross-section, while the cellular divisions could add stiffness and carry electrical wiring, pneumatic tubes, or other utilities (e.g. similar to multi-functional dental tools). Although these applications are still far from reality, they offer many potential advancements from current day engineering approaches.

6.9.2 Design and fabrication

There is currently a tremendous amount of research aimed at making origami feasible for real world applications. The geometric origami design, fabrication methods, materials, and deployment mechanisms, all depend on the scale and function of the origami system. For small applications, origami can be 3D printed with living hinges (Deng and Chen, 2013). More simply however, it is possible to cut out the origami from a flat sheet and fold the system along perforated or etched fold lines. As a proof of concept, we have fabricated several small ($\approx$ 30 cm) paper models (Figures 6.16, 6.18, and 6.19) to highlight the capabilities of the reconfigurable polygonal tubes. All models are manufactured from 160 g/m^2 paper that has an approximate thickness of 0.25 mm. Panel heights and widths vary from 1 to 3 cm, thus maintaining a relatively high length/thickness ratio that is typical for origami. The folds are created by perforating the paper with 0.5 mm cuts spaced evenly at 1 mm. Because the tubes are not developable, we cut out a flat sheet for each of the cross-section edges, and use tabs to adhere the multiple sheets together (Figure 6.18(a)). This or a similar methodology would need to be used for manufacturing the polygonal origami out of flat sheets. When extending

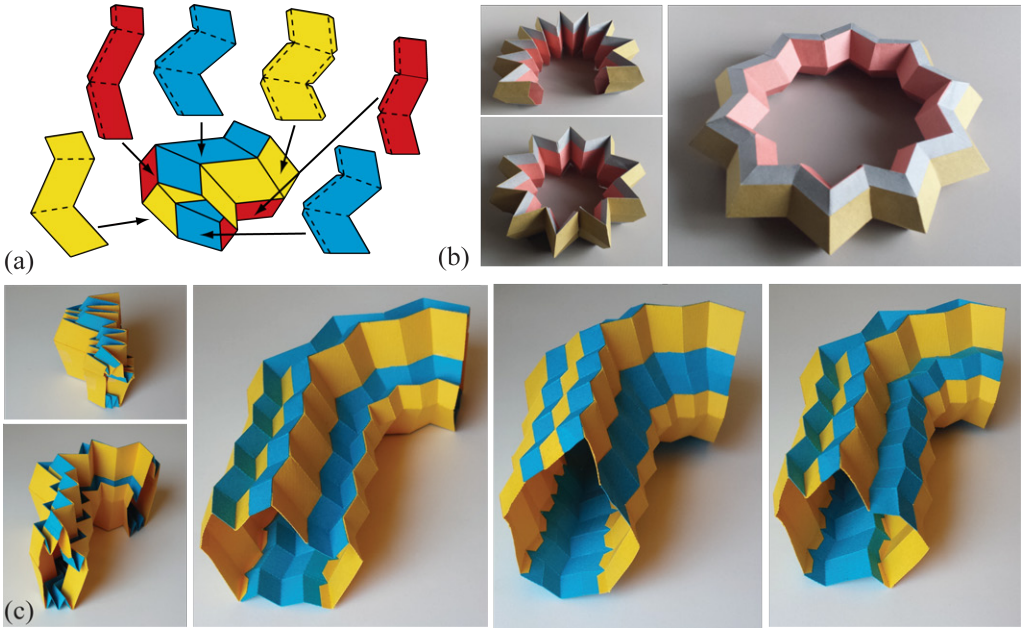

Figure 6.18: (a) Strips of panels cut out from flat sheets can be used to construct the three dimensional, non-developable tube. Dashed lines indicate fold lines, and the tabs at the sides of the sheets can be used to attach sheets together. (b) Physical model of a six-sided polygonal tube that forms a star when fully deployed (c) Physical model of the reconfigurable origami from Figure 6.1 is shown in different configurations. The tabs for attachment are visible on the bottom.

origami to the medium scales it is possible to use layered composites where a flexible sheet that allows folding is sandwiched between more rigid panels (Hawkes et al., 2010; Ma et al., 2012; Peraza-Hernandez et al., 2014). Large origami structures could be constructed by using thickened panels interconnected by hinges rather than fold lines. For various applications in the real world the finite thickness of origami sheets begins to affect the system behavior, and the idealized zero-thickness assumptions are no longer valid. Current research aims to account for thickness in kinematics and manufacturing in order to prevent self-intersection while minimizing the size of the stowed structure (Hoberman, 2010; Tachi, 2011; Chen et al., 2015). To make the reconfigurable polygonal tubes reliable and cost effective for industrial applications more innovation will still be needed. In particular, research should explore: materials and systems to allow multiple folding/unfolding cycles; rapid fabrication methods; mechanisms to facilitate deployment; and incorporating thickness into the tube design. The programmable switches of the polygonal tubes may also require new methods for rapid or remote actuation and reconfiguration.

6.9.3 Non-linear deformations and extensions

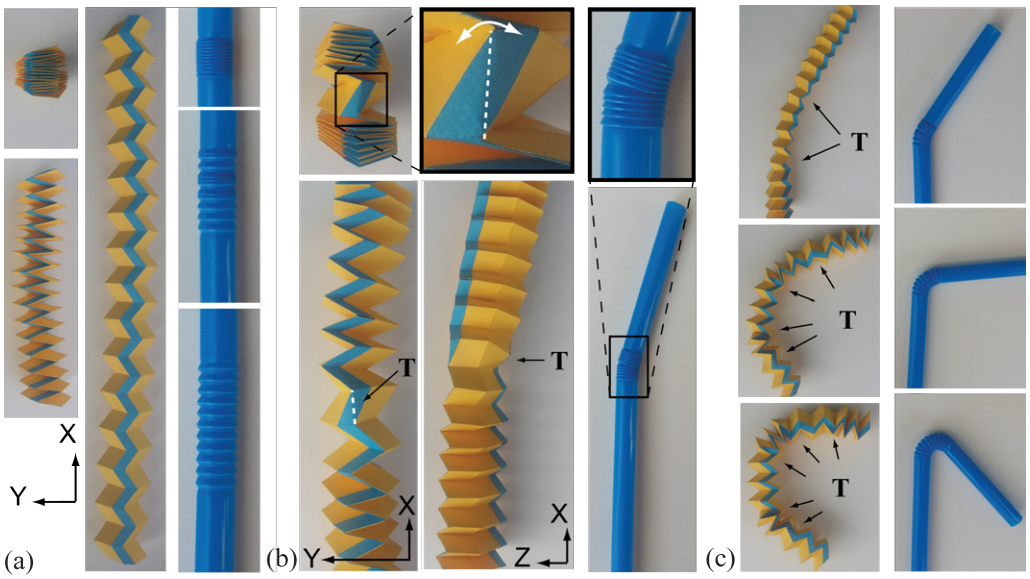

Figure 6.19: Localized distortion in the six-sided origami tube (left) can bring about new non-linear behaviors similar to those of bendable drinking straws (right). (a) Unfolding of the structures in the prescribed *straight* direction. (b) A single *transition* point indicated by a T is introduced in the origami tube. At this point a panel of the reconfigurable segment bends across its diagonal, allowing for a change in configuration to occur in the middle of the tube. (c) Multiple transition points lead to a global curvature over the length of the tube.

Most research on origami, as well as most of this thesis, take advantage of only the rigid and prescribed folding mechanisms of the system. However, some recent findings have shown that there exists a wide range of origami deformations where bending in the panels is encouraged (Silverberg et al., 2014, 2015). These deformations could be substantially more complex than the rigid kinematics, and could correspond to highly non-linear behaviors of the thin sheet origami. In Figure 6.19 (b) we show localized bending that occurs on one of the switch panels of a polygonal tube with six edges. This allows the tube to have different cross-section configurations at different locations of the tube, i.e. Configuration I: below the transition point T and Configuration II: above it. The tube is initially constructed straight with 30 constant angle projections, but with the transition point there is a shift in the direction that the tube follows. Although each transition points causes a localized change in direction, as more transition points are included, the origami tube can go from a straight to a curved structure. This phenomenon is similar to conventional bending drinking straws (Figure 6.19 (c)). The physical models of the polygonal tubes also showed some bistable

and multi-stable effects, similar to other origami structures (Silverberg et al., 2015; Hanna et al., 2014; Waitukaitis et al., 2015). Multi-stability with the reconfigurable tubes could provide new ideas and applications. More complex tube cross-sections where more switches could be augmented, or longer tubes could lead to other interesting bending and non-linear effects.

6.10 Concluding remarks

We introduce a new category of origami tubes that have reconfigurable polygonal cross-sections. The tubes are rigid and flat foldable, and have a continuous perimeter. The cross-sections of the tubes can be a wide variety of convex or non-convex polygonal shapes that follow translational symmetry. Projection is used to define the three dimensional shape of the tube, but non-admissible (e.g. non-symmetric) projections, may limit the flat and rigid foldability of the system. The cross-section geometry can contain any number of n switches that can be used like binary bits to program the geometric reconfiguration of the cross-section. We show that the total number of possible cross-section variations for a tube follow the central binomial coefficient of n. A cellular cross-section or coupling of multiple tubes can be used to create a new variety of assemblages that enhance the functionality and reconfigurable properties of the tubes.

In addition to the geometric variations and reconfigurable kinematics, this chapter also explores some mechanical properties of the polygonal tubes. We show that the tubes have only one flexible mode for kinematic deployment for which the stiffness is not significantly influenced by reconfiguring the cross-section. On the other hand, the cross-section configuration can influence other deformation modes and the out-of-plane stiffness of the tubes. This property can be used to make tunable structures that can change their mechanical properties. If the origami tubes are used as circular pipes, they can be designed to have a high out-of-plane stiffness similar to that of corrugated pipes. Finally, we propose future research directions on applications, fabrication, and non-linear deformations, all of which will enhance the practicality, functionality and capability of the reconfigurable tubes. We envision that the physical attributes, versatility, and programmable characteristics of the polygonal origami tubes will enable solutions of varying scale in science and engineering.

CHAPTER 7

CONCLUSIONS AND FUTURE WORK

This thesis makes contributions to origami engineering in several different aspects. In our work, we explore and quantify the stiffness of local origami behaviors such as bending of panels and fold lines. We improve and verify analytical models that can use the local stiffness characteristics for performing global simulation of origami structures. We use eigenvalues, bandgaps, and structural analyses to explore and characterize different origami strictures. New methods of coupling origami tubes into assemblages are introduced, and generalized methods are developed for creating tubes of desired shapes. We explore the unique mechanical characteristics of the different origami tubes and explore how the structural behaviors can be modified and tuned. In summary, this thesis explores how geometry can be used to tailor the stiffness of origami type structures. This chapter summarizes the main findings and developments from our work, and provides directions for future research.

7.1 Summary

The main topics covered in this thesis are introduced in Chapter 1. We discuss the potential of origami for engineering applications, and we introduce the objectives of our work, which lie at the intersection of the origami geometry and structural behavior. The origami folding pattern can determine the folding characteristics, possible fabrication methods, and the structural behavior of the system. Origami can be used to create a rich variety of three dimensional shapes that can be deployed and possibly reconfigured. The geometry of the origami significantly affects stiffness both on a local and on a global scale. In Chapters 2 and 3 of the thesis, we explore, verify, and inform a bar and hinge approach that can be used for the structural analysis of origami. In Chapters 4, 5 and 6 we introduce new variations of tubular origami structures and investigate their structural and mechanical characteristics.

Chapter 2 explores stiffness scaling of origami with an objective of informing the parameters of the N5B8 model that is later explored in Chapter 3. We create scale and material dependent phenomenological relations to quantify stiffness of the different origami behaviors.

For in-plane loads, the N5B8 model provides an isotropic behavior, and can estimate the stiffness of square and skewed panels. The model overestimates shear stiffness, but captures tensile stiffness well. We verify that the results of Lobkovsky et al. (1995) are appropriate for quantifying out-of-plane panel bending stiffness for large displacements. For small displacement panel bending, we show that the panel geometries that are skewed and elongated increase the origami stiffness. For fold line bending, we explore existing experimental results and verify that stiffness likely scales with the fold length, bending modulus of the sheet, and with the inverse of a length scale parameter (i.e. $1/L^*$) (Lechenault et al., 2014). The length scale parameter is believed to scale with thickness but is also highly dependent on the material, fabrication, and geometric characteristics of the fold. We find that for most origami, bending occurs primarily at the fold lines, with typical fold to panel stiffness ratios of 1/20 to 3.

In Chapter 3, we explore and discuss the improved bar and hinge model that can be used for the global structural analysis of origami systems. The model uses five nodes and eight bars (N5B8 model) to simulate in-plane behavior of origami panels, while rotational hinges are used for out-of-plane bending of the panels and fold lines. The model improves upon existing origami models because it is scalable, isotopic, and incorporates realistic material properties. The model is easy to use and understand, it is versatile, efficient and can be adapted for a wide range of applications. We show possible applications of the model, including simulating rigid folding kinematics, evaluating eigenvalue bandgaps, cantilever analyses, and origami metamaterial characterization. The bar and hinge model cannot capture local effects in origami, but it can be a useful analytical and design tool to facilitate application of origami.

The remainder of the thesis introduces several new types of origami tubes and explores their structural characteristics. In Chapter 4, we study single and coupled origami tubes. We show that tubes coupled in a zipper fashion have a unique property, in that they are easy to deploy yet they are stiff for any other type of bending or twisting motion. The zipper coupled tubes yield an unusually large eigenvalue bandgap that represents the difference in stiffness between the rigid body folding and subsequent deformation modes. The stiffness increase is much larger from the zipper arrangement than could be achieved with other coupling methods or with variations in the fold pattern geometry. The zipper coupled origami tubes engage the thin sheets in tension, compression, and shear for any deformation mode that

does not follow the kinematic deployment sequence. We show local and global variations in obtaining zipper coupling and explore the possibility of using these tubes to create cellular assemblages with adjustable properties.

Chapter 5 provides a more generalized framework for constructing the zipper coupled tubes. The tubes can have different cross-sections, straight or curved profiles, and depending on their definitions they could be reconfigurable (fold through different motions). We explore the coupled tubes by performing three point bending tests, and we evaluate the influence of geometry on the orthogonal stiffness of the structures. We find that straight tubes with square cross-sections typically have the highest maximum stiffness. While tubes that are more zig-zagged and have rhombus cross-sections have higher stiffness during deployment at the cost of a slightly reduced maximum stiffness. We show that the tubes can be used to construct flat slabs, arches, and roof like structures consisting of coupled tubes.

In Chapter 6, we introduce and explore origami tubes with polygonal cross-sections that can be reconfigured into numerous new geometries. The tubes do not need to be straight, and can be constructed to follow a non-linear curved line when deployed. The cross-section, kinematics, and mechanical characteristics of the tubular structures can be reprogrammed by changing the direction of folding at some folds. We discuss the rich variety of structures that can be conceived with the polygonal tubes, and we show limitations that govern the global geometric design. We quantify the global stiffness of the origami tubes through eigenvalue and structural analyses and highlight the interesting mechanical characteristics of these new systems. We show that if the origami tubes are used as a circular pipe, they can be designed to have a high out-of-plane stiffness similar to corrugated pipes.

7.2 Suggestions for future work

Because origami engineering is a relatively young field, there are numerous viable directions for future exploration. This section provides both specific and more broad ideas for future research in the field. Some of the ideas are direct extensions of this thesis while others are somewhat unrelated, yet they are pressing problems in the field of origami research. Some more specific ideas for extending this work are also contained within the discussions and concluding remarks of each of the previous chapters.

7.2.1 Geometric variation beyond the Miura-ori

One of the most interesting problems in the field of origami engineering is extending beyond known patterns and discovering new origami that may posses new and interesting characteristics. Discovery of new patterns can result in novel folding/deployment mechanisms, advanced and tunable mechanical characteristics, adaptable systems with multiple folding motions, new origami-like three dimensional systems.

The overwhelming research in the field, including this thesis, have built upon and extended the well known Miura-ori pattern. Within Miura-ori patterns there have been a variety of pattern explorations and generalizations (Tachi, 2009a, 2010a; Gattas et al., 2013; Xie et al., 2015b). In Chapters 5 and 6, we developed generalized methods for defining single and coupled origami tubes, however these methods still follow many of the same concepts as previous research. The most generalized extensions of the Miura-ori pattern has likely been by Dudte et al. (2016) where a Miura-ori inspired pattern can be developed to match an arbitrary three dimensional surface (although these origami may be non-rigid and non-flat foldable). There are certainly further extensions of the Miura-ori, and there are other existing patterns, however there lies potential in breaking away from these known geometries and exploring entirely new folded systems.

One direction of future pursuit could be to explore origami patterns through optimization or other form finding algorithms. In Section 3.3.1, we briefly discuss how the bar and hinge model could be used to find possible rigid folding motions starting from a known pattern. Other methods have looked at non-rigid folding patterns to design origami based mechanisms (Fuchi et al., 2015b, 2016). There is a potential to explore existing form finding schemes and adapting them for origami pattern discovery, and it would be worthwhile to develop new schemes tailored specifically for origami discovery.

When pursuing new pattern discovery, it would be worthwhile to consider the geometric constraints of origami patterns (flat foldability, rigid foldability, developability, etc...). An interesting concept would be to *study and develop new patterns with more than four folds per vertex*. As an example, the Ron Resch pattern has six folds per vertex and has entirely different characteristics from the Miura-ori. Many other patterns could similarly be developed and explored, and would be unique as they would have multiple degrees of freedom for

rigid folding. The generality of fold placement around a vertex would greatly influence the system kinematics and would change multiple of the system's properties. These patterns would also allow for much more reconfigurability and adaptability than current methods. Coupling multiples of these patterns together could further enhance their characteristics and applications.

7.2.2 Simple and efficient multiphysical models for origami

The analytical bar and hinge model presented in Chapters 2 and 3 can provide a good estimate for the folding kinematics, the three dimensional geometry of origami components (location of folds and panels), and the global elastic behavior. Furthermore, the model is easy to use and efficient (in comparison to detailed FE formulations). Specific extensions of the model are discussed in Section 3.5.3. In addition to those improvements, it would be useful to incorporate multiphysical behaviors within the bar and hinge methodology such that kinematics, elasticity, and other phenomena are considered simultaneously. As origami becomes common in different fields of engineering thermal, acoustic, electromagnetic, and other physical models can be combined and modeled using the simplified framework.

The bar and hinge approach can fill the gap in simulation capabilities between local behaviors and detailed global models. In other words, the bar and hinge model can incorporate local phenomenological behaviors within a global system analysis. The multiphysical behaviors can first be studied on a local scale of the folds and panels and can be appropriately incorporated within the same framework. Reasonable estimates of multiphysical characteristics would be sufficient in understanding the overall global behavior of origami systems. The simple and efficient models could be used to explore how multiphysical behaviors interact with geometry, kinematics, and the elastic behavior of origami.

For example, modeling thermal effects in origami structures could be useful at multiple scales and for different applications. Origami systems with heat actuated hinges would require modeling of the thermal gradients to predict deployment. The deployment kinematics and elastic behavior could also be tailored to minimize the force, and thermal input requirement to achieve actuation. Thermal effects in large scale deployable structures may also be of significant importance. It is possible that due to thermal expansion and contraction

the deployment characteristics of the system become constrained and it is not possible to deploy or actuate a system. The thermal conductivity of origami cellular assemblages could also be explored to develop origami with high insulation or adaptable components with variable thermal conductivity. Another example would be incorporating electromagnetic effects with the origami to use for preliminary research on reconfiguring of antenna components. Electromagnetic systems that employ origami designs can allow for tunable electromagnetic properties along with the other benefits of origami. Other multiphysical analyses could lead to new applications of origami in engineering.

7.2.3 Harnessing stiffness from crumpling origami

Bending, crumpling and connecting thin sheets into cellular assemblages can significantly increases the global stiffness of the system (Vliegenthart and Gompper, 2006; Cambou and Menon, 2011). As we discuss in Chapter 4, we can harness some of these benefits through the zipper coupling, and cellular assemblages. However, our work has focused on small displacement linear analyses, and there is potential for harnessing beneficial effects associated with large displacements, crumpling, and nonlinearity of origami. Firstly, there is more to explore and study about the nonlinear behaviors of thin sheets, and there may be ways to harness their properties for engineering applications. The novel properties could be applied to origami structures or they could be used for other types of assembled thin sheet systems.

As an example, consider the restrained panel bending explored in Section 2.2. We verified that the bending stiffness of the thin sheets increases with large displacements with $\theta^{4/3}$ (Lobkovsky et al., 1995). Being able to capture this stiffening effect in a controlled manner could be used to create metamaterials that stiffen or loose stiffness when compressed (if deformed initially). This property could also be used to store mechanical energy in thin sheet structures. An origami with pre-deformed panels could use the internal energy to snap-open into a deployed configuration where the panels are straight.

The energy dissipative property of crumpling thin sheets has been used and explored for various types of cellular and origami assemblages (e.g. Heimbs (2013); Schenk et al. (2014a)). The multiple energy states associated with the buckling could be built into an origami system to create multi-stable structures. These multi-stable properties could be used for designing

energy storage or energy harvesting devices. Alternatively, crumpling could be used to affix a deploying origami structure such that it would lock into position and not fold back or reconfigure.

7.2.4 Optimization of cellular origami assemblages

In Chapter 5, we present a generalized methodology for zipper coupling of origami tubes. We also show several additional methods in which tubes can be coupled and stacked into cellular systems. We have primarily focused our research on studying the stiffness characteristic of a single or of two coupled tubes. It would be useful to explore and optimize larger systems where multiple tubes are connected and interact together. One specific topic of interests would be to further explore and optimize the properties of arch and slab type systems created by zipper coupling in the horizontal direction (i.e. Figure 4.25). Another topic would be to further explore cellular systems with more generalized geometries. The cellular assemblage presented in this work uses the same tube geometry throughout, however, the generalized cross-sections and projection angles could be applied to generate new cellular systems.

Optimization could be performed to maximize the eigenvalue bandgap or improve stiffness characteristics of the origami. Beyond these it would be useful to begin exploring localized effects in the cellular systems such as crumpling, buckling, and other failure mechanisms (e.g. see Section 7.2.3 above). Optimization for such localized phenomena can be done on a unit cell, before the global geometry of the assemblage is considered. Origami assemblages may be optimized to increase weight-to-stiffness ratios, impact energy dissipation, and other mechanical properties. Cellular origami metamaterials that have multiphysical functions could be optimized to improve tunability and reliability during reconfiguration.

7.2.5 Connecting structural mechanics with the materials and fabrication of origami

The materials and manufacturing of origami is beyond the focus of this work, however, it is a fundamental field of study for moving the field forward. Appendix A of the thesis provides a brief review on applications, materials, and the fabrication of origami. The

intersection between the practical aspects of origami and structural mechanics can provide many interesting and fruitful directions for future research. Both local and global phenomena in origami engineered systems are just now being discovered, and approaching them in the context of mechanics could be useful.

As an example, the presence of non-zero thickness in folding structures can pose problems as stress concentrations occur at the vertices. Some techniques have explored ways to create hinged systems with adapted kinematics that can accommodate the finite thickness (e.g. Hoberman (2010); Tachi (2011); Chen et al. (2015)). Using structural mechanics, it may be possible to explore the origami pattern, vertex design, or the entire fold line system to find solutions that reduce the stress concentrations to an acceptable range.

Structural mechanics could also be used to address issues that occur with fabricating or deploying origami structures. In some origami systems (e.g. hinge and panel structures) the deployment and mobility may be affected by design imperfections or thermal variations. To mitigate these effects the global structure could be redesigned to accommodate larger imperfections or to allow for alternative motions that allow deployment. Locally, folds and hinge geometries may be adapted to reduce adverse deployment scenarios. As the community continues to pursue new applications of origami in engineering, the structural mechanics can provide solutions and receive inspiration for future study.

APPENDIX A

LITERATURE REVIEW: APPLICATIONS, MATERIALS, AND FABRICATION FOR ORIGAMI STRUCTURES

Origami structures can be constructed in a multitude of ways ranging from crumpling a piece of paper to creating a system of panels and hinges that move in a predefined fashion. For our study, we primarily focus on the latter set of origami systems, where at the least there are a predefined set of folds and panels. The materials and fabrication of these types of structures depends highly on the scale of the system. Applications can range in size with the largest possibly being civil engineering mega-structures to small structures in the millimeter or even molecular range. This Appendix focuses more on medium to large scales and is provided to give context of how we can use origami in real world engineering applications. We acknowledge that this is not an all-encompassing review, however it discusses practices and discusses ideas that can make origami engineering a practical and cost effective reality. The contents of this Appendix are: Section A.1 discusses state-of-the-art conceptions and existing applications of origami structures with respect to the scale of the system; Section A.2 explores materials and the systems that can be used to create origami structures; finally, methods for fabricating and deploying origami structures are discussed in Section A.3.

A.1 Applications of origami structures in engineering

Origami can be used to create structures that have adaptable characteristics, for example a building façade could be made more stiff in cases of high winds or snow loads, yet it could be made more flexible to accommodate large displacements in the the event of an earthquake. On the small scale, we could construct material with novel properties, and microscopic devices that can be used for biomedical applications. The ways that the origami structures can be applied in engineering can vary widely as well. We envision that the origami structure will fit in one of the following categories: : (a) folding of initially flat systems to adapt to new space constraints or to serve an alternative function; (b) deployment of initially folded assemblies such that the new structures would fulfill some set of requirements or fill some prescribed space; (c) scenarios where (a) and (b) are coupled; and (d) cases where a structure

would fold and unfold numerous times during its design life to fulfill a single or a multitude of tasks.

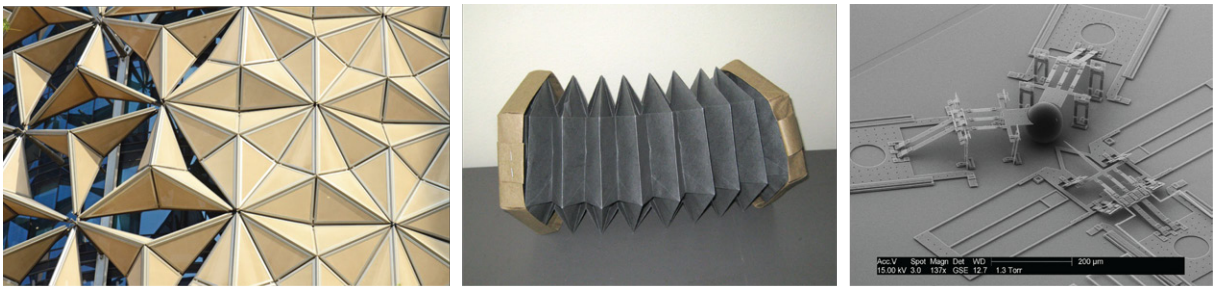

(a) (b) (c)

Figure A.1: **(a)** Shading façade system on the Al Bahr towers designed by Aedas architects, photo courtesy of Inhabitat-Blog (2012), **(b)** Origami bellows model by Joseph Wu (Wu, 2008), **(c)** Microscopic nanoinjector using origami techniques by Aten et al. (2014), photo courtesy of BYU-News-Release (2014).

A.1.1 Large scale applications

Here we discuss the use of origami in large scale structures for example two or more meters in length. Due to the scale, these systems are also likely to require rather thick materials, and are likely to use the hinge and panel type system discussed in Section A.2.1. Various origami patterns have been used for inspiring and conceptualizing the architecture of building structures . The origami forms add interesting form and aesthetic quality to the building façade and other elements. Some prominent examples include the United States Air Force Academy Cadet Chapel in Colorado designed by Skidmore, Owings and Merrill (Skidmore Owings and Merrill, 1962); the Basque Health Department Headquarters in Bilbao, Spain designed by COLL-BARREU ARQUITECTOS (Arquitectos, 2008); and recently the Barclays headquarters building in Paris, France designed by Manuelle Gautrand (Gautrand, 2011). For the most part these designs are static and do not have the capability of changing their configuration. In some cases however, the origami structures are designed with a variable geometry so that they can morph and adapt to different purposes. (Del Grosso and Basso, 2010) discusses some possible advantages that could be achieved by dynamically adapting building skins, and introduces a method for improving the acoustic properties of a facility depending on the usage space. Researchers have also explored the characteristics of folded plate structures are in detail with the objective of using these systems as a building envelopes

(Falk and Von Buelow, 2011; Falk et al., 2012). An adaptive origami based shading façade system (Fig. A.1 a) was adopted by Aedas architects on the Al Bahr building. For civil engineering, origami engineering can be used in the following methods:

- Deployable shelters for use following natural disasters and other emergencies.
- Draw bridges that can carry land vehicles and can reconfigure to allow passage of water traffic as well.
- Deployable systems for large structures (e.g. deployable column and façade assemblies).
- Prefabricated systems that can be stowed tightly for transportation on a truck (e.g. tower structures).
- Façade or other structural elements that can move to change the stiffness of the structure.
- Deployable pipelines, retaining walls, culverts, and other structures that could be deployed.

For large scale architectural purposes we can envision the following potential advantages to be achieved by using origami structures in design:

- Artistic enhancement to the façade, walls, decorations, and other aesthetic elements.
- Shading systems where façade elements can move to reduce the heat gain of the building during sunny days
- Wall and ceiling panels that can adapt to enhance acoustics properties of a concert hall or multifunctional meeting room
- Partition walls that can reconfigure depending on the necessary usage
- Window and panels that can automatically open or close to provide appropriate ventilation for the structure.

Outside of the civil engineering community large scale origami structures could also be used in mechanical and the aerospace industries. Machines that have a multitude of tasks often need to have transformable sections for example recreational and vendor type vehicles need to have expanding components to allow for more room for occupants. In the space industry origami has also become a study of interest since a structure can be launched in a small compartment and can expand into a large functional system. Researchers have developed,

studied, and tested a variety of deployable space array structures ((e.g. Miura, 1985; Malone and Williams, 1996; Jenkins, 2001; Campbell et al., 2006; Zirbel et al., 2013) and many others). The origami type array can deploy to have a much larger surface area, and this allows for a large solar power source. Due to the lack of air in space, a thin membrane can be used for these structures, and it would not experience large forces as may be common on earth. Large scale mechanical, aerospace, and multidisciplinary applications could include:

- Vehicles with deployable sections to increase occupancy.
- Covers for truck and train cars.
- Crane structures that need to change shape and size rapidly to fulfill their function.
- Construction equipment, gantry cranes, and other heavy machines that need adjustable moving components.
- Solar panel arrays that can be deployed in space.
- Space station compartments for astronauts.

A.1.2 Medium scale applications

Medium size origami structures could range in order from a few centimeters to perhaps a meter or so in length. Due to improvements in materials and fabrication methods, we believe that in the future these medium size structures could be constructed using any of the the three systems discussed in Section A.2. Potential applications of origami structures in the medium scale include:

- Robotic arms, legs, and other components.
- Actuators and deployable booms.
- Foldable furniture.
- Deployable cantilevers.
- Devices and systems that can permit thermal expansion or movement of a larger structure (e.g. bellow of a bus or thermal joint in a highway bridge)
- Toys for amusement and entertainment.
- Devices for education in origami, mathematics, and engineering.

Origami has already made groundbreaking advancements in robotics. Origami can allow for easy manufacture and kinetically functional, multi-degree of freedom systems that can

move. The Harvard Microrobotics Lab (Wood and Others, 2014) have made large strides in producing working robotics through the use of origami. For example, they have developed a working flying robot that is assembled from a laser cut plate and is snapped into a three dimensional configuration by folding and bending the thin material at specific locations (e.g. Ma et al., 2012, 2013). A method for folding a reprogrammable material is shown by Hawkes et al. (2010), where heat can be applied to to reconfigure a planar sheet into a 3-dimensional folded object that is several centimeters long. More recently Felton et al. (2014) introduced a walking robot prototype that can be created by cutting a layered sheet and then heating the folds to create a three dimensional walking robot. Larger applications of origami have not yet been realized, but there is a tremendous amount of potential for future applications. For example, the coupled folding tubes discussed in this document have the potential to be used as deployable cantilevers. These could be used to construct transforming legs and deployable arms for humanoid size robots.

In addition to robotics, origami has already been used in more traditional forms of mechanical engineering. Origami techniques have already been used successfully to create tubes that act as actuators or deployable booms. Origami is especially suitable for these application due to the pre-configured small stowing configuration, and thus these systems have seen a tremendous amount of recent study and testing (e.g. Martinez et al., 2012; Schenk et al., 2013, 2014b; Fernandez et al., 2014). Gases or liquids could be pumped in at one of the ends of these structures and can lead the structure to deploy. These types of deployabe boom structures could also be considered as "large" and can be on the order of several meters. In contrast to most other large applications however, these structures can be built from flexible materials and do not need to use thick material or rigid origami kinematics. For completeness we note that there exist a variety of other deployable structures such as scissor trusses, deployable tensegrity structures and many more. For brevity we do not discuss these structures here, but we note that the kinematic considerations for truss structures are similar to those of rigid origami and it is often possible to use a origami in parallel with other deployable mechanisms.

The transformable origami could lend itself to numerous uses in everyday objects and devices. For example tables and chairs that have variable height control can take advantage of origami structures in creating lifting mechanisms and side covers or perhaps counter tops

can increase in area by having folding origami extensions. Bellows and similar origami systems are already common and used in industry, a paper schematic is shown in Fig. A.1 b. In the construction of bellows, however, we note that rigid foldable polyhedra cannot be used, and cannot follow rigid folding motion. Instead bellows would require some form of elastic or plastic deformation, beyond that defined by the kinematics of the system (Connelly et al., 1997). Use of folding and origami in furniture can even be traced in the most traditional folding chairs and tables available on the market. These devices use folding as the backbone in design, to produce a versatile product that can be stowed away compactly when not in use. Some origami furniture has already been made available (e.g. Origami-Resource-Center, 2014; Fuchs and Funke, 2104), and we can expect that it will become more common as these products decrease in cost and simultaneously increase in functionality.

A.1.3 Small scale applications

Small origami in the scale of a centimeter or much less can often take advantage of material and local flexibility to achieve folding of the structure. Micro and nano origami structures do not require rigid folding motions and and can accommodate bending in the panel segments. These structures do not require thickened panels, so it is more common that they would be constructed either from composite type systems (Section A.2.2) or from a homogeneous system (Section A.2.3). The small scale applications are somewhat beyond the global scope of this research, and thus only a brief literature summary is provided here. When considering micro and nano applications we believe that origami has the potential to revolutionize the following topics:

- Biomedical devices.
- Micro and nano robotics and devices.
- Electronics manufacturing and assembly.
- Synthetic material design.
- Molecular and DNA folding for improvements in biochemistry.

An interesting biomedical application was introduced by Kuribayashi et al. (2006) who showed the possibility of using origami titanium/nickel stent grafts to open up blocked arteries. Small robotics have been studied by the Harvard Microrobotics Lab (Wood and Others,

2014) with a potential for various new devices. Guo et al. (2009) have shown methods for folding thin Silicon sheets into cells with the potential of improved photovoltaic properties. Microscopic nanoinjector using origami techniques were created by Aten et al. (2014) (shown in Fig. A.1) can be used for injecting mouse zygotes. Methods for manufacturing micro and nano scale structures that can be used for electronic and optical functionality were recently introduced by Pique et al. (2011) and others. Metamaterials have also become a popular topic in origami, since cellular arrays of patterned origami can behave in unusual ways. Examples of the structured metamaterials developed by origami are discussed in Fuchi et al. (2012); Schenk and Guest (2013); Wei et al. (2013); Lv et al. (2014); Silverberg et al. (2014); Waitukaitis et al. (2015) and others. The mechanics of origami have even been used in the molecular scale to model and tailor the characteristics of molecules and DNA (e.g. Andersen et al., 2009; Schmidt et al., 2011; Han et al., 2011; Yoo and Aksimentiev, 2013). For example, a novel idea has been discussed by Jiang et al. (2012) where origami techniques are used to fold a DNA structure so it can be used to deliver drugs to cancer cells in the body.

A.2 Materials for origami inspired structures

The choice of material and the type of assembly system would depend on several factors such as: scale, purpose of the structure, number of expected folding-unfolding cycles, allowed kinematics, cost, deployment mechanism, and others. In this chapter we discuss three general origami assembly systems, and the materials that are assumed feasible for each of the systems. We show (1) a distinct hinge and panel system; (2) an assembly composed of sandwiched layers, and (3) a homogeneous material system. We believe that large applications will be possible only with hinge and panel systems; small applications are feasibly with sandwich and homogeneous systems; and medium size applications can be created with any of the three discussed methods.

A.2.1 Panel and hinge systems

With rigid foldable structures it is often possible to use thickened panels that will not undergo bending during the operational deployment. For large structures it would be possible to

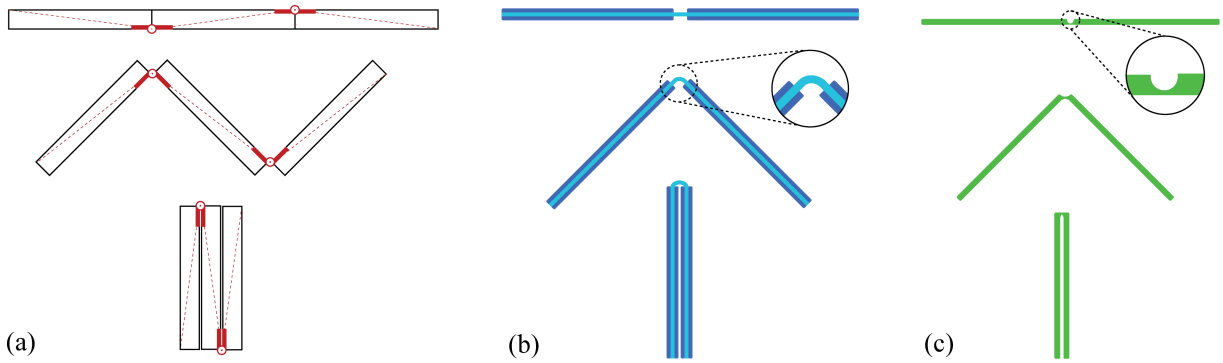

Figure A.2: Section view of the folding kinematics for: **(a)** a hinge and panel type system, **(b)** a composite system ("sandwich system") with stiff material on the top and bottom and a flexible layer in between, **(c)** Homogeneous material systems with a etched living hinge.

use thickened panels interconnected by strong metallic hinges that would act in the same way as the folds do in a simple origami model (Fig. A.2 a). This technique introduces several advantages such as: (i) the hinges can accommodate a large number of folding-unfolding cycles without a change in characteristics; (ii) the thickened panels can serve as structural and architectural elements (e.g. insulation); (iii) other components such as actuating systems or electronic equipment can be accommodated with the thickened panels. The hinges can permit for the deployment of the structure and will transfer loads between the panels. However, although theoretically appealing, the thickened panels pose problems since they cannot follow the rigid body kinematics of zero-thickness origami structures. Some recent research has shown possible realizations for how to create origami structures where the panels have finite thickness (e.g Hoberman, 2004; Tachi, 2009b; Hoberman, 2010; Tachi, 2011; Zirbel et al., 2013). These methods involve placing the hinges on the ends of the panels; inserting additional thin elements to permit kinematics of the thickened material, and designing the global array of panels and folds in a fashion that permits continuous rigid motion of the system. These methods also sometimes discuss the placement of the actual hinge connection, this often needs to be considered for the kinematics and also because the hinges have finite thickness that is in addition to the panel thickness.

The panel-hinge systems can often be constructed with cost effective materials that are commonly available. We believe that the hinges will need to be constructed with stiff metals to be able to carry the large forces. Bearings may also be incorporated in the hinges to allow easy deployment with reduced hinge friction forces. The panels could be constructed

from plastics, wood, metal, concrete, and a variety of engineered composite materials. Metal, wood, and plastic prototypes have already been used for practical applications in architecture and product design (see Section A.1), and there is tremendous potential for innovation of the panel materiality.

A.2.2 Composite systems

Composite material systems have also been used for manufacturing origami prototypes, and although these have a potential for large scale application they currently are mostly used on medium and small scale applications. The systems mostly use some form of sandwiched structure similar to Fig. A.2 b where stiff material layers are attached to a much more flexible material. At the fold lines the stiff material is removed and the flexible material can bend allowing fold rotation. A simple example of this system is the use of stiff panels glued to a cloth. The cloth allows rotation between the two panels, but the panels are mostly restrained from moving apart. The panels in these types of systems can be created from a variety of materials, and depending on the construction method it would also be possible to accommodate finite thickness in these designs. Kinematic considerations may need to be updated similarly to those of the panel and hinge systems.

A wide array of traditional and newly developed materials can be used for both the flexible and the stiff materials. The folds can take advantage of fabrics, polymers, and flexible alloys, while the panels can use metals, engineered plastics, and corrugated material assemblies. Peraza-Hernandez et al. (2014) provide a review of different composite material systems used to create active systems. Zirbel et al. (2013) use Garolite (a type of fiberglass-epoxy laminate) panels placed on a thin Kapton film that is used as backing to connect the thin panels. Lee et al. (2013) use acrylic plates and facilitate the folding using a polyimide film. There is a variety of other methods for these composite systems as well (e.g. Hawkes et al., 2010; Onal et al., 2011; Ryu et al., 2012; Felton et al., 2014).

A.2.3 Homogeneous material systems

These systems are composed of a single material and the bending takes place by deforming the same base material that is used throughout the structure. These types of system do not

necessarily need to take advantage of rigid folding motions, and it is common that the panel segment will be rather flexible. The bending along fold lines of the homogeneous systems can be facilitated either by reducing the cross section along the fold line or changing the mechanical characteristics at that segment.

Reducing the cross section of the material can be achieved in several methods. In typical corrugated cardboard box manufacturing, it is common to pre-crease or score the material (compress the material at the fold line to reduce the cross section). This method for folding thin homogeneous materials has been around for decades and is used in numerous applications for manufacturing and product packaging. Recently Perego and Giampieri (2006), Giampieri et al. (2011), Mentrasti et al. (2013b), Mentrasti et al. (2013a), and others have studied the constitutive relations and behaviors associated with this type of fold creation. Another common method to encourage bending along a specific fold line is to perforate the material along the fold line. The perforation method was used for creating the paper prototypes pictured in this document, and can be achieved easily with a variety of roller and flatbed cutting or punching machines (e.g. Onal et al., 2011). Perforation patterns, methods, and techniques are also being studied in detail for industrial applications of origami (e.g. Industrial-Origami, 2014). Etching and physically reducing the section of the material is also a possible method for prescribing a fold to a specific location. Fig. A.2 c shows a living hinge where the material is cut down at the fold to allow localized bending and rotation of the structural elements (e.g. Mraz, 2004; Deng and Chen, 2013). Living hinges are often made of flexible polymers and can thus facilitate numerous cycles of bending and deformation. The cross section reduction method, is however typically prone to fatigue and fracture of the base material. It is often the case that the material experiences irreversible plastic deformations (e.g. crease lines in most types of paper cannot be removed).

Plastic deformation and micro-fractures along a fold line will reduce the stiffness of the material and often times the fold will become more flexible over time (perhaps experiencing a full fracture and failure after some cycles). Prescribing the fold line can also be done in a similar fashion by creating a localized stress concentration bending the material without prescribing a fold line by removing material. This can be thought of as bending a piece of paper without scoring, or etching it initially. This type of fold is more difficult to prescribe accuratley since its location is more dependent on the global structure geometry and on

the actuation forces. This type of behavior can also be achieved by applying heat, light, electric fields or chemicals to obtain local stresses and bending. Stellman et al. (2007); Pique et al. (2011); Arora et al. (2007) have discussed patterning thin sheets, and applying stress in specific locations to achieve the folding of thin continuous membranes. This does not require that the material is etched or perforated prior to manufacture, and simply concentrating stresses on a line is sufficient to cause the fold to bend. This type of folding can be used with numerous types of traditional and novel materials including metals, polymers, papers, cloth and many more (e.g. Corning, 2014). Recently there have even been promising results in bending and folding of graphene structures (e.g. Cranford et al., 2009; Shenoy and Gracias, 2012; Zhu and Li, 2014).

A.3 Methods for fabrication and deployment

The fabrication and the deployment method could be made different depending on the type of structure, and could be govered by the scale of the structure. Section A.2 discusses the materials and systems that can be used for different origami structures, and often times the type of system, as well as the specific material used are a byproduct of the type of deployment scheme that is implemented for the system. The methods for fabrication and deployment are also similarly affected by the scale of the structure and thus not all different methods are feasible for all scales.

When considering the fabrication of origami structures, there are multiple ways of obtaining the same final result. The hinge and panel systems for example can be assembled in a folded, unfolded, or in an in-between configuration. It is possible to construct the structure in a completely flattened case and then proceed with the deployment, or we can begin with part of the structure and then add on hinges and panels sequentially. Similarly, sandwiched and layered structures could be constructed using one single sheet for the internal flexible layer, or they could also be constructed by using the flexible material only at the specific fold locations. With layered sandwich type systems, it is possible to machine and remove material layers at the prescribed fold line; in this way, the sandwiched structure could be manufactured in a fashion similar to that of the homogenous material systems. The different papers presented in this literature review discuss numerous techniques, materials and

methods in which the different type of systems can be manufactured.

In the past several decades *additive manufacturing* (commonly known as 3D printing) has become a novel and effective method for creating practical objects (France, 2013; Lipson and Kurman, 2013). The appeal of additive manufacturing is that the user can create an discrete, stiff (or flexible), possibly multi-material, 3 dimensional object by only using a machine with only raw material and computational input. The process does not require any molds, specific fixtures and can create arbitrary objects. Additive manufacturing has already been used successfully in structural engineering to print out structures that have been designed with topology optimization (Zegard, 2014). For the design of origami structures additive manufacturing has been used in several applications. Deng and Chen (2013) introduces additive manufacturing integrated with "shrink dinky film" that can be heated to achieve self actuation. In this process the more stiff panels can be created using additive manufacturing to achieve a sandwich type system. Waitukaitis et al. (2015) used 3D printing to create origami patterns interconnected with springs that have multiple stable states. Additive manufacturing has a large potential for revolutionizing the manufacturing and assembly of origami structures. Although multi-material manufacturing is still in its early phases it could be used in constructing the composite type systems. More readily, homogeneous material systems or components of the other systems can be created using additive manufacturing. Additive type processes often have the necessary accuracy, and can easily produce unique patterns.

For large scales, we envision that large forces would need to be applied to the structure, and thus mostly mechanical sources of energy will be necessary to obtain deployment. For example we would need to use external cranes or actuators inside of the structure to obtain a global expansion of the system. These systems may be pre-assembled by simply connecting panels with hinged elements. Recently advancements in robotics, computer science, and automation have made it possible to use computer operated robots to fold simple paper origami patterns (Balkcom and Mason, 2004; Tanaka et al., 2007; Balkcom and Mason, 2008). For larger scales Epps (2014) has also been able to use robotics to bend thin sheet metal into architectural forms. These larger robots (similar to those used in the car assembly industry) could pave the future for large scale structural origami fabrication and manufacturing. Actuation of large systems may also be achieved with vacuumatics where air pressure in a

double membrane system is used to stiffen the structural fold lines (Tachi et al., 2011).

Ongoing research involving shape memory alloys (SMAs) also has the potential for use in large structures. Peraza-Hernandez et al. (2013) show how SMAs can be heated along specific fold lines, and how this can result in relatively large rotations from an initially flat sheet. Tolley et al. (2014) show how pre-manufactured origami patterns with SMAs can simply be uniformly heated and can then transition from a flat to a fully deployed state. SMAs have also been used to facilitate the connections to create folding reprogrammable sheets (Hawkes et al., 2010).

For medium to small scale structures researchers have taken an interest in applying energy in non-mechanical forms to achieve the bending along fold lines and global deployment of the structure. For example Liu et al. (2012) and Ryu et al. (2012) use multi-layered pre-strained polymers and apply light (and thus heat) along specific fold lines to achieve strain on one face of the structure and thus obtain folding of the structure. Gracias (2013) further discusses biochemically responsive materials and possibilities in deploying thin structures using light, heat, application of electrical current and chemical stimulation. A review paper by Peraza-Hernandez et al. (2014) provides a detailed literature review on methods for actuating origami systems. For micro scale structures there has been a variety of methods to achieve bending and deployment of the structure. For example Birnbaum and Pique (2011) use laser induced extraplanar propulsion to fold micro scale nanofilms out of plane to create folded structures. Arora et al. (2007) use ion implantation to induce stress on one side of a silicon nitride cantilever to cause folding at specific locations of a structure. As a summary we provide the following incomplete list of methods for deployment of origami structures:

- Structures deployed using external actuation (e.g. façade panels deployed with a crane).
- Using a system of actuators placed inside of the structure to apply forces.
- Using body and fictitious forces of the structure itself to achieve deployment (e.g. gravity, centrifugal, or electromagnetic forces).
- Internal volume change (e.g. using the origami as a deployable boom/cylinder or using vaccumatics).
- Release of internally stored forces (e.g. pre-stressed fold and panel elements).

- Applying heat, light or using a chemical reaction to cause fold rotation and structural deployment.

In accordance with structural deployment we also note that with some origami designs it may be possible to achieve flexible enough systems where only a minimal amount of energy needs to be applied for the structure to reach a deployed or stowed state. This could be especially beneficial since only a small deployment mechanism may be needed for the structural deployment. These types of systems are referred to as zero-stiffness structures that can have multiple stable configurations and virtually no energy change between the states.

APPENDIX B

SEVENTY CROSS-SECTION RECONFIGURATIONS OF A POLYGONAL ORIGAMI TUBE

This appendix shows the reconfiguration capability of one specific origami polygonal tube. This tube was briefly presented as an example in Figures 6.1 and 6.18 in Chapter 6. The initial cross-section and one of the seventy possible configurations are presented in Figure B.1. The cross-section of the tube has fourteen sides (edges) of which eight have an equal length. The top and bottom portions of the cross-section each have four translationally symmetric edges that can be classified as *switches* ($n = 4$).

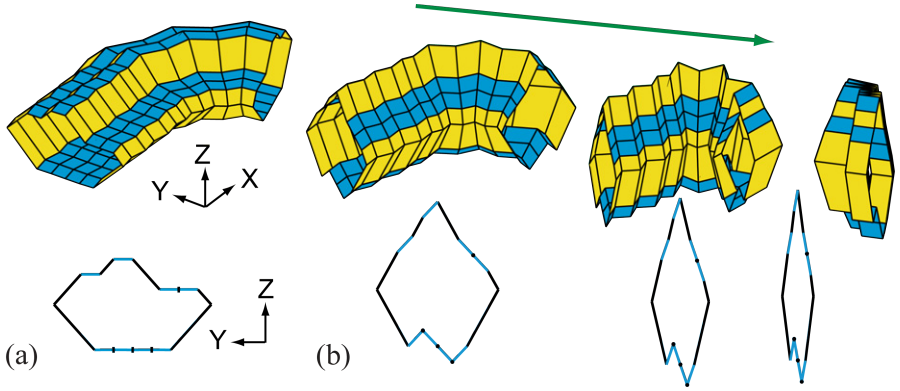

Figure B.1: The reconfigurable polygonal tube with $n = 4$ switches. (a) The tube and cross-section shown at a fully extended state. The tube reconfigures into one of the possible seventy configurations starting from this state. (b) The folding sequence of the tube into configuration XXXVII where the upper switch assignment is [U:1 1 0 0] and the lower section assignment is [L:1 0 0 1], both assignments sum to $k = 2$.

The reconfiguration capabilities of the polygonal tubes are discussed in more detail in Section 6.5. We used a binary assignment to define the switch direction, and we showed that the possible upper section assignments followed the binomial coefficient. The upper section has n switches where the assignment of these switches sum to k and the corresponding lower section had to have an equivalent sum k. The possible upper section assignments for tubes with a $n = 2$, $n = 3$, and $n = 4$ are shown in Figure B.2 (a). The number of possible upper section variations follow Pascal's triangle (Figure B.2 (b)), and the total number of possible configurations follow the central binomial coefficient (Figure B.2 (c)). The tube presented in this appendix has $n = 4$ switches and can thus reconfigure into 70 different configurations.

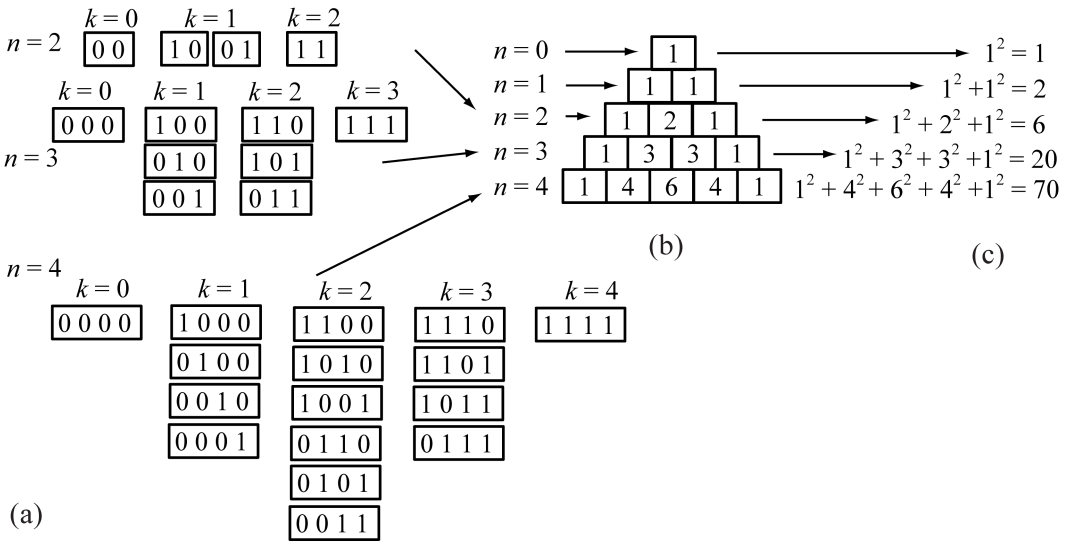

Figure B.2: Variations in reconfiguring polygonal tubes. (a) Possible switch variations for the upper section only, with $n = 2$, $n = 3$, and $n = 4$ switches. The variable k corresponds to the sum of the switch assignments. (b) A Pascal's triangle shows the number of variations for the upper section of the tube only. This is the binomial coefficient with n representing the rows and k the columns. (c) The total number of possible cross-section configurations. This is equivalent to the central binomial coefficient.

The remainder of this Appendix presents the seventy possible cross-section variations. Figure B.3 shows a summary of all the possible switch assignments for the upper and lower sections of the tube. The folding sequence and corresponding cross-sections for the seventy cases are shown in Figures B.4 to B.10. The sum of the switch assignments k is used to organize the cross-sections: $k = 0$ is configuration I; $k = 4$ is configuration II; $k = 1$ are configurations III-XVIII (16 cases); $k = 3$ are configurations XIX-XXXIV (16 cases); and $k = 2$ are configurations XXXV-LXX (36 cases).

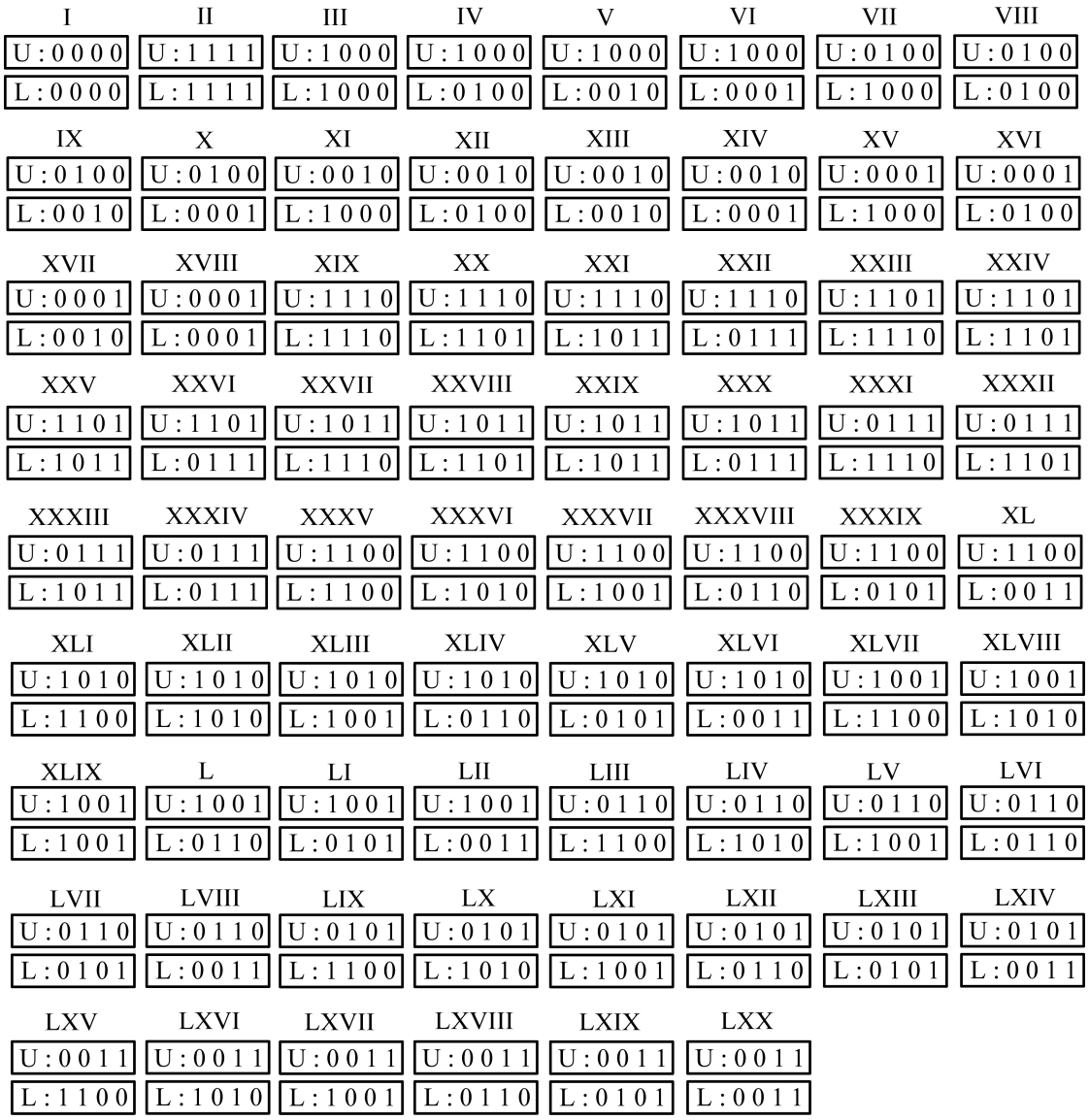

Figure B.3: Summary of the upper (U) and lower (L) switch assignments that can be used to reconfigure the tube. Because there are $n = 4$ switches, it is possible to obtain 70 different cross-sectional variations.

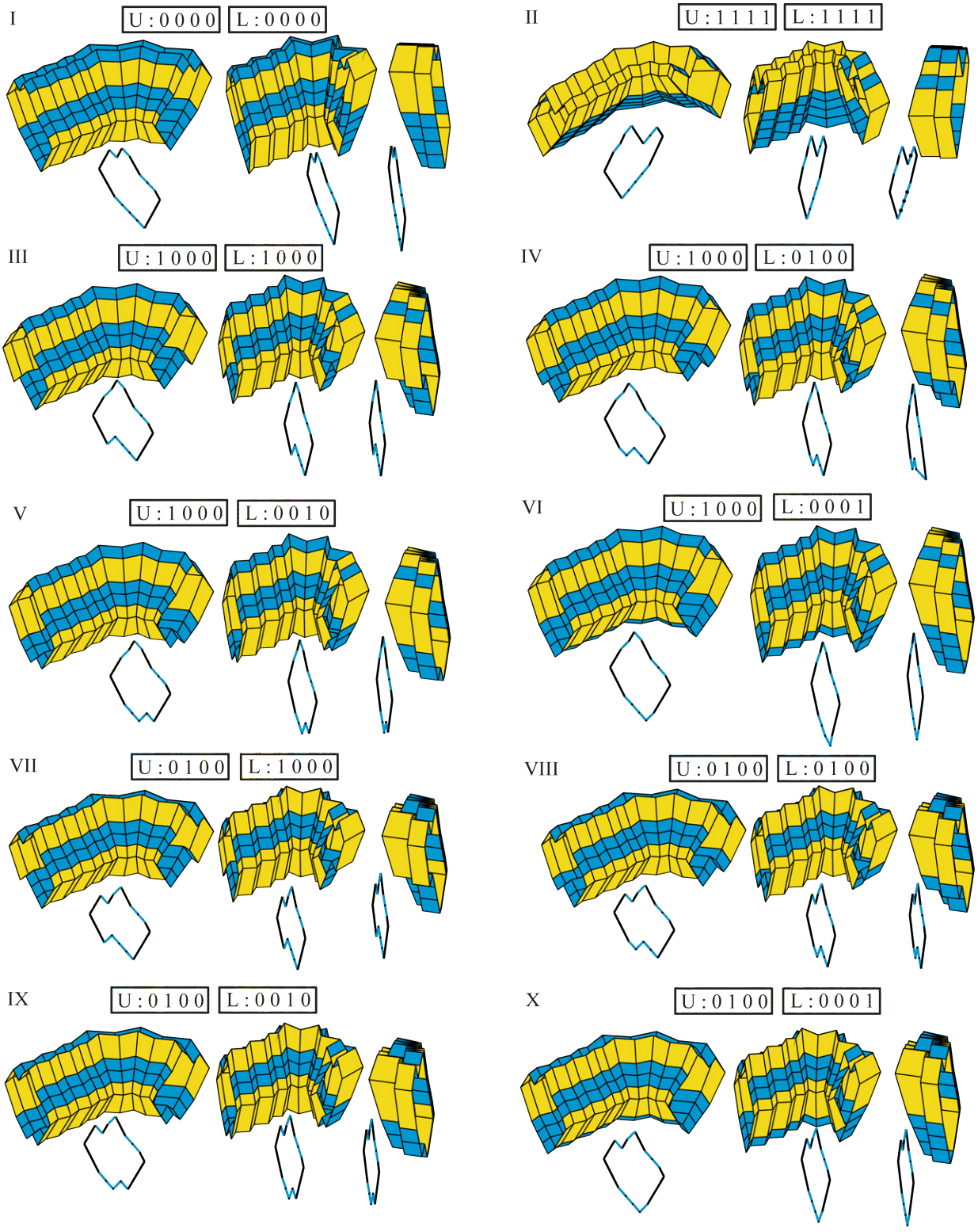

Figure B.4: Folding sequence and cross-section variations I to X for the polygonal tube with four switches.

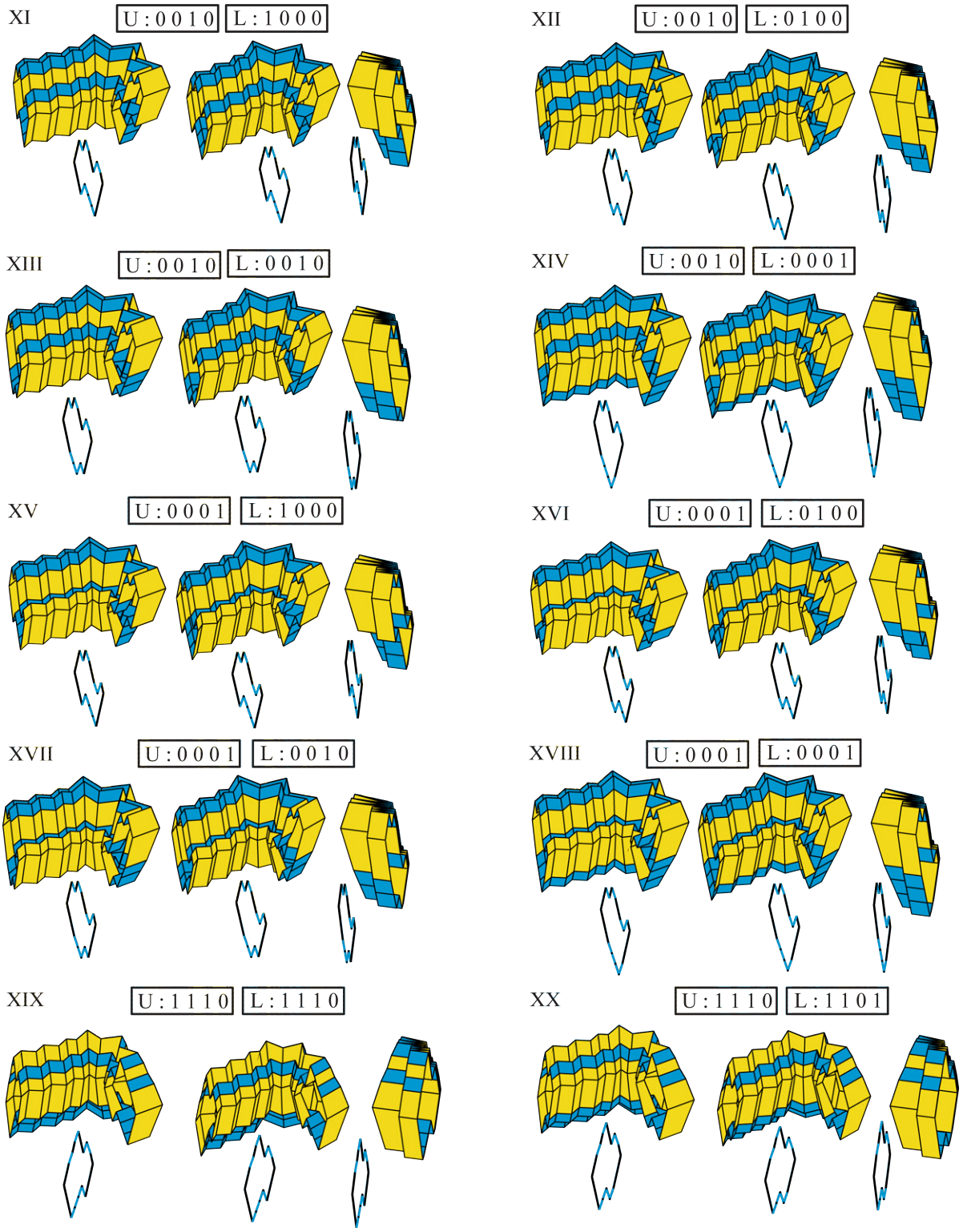

Figure B.5: Folding sequence and cross-section variations XI to XX for the polygonal tube with four switches.

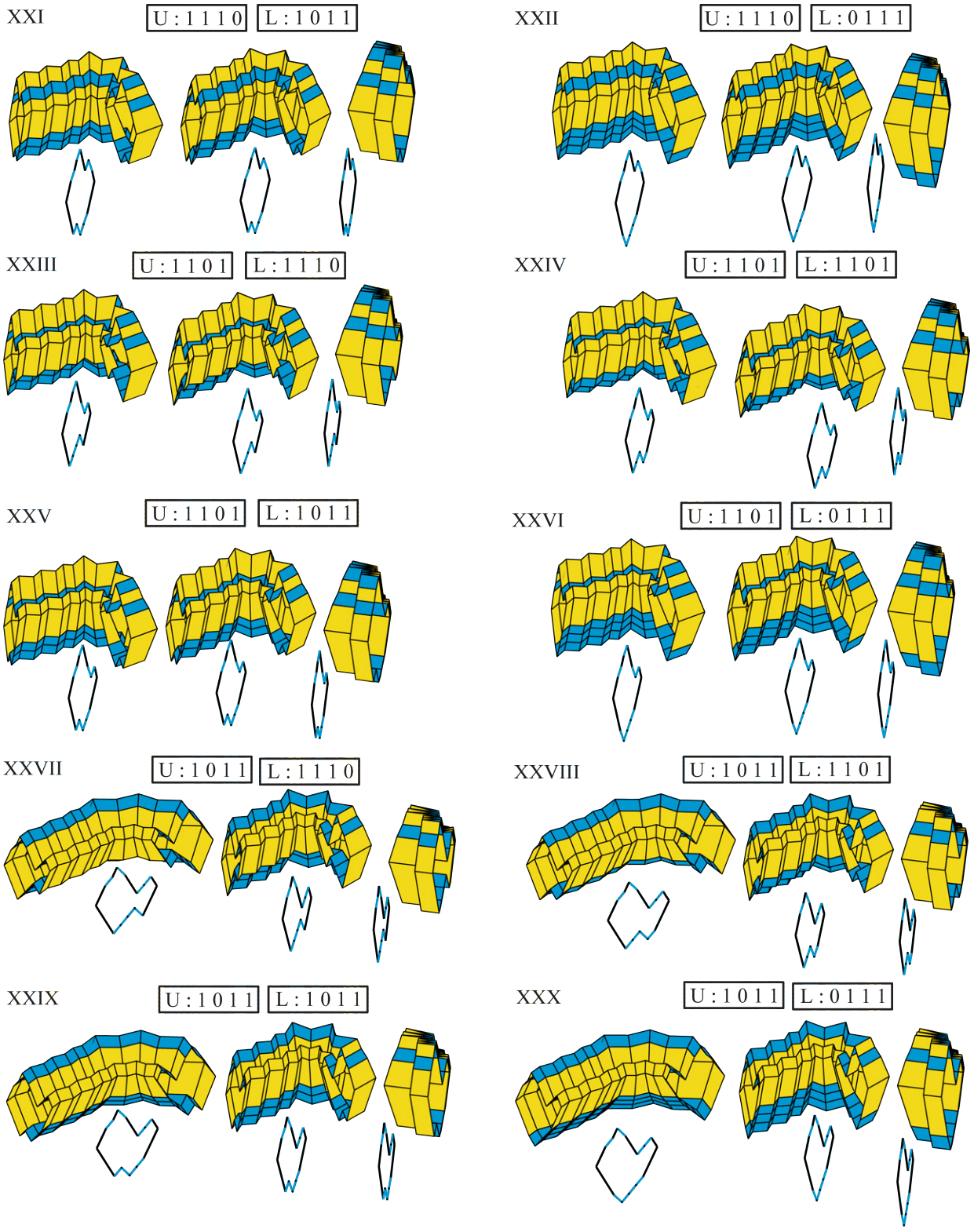

Figure B.6: Folding sequence and cross-section variations XXI to XXX for the polygonal tube with four switches.

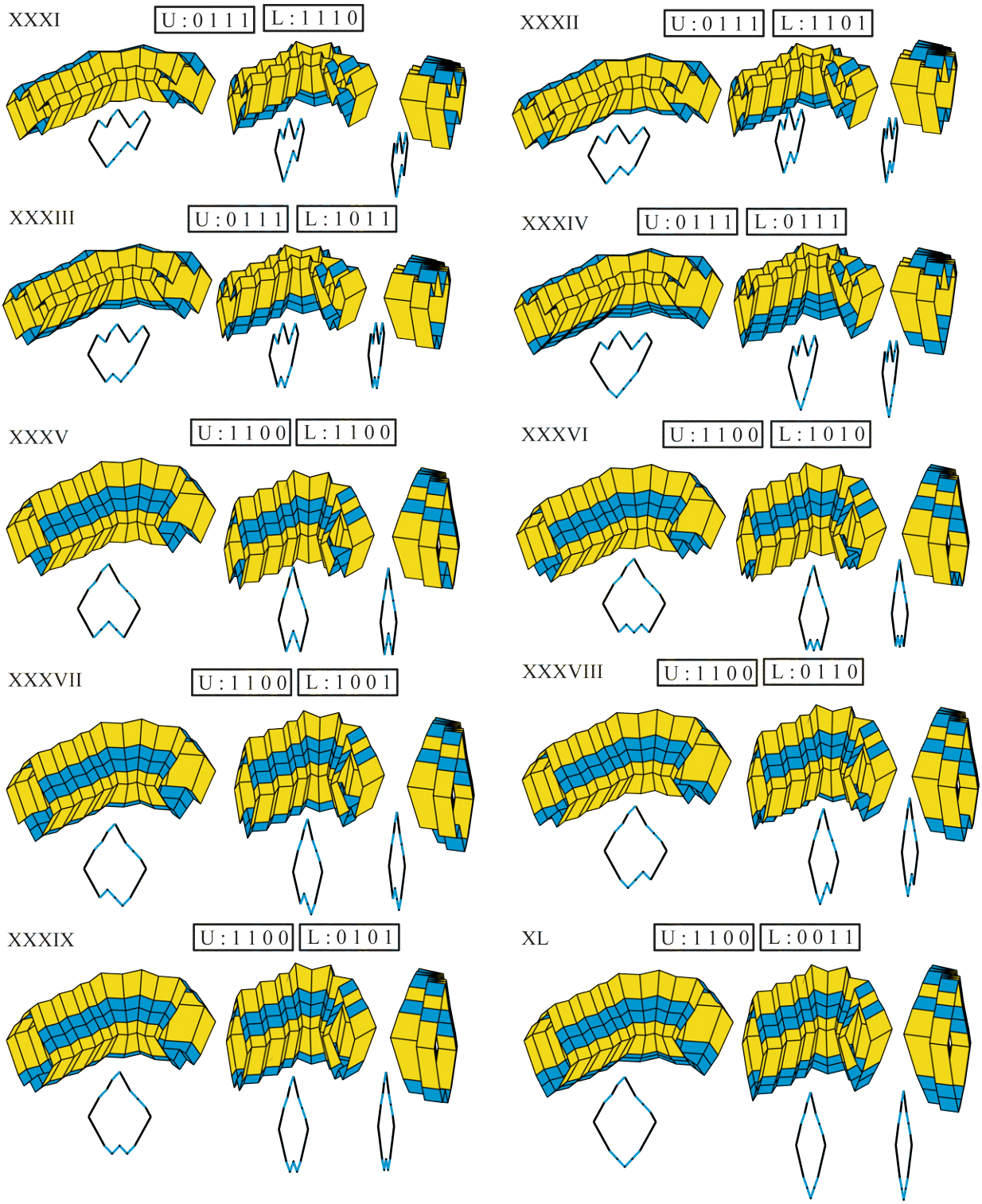

Figure B.7: Folding sequence and cross-section variations XXXI to XL for the polygonal tube with four switches.

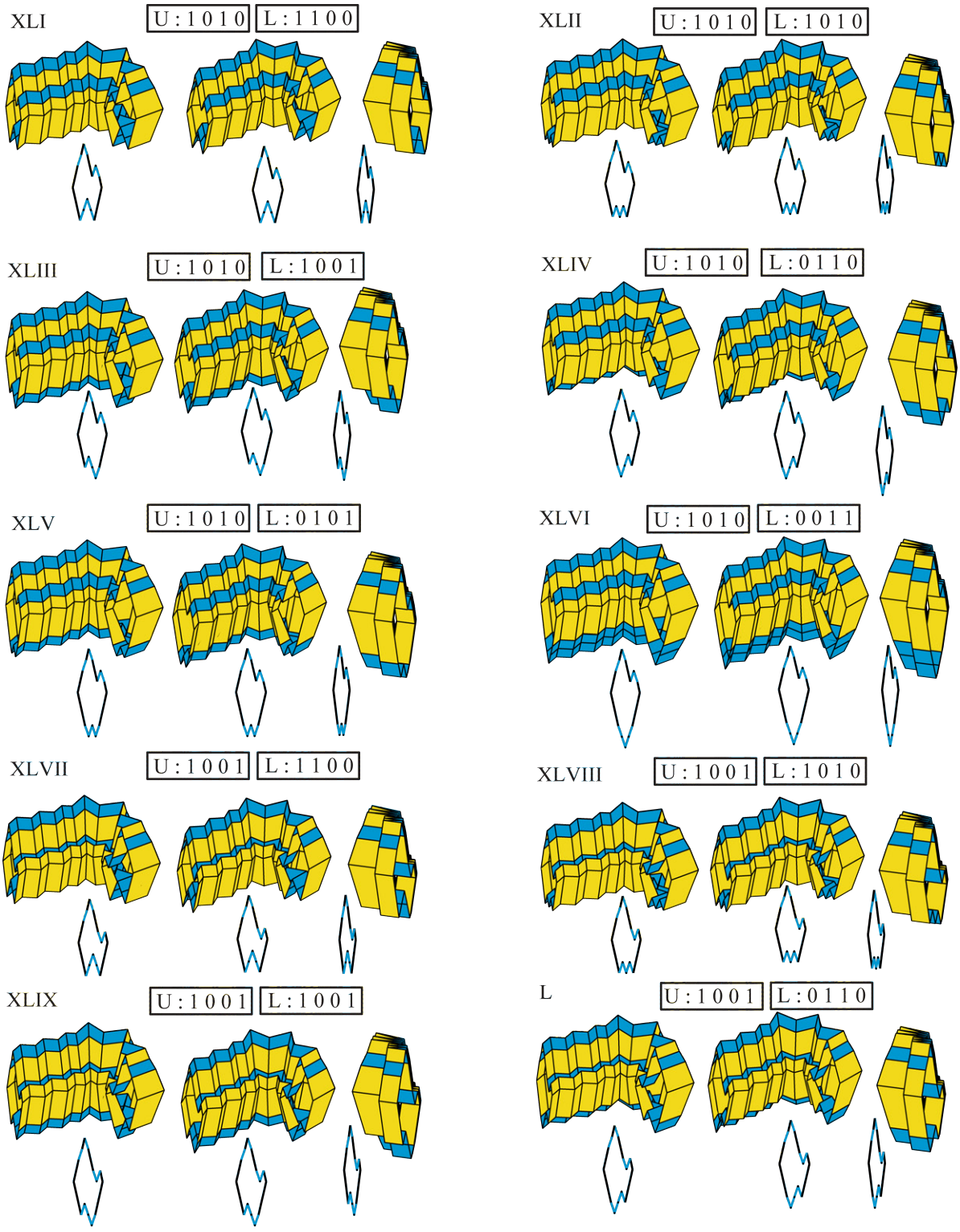

Figure B.8: Folding sequence and cross-section variations XLI to L for the polygonal tube with four switches.

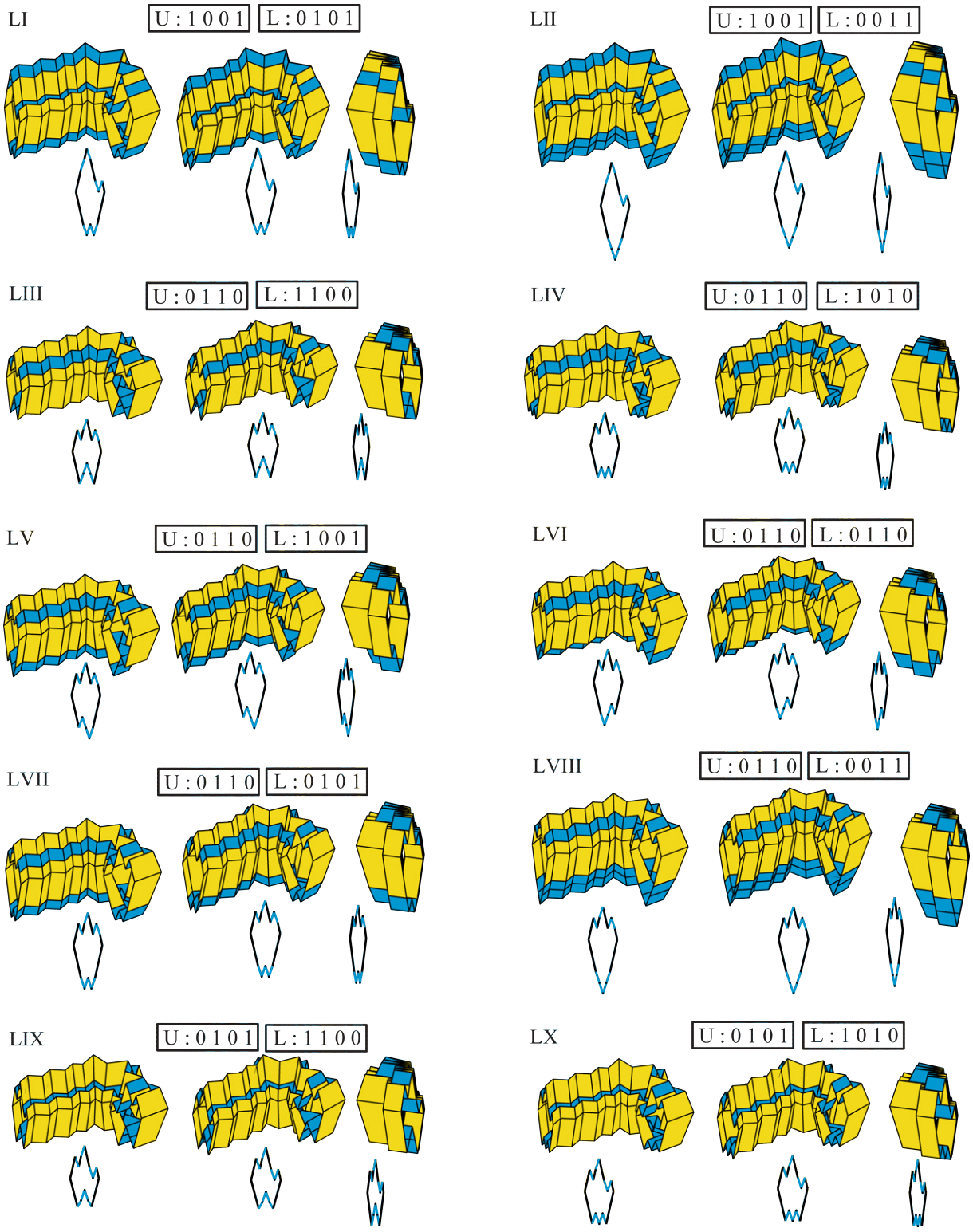

Figure B.9: Folding sequence and cross-section variations LI to LX for the polygonal tube with four switches.

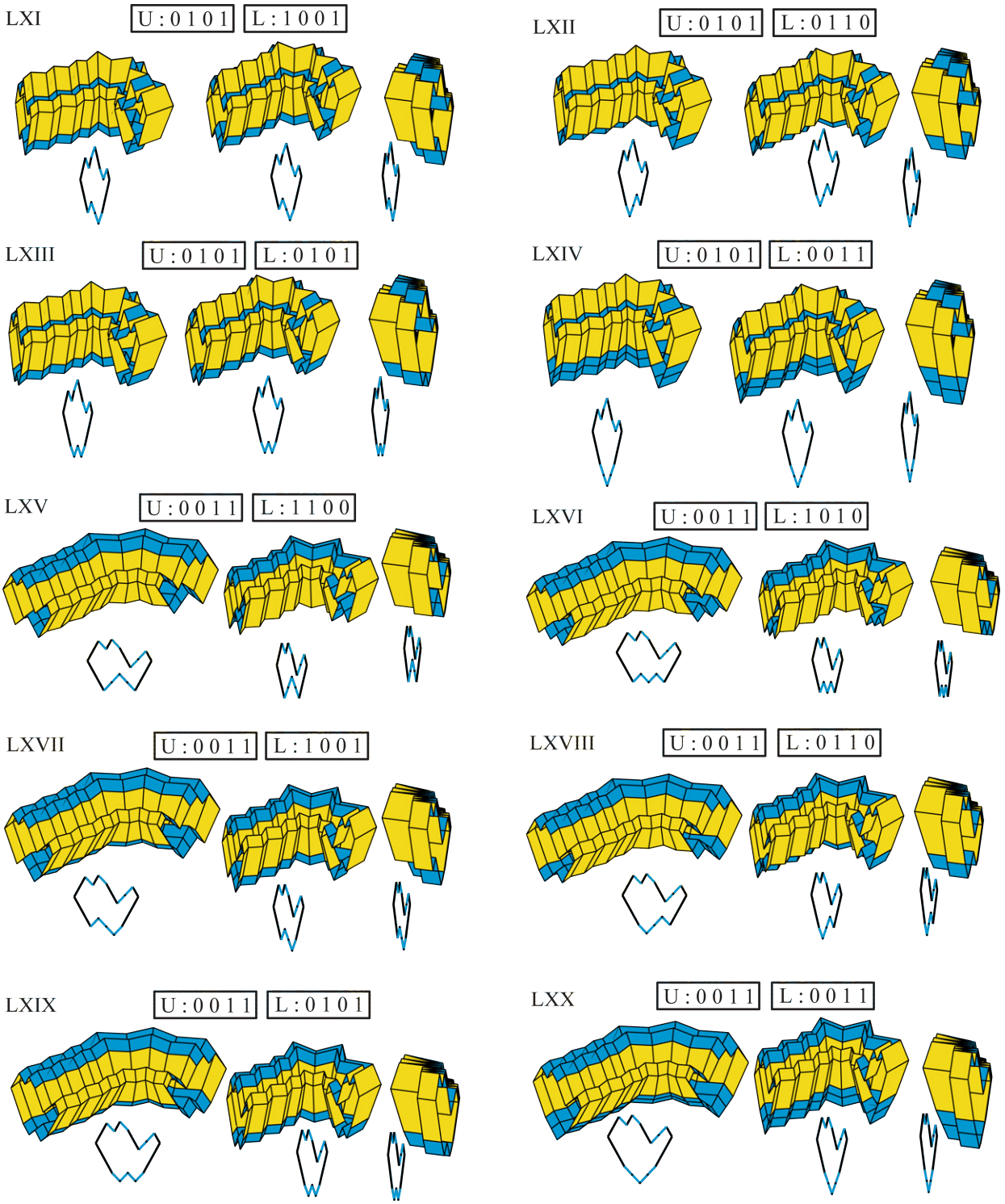

Figure B.10: Folding sequence and cross-section variations LXI to LXX for the polygonal tube with four switches.

REFERENCES

Ahmed, R. and Banerjee, S. (2013). Novel split ring metamaterial for multiple band gaps and vibration control. In *Proc. SPIE 8695, Health Monitoring of Structural and Biological Systems 2013*.

Andersen, E. S., Dong, M., Nielsen, M. M., Jahn, K., Subramani, R., Mamdouh, W., Golas, M. M., Sander, B., Stark, H., Oliveira, C. L. P., Pedersen, J. S., Birkedal, V., Besenbacher, F., Gothelf, K. V., and Kjems, J. (2009). Self-assembly of a nanoscale DNA box with a controllable lid. *Nature*, 459(7243):73–6.

Arora, W. J., Smith, H. I., and Barbastathis, G. (2007). Membrane folding by ion implantation induced stress to fabricate three-dimensional nanostructures. *Microelectronic Engineering*, 84(5-8):1454–1458.

Arquitectos, C. (2008). Basque Health Department Headquarters.

Aten, Q. T., Jensen, B. D., Burnett, S. H., and Howell, L. L. (2014). A self-reconfiguring metamorphic nanoinjector for injection into mouse zygotes. *The Review of scientific instruments*, 85(5):055005.

Atkins, P. W. and Friedman, R. S. (2011). *Molecular Quantum Mechanics*. Oxford University Press.

Balkcom, D. and Mason, M. (2004). Introducing robotic origami folding. In *IEEE International Conference on Robotics and Automation, 2004. Proceedings. ICRA '04. 2004*, volume 4, pages 3245–3250 Vol.4. IEEE.

Balkcom, D. J. and Mason, M. T. (2008). Robotic origami folding. *The International Journal of Robotics Research*, 27(5):613–627.

Barbarino, S., Bilgen, O., Ajaj, R. M., Friswell, M. I., and Inman, D. J. (2011). A Review of Morphing Aircraft. *Journal of Intelligent Material Systems and Structures*, 22(9):823–877.

Beex, L. and Peerlings, R. (2009). An experimental and computational study of laminated paperboard creasing and folding. *International Journal of Solids and Structures*, 46(24):4192–4207.

Bern, M. and Hayes, B. (1996). The complexity of flat origami. In *SODA '96 Proceedings of the seventh annual ACM-SIAM symposium on Discrete algorithms*, pages 175–183, Atlanta, GA. Society for Industrial and Applied Mathematics.

Birnbaum, A. J. and Pique, A. (2011). Laser induced extraplanar propulsion for three-dimensional microfabrication. *Applied Physics Letters*, 98(13):134101.

Briassoulis, D. (1986). Equivalent orthotropic properties of corrugated sheets. *Computers & Structures*, 23:129–138.

Bridson, R., Marino, S., and Fedkiw, R. (2003). Simulation of clothing with folds and wrinkles. In *ACM SIGGRAPH/Eurographics*, pages 28–36. Eurographics Association.

Brunck, V., Lechenault, F., Reid, A., and Adda-Bedia, M. (2016). Elastic theory of origami-based metamaterials. *Physical Review E*, 93(3):033005.

BYU-News-Release (2014). BYU researchers create tiny nano-device in newest gene therapy advance.

Cambou, A. D. and Menon, N. (2011). Three-dimensional structure of a sheet crumpled into a ball. *Proc. Natl. Acad. Sci. U.S.A.*, 108(36):14741–5.

Campbell, D., Barrett, R., Lake, M., Adams, L., Abramson, E., Scherbarth, M., Welsh, J., Freebury, G., Beidleman, N., and Abbot, J. (2006). Development of a Novel, Passively Deployed Roll-Out Solar Array. In *IEEE Aerospace Conference*, pages 1–9. IEEE.

Cerda, E., Chaieb, S., Melo, F., and Mahadevan, L. (1999). Conical dislocations in crumpling. *Nature*, 401(6748):46–49.

Chen, Y., Peng, R., and You, Z. (2015). Origami of thick panels. *Science*, 349(6246):396–400.

Cheung, K. C., Tachi, T., Calisch, S., and Miura, K. (2014). Origami interleaved tube cellular materials. *Smart Materials and Structures*, 23(9):094012.

Cho, J.-H., Keung, M. D., Verellen, N., Lagae, L., Moshchalkov, V. V., Van Dorpe, P., and Gracias, D. H. (2011). Nanoscale Origami for 3D Optics. *Small*, 7(14):1943–1948.

Connelly, R., Sabitov, I., and Walz, A. (1997). The Bellows Conjecture. *Contributions to Algebra and Geometry*, 38(1):1–10.

Corning (2014). Willow Glass - http://www.corning.com.

Côté, F., Deshpande, V., Fleck, N., and Evans, A. (2006). The compressive and shear responses of corrugated and diamond lattice materials. *International Journal of Solids and Structures*, 43(20):6220–6242.

Cranford, S., Sen, D., and Buehler, M. J. (2009). Meso-origami: Folding multilayer graphene sheets. *Applied Physics Letters*, 95(12):123121.

Dassault Systemes Simulia Corp (2010). ABAQUS FEA. Version 6.10.

De Ruysser, T. (2016). Origami Jewlery.

Del Grosso, A. E. and Basso, P. (2010). Adaptive building skin structures. *Smart Materials and Structures*, 19(12):124011.

Demaine, E. D., Demaine, M. L., Hart, V., Price, G. N., and Tachi, T. (2011). (Non)existence of pleated folds: How paper folds between creases. *Graphs and Combinatorics*, 27(3):377–397.

Deng, D. and Chen, Y. (2013). An Origami Inspired Additive Manufacturing Process for Building Thin-Shell Structures. In *Volume 2A: Advanced Manufacturing*, page V02AT02A016. ASME.

DiDonna, B. (2002). Scaling of the buckling transition of ridges in thin sheets. *Physical Review E*, 66:016601.

Dudte, L. H., Vouga, E., Tachi, T., and Mahadevan, L. (2016). Programming curvature using origami tessellations. *Nature Materials*, 15(5):583.

Durney, M. W. and Pendley, A. D. (2004). Method of designing fold lines in sheet material - U.S. Patent #7,440,874 B2.

Edmondson, B. J., Lang, R. J., Magleby, S. P., and Howell, L. L. (2014). An Offset Panel Technique for Thick Rigidily Foldable Origami. In *Volume 5B: 38th Mechanisms and Robotics Conference*, page V05BT08A054. ASME.

Epps, G. (2014). RoboFold and Robots.IO. *Architectural Design*, 84(3):68–69.

Ernst Giselbrecht + Partner (2007). Kiefer Technic Showroom.

Evans, A. A., Silverberg, J. L., and Santangelo, C. D. (2015). Lattice mechanics of origami tessellations. *Physical Review E*, 92(1):013205.

Falk, A. and Von Buelow, P. (2011). Form Exploration of Folded Plate Timber Structures based on Performance Criteria. In *Taller, Longer, Lighter: Meeting growing demand with limited resources. eds. Nethercot, D. and Pellegrino, S. Proceedings of the 35th Annual Symposium of IABSE and the 52nd Annual Symposium of IASS*, London. Hemming Group Ltd.

Falk, A., von Buelow, P., and Kirkegaard, P. H. (2012). Folded Plate Structures as Building Envelopes. In *World Conference on Timber Engineering*, pages 155–164.

Felton, S. M., Tolley, M. T., Demaine, E. D., Rus, D., and Wood, R. J. (2014). A method for building self-folding machines. *Science*, 345(6197):644–646.

Fernandez, J. M., Visagie, L., Schenk, M., Stohlman, O. R., Aglietti, G. S., Lappas, V. J., and Erb, S. (2014). Design and development of a gossamer sail system for deorbiting in low earth orbit. *Acta Astronautica*, 103:204–225.

Filipov, E. T., Paulino, G. H., and Tachi, T. (2016a). Origami tubes with reconfigurable polygonal cross-sections. *Proceedings of the Royal Society of London A: Mathematical, Physical and Engineering Sciences*, 472(2185).

Filipov, E. T., Tachi, T., and Paulino, G. H. (2015a). Origami tubes assembled into stiff, yet reconfigurable structures and metamaterials. *Proceedings of the National Academy of Sciences*, 112(40):12321–12326.

Filipov, E. T., Tachi, T., and Paulino, G. H. (2016b). Toward optimization of stiffness and flexibility of rigid, flat-foldable origami structures. In Miura, K., Kawasaki, T., Tachi, T., Uehara, R., Lang, R. J., and Wang-Iverson, P., editors, *Origami 6*, pages 409–419. American Mathematical Society, Providence, RI.

Filipov, E. T., Tachi, T., Yamaguchi, Y., and Paulino, G. H. (2015b). Foldable Structures and their Manufacturing Method, Manufacturing Device and Program (patent filed).

France, A. K. (2013). *Make: 3D Printing: The Essential Guide to 3D Printers*, volume 19. Maker Media, Incorporated.

Francis, K. C., Rupert, L. T., Lang, R. J., Morgan, D. C., Magleby, S. P., and Howell, L. L. (2014). From Crease Pattern to Product: Considerations to Engineering Origami-Adapted Designs. In *Proceedings of ASME 2014 IEDTC \& CIEC*, page V05BT08A030. ASME.

Fratzl, P. and Weinkamer, R. (2007). Nature's hierarchical materials. *Progress in Materials Science*, 52(8):1263–1334.

Fuchi, K., Buskohl, P., Joo, J., Reich, G., and Vaia, R. (2015a). Numerical analysis of origami structures through modified frame elements. In Miura, K., Kawasaki, T., Tachi, T., Uehara, R., Lang, R., and Wang-Iverson, P., editors, *Origami 6, Proc. 6th Int. Meeting on Origami Science, Mathematics, and Education*, pages 385–395, Tokyo, Japan. American Mathematical Society.

Fuchi, K., Buskohl, P. R., Bazzan, G., Durstock, M. F., Reich, G. W., Vaia, R. A., and Joo, J. J. (2015b). Origami Actuator Design and Networking Through Crease Topology Optimization. *Journal of Mechanical Design*, 137(9):091401.

Fuchi, K., Buskohl, P. R., Bazzan, G., Durstock, M. F., Reich, G. W., Vaia, R. A., and Joo, J. J. (2016). Design Optimization Challenges of Origami-Based Mechanisms With Sequenced Folding. *Journal of Mechanisms and Robotics*, 8(5):051011.

Fuchi, K., Diaz, A. R., Rothwell, E. J., Ouedraogo, R. O., and Tang, J. (2012). An origami tunable metamaterial. *Journal of Applied Physics*, 111(8):084905.

Fuchs and Funke (2104). Fuchs+Funke Papton Chair.

Gattas, J. and You, Z. (2015a). Geometric assembly of rigid-foldable morphing sandwich structures. *Engineering Structures*, 94:149–159.

Gattas, J. M., Wu, W., and You, Z. (2013). Miura-base rigid origami: parameterizations of first-level derivative and piecewise geometries. *J. Mechanical Design*, 135(11):111011.

Gattas, J. M. and You, Z. (2015b). The behaviour of curved-crease foldcores under low-velocity impact loads. *Int. J. Solids Structures*, 53:80–91.

Gautrand, M. (2011). Barclays headquaters building, Paris.

Giampieri, A., Perego, U., and Borsari, R. (2011). A constitutive model for the mechanical response of the folding of creased paperboard. *Int. J. Solids Structures*, 48(16-17):2275–2287.

Gibson, L. J., Ashby, M. F., and Harley, B. A. (2010). *Cellular materials in nature and medicine*. Cambridge University Press.

Gonella, S., To, A. C., and Liu, W. K. (2009). Interplay between phononic bandgaps and piezoelectric microstructures for energy harvesting. *Journal of the Mechanics and Physics of Solids*, 57(3):621–633.

Gracias, D., Kavthekar, V., Love, J., Paul, K., and Whitesides, G. (2002). Fabrication of Micrometer-Scale, Patterned Polyhedra by Self-Assembly. *Advanced Materials*, 14(3):235–238.

Gracias, D. H. (2013). Stimuli responsive self-folding using thin polymer films. *Current Opinion in Chemical Engineering*, 2(1):112–119.

Guo, X., Li, H., Ahn, B. Y., Duoss, E. B., Hsia, K. J., Lewis, J. A., and Nuzzo, R. G. (2009). Two- and three-dimensional folding of thin film single-crystalline silicon for photovoltaic power applications. *Proceedings of the National Academy of Sciences of the United States of America*, 106(48):20149–54.

Han, D., Pal, S., Nangreave, J., Deng, Z., Liu, Y., and Yan, H. (2011). DNA origami with complex curvatures in three-dimensional space. *Science (New York, N.Y.)*, 332(6027):342–6.

Hanna, B. H., Lund, J. M., Lang, R. J., Magleby, S. P., and Howell, L. L. (2014). Water-bomb base: a symmetric single-vertex bistable origami mechanism. *Smart Materials and Structures*, 23(9):094009.

Hawkes, E., An, B., Benbernou, N. M., Tanaka, H., Kim, S., Demaine, E. D., Rus, D., and Wood, R. J. (2010). Programmable matter by folding. *Proceedings of the National Academy of Sciences of the United States of America*, 107(28):12441–5.

Heimbs, S. (2013). Foldcore Sandwich Structures and Their Impact Behaviour: An Overview. In *Dynamic Failure of Composite and Sandwich Strucutures*, pages 491–544. Springer Netherlands.

Hoberman, C. (2004). Folding covering panels for expanding structures - U.S. Patent #6,834,465 B2, 28.

Hoberman, C. (2010). Folding structures made of thick hinged sheets - U.S. Patent #7,794,019 B2, 14.

Huang, G. and Sun, C. (2010). Band gaps in a multiresonator acoustic metamaterial. *Journal of Vibration and Acoustics*, 132:031003.

Huang, H., Hagman, A., and Nygårds, M. (2014). Quasi static analysis of creasing and folding for three paperboards. *Mechanics of Materials*, 69(1):11–34.

Huffman, D. A. (1976). Curvature and Creases: A Primer on Paper. *IEEE Trans. Comput.*, C-25(10):1010–1019.

Hull, T. C. (2012). *Project Origami: Activities for Exploring Mathematics, Second Edition*. CRC Press.

Hunt, G. W. and Ario, I. (2005). Twist buckling and the foldable cylinder: an exercise in origami. *International Journal of Non-Linear Mechanics*, 40(6):833–843.

Industrial-Origami (2014). Design and manufacturing innovation for industrial origami.

Inhabitat-Blog (2012). Al Bahr Towers by AEDAS.

Jenkins, C. H. M. (2001). *Progress In Astronautics and Aeronautics: Gossamer Spacecraft: Membrane and Inflatable Structures Technology for Space Applications*. AIAA.

Jiang, Q., Song, C., Nangreave, J., Liu, X., Lin, L., Qiu, D., Wang, Z.-G., Zou, G., Liang, X., Yan, H., and Ding, B. (2012). DNA origami as a carrier for circumvention of drug resistance. *Journal of the American Chemical Society*, 134(32):13396–403.

Jun, M., Knutti, R., and Nychka, D. W. (2008). Local eigenvalue analysis of CMIP3 climate model errors. *Tellus A*, 60(5):992–1000.

Justin, J. (1986). Mathematics of origami, part 9. *British Origami*, pages 28–30.

Kawasaki, T. (1989). On the relation between mountain-creases and valley-creases of a flat origam. In H., H., editor, *Proceedings of the 1st International Meeting on Origami Science and Technology*, pages 229–237. Commune di Ferra and Centro Origami Duffusion.

Kuribayashi, K., Tsuchiya, K., You, Z., Tomus, D., Umemoto, M., Ito, T., and Sasaki, M. (2006). Self-deployable origami stent grafts as a biomedical application of Ni-rich TiNi shape memory alloy foil. *Materials Science and Engineering: A*, 419(1-2):131–137.

Lang, R. J. (2011). *Origami Design Secrets*. CRC Press, Boca Raton, FL, 2nd edition.

Lechenault, F., Thiria, B., and Adda-Bedia, M. (2014). Mechanical Response of a Creased Sheet. *Phys. Rev. Lett.*, 112(24):244301.

Lee, D.-Y., Kim, S.-R., Kim, J.-S., Park, J.-J., and Cho, K.-J. (2013). Fabrication of Origami Structure using Pattern Enclosed Composite (PEC). In *13th International Conference on Control, Automation and Systems (ICCAS 2013)*.

Li, S. and Wang, K. W. (2015). Fluidic origami with embedded pressure dependent multi-stability: a plant inspired innovation. *Journal of the Royal Society, Interface*, 12(111):20150639.

Lipson, H. and Kurman, M. (2013). *Fabricated: The New World of 3D Printing*. John Wiley & Sons.

Liu, Y., Boyles, J. K., Genzer, J., and Dickey, M. D. (2012). Self-folding of polymer sheets using local light absorption. *Soft Matter*, 8(6):1764.

Lobkovsky, A. E., Gentges, S., Li, H., Morse, D., and Witten, T. A. (1995). Scaling properties of stretching ridges in a crumpled elastic sheet. *Science*, 270(5241):1482–1485.

Lv, C., Krishnaraju, D., Konjevod, G., Yu, H., and Jiang, H. (2014). Origami based mechanical metamaterials. *Scientific reports*, 4:5979.

Ma, J. and You, Z. (2013). Energy absorption of thin-walled beams with a pre-folded origami pattern. *Thin-Walled Structures*, 73:198–206.

Ma, K. Y., Chirarattananon, P., Fuller, S. B., and Wood, R. J. (2013). Controlled flight of a biologically inspired, insect-scale robot. *Science (New York, N.Y.)*, 340(6132):603–7.

Ma, K. Y., Felton, S. M., and Wood, R. J. (2012). Design, Fabrication, and Modeling of the Split Actuator Microrobotic Bee. In *IEEE/RSJ International Conference on Intelligent Robots and Systems*, pages 1133–1140, Vilamoura, Portugal.

Mahadevan, L. and Rica, S. (2005). Self-organized origami. *Science*, 307(5716):1740.

Malone, P. K. and Williams, G. T. (1996). Lightweight Inflatable Solar Array. *Journal of Propulsion and Power*, 12(5):866–872.

Marras, A. E., Zhou, L., Su, H.-J., and Castro, C. E. (2015). Programmable motion of DNA origami mechanisms. *Proceedings of the National Academy of Sciences*, 112(3):713–718.

Marszalek, W. and Trzaska, Z. (2005). Singularity-Induced Bifurcations in Electrical Power Systems. *IEEE Transactions on Power Systems*, 20(1):312–320.

Martinez, R. V., Fish, C. R., Chen, X., and Whitesides, G. M. (2012). Elastomeric Origami: Programmable Paper-Elastomer Composites as Pneumatic Actuators. *Advanced Functional Materials*, 22(7):1376–1384.

Mentrasti, L., Cannella, F., Pupilli, M., and Dai, J. S. (2013a). Large bending behavior of creased paperboard. I. Experimental investigations. *International Journal of Solids and Structures*, 50(20-21):3089–3096.

Mentrasti, L., Cannella, F., Pupilli, M., and Dai, J. S. (2013b). Large bending behavior of creased paperboard. II. Structural analysis. *International Journal of Solids and Structures*, 50(20-21):3097–3105.

Miura, K. (1969). Proposition of pseudo-cylindrical concave polyhedral shells. Technical report, Institute of Space and Aeronautical Science, University of Tokyo, Tokyo.

Miura, K. (1985). Method of Packaging and Deployment of Large Membranes in Space. *The Institute of Space and Astronautical Science report*, 618:1–9.

Miura, K. (2002). PCCP Shells. In Drew, H. and Pellegrino, S., editors, *New Approaches to Structural Mechanics, Shells and Biological Structures*, pages 329–339. Springer Netherlands.

Miura, K. (2009). The science of Miura-ori: A review. In Lang, R. J., editor, *Origami 4*, pages 87–99. AK Peters.

Miura, K., Kawasaki, T., Tachi, T., Uehara, R., Lang, R. J., and Wang-Iverson, P., editors (2015). *Origami6: Proceedings of the 6th International Meeting of Origami Mathematics, Science, and Education*. American Mathematical Society, Tokyo, Japan.

Miura, K. and Tachi, T. (2010). Synthesis of rigid-foldable cylindrical polyhedra. *Journal of the International Society for the Interdisciplinary Study of Symmetry*, pages 204–213.

Mraz, S. (2004). Care and feeding of living hinges. *Machine Design*.

Nagasawa, S., Endo, R., Fukuzawa, Y., Uchino, S., and Katayama, I. (2008). Creasing characteristic of aluminum foil coated paperboard. *Journal of Materials Processing Technology*, 201(1):401–407.

Nagasawa, S., Fukuzawa, Y., Yamaguchi, D., Nagae, S., Katayama, I., and Yoshizawa, A. (2001). Deformation Characteristics on Creasing of Paperboard Under Shallow Indentation. In Ravi-Chandar, K., Karihaloo, B., Kishi, T., Ritchie, R., Yokobori Jr., A., and Yokobori, T., editors, *Proceedings of the 10th International Conference on Fracture*, pages ICF10–0202OR, Honolulu, HI. Elsevier Science.

Nagasawa, S., Fukuzawa, Y., Yamaguchi, T., Tsukatani, S., and Katayama, I. (2003). Effect of crease depth and crease deviation on folding deformation characteristics of coated paperboard. *Journal of Materials Processing Technology*, 140(1):157–162.

Narain, R., Pfaff, T., and O'Brien, J. F. (2013). Folding and crumpling adaptive sheets. *ACM Transactions on Graphics*, 32(4):1.

NASA (2009). International Space Station.

Onal, C. D., Wood, R. J., and Rus, D. (2011). Towards Printable Robotics: Origami-Inspired Planar Fabrication of Three-Dimensional Mechanisms. In *2011 IEEE International Conference on Robotics and Automation (ICRA)*, pages 4608 – 4613, Shanghai.

Origami-Resource-Center (2014). Origmi Furniture, Architecture and Sports.

Peraza-Hernandez, E., Hartl, D., Galvan, E., and Malak, R. (2013). Design and Optimization of a Shape Memory Alloy-Based Self-Folding Sheet. *Journal of Mechanical Design*, 135(11):111007.

Peraza Hernandez, E. A., Hartl, D. J., Akleman, E., and Lagoudas, D. C. (2016). Modeling and analysis of origami structures with smooth folds. *Computer-Aided Design*, 78:93–106.

Peraza-Hernandez, E. A., Hartl, D. J., Malak Jr, R. J., and Lagoudas, D. C. (2014). Origami-inspired active structures: a synthesis and review. *Smart Materials and Structures*, 23(9):094001.

Perego, U. and Giampieri, A. (2006). An interface element to model the mechanical response of crease lines for carton-based packaging. In *XIX Aimeta National Conference*.

Pereira, V. M., Castro Neto, A. H., Liang, H. Y., and Mahadevan, L. (2010). Geometry, Mechanics, and Electronics of Singular Structures and Wrinkles in Graphene. *Physical Review Letters*, 105(15):156603.

Phaal, R. and Calladine, C. R. (1992a). A simple class of finite elements for plate and shell problems. II: An element for thin shells, with only translational degrees of freedom. *International Journal for Numerical Methods in Engineering*, 35(5):979–996.

Phaal, R. and Calladine, C. R. (1992b). A simple class of finite elements for plate and shell problems. II: An element for thin shells, with only translational degrees of freedom. *International Journal for Numerical Methods in Engineering*, 35(5):979–996.

Pique, A., Mathews, S., Birnbaum, A. J., and Charipar, N. (2011). Microfabricating 3D structures by laser origami. *SPIE Newsroom*.

Pradier, C., Cavoret, J., Dureisseix, D., Jean-Mistral, C., and Ville, F. (2016). An Experimental Study and Model Determination of the Mechanical Stiffness of Paper Folds. *Journal of Mechanical Design*, 138(4):041401.

Qiu, C., Zhang, K., and Dai, J. S. (2016). Repelling-Screw Based Force Analysis of Origami Mechanisms. *Journal of Mechanisms and Robotics*, 8(3):031001.

Randall, C. L., Gultepe, E., and Gracias, D. H. (2012). Self-folding devices and materials for biomedical applications. *Trends in biotechnology*, 30(3):138–46.

Resch, R. and Christiansen, H. (1971). Kinematic Folded Plate System. In Krapfenbauer, R., editor, *IASS Symposium on Folded Plates and Prismatic Structures*, Vienna, Austria.

Rubio, W. M., Paulino, G. H., and Silva, E. C. N. (2011). Tailoring vibration mode shapes using topology optimization and functionally graded material concepts - Abstract - Smart Materials and Structures - IOPscience.

Ryu, J., D'Amato, M., Cui, X., Long, K. N., Jerry Qi, H., and Dunn, M. L. (2012). Photo-origamiBending and folding polymers with light. *Applied Physics Letters*, 100(16):161908.

sarah-marie Belcastro and Hull, T. C. (2002a). A mathematical model for non-flat origami. In Hull, T. C., editor, *Origami3: Proceedings of the 3rd International Meeting of Origami Mathematics, Science, and Education*, pages 39–51. A K Peters/CRC Press.

sarah-marie Belcastro and Hull, T. C. (2002b). Modelling the folding of paper into three dimensions using affine transformations. *Linear Algebra and its Applications*, 348(1-3):273–282.

Schenk, M. (2011). *Folded shell structures*. Ph.d. thesis, University of Cambridge.

Schenk, M., Guest, S., and McShane, G. (2014a). Novel Stacked Folded Cores for Blast-Resistant Sandwich Beams. *International Journal of Solids and Structures*.

Schenk, M. and Guest, S. D. (2011). Origami folding: A structural engineering approach. In Wang-Iverson, P., Lang, R. J., and Yim, M., editors, *Origami 5*, pages 293–305. CRC.

Schenk, M. and Guest, S. D. (2013). Geometry of Miura-folded metamaterials. *Proc. Natl. Acad. Sci. U.S.A.*, 110(9):3276–81.

Schenk, M., Kerr, S., Smyth, A., and Guest, S. (2013). Inflatable Cylinders for Deployable Space Structures. In *Proceedings of the First Conference Transformables 2013 in the Honor of Emilio Perez Piñero*, Seville, Spain.

Schenk, M., Viquerat, A. D., Seffen, K. A., and Guest, S. D. (2014b). Review of Inflatable Booms for Deployable Space Structures: Packing and Rigidization. *Journal of Spacecraft and Rockets*, 51(3):762–778.

Schmidt, B. V. K. J., Fechler, N., Falkenhagen, J., and Lutz, J.-F. (2011). Controlled folding of synthetic polymer chains through the formation of positionable covalent bridges. *Nature chemistry*, 3(3):234–38.

Shenoy, V. B. and Gracias, D. H. (2012). Self-folding thin-film materials: From nanopolyhedra to graphene origami. *MRS Bulletin*, 37(09):847–854.

Silverberg, J. L., Evans, A. A., McLeod, L., Hayward, R. C., Hull, T., Santangelo, C. D., and Cohen, I. (2014). Using origami design principles to fold reprogrammable mechanical metamaterials. *Science*, 345(6197):647–650.

Silverberg, J. L., Na, J.-H., Evans, A. A., Liu, B., Hull, T. C., Santangelo, C. D., Lang, R. J., Hayward, R. C., and Cohen, I. (2015). Origami structures with a critical transition to bistability arising from hidden degrees of freedom. *Nature Materials*, 14(4):389–393.

Skidmore Owings and Merrill (1962). United States Air Force Academy Cadet Chapel.

Song, J., Chen, Y., and Lu, G. (2012). Axial crushing of thin-walled structures with origami patterns. *Thin-Walled Structures*, 54:65–71.

Stellman, P., Buchner, T., Arora, W. J., and Barbastathis, G. (2007). Dynamics of Nanostructured Origami. *Journal of Microelectromechanical Systems*, 16(4):932–949.

Tachi, T. (2009a). Generalization of rigid foldable quadrilateral mesh origami. In *Proc. Int. Assoc. Shell and Spatial Structures*, pages 2287–2294, Valencia, Spain.

Tachi, T. (2009b). One-dof cylindrical deployable structures with rigid quadrilateral panels. In *Proc. Int. Assoc. Shell and Spatial Structures*, pages 2295–2305, Valencia, Spain.

Tachi, T. (2009c). Simulation of rigid origami. In Lang, R. J., editor, *Origami4*, pages 175–187. AK Peters.

Tachi, T. (2010a). Freeform rigid-foldable structure using bidirectionally flat-foldable planar quadrilateral mesh. In Ceccato, C., Hesselgren, L., Pauly, M., Pottmann, H., and Wallner, J., editors, *Advances in Architectural Geometry*, pages 87–102, Vienna. Springer Vienna.

Tachi, T. (2010b). Geometric considerations for the design of rigid origami structures. In *Proceedings of the International Association for Shell and Spatial Structures (IASS) Symposium*, Shanghai, China.

Tachi, T. (2011). Rigid-foldable thick origami. In Wang-Iverson, P., Lang, R. J., and Yim, M., editors, *Origami 5*, pages 253–263. CRC.

Tachi, T., Filipov, E. T., and Paulino, G. H. (2015). Deployable folded-core sandwich panels guided by a generating surface. In *Proc. Int. Association for Shell and*, Amsterdam, Netherlands.

Tachi, T. and Hull, T. (2016). Self-folability of rigid origami. In *Proc. ASME 2016 IDETC/CIE*, page 60546, Charlotte, NC.

Tachi, T., Masubuchi, M., and Iwamoto, M. (2011). Rigid Origami Structures with Vacuumatics: Geometric Considerations. In *Proceedings of the IASS-APCS*, Seoul, South Korea.

Tachi, T. and Miura, K. (2012). Rigid-foldable cylinders and cells. *J. Int. Assoc. Shell and Spatial Structures*, 53(4):217–226.

Tanaka, K., Kamotani, Y., and Yokokohji, Y. (2007). Origami folding by a robotic hand. In *2007 IEEE/RSJ International Conference on Intelligent Robots and Systems*, pages 2540–2547. IEEE.

Thrall, A. and Quaglia, C. (2014). Accordion shelters: A historical review of origami-like deployable shelters developed by the US military. *Engineering Structures*, 59:686–692.

Tolley, M. T., Felton, S. M., Miyashita, S., Aukes, D., Rus, D., and Wood, R. J. (2014). Self-folding origami: shape memory composites activated by uniform heating. *Smart Materials and Structures*, 23(9):094006.

Tsunoda, Hiroaki, Senbokuya, Y., and Watanabe, M. (2005). Deployment characteristics evaluation of inflatable tubes with polygon folding under airplane microgravity environment. *Space Technology*, 25:127–137.

Tyas, A., Pichugin, A. V., and Gilbert, M. (2011). Optimum structure to carry a uniform load between pinned supports: exact analytical solution. *Proceedings of the Royal Society of London A: Mathematical, Physical and Engineering Sciences*, 467(2128).

Vatanabe, S. L., Paulino, G. H., and Silva, E. C. N. (2014). Maximizing phononic band gaps in piezocomposite materials by means of topology optimization. *The Journal of the Acoustical Society of America*, 136(2):494–501.

Vliegenthart, G. A. and Gompper, G. (2006). Forced crumpling of self-avoiding elastic sheets. *Nature Materials*, 5(3):216–221.

Waibel, J. (2016). Origami Dresses.

Waitukaitis, S., Menaut, R., Chen, B. G.-g., and van Hecke, M. (2015). Origami Multistabilty: From Single Vertices to Metasheets. *Physical Review Letters*, 114:055503.

Wei, Z. Y., Guo, Z. V., Dudte, L., Liang, H. Y., and Mahadevan, L. (2013). Geometric mechanics of periodic pleated origami. *Phys. Rev. Lett.*, 110(21):215501.

Witten, T. A. (2007). Stress focusing in elastic sheets. *Rev. Mod. Phys.*, 79(2):643–675.

Wood, R. (2008). The First Takeoff of a Biologically Inspired At-Scale Robotic Insect. *IEEE Transactions on Robotics*, 24(2):341–347.

Wood, R. and Others (2014). Harvard Microbiotics Lab.

Woodruff, J. and Brown, P. (2009). Connecticut Science Center by César Pelli & Associates.

Wu, J. (2008). Origami Bellows.

Xi, Z. and Lien, J.-M. (2015). Folding and unfolding origami tessellation by reusing folding path. In *2015 IEEE International Conference on Robotics and Automation (ICRA)*, pages 4155–4160. IEEE.

Xie, R., Chen, Y., and Gattas, J. M. (2015a). Parametrisation and Application of Cube and Eggbox-type Folded Geometries. *International Journal of Space Structures*, 30(2):99–110.

Xie, R., Li, J., and Chen, Y. (2015b). The Graded Origami Structures. In *Volume 5B: 39th Mechanisms and Robotics Conference*, page V05BT08A026. ASME.

Yasuda, H. and Yang, J. (2015). Reentrant Origami-Based Metamaterials with Negative Poisson's Ratio and Bistability. *Physical Review Letters*, 114(18):185502.

Yasuda, H., Yein, T., Tachi, T., Miura, K., and Taya, M. (2013). Folding behaviour of TachiMiura polyhedron bellows. *Proceedings of the Royal Society A: Mathematical, Physical and Engineering Sciences*, 469:20130351.

Yenn, T. (2000). Flip-Flop.

Yokozeki, T., Takeda, S.-i., Ogasawara, T., and Ishikawa, T. (2006). Mechanical properties of corrugated composites for candidate materials of flexible wing structures. *Composites Part A: Applied Science and Manufacturing*, 37(10):1578–1586.

Yoo, J. and Aksimentiev, A. (2013). In situ structure and dynamics of DNA origami determined through molecular dynamics simulations. *Proceedings of the National Academy of Sciences of the United States of America*, 110(50):20099–104.

Zegard, T. (2014). *Structural optimization: From Continuum and ground structures to additive manufacturing*. Phd dissertation, University of Illinois at Urbana Champaign.

Zhu, S. and Li, T. (2014). Hydrogenation-assisted graphene origami and its application in programmable molecular mass uptake, storage, and release. *ACS nano*, 8(3):2864–72.

Zirbel, S. A., Lang, R. J., Thomson, M. W., Sigel, D. A., Walkemeyer, P. E., Trease, B. P., Magleby, S. P., and Howell, L. L. (2013). Accommodating Thickness in Origami-Based Deployable Arrays. *J. Mechanical Design*, 135(11):111005.